SHEAR-WAVE ATTENUATION AND VELOCITY STUDIES IN SOUTHEASTERN ASIA

Alemayehu Lakew Jemberie, B.Sc., M.Sc.

A Digest Submitted to the Faculty of the Graduate School
of Saint Louis University in Partial Fulfillment of
the Requirements for the Degree of
Doctor of Philosophy

2002

Digest

Models of shear-wave Q (Q_μ) have been obtained for southeastern Asia using two methods. The first method inverts attenuation coefficients of the fundamental Rayleigh mode obtained using a standard two-station technique. The second method matches theoretical amplitude spectra for the fundamental and higher-mode Rayleigh waves computed for previously obtained velocity and assumed Q_μ models, and earthquakes with known source depths and focal mechanisms, to observed spectra. The latter method provides much better regional coverage than the first and allows us to map lateral variations of Q_μ at various levels in the crust and uppermost mantle.

For the single-station, multi-mode method, I assumed an Earth model consisting of three layers, layer 1 being 10 km, layer 2 being 20 km, and layer 3 being 30 km in thickness. Q_μ in layer 1 achieves lowest values (about 40) in the southern part of the Tibetan Plateau and in the Tarim basin and is highest (about 250) in southeastern China. The Q_μ map of layer 2 indicates that the highest Q_μ values (about 150) lie in the central part of China and in parts of the Sino-Korean platform. The lowest Q_μ value (about 50) occurs in Tibet and the Pamir thrust system. Layer 2 exhibits an overall increase in Q_μ going from south to north. For layer 3 the resolution of crustal variations in Q_μ is poorer than layers 1 and 2. Available results, however, indicate that Q_μ is highest (about 180) under southern Mongolia and the Tarim basin, somewhat lower (100) beneath the southern portion of the Baikal Rift, and lowest (80) under

the Pamir thrust system.

SHEAR-WAVE ATTENUATION AND VELOCITY STUDIES IN SOUTHEASTERN ASIA

Alemayehu Lakew Jemberie, B.Sc., M.Sc.

A Dissertation Submitted to the Faculty of the Graduate School
of Saint Louis University in Partial Fulfillment of
the Requirements for the Degree of
Doctor of Philosophy

2002

COMMITTEE IN CHARGE OF CANDIDACY:

Professor Brian J. Mitchell,
Chairperson and Advisor

Associate Professor John P. Encarnación

Professor Robert B. Herrmann

Dedication

This dissertation is dedicated to the memory of my father

Lakew Jemberie Kassa.

Acknowledgments

Above all, thank to the almighty God for everything! I have a great respect for my advisor Prof. Brian Mitchell. I thank him for his personal advice and guidance in this work. His excellent personal character made me stay and finish my study in this department. I thank Drs. Robert Herrmann and John Encarnación for reading the dissertation and their comments. Thanks also to Dr. David Kirschner for his moral support and for leading the field trips I enjoyed. I also thank Dr. Charles Graves for setting up the Latex commands script, without which writing the dissertation would have been much more time consuming.

I went through a very hard time during my study, both financially and socially. Without the moral support of my friends things would have been harder. I do not have enough words to thank Birhane Tsegaye and Beyene Asmare who helped me a lot in those hard times. Thanks to my friend Muluken, for his help whenever I needed it. I also thank the families of Moges and Silas, Negassie and Belaynesh for helping me in many ways. I thank the Ethiopian community in Saint Louis in general, and Ato Gedlu Metaferia in particular for his moral support. The Saint Gabriel/St. Mary Ethiopian Orthodox Church has been a good place for me to ask God for help. I thank Aba Wolde Tsadik, Aba Wolde Mariam and the church members for praying for me. I thank my friends, Mesfine Janka, Mesfine Tsige, Dagnachew, Tsegaye, Negussie, Abebe and others, for giving me moral support.

My wife, Menbere Ejigu, and my children, Biruh Alemayehu, Wossenyelesh Alemayehu and Befekadu Alemayehu have also gone through those hard times with me. Their strong support and patience was very crucial for finishing my study. I thank my family in Ethiopia for their prayers asking God to help me finish this study and to my brother Tadele for his constant moral support and for coming here to see me. I thank sister Judy for comeing to my home every Monday and Friday to teach my wife the basics of the english language.

I thank Beshara,Young-Soo, Fabrizio, Luca, Mohamed, Minoo, Hogn-yi and others for being very good friends of mine. I am very fortunate to be in the United States. I thank America for giving me the opportunity to study here.

Table of Contents

List of Tables

List of Figures

1. Introduction

1.1 The problem

Delineation of elastic, or velocity, structure of the Earth has long been a goal of the world's seismologists. For the first few decades of seismological research, research on velocity structure was restricted to the determination of one-dimensional models of the solid Earth and of various regions within it. Seismologists are currently obtaining three-dimensional velocity models and are working to resolve finer and finer features in the Earth.

Knowledge of seismic velocity structure of the crust and the upper mantle is important for several reasons. These include accurate location of earthquakes, determination of the composition and origin of the outer layers of the earth, improvement of our ability to discriminate nuclear explosions from earthquakes, and interpretation of large-scale tectonics.

Earth material is, however, not perfectly elastic. Departure from perfect elasticity, at seismic frequencies, is termed anelasticity and is commonly described by the parameter Q, or quality factor. The inverse of Q (Q^{-1}) is termed the internal friction. The higher the value of Q (or the lower the value of Q^{-1}), the more efficiently seismic waves will propagate through the Earth. Q^{-1} is defined as

$$Q^{-1} = \frac{\Delta E}{2\pi E_{max}} \tag{1.1}$$

where ΔE is the amount of energy lost per cycle and E_{max} is the maxi-

mum amount of elastic energy contained in a cycle.

We can also write an equation for amplitude as a function of distance traveled:

$$A(x) = A_0 e^{-(\frac{f\pi}{Qv})x} \tag{1.2}$$

where f is frequency, u is group velocity and x is distance traveled. Models of seismic Q are much less common than those of seismic velocities in the Earth. The primary reason for this is that valid measurements of amplitude decay due to Q in the Earth are much more difficult to obtain than are valid measurements of arrival times due to the velocity structure of the Earth. Velocity studies usually entail measuring arrival times of the onsets of various body-wave phases or the phase or group arrival times of portions of surface-wave trains. Time measurements for the early portions of these waves are usually not greatly degraded by propagation through three-dimensional complexities in the Earth. Seismic amplitudes, since they are usually measured at times later than the wave onsets, can be adversely affected by such factors as focusing/defocusing, multipathing, scattering, and wave conversions that occur along the wave path and beneath recording stations.

Although determinations of seismic Q have much greater uncertainties than velocity determinations, we are helped by the wide range of Q values that occur in the crust and upper mantle. If we consider only crystalline rock (and exclude sedimentary basins), seismic velocities in continents may vary laterally by no more than 5 or 10%. In contrast, seismic Q values may vary laterally by nearly two orders of magnitude.

Thus, if we are interested primarily in regional variations in Q (and not precise absolute values), we can often obtain useful Q information even though random and systematic errors may be relatively large.

It is important to obtain models of Q for the Earth because those models are sensitive to factors not easily determined from velocity studies. These include temperature and fluid content in the crust and temperature, partial melt, and the presence of solid state defects in the upper mantle.

Previous studies have shown that Q varies regionally and that variation appears to be closely related to the tectonic history of the crust. Tectonically active regions and regions which were active in the recent past invariably exhibit lower Q values than do old stable cratons. This study concentrates on a region that includes a diffuse plate boundary undergoing collisional tectonics in southeastern Asia. My results show that even in this relatively small region, shear-wave Q exhibits clearly measurable regional variations.

My purpose is to map the shear-wave attenuation structure of southeastern Asia (60^oE - 140^oE and 20^oN - 60^oN), a region that is complex both in its topography and its tectonics. I will present models of shear-wave Q and show how that parameter varies laterally in selected depth ranges. Since shear-velocity models are necessary preliminary information for Q studies, I will also determine velocity models for the region of study.

1.2 Review of related literature

1.2.1 Seismic wave velocities

Studies of a large heterogeneous region using surface wave dispersion methods often include three steps: (1) Measurement of surface wave dispersion for numerous wave paths crisscrossing the region, (2) subdivision of the region into a number of small elements and determination of pure-path dispersion curves for each element from the mixed-path measurements obtained in step 1, and (3) inversion of the pure-path dispersion curves for seismic velocity models appropriate for each element (Feng and Teng, 1983).

The second step is often referred to as regionalization. This step is needed because no practical theory has thus far been available to calculate theoretical dispersion for a laterally heterogeneous earth model. Early methods of regionalization, (Toksoz and Anderson, 1966), consisted of dividing a surface-wave path into oceanic, shield, and tectonically active regions. Each type of region was known to have a different effect upon the average group velocity. Toksoz and Anderson (1966) noted that shield areas raise the average group velocity, whereas active tectonic regions have the effect of lowering it. As a result, surface wave paths crossing different tectonic regions should show different trends in their average group velocity dispersion curves.

A common procedure in regionalization is to subdivide a region into geological provinces each of which is assumed to be laterally relatively uniform, then to determine the pure-path dispersion curves from mixed-path data by a least squares procedure (e.g., Yu and Mitchell, 1979; Pat-

ton, 1980). Within each of these laterally relatively homogeneous geological provinces (pure paths) inversion of the dispersion data is carried out by assuming a layered half-space model (Haskell, 1953; Harkrider, 1964).

There are a number of shear-velocity studies of eastern Asia. Some of these use continental surface waves that have propagated across the Eurasian continent and include paths through southeastern Asia (e.g., Patton, 1980; Feng and Teng, 1983). The rest are regional studies using very few paths confined to eastern Asia (e.g., Wier, 1982; Pines et al., 1980; Zhang, 1998; and many others in Chinese).

Papers published in China (both in English and Chinese) are very difficult to obtain and may be available only to Chinese scientists. The same is true for publications in Russian for studies of the Siberian crust.

Using the tripartite method of measuring Rayleigh wave phase velocities, Tseng and Sung (1963) obtained velocities (at 20-30 sec) over a large area of China. They interpreted the observations by comparing them to standard dispersion curves (Press et al., 1956) to determine crustal thickness. West of Chengdu they found crustal thickness to be between 50 and 76 km. North of Sian and Nanking crustal thicknesses range from 40 to 55 km. These thickness are generally greater than those found for the South China plate, where they range between 34 and 44 km. The crust in both the northern and southern regions is thinner near the coastline.

In the South China plate, Rosenthal and Teng (1977) inverted group velocities of Love and Rayleigh waves over the period range 10-60 sec to

obtain crust and upper mantle structure. Their model shows a crustal thickness of 40 km. The S_n velocity is $4.5 \pm 0.1 km/s$, and the lid (the uppermost mantle above the low-velocity zone)is believed to be thin, between 20 and 30 km.

A detailed picture of the crustal thickness under Japan is known from studies of Rayleigh and Love wave phase velocities (Aki, 1961; Aki and Kaminuma, 1963; Kaminuma and Aki, 1963; Kaminuma, 1966). The maximum thickness is 36 km under central Honshu and thins to 24 km along the coastlines.

Pines et al., (1980) used a single source-single station method to study the shear-velocity structure of China along four paths, two across the Tibet plateau, one across the northern and northwestern China sub-plates, and one across coastal China. They used large aftershocks of several great $(M \geq 7)$ earthquakes, which occurred in China in the $1970's$, to measure Rayleigh and Love-wave fundamental- and first higher-mode group velocities. All events in their study were recorded at two seismological Research Observatory (SRO) stations located in Iran (MAIO) and Taiwan (TATO). Rayleigh-wave group velocities ranged between 2.60 and 3.65 km/s, and steep slopes occurred in the dispersion curves between 40 and 60 sec.

Their results can be summarized as follows:

1. Group velocities obtained for pure paths across the Tibetan plateau are unusually low compared to average continental dispersion (Ewing et al., 1957). Results of velocity inversions indicate that a four-layer 70-km-thick crust is an adequate model for the Tibetan plateau. The first layer is 15 km thick and has shear velocities between 2.87 and 3.06

km/s. The second layer is approximately 15 km thick and has shear velocities between 3.20 and 3.40 km/s. The third layer is 15-20 km thick and has shear velocities between 3.40 and 3.70 km/s. The fourth layer is 20-25 km thick and has shear velocities between 3.85 and 3.95 km/s. The velocity at the top of the mantle is approximately 4.4 km/s. At all depths shear velocities are lower than either the Gutenburg earth model (Takeuchi et al., 1964) or the Brune and Dorman (1963) model for the Canadian Shield.

2. Group velocities for mixed great circle paths crossing the North China sub-plate, the Northwest China sub-plate, and central Asia (from Tangshan in northern China to Mashad in Iran) are lower than average continental velocities. Results of their inversion indicate that a three-layer, 45-km-thick crust explains the dispersion data. The first layer is approximately 10 km thick and has an average shear velocity of approximately 3.0 km/s. The second layer is 15-20 km thick and has an average shear velocity of 3.55 km/s. The layer at the base of the crust, 20-25 km thick, has an average shear velocity of approximately 3.80 km/s. The average shear velocity at the top of the mantle is 4.40-4.45 km/s. Comparison of the Canadian Shield model (Brune and Dorman, 1963) with the average shear-velocity model of this path shows that both models have higher shear velocities in the crust and the top of the mantle.

3. Group velocities for the path along the eastern coast of China between Tangshan in northern China and Taipei in Taiwan, are the closest of the three regions to having average continental dispersion. Inversion of these velocities indicate that a three-layer 30-km thick crust is

an adequate model. The first layer, approximately 5-7 km thick, has a shear-velocity of approximately 2.95 km/s. The second layer is approximately 10 km thick. The third layer, approximately 15-20 km thick, has a shear-velocity of approximately 3.85 km/s. The shear-velocity of 4.46 km/s at the top of the mantle is lower than the shear velocity of the Canadian shield (4.65 km/s). Tung and Teng (1974) also inferred a shear-velocity of 4.42 km/s at the top of the mantle from the inversion of Rayleigh wave velocities along a path crossing northeastern China and recorded in Hong kong.

Weir (1982) obtained a shear-velocity model for southeastern China from the simultaneous inversion of Rayleigh- and Love-wave dispersion. His results suggest that the crust of southeastern China is typical of continents, but the upper mantle has an unusually low shear-wave velocity. The shear-wave velocity of the uppermost mantle may be as low as 4.35 km/s which is in agreement with the Pines et al. (1980) result.

Feng and Teng (1983) used 109 wave paths to obtain the group velocities of fundamental-mode Rayleigh waves within the Eurasian continent. They applied stochastic inversion theory to mixed-path measurements to extract pure-path group velocities for $10^o \times 10^o$ grid elements that form the subdivisions of Eurasia. They then constructed a three-dimensional crust and upper mantle structure of the Eurasian continent to a depth of 300 km. They found the average crustal thickness of Eurasia to be about 40 km. They obtained abnormally thick crust between 50 and 65 km, in areas of the Tien Shan, the Altai mountains, Afghanistan, Pamir, Tibet, and Burma. Among them, Tibet

has the least dense crust and highest elevation. Feng and Teng (1983) found that, upper mantle seismic velocities of the tectonically active regions of Asia are considerably lower than those of the European and Siberian cratons.

Zhang (1998) studied three-dimensional shear-velocity variations, and their possible dynamic implications, in the upper mantle beneath eastern Asia, including the Tibetan Plateau and surrounding regions. He found that the velocity structure beneath eastern Asia at a depth of 50 km is highly correlated with the crustal thickness (thicker crust has higher velocities) and that velocities at depths of 100 and 400 km can be divided into several blocks that correlate with surface tectonics. Fast material underlies the old platforms, and the slow material lies beneath the active fold systems.

The shear-wave velocity structure in the upper 50 km under eastern Asia does not correlate with the geological setting. This lack of correlation may indicate that many centers of small-scale activity or chemical variations occur in this region. Backarc basins and sites of recent subduction explain slow velocities above 200 km depth and moderately fast velocities below that depth. Velocities in the Tianshan, the Altai Mountains, and the Baikal rift all have different depth distributions. Zhang (1998) interpreted that difference as indicating that this tectonic belt is related to externally induced tension, possibly due to collision of India and Eurasia.

Zhang (1998) reported that fast velocities appear to extend from the Indian sub-continent to the north and east of the Tibetan Plateau with a small dip-angle of $10^0 \pm 3^0$ over a length of more than 1000 km.

High-velocity materials occur in the mantle below the Pamir, Tarim and Junggar regions at depths between 100 and 300 km.

Wu and Levshin, (1994) used group velocities of both Rayleigh and Love waves in the period range 30-70 s to obtain tomographic group velocity maps of eastern Asia ($60^oE - 140^oE$ and $20^oN - 60^oN$). Wu et al. (1997) expanded the range of this study to include Siberia and other nearby regions ($40^oE - 160^oE$ and $20^oN - 70^oN$).

Both studies show that Tibet appears as a region of prominently low velocity (about 15% below average) structure, with western and central Tibet often having the lowest velocities. The central Asian fold belt and the Angara craton show consistently high group velocities. Some lesser tectonic features are also recognizable. For example, Lake Baikal is seen as a high-velocity feature at periods greater than 40 seconds. However, the high velocities extend beyond the southern end of Lake Baikal to Mongolia. The North China Plain is an area of high velocities as a result of relatively thin crust. The South-China block, the least tectonically active region of China, is generally an area of high velocity. For periods greater than 40 seconds, a NNE trending high group-velocity gradient exists in eastern China. From the group velocity maps, average dispersion curves at twelve locations were determined and inverted to obtain velocity structure. The main results of the group-velocity inversion are that: (1) the Tibetan crust is about 60 km thick, with low crustal and upper mantle shear velocities of 3.3 km/s and 4.2 km/s, respectively; (2) with the Moho constrained at 40-43 km, the Angara craton and the Central Asian fold belt have a Vs in excess of 4.6 km/s; (3) relatively low shear velocities are obtained for tectoni-

cally active areas. In many parts of the study area, where Precambrian basement is exposed, processes in the crust and upper mantle, related to recent tectonic activity, have modified the velocity structure so those regions are no longer underlain by high-velocity crust and mantle.

1.2.2 Seismic wave attenuation

Seismologists have long known that seismic waves in the Earth attenuate with distance at rates greater than those predicted by geometrical spreading of the wave fronts. The excess attenuation might be caused by intrinsic anelasticity of the earth, such as movement along mineral dislocations, shear heating at grain boundaries and movement of interstitial fludis or by inhomogeneities which refract, reflect, or scatter seismic energy (Anderson et al., 1965; Jackson and Anderson, 1970; Mitchell, 1995).

The decrease in seismic wave amplitudes produced by those factors must be taken into account when determining magnitudes of earthquakes or yields of explosions. This practical need generated much of the research on seismic wave attenuation during past decades.

If we can isolate the component of attenuation which is produced by intrinsic anelasticity, we can obtain information about properties such as temperature, state, fluid content of permeable rock, and movement of solid-state defects, factors which are closely tied to the tectonic history of the crust and upper mantle and which are not easily studied using only seismic velocities (Anderson, et al., 1965; Kovach, 1978; Jackson and Anderson, 1970; Mitchell, 1995.)

The effects of intrinsic attenuation on amplitudes of surface waves

may be masked by amplitude variations due to lateral refraction, multipathing, or focusing/defocusing. It is important to try to remove, or at least minimize, the effects of lateral structural complexities before making interpretations of attenuation data in terms of intrinsic Q. Experience has shown that determinations of surface-wave attenuation coefficients can be uncertain because of all of these effects. Attenuation measurements therefore require great care and careful selection of sources, station locations, and paths (Patton, 1980; Mitchell, 1995; Mitchell, et al., 1997).

McGarr (1969) studied horizontal refraction of Rayleigh waves at 20 sec caused by lateral heterogeneities of phase velocity along Pacific and Atlantic oceanic paths. In his study, amplitude fluctuations across stations on the coast of the western United States were shown to be due to effects of lateral variation of phase velocity, causing focusing and defocusing of surface-wave energy.

Patton (1980) obtained ray paths of 40 s period Rayleigh waves from a synthetic ray tracing experiment to study lateral refraction of surface waves in Eurasia. His study showed that rays are defocused when crossing a rapid velocity transition zone such as that from the Tarim Basin (high velocity) to the Tien Shan and Kunlun fold belts (low velocity). Focusing and crossing of rays, which imply multipathing, are found for azimuths in southeastern Asia.

The study of Pines et al. (1980) of Love wave propagation across the Tibetan plateau shows no amplitude maxima in the fundamental-mode dispersion curves of these waves between 40 and 60 sec. They inferred that this occurred because the Love waves did not follow a

least-time path. A possible structural implication is that there may be structures along the path corresponding to wavelengths of the Love waves, causing the wave energy to travel along a non-least time path with slower velocities.

One way to minimize the effects of lateral structural variations is to use paths which are as short as possible. Surface waves, however, attenuate very slowly with distance, especially in high-Q regions. Since amplitude decay is small for short distances of travel, it is difficult to obtain precise and reliable measurements of the attenuation coefficients for short paths. To obtain precise measurements of attenuation, it is preferable to use long paths, but with long paths we increase the chance of introducing systematic errors, from factors such as focusing, into our measurements (Mitchell, 1995).

The best method to use for a particular region will depend on several factors, including the availability of great circle paths and two in-line stations, suitably located sources and, in the case of single-station measurements, the availability of sources with known focal mechanisms. Because we cannot always count on the occurrence of earthquakes in places that would be suitable for the application of a particular method, several methods for determining surface wave attenuation coefficients have been developed; some of these are described by Mitchell (1995).

There were no known surface-wave attenuation studies in the Eurasian continent, particularly in eastern Asia, prior to the study of Yacoub and Mitchell (1977). Tryggvason (1965) and Burton (1974) had, however, obtained worldwide Rayleigh wave attenuation data for which some paths, and portions of paths, traverse Eurasia. They may

not have considered purely Eurasian paths because of difficulty in determining attenuation coefficients for paths across Eurasia, because of the small number of available stations, or because paths between sources and stations are necessarily long and usually cross more than one tectonic province. These factors are likely to produce large errors in measured attenuation coefficient values.

Yacoub and Mitchell (1977) used surface waves (5 to 50 sec) generated by six earthquakes and two nuclear explosions to study the attenuation coefficients of the fundamental Rayleigh mode across the Eurasia landmass. Because of the great scatter in the then available amplitude observations, they divided Eurasia into only two provinces guided by a Bouguer anomaly map and topographic features of Eurasia.

They separated Eurasia into stable provinces comprised of Siberia, northern Europe, India, and the Arabian Peninsula, and a tectonic province comprised of a zone extending from China and eastern Siberia into southern Europe. The latter region includes the fold systems of China, the Tibetan Plateau, the Himalayas, and countries adjacent to the Mediterranean.

Their results show that Rayleigh-wave attenuation coefficients for stable regions decrease from values between $3 \times 10^{-4} km^{-1}$ and $4 \times 10^{-4} km^{-1}$ at the shorter periods to values near $2 \times 10^{-4} km^{-1}$ at longer periods. Tectonic regions are characterized by values as high as $7.5 \times 10^{-4} km^{-1}$ at the short periods and by values near $3 \times 10^{-4} km^{-1}$ at the longer periods. Considerable overlap of the standard deviation bars occurs at all periods between stable and tectonic regions when the results for four events are averaged. Some individual events, however, indicate

that real differences in the attenuation coefficients occur at short periods, tectonic regions being characterized by greater attenuation than shield regions.

Patton (1980) proposed a Rayleigh-wave phase-velocity regionalization of Eurasia based on crustal conditions and topography involving five continental provinces: the Indian shield, northern Platforms and Shields, forelands and coastal plains, tectonically active regions, and plateaus. He observed a negative correlation between phase velocities and attenuation across eastern and southern Asia. For example, over Tibet, where attenuation has been reported to be high in the frequency range 0.02-0.03 Hz (Bird, 1976), he observed low velocities at 50 sec periods, but very small, if not negative, attenuation coefficients. Phase velocity was found to increase from southern to northern China and attenuation was found to increase in the same direction. Stations in India record the highest phase velocities in southern Asia and also the highest apparent attenuation. The expected correlation is that the lower the phase velocity, the lower the value of Q (or higher the attenuation), as in the western United States (Lee and Solomon, 1975), or vise versa. These observations suggest that factors other than intrinsic Q of the medium enter into determining the amplitudes of surface waves in and around the Eurasian continent. These factors include lateral refraction and focussing/defocussing of surface waves due to lateral changes in elastic structure.

Mitchell et al., (1997) derived a tomographic image of broad-scale variations of L_g coda Q for most of Eurasia. Their image indicates that L_g coda Q, at a frequency of 1 Hz, varies between about 200 and

1000. Lowest Q values (≤ 350) all lie within the Tethysides orogenic belt which includes most of southern Asia. They interpreted the low Q as resulting largely from hydrothermal fluids, generated by tectonic activity and heating, that now reside in cracks and permeable portions of the Eurasian crust.

1.3 Research questions

I will try to answer the following questions in this research.

1. How does the Q_{μ}^{-1} depth distribution vary from place to place throughout southeastern Asia? Is there a systematic variation from south to north? Are there east-west variations throughout Southeastern Asia? Does this variation correlate with the tectonics of the region?

2. How does $Q\mu^{-1}$ structure correlate with shear-velocity structure in regions where both types of model are available? If there is correlation, what is the reason for it?

3. How do variations in shear-velocity distribution with depth correlate with the regional tectonics of eastern Asia?

4. How does the shear-velocity structure obtained in this study agree with models obtained from earlier studies in the Eurasian continent?

5. How do the $Q\mu^{-1}$ and shear-velocity structures of southeastern Asia compare with those in other regions?

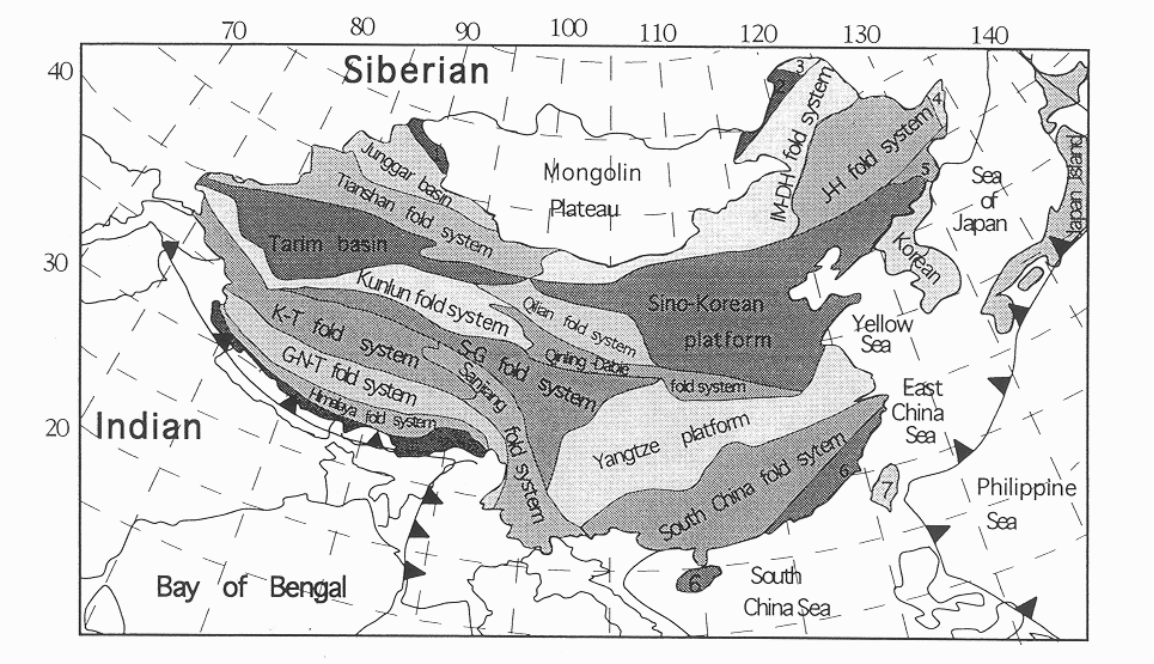

Figure 1.1: Tectonic map of China (Ren et al., 1987; Zhang, 1998)

1.4 Tectonics of Southeastern Asia

1.4.1 Tectonic settings

Figure 1.1 shows the different tectonic units of China. Brief descriptions of them mostly follow after Ren et al., 1987. The South China Block is composed of the Yangteze platform and the south China fold system. The basement rocks of the Yangtze platform are Proterozoic in age (Yang et al.,1986). The South China geosynclinal fold systems were formed during the late Cambrian to the end of the Silurian (Ren et al., 1987). At present, this region is one of the least tectonically active parts of southeastern Asia. The seismicity is very low except in southeastern coastal China near Taiwan, where some seismicity is present, probably related to the collisional tectonics there (Wu et al., 1994, 1997).

The Sino-Korean paraplatform (North-China Craton) is the oldest

platform in China. It achieved its present form 1700 my ago (Proterozoic), although the first continental nucleus may have originated 3000 my (Archean) ago (Ren et al., 1987). This paraplatform, roughly triangular in shape, consists of several tectonic units separated by active structures that differ in their geological history and intensity of recent tectonics. In this paraplatform, the North China plain is active, mainly as an extensional basin under NNW tension (Nabelek et al., 1987). The older blocks west of the plain, such as the Ordos platform, remain inactive (Wu et al., 1997).

Northeastern China consists of two fold systems: the Inner Mongolian-Greater Hinggan fold system and the Jilin-Heilongjiang fold system. The Inner Mongolian-Greater Hinggan geosynclinal fold system occupies the south-central part of the Geater Hinggan Mountains and the Inner Mongolian grassland. Most parts of the region are connected with corresponding fold belts in Mongolia. The main outcrops in the region are of late Paleozoic strata, generally not metamorphosed or very slightly metamorphosed.

The Jilin-Heilongjiang fold system is located in the Zhangguangcai Mountain and the Lesser Hinggan Mountains. It is bounded on the south by the Jiaoliao platform uplift of the Sino-Korean platform, on the west by the Inner Mongolian-Greater Hinggan fold system, and on the east by the Nadanhada fold belt.

The Altay geosynclinal fold system is located in northwestern China and is averted in a northwesterly direction, parallel to the Altay Mountains. It extends northwestward across the border between Mongolia and China and is connected with the mountainous Altay fold belt in

the former Soviet Union and extends southeastward across the China-Mongolia border and connects with the Mongolian Altay fold belt. In the south it is separated from the Junggar fold system by a zone of fractured crust. The oldest exposed strata are of Middle and Upper Ordovician age represented by metamorphic rocks of different grades.

The Junggar fold system is located in a vast area south of the Altay Mountains and north of the Tianshan Mountains. Westward, it crosses the China-Mongolia border and connects with the Junggar-Balkgash geosyncline. To the east it crosses the border and connects with the southern Mongolian geosyncline. At present the oldest known strata exposed in the Junggar geosynclinal system are those in the Middle Ordovician.

The Tianshan geosynclinal fold system is located in northwestern China. Its areal extent largely corresponds to that of the Tianshan Mountains. It extends westward across the China-Mongolia border and connects with the Tianshan Mountains of the former Soviet Union. To the east connects with the Inner Mongolian-Greater Hinggan fold system. In the south a zone of crustal fractures on the southern margin of the Tianshan Mountains separates it from the Tarim Platform, while in the north the deep fractures on the northern margin of the Tianshan Mountains separate it from the Junggar Geosynclinal fold system.

The Tarim Platform, rhombic in form, lies to the south of the Tianshan Mountains and to the north of the Kunlun Mountains. Cenozoic deposits cover this broad platform everywhere except at its peripheries where basement made up of pre-Sinian metamorphic rocks and Paleozoic sedimentary cover are exposed. The age of the basement in the

platform varies from Archean to late Proterozoic.

The Tarim Platform began to transform into a depression region during the Tertiary. The basement surface of the depression is uneven. It is separated into northern and southern depressions by a median uplift. The amplitude of the subsidence of the two depressions increases towards the piedmonts. Geophysical data and Landsat photographs show that the interior of the depression, like its margins, is also cut by WNW and ENE trending fractures.

Owing to the northward movement of the Indian plate, movement of the Tarim platform and its surrounding area during that time took two forms. These were uplift and subsidence of fault blocks, and thrusting of older strata over the Upper Tertiary, with the latter forming overturned folds.

The Qilian fold system, NW-trending in general, occupies the area where the Qilian mountains lie. In the south it is bounded by the Kunlun fold system along the Nashan deep fractures in Danghe, and by the Qinling fold system along the Tianshi-Baoji deep fracture and the Nanshan deep fracture in Qinghi (the western segment of the Qinghai Lake-northern Huaiyang fracture). In the north it shows a transitional relation to the Sino-Korean paraplatform, with the northwestern end being cut by the Altun deep fracture.

The Qinling fold system is located in the heart of China. On the north, it adjoins the Sino-Korean paraplatform along the deep fracture on the northern margin of the Qinling axis (its eastern extension is known as the Queshan-Feidong deep fracture) and is separated from the Qilian fold system by the Tianshui-Baoji fracture. To the

south, it is bounded by the Yangtze paraplatform along the Chengkou-Fangxian deep fracture and the Xiangfan-Guangji deep fracture; and by the Songpan-Garze fold system along the Maqen-Lueyang deep fracture. Its eastern end is cut by the Tancheng-Lujiang deep fracture. Its western end is inserted between the Kunlun fold system and the Qilian fold system south of Qinghai Lake. The Kunlun fold system is divided into two parts, the western Kunlun and eastern Kunlun fold systems, by the Ruoqiang-Lazhulong fault.

The northern part of the eastern Kunlun fold system adjoins the Qilian fold system. Its southern part bounds the Songpan-Garze fold system along the deep fracture on the southern margin of the Kunlun Mountains and its western part is separated from the Tarim platform by the Ruoqiang-Lazhulong deep fracture. The Qinling Indosinian geosynclinal fold belt overlaps its westernmost part in the Xinghai area east of Dulan.

The Qaidam Depression is a large Meso-Cenozoic intermontane depression. It resulted from strong activity in the Tethys-Himalayan tectonic domain in western China that has occurred since the Mesozoic, particularly the Cenozoic. The Western Kunlun fold system is located to the west of the Ruoqiang-Lazhulong fracture. It occurs as a reversed S-shaped fold mountain system towering to the southwest of the Tarim platform.

The Songpan-Garze fold system occupies a triangular area south of the Eastern Kunlun deep fracture, west of the Longmen Mountain deep fracture, north and east of the Jinshan River-Red River deep fracture. The entire area has been almost completely covered by Triassic

geosynclinal sediments, the Paleozoic rocks being exposed only in the eastern margins that adjoin the Yangtze paraplatform.

The Sanjiang fold lays in western Yunnan and the Qamdo area of Tibet east of the Nujiang River and west of the Jinsha River. In eastern Tibet the Jinshan, Lancang and Nujiang Rivers turn suddenly to the south to form the Sanjiang (Three-River) Valley. To the south it extends into the Indo-China peninsula, and its western end is overlapped by the Tanggula Yanshanian fold system.

The Karakorum-Tanggula fold system has the western segment of the Jinsha River-Red River deep fracture serving as its northern boundary and the Bangong lake-Nujiang River deep fracture as its southern boundary. The southeastern part of the fold system overlaps the Sanjiang Indosinian fold system, and westwards it extends through the Karakorum mountains across the border line.

The Gangdise-Nyainqentanglha fold system embraces a wide area between the Bangong Lake-Nujiang River deep fracture and the Yarlung-Zangbo-River deep fracture, and constitutes the southernmost geosynclinal fold system of the Northern Tethyan Mesozoic geosynclinal Region. The Himalayan geosynclinal fold region forms the southern margin of the Qinghai-Tibet plateau, adjoining the Gangdise-Nyainqentanglha fold system along the Yarlung-Zangbo-River deep fracture on the north.

1.4.2 Present day tectonics

Southeastern Asia is known to have formed essentially as an assembly of several continental blocks that split from Gondwanaland and

drifted northward in Paleozoic time. These blocks later amalgamated to form the present configuration (Metcalfe, 1990; Chung et al., 1998). Current tectonic activity in Asia is often cited as the consequence of continental collision, in progress, between India and Eurasia (Molnar and Tapponnier, 1975).

Continental reconstructions show steady convergence of India and Eurasia since the late Cretaceous, but suggest that since the collision between them in the Eocene the rate of convergence has decreased by one half. Due to the collision of the Indian and Eurasian plates, the Tethyan ocean, which existed between the Indian and Eurasian continents, was consumed (Molnar, 1989). At least 1500 km of crustal shortening must have occurred by deformation solely within continental lithosphere. Both seismic data, including the spatial distribution of earthquakes, associated fault plane solutions, and surface deformation, and geological evidence of recent tectonic activity, imply that deformation occur throughout a broad zone extending as much as 3000 km northeast of the Himalayas (Molnar and Tapponnier, 1975).

Crustal shortening and underthrusting of India beneath the Himalayas and Tibet is estimated to be at least 300 and perhaps 700 km. Probably another 200 to 300 km can be accounted for by thrusting and crustal thickening in the Pamir, Tien Shan, Altai, Nan Shan, and other mountain belts. A major fraction of the convergence occurs on major east-west trending strike-slip faults in China and Mongolia. Movement on those faults may allows material lying between the stable portions of the India and Eurasia plates to move laterally out of the way of the two plates. A total of 500 km, and conceivably 1000 km of

east-west motion could have occurred there (Molnar and Tapponnier, 1975).

Two quite different scenarios have been proposed to explain the particular tectonic process responsible for the Tibetan plateau. One hypothesis infers that extensive underthrusting of Indian continental lithosphere beneath Eurasia produced the uprising Tibetan plateau (Zhang, 1998; Powell and Conagham, 1975), while another hypothesis explains that the 70 km thick crust of the Plateau is formed by horizontal shortening and vertical stretching of the Asian crust since collision (Zhang, 1998; Dewey and Bird, 1970; Dewey and Burke, 1973).

Fault-plane solutions indicate an approximately consistent north to northeast orientation of the P axis throughout central and eastern Asia (Tapponnier and Molnar, 1977). Molnar et al. (1973) suggested that the Indian-Eurasia collision may cause high stresses to be transmitted over this broad area.

Reverse faulting dominates the tectonics of the Tien Shan. This faulting coexists prominent northwest trending right-lateral strike-slip fault systems. Both types of faulting imply approximately a north-south maximum compressive stress direction. The active tectonics of the Altai range and of southern Mongolia is controlled by large scale conjugate strike slip faulting; left lateral on east-west planes and right lateral on north-northwest planes. This implies that the maximum compressive stress is oriented approximately northeast-southwest. Farther north, strike-slip faulting gives way to predominantly normal faulting (Tapponnier and Molnar, 1979).

Miocene to Recent volcanism in central and southeastern Asia is at-

tributed to progressive fracturing of the China plate caused by the impact of India into the southern margin of the continent, superimposed on developing hotcell conditions caused by the insulating effect of the overlying lithosphere (Smith, 1998). Continental rift-related basalts containing aboundant upper mantle peridotite xenoliths are widely distributed in eastern China.

2. The procedure

In this research I obtain shear-velocity structure and attenuation models of the crust and upper mantle across a broad portion of south-eastern Asia using measurements of the dispersion and attenuation of Rayleigh waves. I use two-station measurements of fundamental-mode Rayleigh-wave phase velocity and attenuation and single-station measurements of group velocity and multi-mode attenuation.

The following paragraphs I will explain the methodologies used in this study.

2.1 Instrument and geometrical spreading corrections

Before doing any analysis of the seismogram the magnification, group delay and phase delay of the recording system must be removed. This is done by deconvolving the instrument from the seismogram using the "transfer" command of SAC. The poles and zeros of the instrument required to do the deconvolution come with the seed file of each event when requested from the IRIS Data Management Center (DMC).

In the two-station method the amplitudes obtained for two seismograms generated by the same event are multiplied by the square root of the sine of the great circle arc distance from event source to station in order to correct for geometrical spreading. This correction is not required in the single-station method since the theoretical amplitude spectra used in that method are computed with geometrical spreading included.

2.2 Multiple-filter analysis

Difficulties are often encountered in the analysis of surface-wave seismograms. Disturbances, such as microseisms, sometimes tend to obscure the signal of interest. Several dispersive modes or several branches of the same mode may arrive simultaneously at the recording site. These difficulties are especially severe for data at short periods. Because the surface-wave spectrum for short periods is a superposition of many modal contributions, the resultant spectrum may be highly oscillatory, making analysis difficult (Dziewonski et al., 1969; Herrmann, 1973).

To study individual modes we need to be able to separate them in either time or frequency. The only way to do this exactly is by using a linear array of detectors spaced along the same azimuth from the source. Having this, wave number-frequency analysis can be performed to recover both phase velocities and spectral amplitudes of the individual modes as a function of frequency (Herrmann, 1973).

Such array data, however, are usually not available. The peak and trough method, which is based on careful observation of the times of arrival of individual crests and troughs in the dispersed wave train (Ewing, Jardetzky and Press 1957; Brune et al., 1960), often fails when the signal-to-noise ratio is small or when the signal is contaminated by other arrivals. Similar difficulties have been noted when the phase delay calculated by ordinary Fourier analysis (Sato 1955, 1956, 1958) are differentiated in order to obtain the group velocity (Dziewonski and Hales, 1972).

Dziewonski et al.,(1969) developed the multiple-filter analysis technique to determine group velocities of dispersed waves. This technique converts an ordinary time series (amplitude vs. time) into a two-dimensional display of velocity (rows) versus period (columns) plane. The multiple-filter technique is a fast and efficient method of analyzing multiply dispersed signals. The amplitudes and phases of signals passed by an array of narrow-band filters centered at selected frequencies can be used to measure group velocity as a function of period. Application of this method of analysis to the recordings of mutually orthogonal detectors permits the measurement of lateral refraction and the separation of Love waves from Rayleigh waves. It is also useful in the identification of fundamental and higher modes.

A flow chart describing the multiple filter analysis is given by Dziewonski et al. (1969). Instead of following the procedure outlined by Dziewonski et al. (1969), however, I followed that of Herrmann (1973). Herrmann (1973) interpreted the envelope of the filtered time history by assuming a flat spectrum (constant amplitude spectrum $A(\omega)$) of the signal within the band-pass region of the filter.

The program MFT(II) (Herrmann, 1987), searches for the four largest amplitude values of the envelope. The program provides two plots per run. The first plot gives spectral amplitudes versus period or frequency and shows the four largest spectral amplitudes at each frequency (Figure 2.2). The second plot gives the group velocity (versus period or frequency) corresponding to each peak (Figure 2.1).

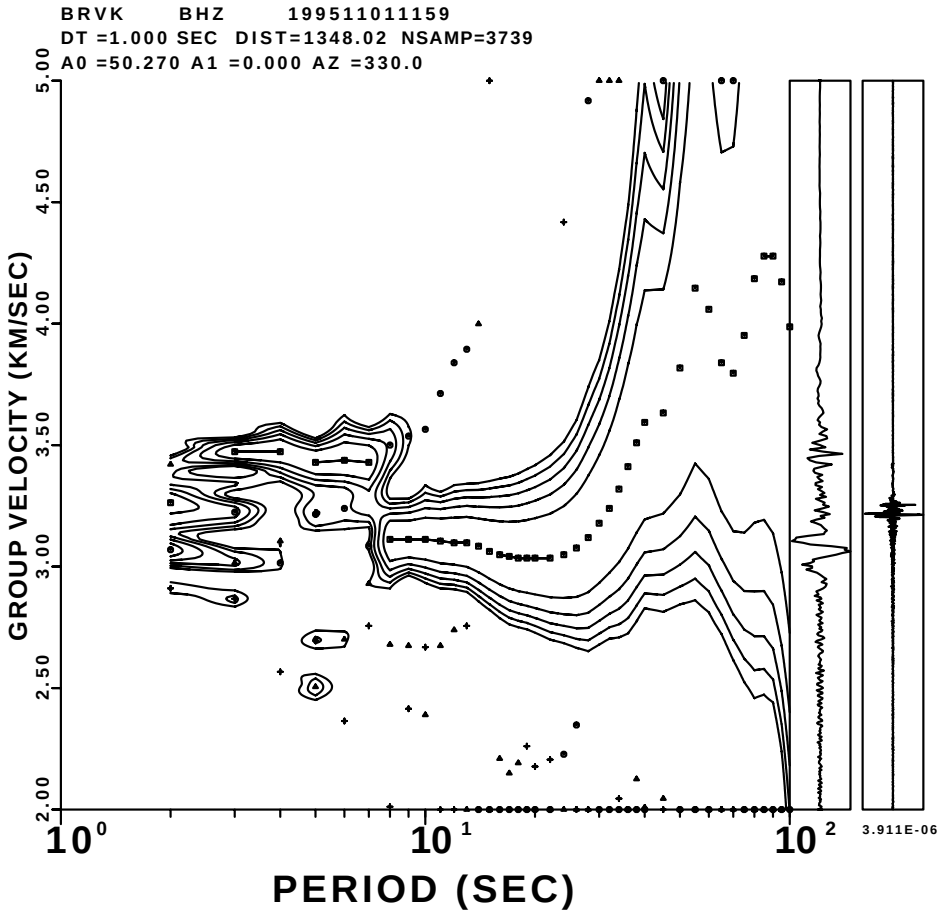

Figure 2.1: Group velocity dispersion curve for Rayleigh waves recorded at station BRVK from the earthquake that occurred in Kazakhstan on Nov. 01, 1995 at an epicentral distance of 1348.0 km. The plot was obtained using the MFT following the method of Herrmann (1987). The fundamental mode between about 8 and 60 sec (with group velocities between about 3.1 and 4.2 km/s) and the higher modes between about 2 and 10 sec (with group velocity of about 3.4 km/s) are clearly seen on the MFT map.

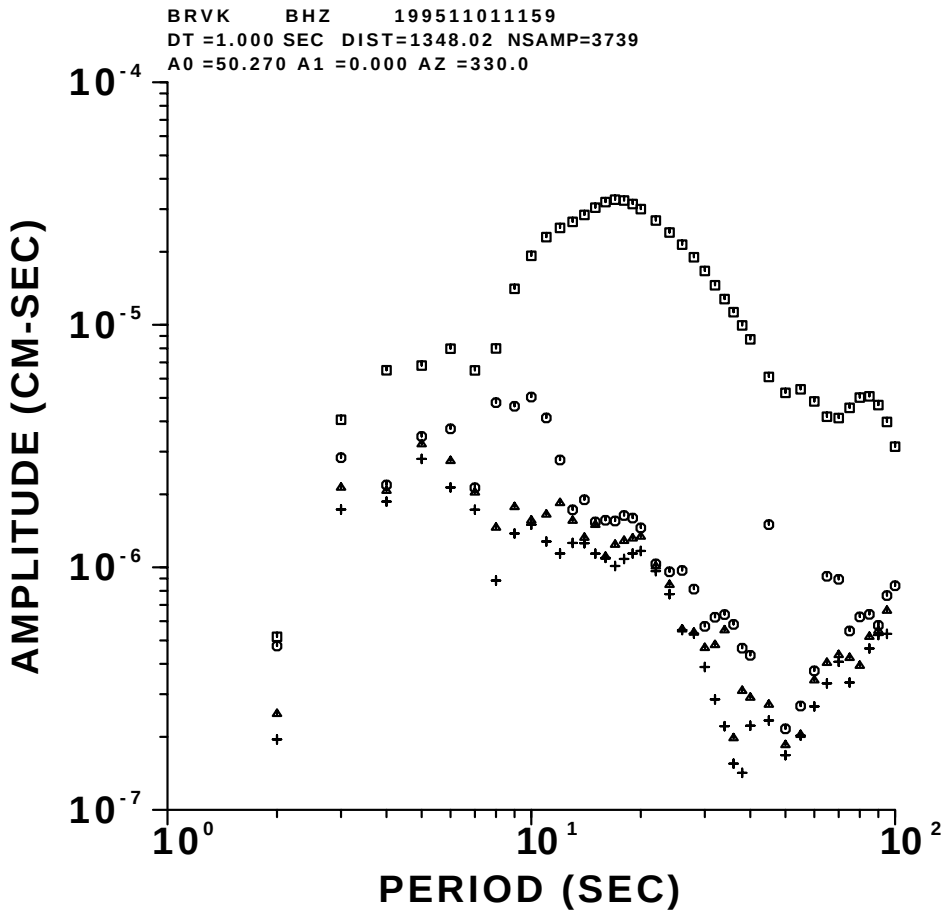

Figure 2.2: Amplitudes for the four largest spectral components obtained from the MFT.

2.3 Phase match filtering

The presence of multipaths in a surface-wave train, interfering with the great circle path arrival, will bias conventional methods for determining apparent group-velocity dispersion curves such that the estimates will be too slow. The effect of multipaths can be reduced using the process of "phase match filtering" developed by Herrin and Goforth (1977). This method removes the bias mentioned above and thus improves the accuracy of the estimate of group velocity. The method is developed based on "the matched filter" defined by Turin (1960).

Multipath interference can cause ripples and spectral holes, in addition to those caused by some effects, to appear in the signal spectrum. The removal of these effects of multipaths using phase-matched filtering provides Rayleigh-wave spectra which are much more closely related to source characteristics than are those obtained from Fourier transforms of the entire signal, and at the same time results in a substantial improvement in the signal-to-noise ratio (Herrin and Goforth, 1977).

The phase-match filtering program, MATCH(IV) (Herrmann, 1987) is applied to the spectrum of a seismogram after passing it through the instrument correction and multiple filter analysis steps.

2.4 Inter-station phase velocities, group velocities and attenuation coefficients

To avoid the azimuthal effect of the source radiation pattern, we can measure amplitudes at two stations that lay at two distances on the

same great circle path from an earthquake. The inter-station phase velocity is given by

$$\begin{aligned} C(\omega) &= \frac{\omega}{k(\omega)} \\ &= \frac{\omega(r_2 - r_1)}{\phi_2 - \phi_1 - \phi_{i2} - \phi_{i1} - 2n\pi} \end{aligned} \tag{2.1}$$

where ϕ_1 and ϕ_2 are the phase spectrum functions of the signal recorded at stations 1 and 2, ϕ_{i1} and ϕ_{i2} are instrumental phase shifts at stations 1 and 2, and the integer n reflects the non-uniqueness of the phase measurements. n can be determined directly if there is a third station or the same great-circle path, or can be estimated from knowledge of the possible range of the phase velocity values (Dziewonski and Hales, 1972).

Inter-station group velocities can be calculated by differentiating the phase velocity curve or by measuring group arrival times at each station either directly from the seismograms or by narrow-band filtering each seismogram and dividing the group delay into the station separation. The two-station method of phase velocity measurement avoids difficulties with the source phase shift.

Ben-Menahem (1965) defined the inter-station attenuation coefficient (γ) for a travelling wave as

$$\gamma(\omega) = \frac{\ln\left[\left\{\frac{A_2(\omega,\theta,r_2)}{A_1(\omega,\theta,r_1)}\right\}\left\{\frac{\sin\Delta_2}{\sin\Delta_1}\right\}^{\frac{1}{2}}\right]}{r_2 - r_1} \tag{2.2}$$

where $A_{1,2}$ are observed spectral amplitudes at stations 1 and 2 at distances $r_{1,2}$ (in kilometres) and $\Delta_{1,2}$(in radians) from the source and ω is angular frequency. θ is the azimuth of the event from the stations.

Measurements of inter-station phase velocities by calculating phase differences (equation 2.1) are however, strongly affected by noise and therefore the phase velocity curves are very rough (Dziewonski et al., 1968; Dziewonski and Hales, 1972). Spectral holes or peaks caused by scattering, multipathing, or noise, severely affect spectral ratio measurements (equation 2.2) resulting in a very unstable attenuation curve.

To reduce these problems, Landisman et al. (1969) suggested measuring inter-station phase velocities from the windowed cross correlogram. Windowing where the correlation is high reduces the effect of random noise in the phase spectrum and stabilizes the phase velocities. Landisman et al. (1969) also noted that the cross-correlation function approximates the inter-station impulse response and application of the moving window or multiple-filter technique (Dziewonski et al. 1969) can be used to calculate inter-station group velocities.

Taylor and Toksöz (1982) developed a method for calculating inter-station phase and group velocities which is equivalent to the cross-correlogram method of Landisman et al. (1969) but uses a method for measuring the inter-station attenuation coefficient that is greatly improved over that given by equation (2.2).

This method uses a Wiener (least-squares) filtering technique to estimate the inter-station Green's (or transfer) function from surface-wave data from two stations lying along the same great-circle path. The Wiener filter is constructed to estimate the signal recorded at the station further from the source from the signal recorded at the nearer station.

Inter-station group velocities are obtained by applying the multiple-

filter technique to the Green's function and the inter-station phase velocity from the phase spectrum of the Green's function. The amplitude spectrum of the Green's function is used to calculate average attenuation between the two stations. Using synthetic seismograms contaminated by noise, Taylor and Toksöz (1982) showed that the Q values calculated from the Green's function are significantly more stable and accurate than those obtained by taking spectral ratios (equation 2.2). They pointed out that, the method is particularly useful for paths involving short station separations.

The program XSPRAT(IV) (Herrmann, 1987) uses the algorithm of Taylor and Toksöz (1982) to determine the inter-station Green's functions in the frequency domain. The individual station spectra are run through MATCH(IV) (Herrmann,1987) first to correctly isolate modes and, in addition, to smooth the spectrum. The spectrum and dispersion output of the program MATCH(IV) are then used by XSPRAT(IV). The program XSPGAM (IV) (Herrmann, 1987) uses the spectral ratio output from the program XSPART(IV) to determine the spatial attenuation coefficient (γ) as a function of frequency or period.

2.5 Single source-single station method for attenuation measurement

One of the goals of this research is to characterize regional variations of Q_μ across southeastern Asia. However, when using the two-station method, it is a very difficult to find enough paths for good continental coverage. The reason for this is that two stations may not be available that lie along great-circle paths to a useful earthquake, or

the source-station configuration may be adequate but paths between the source and station pair may be long and cross complex structures that produce focusing or defocusing of surface waves.

Cheng and Mitchell (1981) developed single station-single source method which avoids the necessity of having two stations that lie along a single great-circle path through the source. This method has the advantage that it is often possible to find earthquake sources that lie within the same tectonic province as that of the station and therefore may provide a relatively uniform path of travel for surface waves. However, to use this method, either we must know the source depth and focal mechanism for each earthquake used, or we must be able to determine those parameters from the available data.

The single-station method consists of generating theoretical amplitude spectra for fundamental-mode and higher-mode Rayleigh waves and comparing them to corresponding observed spectra to obtain Q models of the crust and, if possible, the upper mantle (Cheng and Mitchell, 1981). The Programs SURFACE85(III), REIGEN85(III), WIG85(III), and SPEC85(III) (Herrmann, 1985) are used to generate theoretical amplitude spectra for fundamental- and higher-mode Rayleigh waves used in this study.

2.6 Inversion theory for shear-wave Q structure

The phase-velocity dispersion equation (Haskell, 1953) for elastic surface waves of Rayleigh type on multi layered solid earth gives an implicit relationship between phase velocity C and wave number k. This implicit equation also shows the dependence of the phase velocity on density ρ , thickness h, shear wave velocity β, and compressional wave velocity α of each layer of the earth. The functional dependence of phase velocity on these parameters at an angular frequency ω may be expressed (Anderson et al., 1965) as

$$c(\omega) = \frac{\omega}{k} = f(\beta, \alpha, \rho). \tag{2.3}$$

Since, in general, the above equation is non-linear we have to linearize it by applying Taylor's expansion to the phase velocity about a starting Earth model $(\beta_0, \alpha_0, \rho_0)$, ie.,

$$c(\beta,\alpha,\rho) = c(\beta_0,\alpha_0,\rho_0) + \left.\frac{\partial c}{\partial \beta}\right|_{\beta_0} (\beta - \beta_0) + \cdots \left.\frac{\partial c}{\partial \alpha}\right|_{\alpha_0} (\alpha - \alpha_0) + \cdots \left.\frac{\partial c}{\partial \rho}\right|_{\rho_0} (\rho - \rho_0) + \cdots \tag{2.4}$$

and

$$c(\beta,\alpha,\rho) - c(\beta_0,\alpha_0,\rho_0) = \left.\frac{\partial c}{\partial \beta}\right|_{\beta_0} (\Delta\beta) + \cdots \left.\frac{\partial C}{\partial \alpha}\right|_{\alpha_0} (\Delta\alpha) + \cdots \left.\frac{\partial c}{\partial \rho}\right|_{\rho_0} (\Delta\rho) + \cdots . \tag{2.5}$$

Here $c(\beta, \alpha, \rho)$ is the observed phase velocity at a seismic station and $c(\beta_0, \alpha_0, \rho_0)$ is the phase velocity predicted by a starting Earth model, using Haskell's (1953) matrix method or its improved versions. The

change in phase velocity Δc is the difference between the observed and theoretically predicted phase velocities. If we drop the higher order terms in the Taylor's expansion, then Δc becomes

$$\Delta c = \left.\frac{\partial c}{\partial \beta}\right|_{\beta_0} (\Delta\beta) + \left.\frac{\partial c}{\partial \alpha}\right|_{\alpha_0} (\Delta\alpha) + \left.\frac{\partial C}{\partial \rho}\right|_{\rho_0} (\Delta\rho). \tag{2.6}$$

A Rayleigh wave traveling in a vertically heterogeneous layered anelastic Earth of N-layers (Anderson et al., 1965; Ben-Menahem and Singh, 2000) has an inverse quality factor Q_R^{-1} given by

$$Q_R^{-1} = \sum_{i=1}^{N} \left(\frac{\beta_i}{c_R}\frac{\partial c_R}{\partial \beta_i}\right)\Bigg|_{k,\rho,\alpha} \frac{1}{Q_{\beta,i}} + \sum_{i=1}^{N} \left(\frac{\alpha_i}{c_R}\frac{\partial c_R}{\partial \alpha_i}\right)\Bigg|_{k,\rho,\beta} \frac{1}{Q_{\alpha,i}}. \tag{2.7}$$

The subscript i is the layer index, α and β are compressional and shear wave velocities, respectively, and k is the wave number.

The Rayleigh wave spatial attenuation coefficient $\gamma_R(\omega)$ is related to the quality factor Q_R (Futterman, 1962) by

$$Q_R(\omega) = \frac{\omega}{2\gamma_R(\omega) c_R}. \tag{2.8}$$

This implies that

$$\gamma_R(\omega) = \frac{\omega}{2c_R} Q_R^{-1} \tag{2.9}$$

and thus

$$\gamma_R(\omega) = \frac{\pi}{T}\left\{\sum_{i=1}^{N} \left(\frac{\beta_i}{c_R^2}\frac{\partial c_R}{\partial \beta_i}\right)\Bigg|_{k,\rho,\alpha} Q_{\beta,i}^{-1} + \sum_{i=1}^{N} \left(\frac{\alpha_i}{c_R^2}\frac{\partial c_R}{\partial \alpha_i}\right)\Bigg|_{k,\rho,\beta} Q_{\alpha,i}^{-1}\right\}. \tag{2.10}$$

Q_R depends on the distributions of $\alpha, \beta, \rho, Q_\alpha$ and Q_β with depth (Anderson et al. 1965). The functional dependence of γ with $\beta, Q_\beta^{-1}, \alpha$ and Q_α^{-1} can be expressed as

$$\gamma = \gamma(\beta, Q_\beta^{-1}, \alpha, Q_\alpha^{-1}). \tag{2.11}$$

Taylor's expansion of this about a starting earth model $(\beta_0, Q_{\beta,0}, \alpha_0, Q_{\alpha,0})$ gives

$$\begin{aligned}\gamma(\beta, Q_\beta, \alpha, Q_\alpha) = \\ \gamma(\beta_0, Q_{\beta_0}, \alpha_0, Q_{\alpha_0}) + \left.\frac{\partial\gamma}{\partial\beta}\right|_{\beta_0}(\beta-\beta_0) + \cdots + \left.\frac{\partial\gamma}{\partial\beta}\right|_{\beta_N}(\beta-\beta_N) + \\ \left.\frac{\partial\gamma}{\partial Q_{\beta_0}^{-1}}\right|_{Q_{\beta_0}^{-1}}(Q_\beta^{-1}-Q_{\beta_0}^{-1}) + \cdots + \left.\frac{\partial\gamma}{\partial Q_{\beta_N}^{-1}}\right|_{Q_{\beta_N^{-1}}}(Q_\beta^{-1}-Q_{\beta_N}^{-1})\end{aligned} \tag{2.12}$$

and

$$\begin{aligned}\Delta\gamma = \\ \left.\frac{\partial\gamma}{\partial\beta}\right|_{\beta_0}(\beta-\beta_0) + \cdots + \left.\frac{\partial\gamma}{\partial\beta}\right|_{\beta_N}(\beta-\beta_N) + \\ \left.\frac{\partial\gamma}{\partial Q_{\beta_0}^{-1}}\right|_{Q_{\beta_0}^{-1}}(Q_\beta^{-1}-Q_{\beta_0}^{-1}) + \cdots + \left.\frac{\partial\gamma}{\partial Q_{\beta_N}^{-1}}\right|_{Q_{\beta_N^{-1}}}(Q_\beta^{-1}-Q_{\beta_N}^{-1}).\end{aligned} \tag{2.13}$$

Equations (2.6 and 2.13) can be written in short form as

$$d = Gm \tag{2.14}$$

where d is an $N \times 1$ matrix in which the elements are the differences between the observed and the predicted phase velocities or attenuation coefficients, G is an $N \times M$ matrix of partial derivatives of either phase velocity or attenuation coefficient with respect to layer parameters α, β, Q_β and Q_α. m is an $M \times 1$ matrix in which elements are the differences between Earth parameters computed from the observed phase velocities, or attenuation coefficients, and the starting Earth model.

If G is a square matrix, which implies that $N = M$ (the number of equations is equal to the number of unknowns) we could simply multiply both sides of the equations by G^{-1} , assuming it exists. By definition, $G^{-1}G = I$, where I is the identity matrix, so a new system of equations is formed:

$$G^{-1}d = m \tag{2.15}$$

Thus we could solve for m directly. This is a simple equation and is in principle easy to solve. Unfortunately, because of the complexity of the Earth, this is never the case in seismology. We are dealing with data that have errors, such as those associated with the measurement of phase velocities or attenuation coefficients. Similarly, the above equation assumes that our derived model can perfectly predict the data. In the case of phase velocities or attenuation coefficients, this means that we must be able to infer the shear-velocity and shear-wave Q structure between the source and receiver extremely well. In fact, we usually do not; thus, we are dealing with inconsistent equations, making it impossible to use the above equation (Lay and Wallace, 1995).

2.6.1 Least-squares solution

The fact that the equation $d = Gm$ cannot be satisfied by every data point means that it has no exact solution. Since we cannot solve $d = Gm$ deterministically, it leads us to use statistics (Mendenhall and Scheaffer, 1973). The simplest method for solving the linear inverse problem $Gm = d$ is based on measures of the size, or length, of the estimated model parameters m^{est} and of the predicted data $d^{pre} = Gm^{est}$. For each

observation one defines a prediction error, or misfit, $e_i = d_i^{obs} - d_i^{pre}$. Here the superscripts, obs and pre, mean observed and predicted, respectively. The best approximate solution is the one with model parameters that lead to the smallest overall error (the sum of the squares of the individual errors) E, defined as

$$E = \sum_{i=1}^{N} e_i^2. \tag{2.16}$$

The total error E is exactly the squared Euclidean length of the vector e, or $E = \mathbf{e^T e}$, which is the L_2 prediction error (Menke, 1984). This is the method of least-squares estimates for the solution of an inverse problem. It finds model parameters that minimize the Euclidean length. Therefore we seek values of the model parameters that solve $d = Gm$ approximately, where the goodness of the approximation is given by the total error

$$\begin{aligned} E &= e^T e & (2.17)\\ &= (d - Gm)^T (d - Gm) \\ &= \sum_{i}^{N} \left[d_i - \sum_{j}^{M} G_{ij} m_j \right] \left[d_i - \sum_{k}^{M} G_{ik} m_k \right]. & (2.18) \end{aligned}$$

Multiplying out the terms and reversing the order of the summations lead to

$$E = \sum_{j}^{M} \sum_{k}^{M} m_j m_k \sum_{i}^{M} G_{ij} G_{ik} - 2 \sum_{j}^{M} m_j \sum_{i}^{N} G_{ij} d_i + \sum_{i}^{N} d_i d_i. \tag{2.19}$$

From calculus, the minimum of the function E is found by setting the derivatives of E with respect to m_q to zero and solving the resulting

equations, i.e,

$$\frac{\partial E}{\partial m_q} = 0 \tag{2.20}$$

gives (Menke, 1984)

$$G^T G m - G^T d = 0. \tag{2.21}$$

Note that the quantity $G^T G$ is a square an $M \times M$ matrix and that it multiplies a vector m of length M. The quantity $G^T d$ is also a vector of length M. This equation is therefore a square matrix equation for the unknown model parameters. Presuming that $[G^T G]^{-1}$ exists, we have the following solution

$$m^{est} = [G^T G]^{-1} G^T d \tag{2.22}$$

which is the least-squares solution to the inverse problem $Gm = d$ (Menke, 1984; Jackson, 1972). The quantity $[G^T G]^{-1} G^T$ is called the generalized inverse and is given the symbol G^{-g} (Menke, 1984).

However, the least-squares solution fails if the number of solutions (m^{est}) that give the same minimum prediction error E is greater than one. This occurs when the matrix $[G^T G]^{-1}$ does not exist (becomes infinite or $[G^T G]$ is singular), which also makes the solution m^{est} infinite (non-unique). The matrix $[G^T G]^{-1}$ becomes infinite for under-determined problems, where we have fewer data than unknown model parameters, because the equation $Gm = d$ does not provide enough information to uniquely determine all the model parameters. In even-determined problems there is exactly enough information to determine the model parameters; therefore, there is only one solution, and it has

zero prediction error.

Most problems in seismology are over-determined, where there are many more data than model parameters (Lay and Wallace, 1995). In this case there is too much information contained in the equation $Gm = d$ for it to possess an exact solution. Therefore, we can employ least-squares to select a "best" approximate solution. However, it is difficult to practically use least-squares because there are numerical errors in the computation of $[G^T G]^{-1}$ which make it infinite. This difficulty is seen when the fundamental decomposition theorem for a non-symmetric matrix G of size $N \times M$ is applied (Lanczos, 1997).

According to the fundamental decomposition theorem (also called, the singular-value decomposition theorem), the matrix G can be written as

$$G = U\Lambda V^T \tag{2.23}$$

where U is an $N \times N$ orthogonal matrix with the eigenvectors of G in the columns , Λ is an $N \times M$ diagonal matrix with the eigenvalues of G along the diagonal, and V^T is the transpose of an $M \times M$ orthogonal matrix V with the eigenvectors of G^T in the columns. The diagonal elements of Λ are non-negative and are called singular values (Menke, 1984).

If one or more of the eigenvalues λ_i are zero, then we have to separate them from the non-zero eigenvalues:

$$\Lambda_p = \begin{pmatrix} \lambda_1 & 0 & 0 & \cdots & 0 \\ 0 & \lambda_2 & 0 & \cdots & 0 \\ 0 & 0 & \lambda_3 & \cdots & 0 \\ \vdots & \vdots & \vdots & \ddots & \vdots \\ 0 & 0 & 0 & \cdots & \lambda_p \end{pmatrix}, \tag{2.24}$$

where $p \leq M$.

The matrix U formed from the corresponding eigenvectors u_i is

$$U = \begin{pmatrix} u_1 & u_2 & \cdots & u_p & u_{p+1} & \cdots & u_N \end{pmatrix} \tag{2.25}$$

where

$$u_i = \begin{pmatrix} u_{1i} & u_{2i} & \cdots & u_{Ni} \end{pmatrix}^T. \tag{2.26}$$

Since both G and G^T have the same eigenvalues, the eigenvectors v_i that form matrix V are

$$V = \begin{pmatrix} v_1 & v_2 & \cdots & v_p & v_{p+1} & \cdots & v_M \end{pmatrix} \tag{2.27}$$

where

$$v_i = \begin{pmatrix} v_{1i} & v_{2i} & \cdots & v_{Mi} \end{pmatrix}^T. \tag{2.28}$$

We discard the zero eigenvalues and the corresponding eigenvectors. Therefore the decomposition theorem becomes

$$G = U_p \Lambda_p V_p^T \tag{2.29}$$

which gives an $N \times M$ matrix G as a product of the semi-orthogonal $N \times p$ matrix U, the $p \times p$ diagonal matrix Λ_p and the transpose of a semi-orthogonal $M \times p$ matrix V (Lanczos, 1997).

The least-squares solution can be constructed from the singular value decomposition (Menke, 1984) of G:

$$\begin{aligned} m^{est} &= (G^T G)^{-1} G^T d \\ &= V_p \Lambda_p^{-1} U_p^T d. \end{aligned} \tag{2.30}$$

We can define the a generalized inverse operator G^{-g} as:

$$G^{-g} = V_p \Lambda_p^{-1} U_p^T \tag{2.31}$$

such that

$$m^{est} = G^{-g} d \tag{2.32}$$

where Λ_p^{-1} is given by

$$\Lambda_p^{-1} = \begin{pmatrix} \frac{1}{\lambda_1} & 0 & 0 & \cdots & 0 \\ 0 & \frac{1}{\lambda_2} & 0 & \cdots & 0 \\ 0 & 0 & \frac{1}{\lambda_3} & \cdots & 0 \\ \vdots & \vdots & \vdots & \ddots & \vdots \\ 0 & 0 & 0 & \cdots & \frac{1}{\lambda_p} \end{pmatrix}. \tag{2.33}$$

.

Eigenvalues that are identically zero are theoretically ignored in the decomposition of G. In practice, however, because of numerical errors, normally very small eigenvalues are encountered (Crosson, 1976). These small eigenvalues can cause large and unstable changes in one or more of the components of the estimated m^{est} model.

Ideally, we seek a solution procedure that results in suppression of those model components associated with small or near-zero eigenvalues. This requires a modification of the least-squares procedure.

2.6.2 The damped least-squares solution

The so called damped least-squares solution method (Levenberg, 1944; Marquardt, 1963) tries to estimate a solution that minimizes some combination Φ of the prediction error E and the solution length $m^T m$ (Menke, 1984):

$$\Phi(m) = E + \theta^2 L = e^T e + \theta^2 m^T m \tag{2.34}$$

where the weighting factor θ^2 determines the relative importance given to the prediction error and solution length.

By minimizing $\Phi(m)$ with respect to the model parameters in a manner exactly analogous to the least-squares derivation, we can obtain

$$m^{est} = [G^T G + \theta^2 I]^{-1} G^T d. \tag{2.35}$$

The generalized inverse for this case is:

$$G^{-g} = [G^T G + \theta^2 I]^{-1} G^T. \tag{2.36}$$

This estimate of the model parameters is called the damped least-squares solution.

The Model Resolution Matrix

We may be interested in knowing how closely a particular estimate of the model parameters m^{est} is to a "true" but unknown set of model parameters (m^{true}), that solve $Gm^{true} = d^{obs}$. Plugging the expression for the observed data $Gm^{true} = d^{obs}$ into the expression for the estimated

model $m^{est} = G^{-g} d^{obs}$ gives

$$\begin{aligned} m^{est} &= G^{-g} d^{obs} \\ &= G^{-g}[G m^{true}] \\ &= [G^{-g} G] m^{true} \\ &= R m^{true}. \end{aligned} \tag{2.37}$$

Here the $N \times M$ matrix $R = G^{-g} G$ is called model resolution matrix (Menke, 1984). If $R = I$, then each model parameter is uniquely determined. If R is not an identity matrix, then the estimates of the model parameters are weighted averages of the true model parameters.

The Data Resolution Matrix

To know how well the estimate of model parameters fits the data, we plug in m^{est} into the equation $Gm = d$

$$\begin{aligned} d^{pre} &= G m^{est} \\ &= G[G^{-g}] d^{obs} \\ &= [G G^{-g}] d^{obs} \\ &= S d^{obs}. \end{aligned} \tag{2.38}$$

The $N \times N$ square matrix $S = G G^{-g}$ is called the data resolution matrix (Menke, 1984), or the 'information' distribution matrix (Wiggins, 1972). This matrix describes how well the predictions match the data. It characterizes whether the data can be independently predicted, or resolved. If $S = I$, then $d^{pre} = d^{obs}$ and the prediction error is zero. On

the other hand, if the data resolution matrix is not an identity matrix, the prediction error is nonzero.

Covariance of estimated model parameters

The data contain noise that cause errors in the estimates of the model parameters. We can calculate how this measurement error maps into errors in m^{est}. If the data have a distribution characterized by some covariance matrix $[Covd]$, then the estimates of the model parameters have a distribution characterized by a covariance matrix (Menke, 1984):

$$[Covm^{est}] = G^{-g}[Covd]G^{-gT}. \tag{2.39}$$

If the data are uncorrelated and all of equal variance σ_d^2, then

$$[Covm^{est}] \;\; = \;\; G^{-g}\sigma_d^2 I(G^{-g})^T. \tag{2.40}$$

Application of the singular value decomposition theorem to $G^{-g} = [G^T G + \theta^2 I]^{-1}G^T$, for the damped least-squares solution, gives

$$\begin{aligned} G^{-g} &= [(U_p\Lambda_p V_p^T)^T(U_p\Lambda_p V_p^T) + \theta^2 I)]^{-1}(U_p\Lambda_p V_p^T)^T \\ &= V_p[\Lambda_p^2 + \theta^2 I]^{-1}\Lambda_p U_p^T \end{aligned} \tag{2.41}$$

where the elements of the matrix $[\Lambda p^2 + \theta^2 I]^{-1}$ are (Crosson, 1976)

$$\frac{\lambda_i}{(\lambda_i^2 + \theta^2)}. \tag{2.42}$$

This last expression shows that, in the presence of near-zero eigenvalues, G^{-g} will no longer be infinite.

2.7 The inversion procedure

Surface waves are more sensitive to shear velocity than compressional-velocity or density (Wiggins, 1972; Der et al., 1970; Jackson and Burkhard, 1976; Kovach, 1978). Therefore, surface-wave inversions are usually made only for shear-velocity models. However, the compressional-velocity and density values are derived assuming values for Poisson's ratio and density as obtained from emprical relationships (e.g. Nafe, 1970) between compressional velocity and density.

Intrinsic anelasticity can be described by the shear-wave quality factor Q_μ and the bulk quality factor Q_κ. The Rayleigh-wave quality factor Q_R is not an intrinsic property of the Earth but refers to the attenuation of surface waves. Q_R is a weighted average of Q_μ and Q_κ and is also affected by intrinsic velocities over a range of crustal and upper mantle depths. Because of the relative insensitivity of surface wave attenuation to Q_κ, inversion of surface wave attenuation values lead to models of Q_μ or its inverse Q_μ^{-1} (Mitchell, 1995). Shear-velocity and Q_μ models are obtained using the inversion program SURF(IV)(Herrmann, 1987).

3. Group velocities, phase velocities, and attenuation coefficients in southeastern Asia using the two-station method

3.1 Introduction

It has been recognized (Anderson et al., 1965) that the rate of energy dissipation, or attenuation of seismic energy in the earth, being a direct measure of anelasticity, is a more sensitive indicator of changes in crystalline structure due to temperature and phase change than is elasticity. It is also a more pertinent quantity for many geological problems.

However, accurate amplitude information is very difficult to obtain and interpret. Instrumental effects, local geology, mode conversion, scattering, and source characteristics have tended to obscure the amplitude variations due to true energy dissipation (Anderson et al., 1965).

Amplitudes of body waves are particularly difficult to interpret because of mode conversion at interfaces, scattering, and complicated spreading losses. Direct waves that bottom in the crust or upper mantle are also very sensitive to velocity gradients in that depth range.

The attenuation of long-period waves depends in a very complicated way on the distribution of elastic and anelastic parameters of the depth Earth. However, complications of source, instrument, and path differences are minimized in studies of this sort. Because of the long wavelengths of these vibrations, such effects as scattering and mode-conversion are reduced, and we are more likely to be measuring an intrinsic property of the material. The same inhomogeneity which may

cause scattering of body waves at frequencies of 1Hz and higher may allow surface waves at much lower frequencies to be transmitted without significant scattering. Complications due to discontinuities and low-velocity zones are also minimized (Anderson and Archambeau, 1964; Anderson et al., 1965)

Since Love waves are more sensitive to lateral structural heterogeneities than are Rayleigh waves (Lysmer and Drake, 1971), they are more greatly affected by scattering and multi-pathing than the latter. Therefore I use Rayleigh waves from earthquakes that occur in and around southeastern Asia.

3.2 Data

A large number of events which occurred between 1993 and 1999 in the region enclosed by geographic coordinates 60^0E to 165^0E and 10^0N to 70^0N were searched from the PDE catalog. Because most of the stations in this geographic region were not installed before 1993, I looked for events from this year onwards. A program developed to search for events recorded by two stations at a specified angular deviation from the great circle path of the seismic wave was used. The search was made with the following criteria:

1. The allowable angular deviation of the path of an earthquake from the great circle path joining two recording stations is 8 degrees or less. By restricting selected events in this way I hope to minimize adverse effects that may be caused by seismic energy arriving at the two stations that leave the focal region at differ-

ent angles (Knopoff et al., 1966; Bloch and Hales, 1968). It is difficult to find an event recorded by two stations with very small deviations from the great circle path.

2. m_b of events used in this study range between 4.8 and 6.2. Events which have magnitudes below 4.8 were found to be too small to generate surface waves that are well recorded at two stations. Those above magnitude 6.2 are very large and source effects such as directivity and radiation pattern may affect the amplitudes, especially for those events recorded by stations which deviate from the true great circle path.

3. Since surface-wave amplitudes are usually larger for shallow events I have restricted my search to those events that occur at depths less than about 50 km.

4. The distances between the event and the stations are in the range 300 km to 3000 km. This is because my study is regional and I hope to minimize the degree of lateral complexity along the surface-wave path. Near-distance events do not have enough time to develop well-dispersed surface waves, while teleseismic events are affected much by multipathing, focusing and defocusing which in turn affect the amplitude of the signal.

Since I am interested in Rayleigh waves, the broadband vertical component (BHZ) of those events which satisfy the above criteria were requested from the IRIS DMC data bank using the Breakfast web request method. Seismograms, which have well-developed surface waves,

were selected for further processing. Fifty-six events (Table 3.2), recorded by the station pairs shown in Figure 3.1, were used in the two-station method

The phase and group velocities are average values over the entire great-circle path of the Rayleigh wave. Variations in the average values are correlated with the composition of the paths (Toksöz and Anderson, 1966; Patton, 1980).

In the following section I will explain how southeastern Asia is regionalized based on inter-station phase- and group-velocity variations. The methods for obtaining inter-station group velocities, phase velocities and attenuation coefficients were described in Chapter 2.

3.3 Regionalization based on inter-station group velocities and phase velocities

Eighty percent of my region of study in southeastern Asia consists of China, which has been divided tectonically into four major subplates (Pines et al., 1980 and references there in) based on surface geology. These subplates include (1) Chinghai-Tibet (southwestern China), (2) northern China, (3) southern China, and (4) northwestern China (including the Tien Shan fold belt). Each subplate has different geomorphologic features, gravity anomalies, and crustal thickness.

The concept of regionalization, first proposed by Toksöz and Anderson (1966), consists of dividing a surface-wave path into oceanic, shield, and tectonic regions. Each region has a different effect upon the average group velocity. Toksöz and Anderson (1966) noted that shield areas raise the average group velocity, whereas active tectonic regions have

Number	Origin date	Origin Time	EVLA	EVLO	d(km)	m_b
1	03/19/93	15:53:52.8	12.15	95.08	25	5.4
2	08/24/93	22:52:21.3	10.21	93.85	23	4.9
3	08/24/93	23:35:55.6	10.35	93.73	22	4.8
4	03/19/93	15:53:52.8	12.15	95.08	25	5.4
5	02/20/93	11:40:33.0	47.08	154.05	17	5.0
6	02/26/93	19:16:40.8	47.58	154.36	32	5.1
7	04/28/93	05:16:15.4	47.38	153.58	33	5.3
8	05/06/93	07:58:47.9	46.71	153.51	37	5.7
9	07/11/93	17:48:11.0	47.63	154.16	28	5.6
10	07/14/93	17:38:33.9	43.18	139.12	20	5.5
11	07/19/93	19:18:38.7	43.12	139.15	19	5.0
12	04/08/93	03:49:33.2	35.65	77.65	42	5.0
13	06/14/93	07:30:17.4	35.57	78.41	33	5.1
14	06/15/93	23:12:24.8	35.63	77.79	33	4.9
15	05/29/94	14:11:50.9	20.56	94.16	36	6.2
16	04/26/94	18:59:27.3	56.73	117.87	18	5.3
17	11/18/94	01:13:00.2	13.06	121.09	20	5.4
18	11/18/ 94	05:14:03.4	13.02	120.95	33	4.9
19	03/24/95	04:13:46.4	24.58	121.97	45	5.0
20	04/03/95	11:54:43.5	24.07	122.29	33	5.6
21	03/04/95	22:33:26.0	24.07	122.30	26	5.2
22	05/27/95	18:11:11.9	23.01	121.43	29	5.2
23	02/25/95	03:15:05.9	24.33	118.69	10	4.9
24	06/05/95	20:20:17.5	18.43	120.85	48	5.4
25	06/28/95	14:14:53.3	22.09	121.57	33	5.3
26	02/12/97	12:50:22.6	52.05	171.30	33	5.0
27	05/16/97	22:41:03.5	55.58	162.54	33	5.2
28	12/04/97	22:41:50.4	55.22	162.62	33	5.1
29	12/10/97	08:08:17.6	54.85	162.95	33	5.2
30	12/11/97	14:55:15.5	54.88	162.84	33	5.1
31	10/08/97	21:20:59.7	41.91	144.82	33	5.5
32	10/09/97	03:29:10.7	42.13	144.44	33	5.1
33	05/30/97	17:54:53.0	37.15	78.05	33	5.2
34	07/18/97	18:59:41.9	29.59	68.40	33	5.0
35	12/13/97	03:41:35.6	29.63	68.34	33	4.9
36	03/12/97	14:51:49.2	13.44	120.99	33	5.2
37	05/22/97	13:21:36.3	18.92	121.34	34	5.7
38	07/01/97	18:24:24.4	19.08	121.20	33	5.1
39	05/12/98	17:01:03.8	45.31	150.36	33	5.6
40	06/12/98	00:29:33.6	48.30	155.62	33	5.0
41	12/13/98	13:17:54.7	48.09	155.29	33	5.3
42	08/20/98	19:41:41.9	51.58	175.35	33	5.3
43	08/28/98	15:31:38.2	51.44	175.53	33	5.5
44	05/08/98	17:37:05.4	22.36	125.44	33	5.0
45	05/27/98	01:16:30.4	22.03	125.60	33	5.4
46	01/10/98	03:50:41.5	41.08	114.50	30	5.8
47	11/06/98	20:29:24.1	11.06	92.46	33	5.0
48	11/06/98	22:52:09.3	11.05	92.51	33	5.2
49	05/12/98	17:01:03.8	45.31	150.36	33	5.6
50	06/12/98	00:29:33.6	48.30	155.62	33	5.0
51	12/13/98	13:17:54.7	48.09	155.29	33	5.3
52	08/20/98	19:41:41.9	51.58	175.35	33	5.3
53	08/28/98	15:31:38.2	51.44	175.53	33	5.5
54	02/12/99	17:44:48.5	44.47	149.68	33	5.6
55	03/11/99	13:18:09.3	41.13	114.66	33	5.1
56	02/25/99	08:41:17.7	52.23	173.96	33	5.1

Table 3.1: Events used in the two-station method with hypocentral information. EVLA and EVLO are event latitude and longitude, respectively. d is focal depth and m_b is the body-wave magnitude. A depth of 33 km normally indicates a default value; this does not affect the two-station technique.

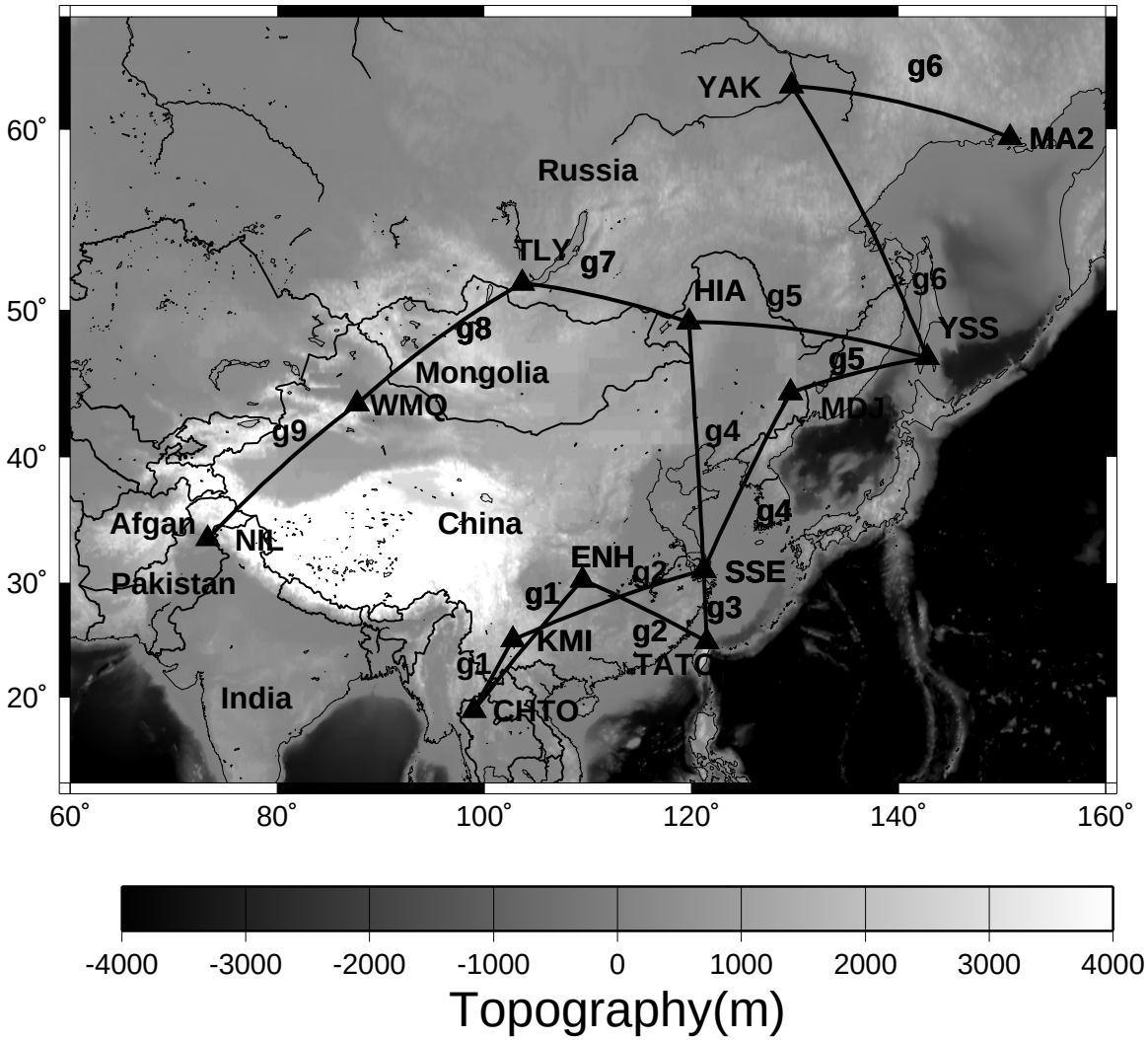

Figure 3.1: Two-station paths.

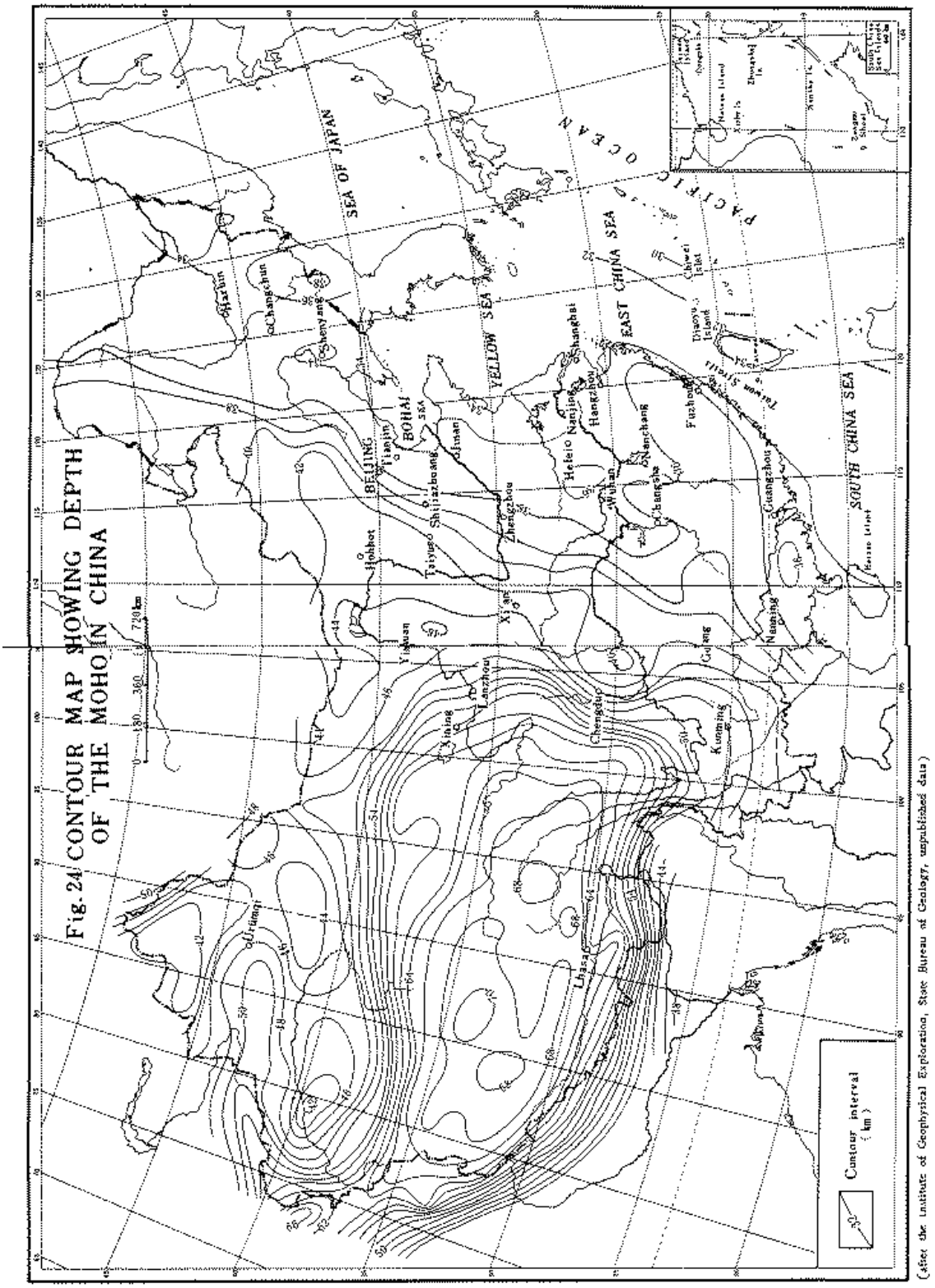

Figure 3.2: Moho depth in China (Ren et al., 1987).

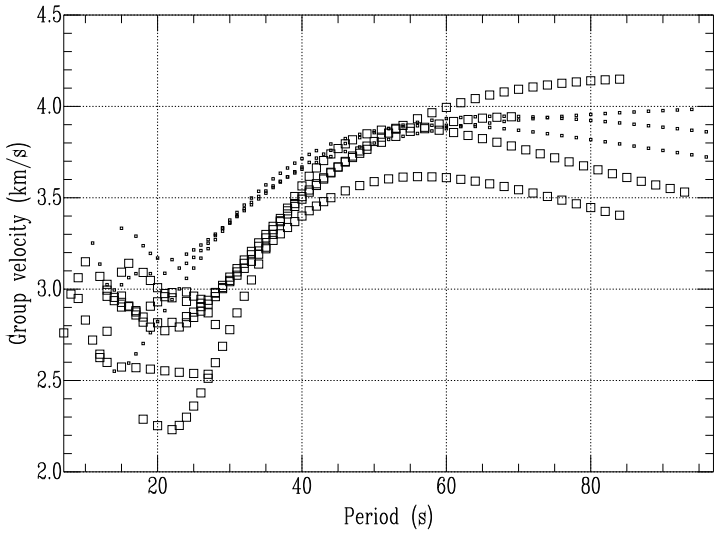

Figure 3.3: Group velocity comparisons between group 1(boxes) and group 2 (dots).

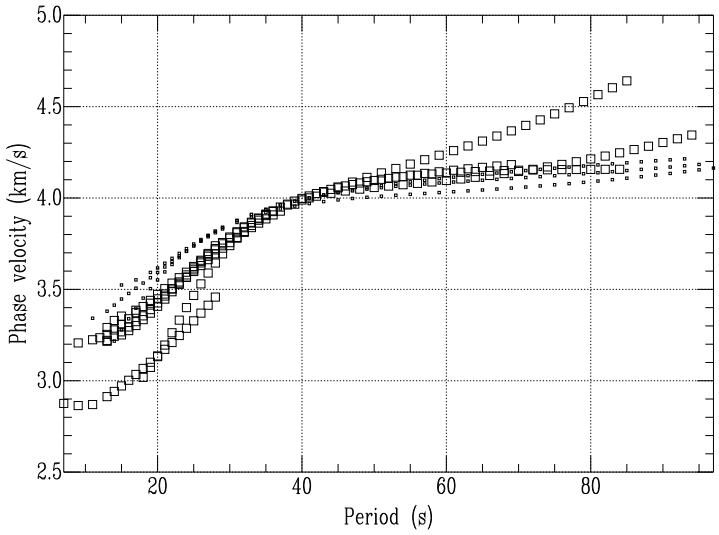

Figure 3.4: Phase velocity comparisons between group 1(boxes) and group 2 (dots).

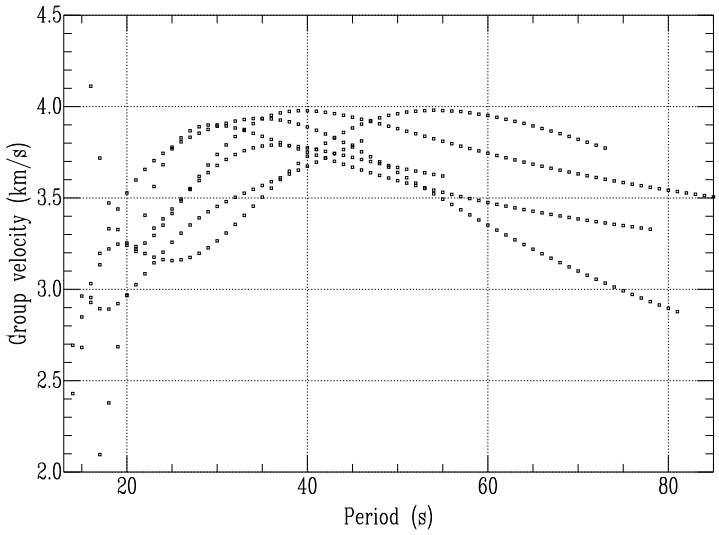

Figure 3.5: Group velocities for group 3.

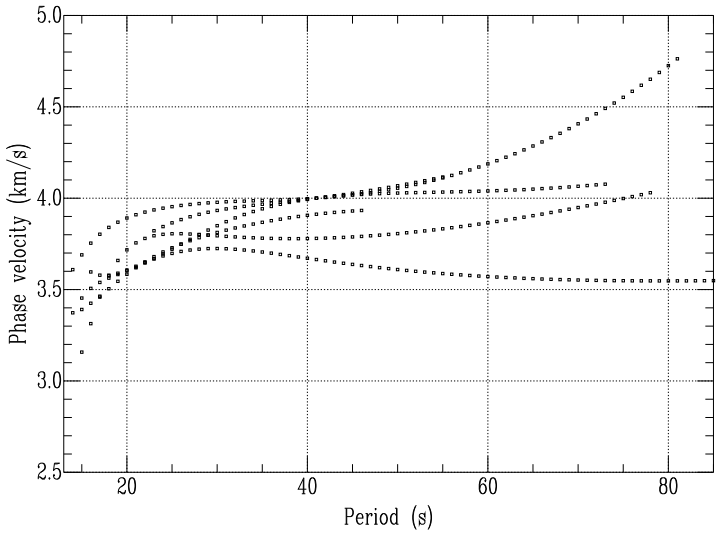

Figure 3.6: Phase velocities for group 3.

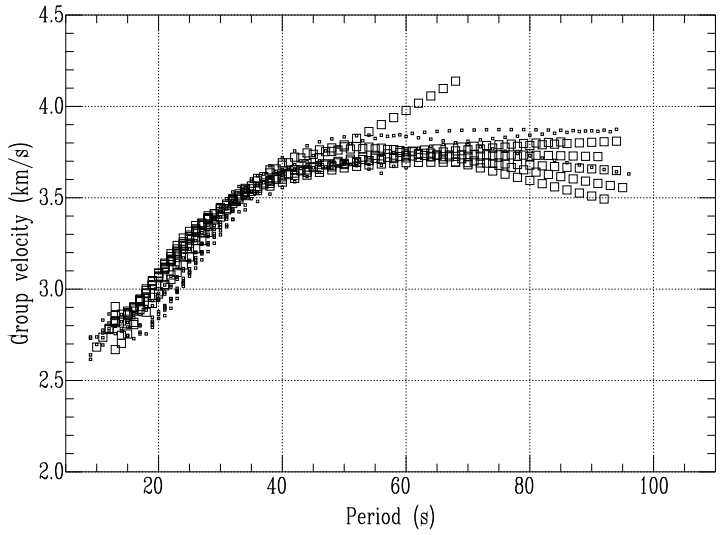

Figure 3.7: Group velocity comparisons between group 4(dots) and group 5 (boxes).

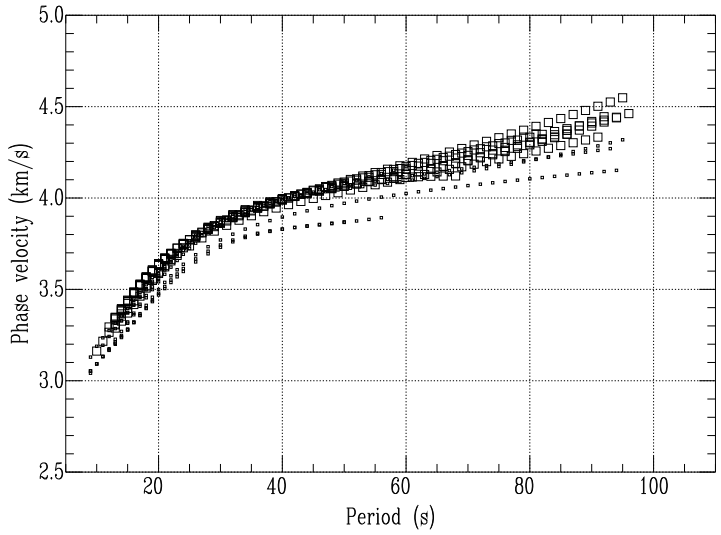

Figure 3.8: Phase velocity comparisons between group 4(dots) and group 5 (boxes).

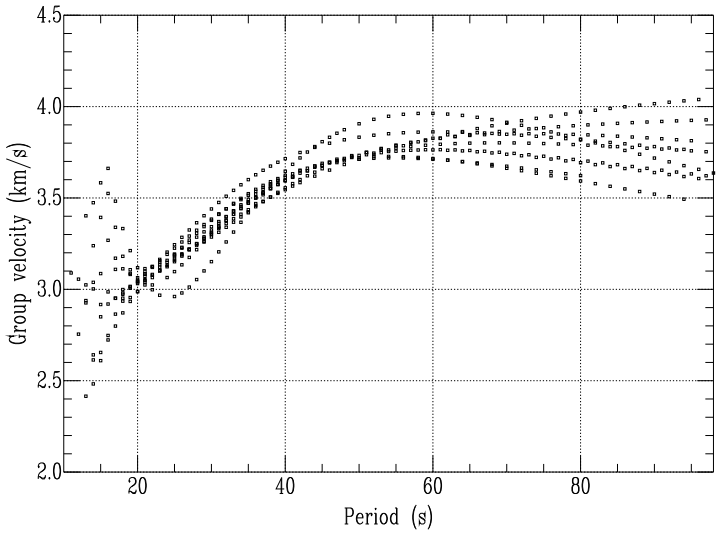

Figure 3.9: Group velocities of group 6.

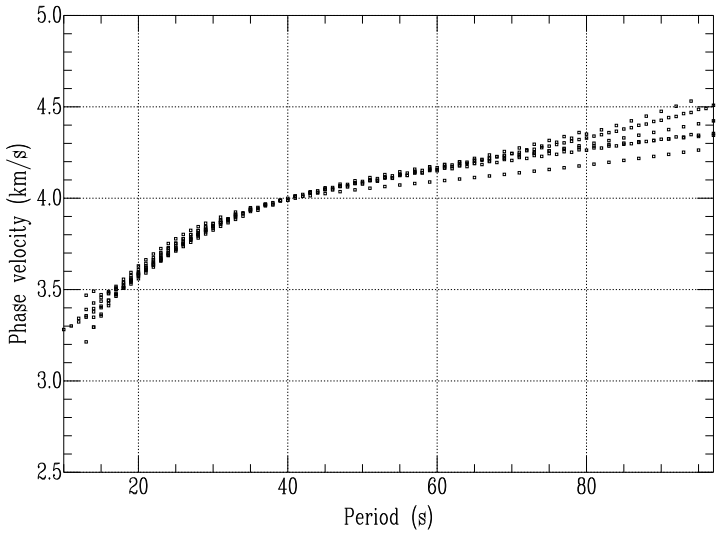

Figure 3.10: Phase velocities of group 6.

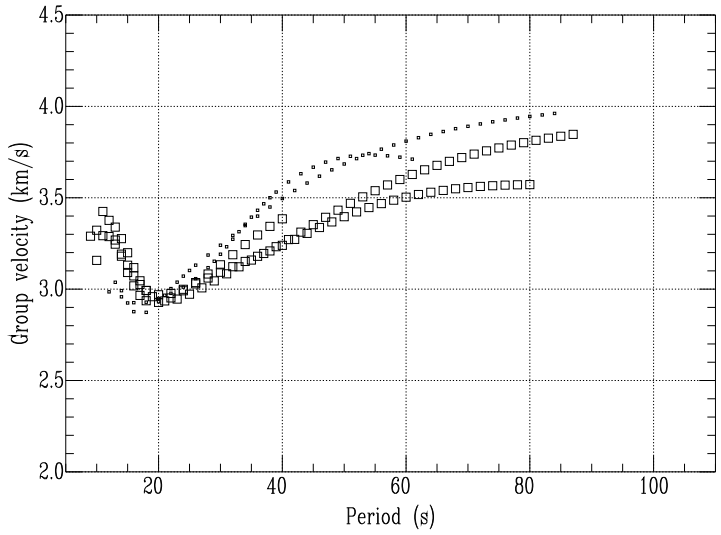

Figure 3.11: Group velocity comparisons between group 7(dots) and group 8 (boxes).

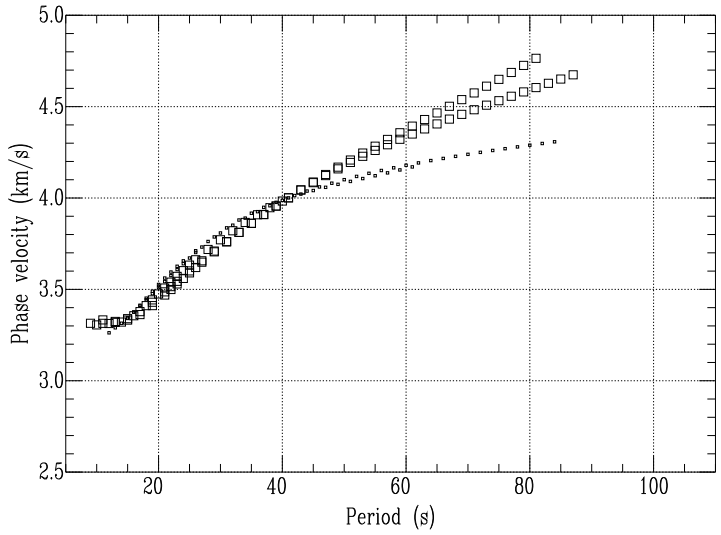

Figure 3.12: Phase velocity comparisons between group 7(dots) and group 8 (boxes).

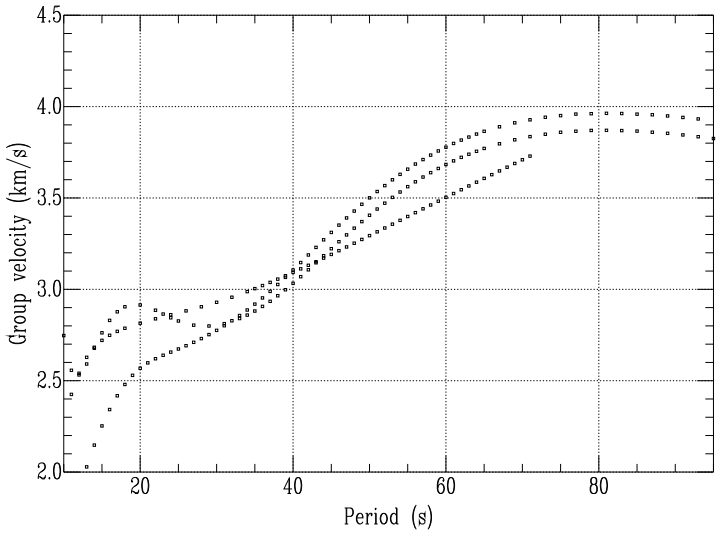

Figure 3.13: Group velocities of group 9.

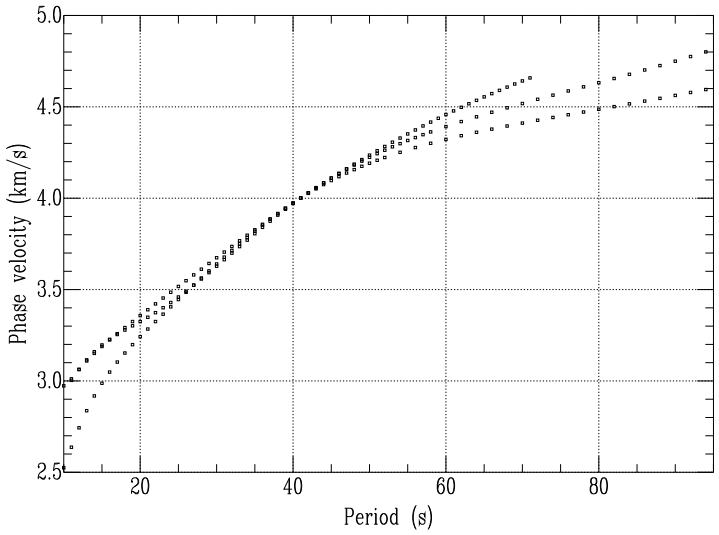

Figure 3.14: Phase velocities of group 9.

the effect of lowering the average group velocity. As a result, surface-wave paths crossing different tectonic regions should show different trends in their average group-velocity dispersion curves.

I plotted inter-station group-velocity curves on the same scale for paths crossing approximately the same region. The same thing is done for phase velocities. The paths between stations cover different tectonic regions. These are: (1) southeastern China, (2) eastern China, (3) northeastern China, (4) the southern Russia, (5) the Mongolia region and the Junggar block, (6) The Tien-Shan fold belt system, the Tarim Basin and the western Kunlun fold system (Figure 1.1).

In the two-station method the Tibetan Plateau is not studied for the following main reasons:

1. Seismic waves propagate across the highly variable Tibetan crust and topography. These factors may cause multipathing and scattering of the seismic waves in that region (Pavlis and Mahdi, 1996; Mahdi and Pavlis, 1998).

2. There are no permanent stations other than LSA within the Tibetan Plateau.

The 1991-92 temporary array of stations on the Tibetan plateau are aligned along only one direction, northeast-southwest. If I try to use data from these stations, because of reason 1 it is hard to apply the two-station method for the Tibetan Plateau.

In the following subsections, I will explain how different regions (groups) are formed based on differences in the group-velocity and phase-

velocity dispersion curves. The groups so formed and the station names are shown in Figure 3.1.

3.3.1 The South China Block

Inter-station group velocities for paths in the South China Block are plotted in Figure 3.3. Paths between stations CHTO and KMI and between ENH and CHTO have lower group velocities than do paths ENH-TATO and KMI-SSE, for periods between 20 sec and 40 sec. The same difference is also seen for phase velocities (Figure 3.4) for the period range 15 sec to 35 sec. According to these figures, paths CHTO-KMI and ENH-CHTO form group 1 and paths ENH-TATO and KMI-SSE form group 2.

The phase and group velocities of the path SSE-TATO exhibit substantial scatter (Figures 3.5 and 3.6) which may be due to the short travel distances between the earthquakes and stations. Comparison of these curves with published oceanic and continental phase- and group-velocity curves show that they are more like oceanic dispersion curves. This may be due to a large thickness of low-velocity sediments in this shelf region. This path forms group 3.

3.3.2 Northeastern China

This region consists of most of east-central China, northeastern China, the Yellow Sea, and North Korea. The paths crossing these regions are SSE-HIA, SSE-MDJ, MDJ-YSS and HIA-YSS.

Figure 3.7 shows that the group velocities for paths HIA-SSE and MDJ-SSE are lower than those for paths MDJ-YSS and HIA-YSS, for

periods between 15 sec and 40 sec. Differences in phase velocities are also seen for the entire period range (Figure 3.8). Therefore, paths HIA-SSE and MDJ-SSE form group 4, while paths MDJ-YSS and HIA-YSS form group 5.

3.3.3 Southeastern Russia

In this region the phase and group velocity curves for paths YSS-YAK and YAK-MA2 overlap (Figures 3.9 and 3.10), so are grouped together to form group 6. These paths cross the tectonically stable Siberia craton.

3.3.4 The Mongolian Plateau and the Junggar basin

Path HIA-TLY crosses the region south of Lake Baikal in an east-west direction in the northern periphery of Mongolia. Path TLY-WMQ crosses western Mongolia and the Junggar basin, in northwestern China, in a southwesterly direction. The group-velocity curves (Figure 3.11) of these two paths show clear differences at periods greater than 20 s. This difference is also seen in phase velocities (Figure 3.12) for periods between 15 sec and 35 sec. Therefore path HIA-TLY forms group 7, and path TLY-WMQ forms group 8. The southern end of the Junggar basin stops at the southern end of Group 8 (Figures 3.1 and 1.1).

3.3.5 The Tianshan fold system, the Tarim Basin, and the Western Kunlun fold system

Path WMQ-NIL starts from the northern part of the Tienshan fold system (Figures 3.1 and 1.1), crosses the Tarim Basin and the Western Kunlun fold system in a southwesterly direction, and ends in northern

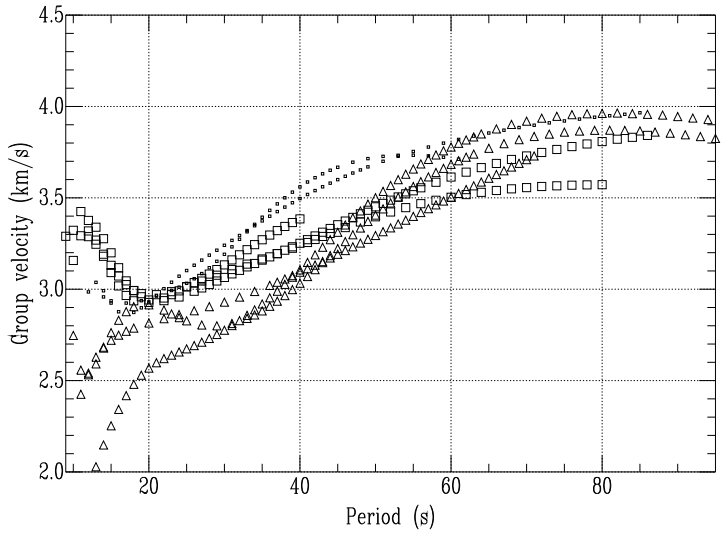

Figure 3.15: Group velocity comparisons for group 7(dots), group 8 (boxes) and group 9 (triangles).

Pakistan. When the group-velocity curves (Figure 3.15) for this path are plotted with those of paths HIA-TLY and TLY-WMQ, they are different at periods greater than 20 s. The phase velocities (Figure 3.16) are also different between the periods 5 sec and 40 sec. Therefore I let path WMQ-NIL form group 9.

3.4 Average inter-station group velocities, phase velocities and attenuation coefficients

From elementary statistical theory, the average (statistical mean) of a set of n measured quantities $y_1, y_2, \cdots, y_n$ is defined by

$$\bar{y} = \frac{1}{n} \sum_{i}^{n} y_i \tag{3.1}$$

Here each $\bar{y}$ is computed at each period. The $y_i's$ are either group velocities, phase velocities or attenuation coefficients of the i^{th} event.

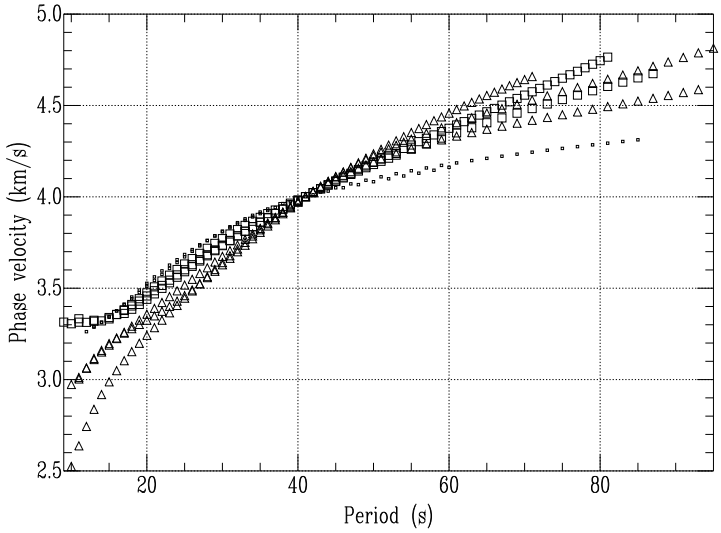

Figure 3.16: Phase velocity comparisons for group 7(dots), group 8(boxes) and group 9(triangles).

The standard deviation is a measure of how widely values are dispersed from the mean value. The Microsoft Excel utility STDEV is used to compute the standard deviation at each period. It estimates the standard deviation based on a sample and is calculated using the "nonbiased" or "n-1" method.

STDEV uses the formula

$$\sqrt{\frac{n\sum_i^n y_i^2 - (\sum_i^n y_i)^2}{n(n-1)}} \tag{3.2}$$

where the y_i's are observations and n is the number of observations. The average group velocities, phase velocities, and attenuation coefficients for all groups are shown in Figures 3.17 , 3.18 and 3.19.

If the number of data points at each period is less than two, then it is not possible to compute the average and standard deviation at that period. Therefore, I assigned the maximum STDV in the entire period

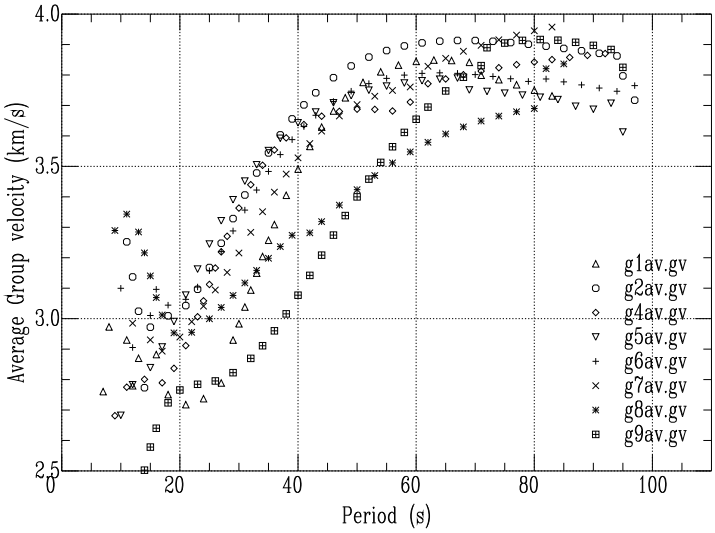

Figure 3.17: Average group velocity comparisons for groups 1 through 9, except that for group 3.

range to those data points with only one value at a period.

3.5 Comparisons of average group and phase velocities between regions

The average group velocities of group 1 are lower at all periods than those of group 2 (Figure 3.17). The average phase velocities of group 1 are also lower than those of group 2 for periods less than 40 sec (Figure 3.18). Both group 1 and group 2 paths are within the South China Block. However, as can be seen from Figure 3.1, paths of group 1 cross higher topographic regions at the transition from Tibet to southeastern China. Most of the group 2 paths are in the lowland part of the South China Block, crossing the South China fold system and part of Yangtze platform (Figures 1.1 and 3.1).

Group 1 has also lower average group velocity values than those

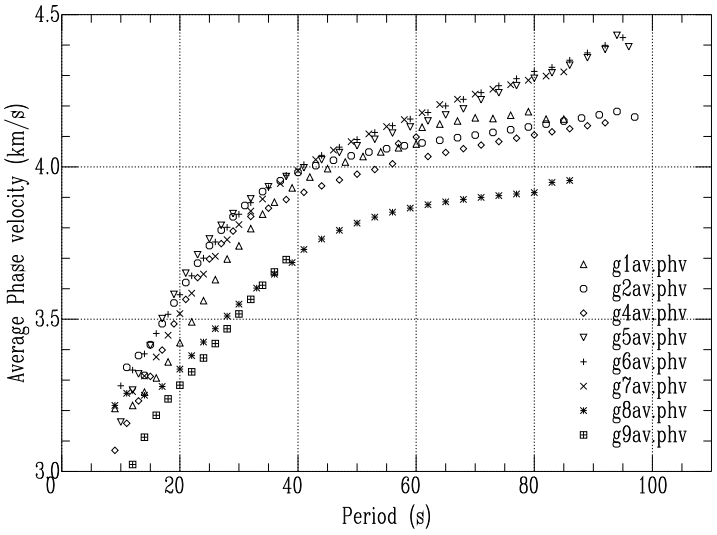

Figure 3.18: Average phase velocity comparisons for groups 1 through 9, except that for group 3.

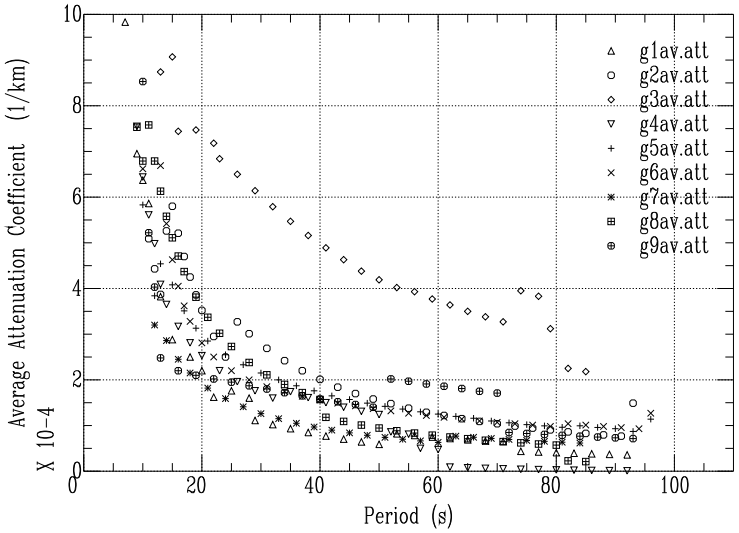

Figure 3.19: Average attenuation comparisons for groups 1 through 9.

of groups 4, 5, 6, and 7 for periods between about 15 sec and about 45 sec. However, the relation is reversed between 40 to 50 sec and 65 to 80 sec. The average phase-velocity comparisons show that group 1 has lower values than does group 4 for periods between 15 sec and 35 sec but a reversed relation beyond 35 sec. Group 1 has lower average phase velocities at all periods compared to those of groups 5, 6, and 7. These comparisons show that the thicker crust, as shown in a Moho map for China (Figure 3.2, Ren et al.,1987), crossed by group 1 slows the seismic waves propagating across it.

Groups 8 and 9 have lower average group velocities than does group 1 for periods between about 35 sec and 80 sec. But, the relation is reversed for periods less than 35 sec. If average group-velocities are correct (and are not badly contaminated by lateral refraction of energy), then at shallower depths, shear velocities are higher in western China than in the transition from Tibet to southeastern China, but the relations are reversed at greater depths. However, comparisons of average phase velocities show that group 1 has higher values at all periods compared to those of groups 8 and 9.

The average group-velocity curves of groups 2 and 4 overlap between 30 sec and 40 sec. Beyond 40 sec, group 2 has higher values than does group 4. The average phase velocity of group 2 is higher than that of group 4 at all periods.

Between 20 sec and 40 sec, group 2 has lower average group velocities than group 5. For periods greater than 40 sec, group 2 has higher average group velocities. There is an overlap between the average phase velocities of these groups between 15 and 45 sec. Above 45

sec, group 5 has higher phase velocities.

Comparison between groups 2 and 6 shows that the average group velocity of group 2 is higher than that of group 6 at all periods. There is an overlap in average phase velocities for periods less than 40 sec. At periods longer than 40 sec, group 6 has higher average phase velocities.

Group 2 has higher average group velocities at almost all periods when compared with group 7. The phase velocity comparison shows that for periods less than 40 sec, group 2 has higher values than group 7, but the relation is reversed beyond 40 sec. Groups 8 and 9 have lower average group and phase velocities at almost all periods compared to group 2.

Group 4 has lower average group velocities for periods less than about 70 sec when compared with group 5. The average phase velocities of group 4 are lower than those of group 5 at all periods. There is an overlap between the average group velocities of groups 4 and 6 between periods 30 sec and 45 sec. Below 30 sec and between 45 sec and 65 sec, group 4 has lower values. Beyond 65 sec group 4 has higher values. The comparison of average phase velocities shows that group 4 has lower values at all periods compared to that of group 6.

For periods between 25 sec and 50 sec, the average group velocities of group 4 are higher than those of group 7. Below 25 sec and above 50 sec, group 7 has higher values. Average phase velocities agree for periods less than 35 sec but group 7 has higher values beyond 35 sec.

Group 4 has higher average group and phase velocities at almost all periods when compared with groups 8 and 9.

The average group velocity of group 5 is slightly higher than that

of group 6 for periods between 20 sec and 40 sec, but the relation is reversed for periods less than 20 sec and greater than 70 sec. Between 40 sec and 70 sec, the average group velocities of groups 5 and 6 approximately coincide. The average phase velocities of these groups approximately coincide for all periods.

The average group and phase velocity curves of group 5 are higher than those of group 7 for periods between 15 sec and 60 sec. Beyond 60 sec group 7 has higher values. Group 5 has higher average phase and group velocities than do groups 8 and 9 at all periods.

The average group-velocities of group 6 are higher than those of group 7 for periods less than 60 sec. Beyond 60 sec group 7 has higher values. The phase-velocity curves show that group 6 has higher values for periods less than 40 sec but there is an agreement between groups 6 and 7 beyond 40 sec. Groups 6 and 7 have higher average group and phase velocity values when compared with groups 8 and 9 at all periods.

Group 8 has higher average group velocity values than group 9 for periods less than 55 sec. For periods above 55 sec, group 9 has higher values. The average phase velocities of group 8 are higher than that of group 9 for periods less than 40 sec.

3.5.1 Relations between tectonics and group and phase velocity variations

From the Nafe-Drake curve (Ludwig et al. 1970), the shear- and compressional- wave velocities are directly proportional to the densities of rocks in the Earth. Higher densities are therefore associated with

the higher velocities known to be present in the mantle.

Low group velocities may arise form a combination of low velocities in the crustal column and a thick crust. Rayleigh waves that are trapped in the crust will have low group velocities (Wu and Levshin, 1994).

From the contour map showing the depth of Moho in China (Figure 3.2) the crustal thickness in eastern Tibet reaches about 65 km and thins to 50 km at the transition from Tibet to the South China Block. In southeastern China, the crustal thickness ranges between 45 and 50 km in the west and thins to 36 km near the east coast. Wier(1982) shows that the crust along the eastern coast thins to about 30 km.

The crust is thin, between 42 km and 34 km, in almost all parts of eastern China, including parts of the Sino-Korean platform, and the fold systems in northeastern China (Figures 1.1 and 3.2). The western parts of the study area have relatively thick crust except in the Junggar and Tarim basins where the crust thins to about 42 km.

These differences in crustal thickness between the east and the west give rise to differences in the average group-velocity curves. The western part (groups 8 and 9) has the thickest crust and is tectonically more active. The seismicity of the region (Figure 3.20) shows that the western part of southeastern Asia is more active than the eastern part. The western region is also characterized by lower group velocity values (see the values for groups 8 and 9) than the southeastern part (groups 1 to 6).

The eastern part of the North China Craton (the Sino-Korean platform) (Figure 1.1) crossed by group 4, has relatively low average group

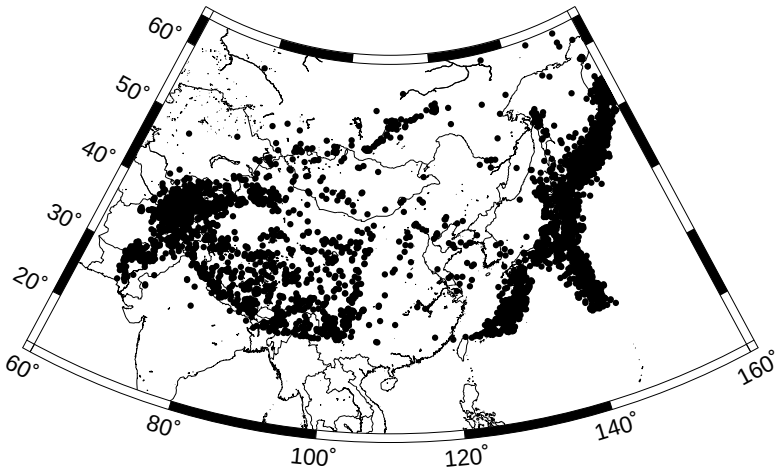

Figure 3.20: Seismicity map of southeastern Asia for the past 10 years.

velocities compared to group 2. The North China Basin is a region of active extensional tectonics (Nabelek et al., 1987) while the South China Block crossed by group 2 is one of the least tectonically active regions in southeastern Asia (Wu et al., 1994). They show little difference in their crustal thickness, but the higher tectonic activity in the North China Basin may cause the average group velocities of group 4 to be lower than those of groups 2, 5, and 6.

Recent seismic and surface heat flow studies (Liu, 1992; Menzies and Xu, 1998) show that the present-day lithosphere in the eastern part of the North China Craton is thin (less than 80 km) and hot with low velocities at shallow depths. This is consistent with the result for group 4 when compared with groups 2, 5, and 6.

The high group velocities in the fold systems of northeastern China (Figure 3.1), crossed by group 5, coincide with an area of Cenozoic basalts (Figure 3.21). The crustal thickness is as small as 23 km in the Songliao Basin (Figure 3.21) in northeastern China (Zhang, 1998).

But it thickens to 38 km near the eastern and western boundaries. Surface heat flow decreases gradually from the center of the basin (up to 95 mWm^{-2}) towards the northern margin (44 mWm^{-2}). This indicates that northeastern China is tectonically active. However, the small crustal thickness may be responsible for the higher average group velocity of group 5 when compared with group 2 (between 20 sec and 40 sec), group 4 (at all periods) and group 6 (between 20 and 70 sec). Group 6 crosses the Siberian craton which is one of the most stable regions in the world.

Group 7, and most parts of group 8, are within the Mongolian Plateau (Figure 3.1; Windley and Allen, 1993). This region is tectonically very active as indicated by high seismicity (Figure 3.20) and high heat flow (Khutorskoy and Yarmoluk, 1989). The heat flow is high, reaching 120 mW/m^2. The lithospheric thickness of the region crossed by group 7 ranges from 100 to 150 km (Windley and Allen, 1993). Part of the path crossed by group 8 is in central Mongolia where the lithosphere is as thin as 50 km. The crustal thickness is not well defined in the Mongolian Plateau (Windley and Allen, 1993).

Most parts of the paths for group 8 are within the thicker lithosphere in western Mongolia. The crust in the Junggar fold system is as thick as 50 km in its northern part (Figure 3.2). This might be partly responsible for the low average group velocities of group 8 compared to most of the others.

The crustal thickness crossed by group 9 varies from place to place. In the Western Kunlun fold system it reaches 65 km whereas in the Tarim and Junggar basins it is 42 km. The relatively thick crust, com-

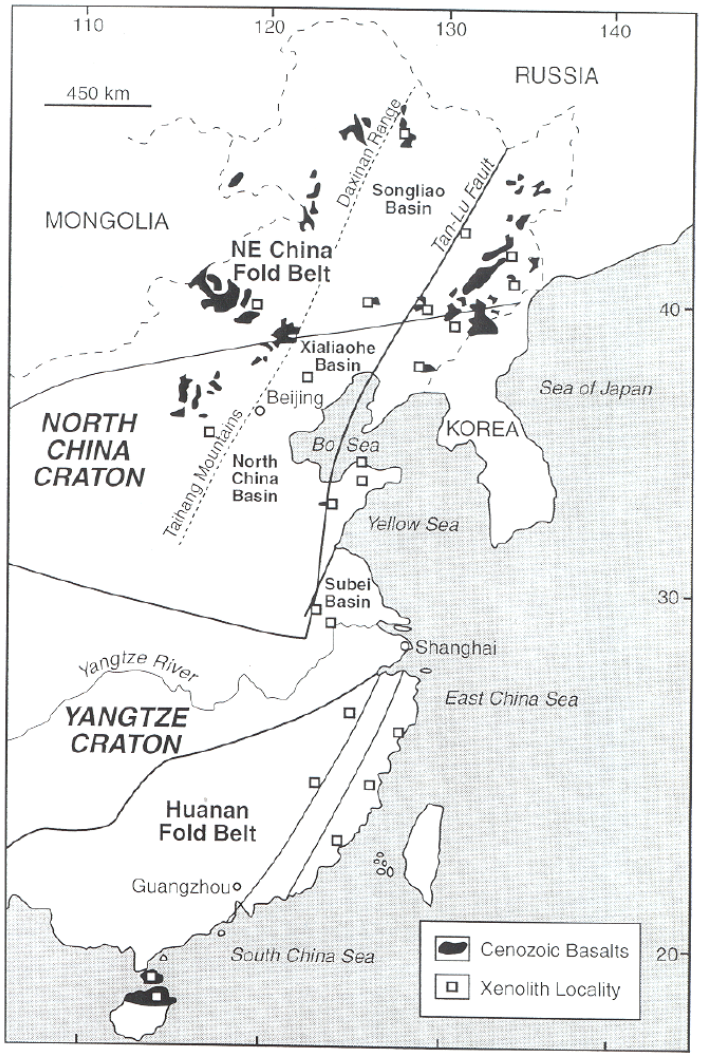

Figure 3.21: Cenozoic basalts in northeastern East China (Zhang et al., 1998).

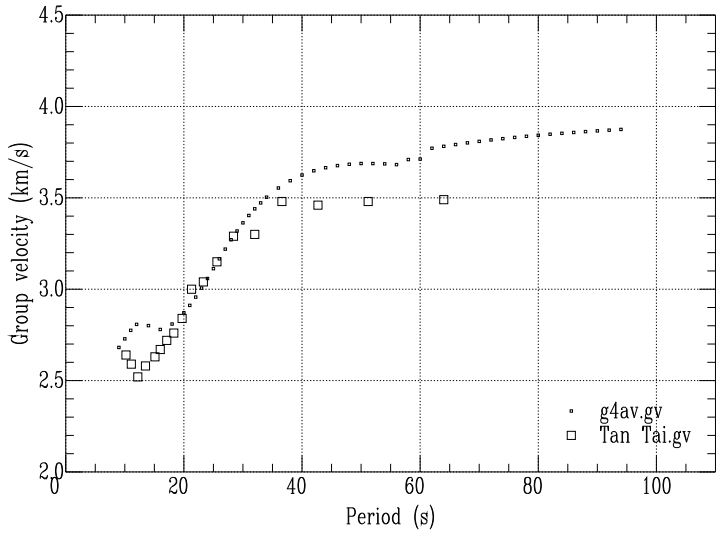

Figure 3.22: Comparison of the average velocities of group 4 (g4av.gv) with that of Pines et al. (1980) for the path Tangshan to Taipei (Tan Tai.gv) in southeastern China.

pared to the other parts of southeastern Asia, gives rise to the lowest group and phase velocities of the region of study.

3.6 Comparison with results of previous studies in southeastern Asia

I compare the average group velocity curve of group 4 to a study by Pines et al. (1980) for the eastern coast of China along the path from Tangshan to Taipei. The comparison shows that the two curves agree well between 20 sec and 40 sec, but differ at shorter and longer periods (Figure 3.22).

Wier (1982) obtained fundamental-mode Rayleigh-wave group velocities for southeastern China. I compared the group velocities for his model “6-ANP” with the group-velocity dispersion curve of group 2 in

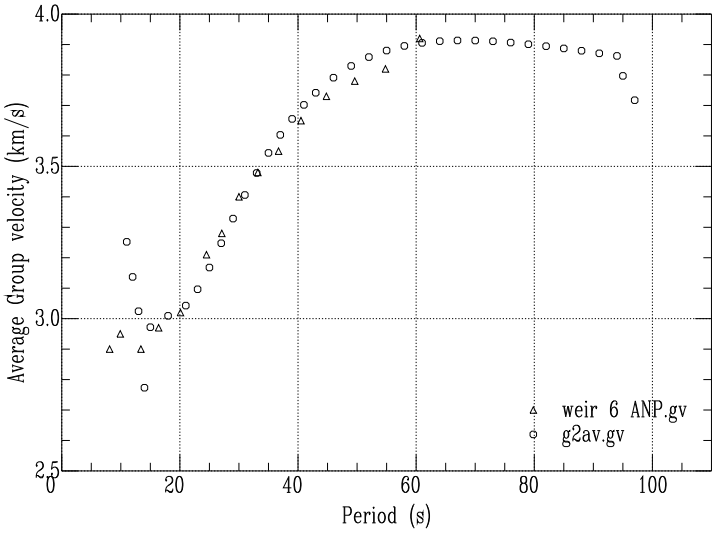

Figure 3.23: Comparison between average group velocities of group 2 (g2av.gv) and Wier's 1982 "6-ANP" group velocity curve for southeast China (weir 6 ANP.gv).

my study. Figure 3.23 shows that the two agree very well at all periods where "6-ANP" dispersion values are available. Comparison between the dispersion for "6-ANP" and group 1 shows that the latter is much lower for periods less than about 50 sec.

3.7 Comparison with the Canadian Shield

The Canadian Shield has been stable for more than a half billion years. It is characterized by low relief, very few earthquakes, no volcanism, and low heat flow (Brune and Dorman, 1963). I have compared (Figure 3.24) phase velocities predicted by the shear-velocity structure of the Canadian Shield with phase velocities of all groups in this study. For periods less or equal to about 50 sec, the phase velocity of the Canadian Shield is higher than that for all of the nine groups used in this

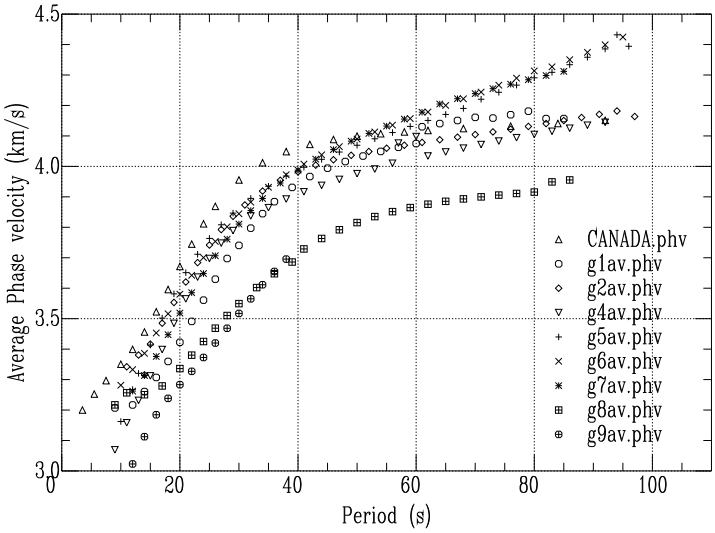

Figure 3.24: Comparison of the phase velocities for the Canadian Shield (CANADA.phv) with the average phase velocities for groups 1 through 9, excluding group 3, in southeastern Asia.

study. However for periods greater than about 50 sec groups 5, 6, and 7 show higher phase velocities than does the Canadian shield.

Group 6 crosses the southeastern part of southeastern Russia. Group 7 crosses part of southern Russia parallel to the border with Mongolia, beginning from the northern tip of China and ending at the southern tip of the Baikal rift. These are the two fastest groups found in my study. The high group and phase velocities of groups 5, 6, and 7 compared to that of the Canadian Shield at longer periods might be due to differences in the deep Earth structure.

3.8 Inter-station attenuation coefficients

Figure 3.19 shows the average attenuation coefficient curves of all groups. On the basis of previous work we expect that there will be an

inverse relationship between attenuation and velocity. However, the average attenuation coefficient values for some groups are not consistent with that relationship. For example, group 2 has high average group and phase velocities but the attenuation coefficient values between 15 and 55 sec are the highest I have found.

Another example is group 1, which shows that the lowest average group/phase velocities occur in eastern China. However this group has the lowest average attenuation coefficient values between 20 sec and 50 sec that I have observed.

This inconsistency between attenuation coefficient values and velocity may be due to effects of lateral heterogeneity which focus or defocus the seismic rays. This will result in an increase or decrease, respectively, in the amplitudes of seismic waves. Because attenuation coefficients are computed from ratios of amplitudes at two stations, heterogeneity in velocity structure, rather than attenuation may dominate the attenuation coefficient determinations.

Group 7 has low attenuation coefficients for the entire period range. This is consistent with its relatively high group/phase velocity compared to groups 8 and 9. Group 8 has high attenuation coefficient values for periods less than 40 sec and group 9 has high attenuation coefficient values for periods greater than 35 sec. These values are consistent with the low group/phase velocities for those groups.

4. Models of shear-wave velocity and shear-wave Q structures in southeastern Asia from interstation measurements of phase velocity and attenuation

In this chapter I present shear-wave velocity and Q_μ structures of southeastern Asia obtained from the inversion of average interstation phase velocities and attenuation coefficients, respectively, using the two-station method. Also, I discuss the results in relation to the tectonics of the region and results of previous studies there.

4.1 Shear velocity structure: Results and discussion

Group- and phase-velocity dispersion curves contribute generally the same information about a structural model (e.g., Bloch et al., 1969; Wiggins 1972, Yu and Mitchell, 1979). However, there exists an additional degree of non-uniqueness in the inversion of group-velocity data compared with the inversion of phase-velocity data, independent of the other points of non-uniqueness that apply uniformly to the inversion of dispersion data of both types. If the group velocities for two regions are the same, it does not follow that the two structures are the same (Pilant and Knopoff, 1970). For this reason, I use phase velocities for the inversion of shear wave velocity structure in southeastern Asia.

Figures 4.1, 4.2 and 4.3 show average interstation phase velocities as a function of period for each of the nine groups in the study area. The areas corresponding to these groups were described in Chapter 3. The vertical bars are standard deviations calculated at each period. Tables

Period (sec)	C(km/s)	STDEV (km/s)
10	3.21742	0.
12	3.21665	2.63610E-02
14	3.26066	2.74660E-02
16	3.30699	2.85840E-02
18	3.35956	3.22830E-02
20	3.42243	3.75610E-02
22	3.49101	3.87560E-02
24	3.56077	4.02560E-02
26	3.62961	4.62380E-02
28	3.69747	5.76990E-02
30	3.74051	6.01370E-02
32	3.79720	7.05130E-02
34	3.84475	8.10160E-02
36	3.88416	8.97950E-02
38	3.91683	9.66270E-02
40	3.94394	1.01851E-01
42	3.96663	0.105570
44	3.98569	0.108078
46	4.00194	0.109714
48	4.01595	0.110577
50	4.02833	0.110859
52	4.03924	0.110543
54	4.04916	0.109842
56	4.05826	0.108705
58	4.06683	0.107336
60	4.07496	0.105773

Table 4.1: Average interstation phase velocities used in the inversion for shear-wave velocity structure for group 1.

of average interstation phase velocities of each group, with standard deviations, used for the inversion of the shear-wave velocity structure, are provided. I have presented grid plots of the inversion results for clarity of discussion (Figures 4.4, 4.5 and 4.6). The starting model used has a uniform shear velocity value 4 km/sec throughout all depths.

4.1.1 Group 1

Phase velocities (Table 4.1, and Figure 4.1) for group 1 were used to obtain models of shear-wave structure at depths between 0 and 200 km. This region covers the transition between the Tibetan plateau and the South China Block. The shear-velocity structure of group 1 (Figures 4.7 and 4.4 and Table 4.2) starts at about 3.16 km/sec for the top

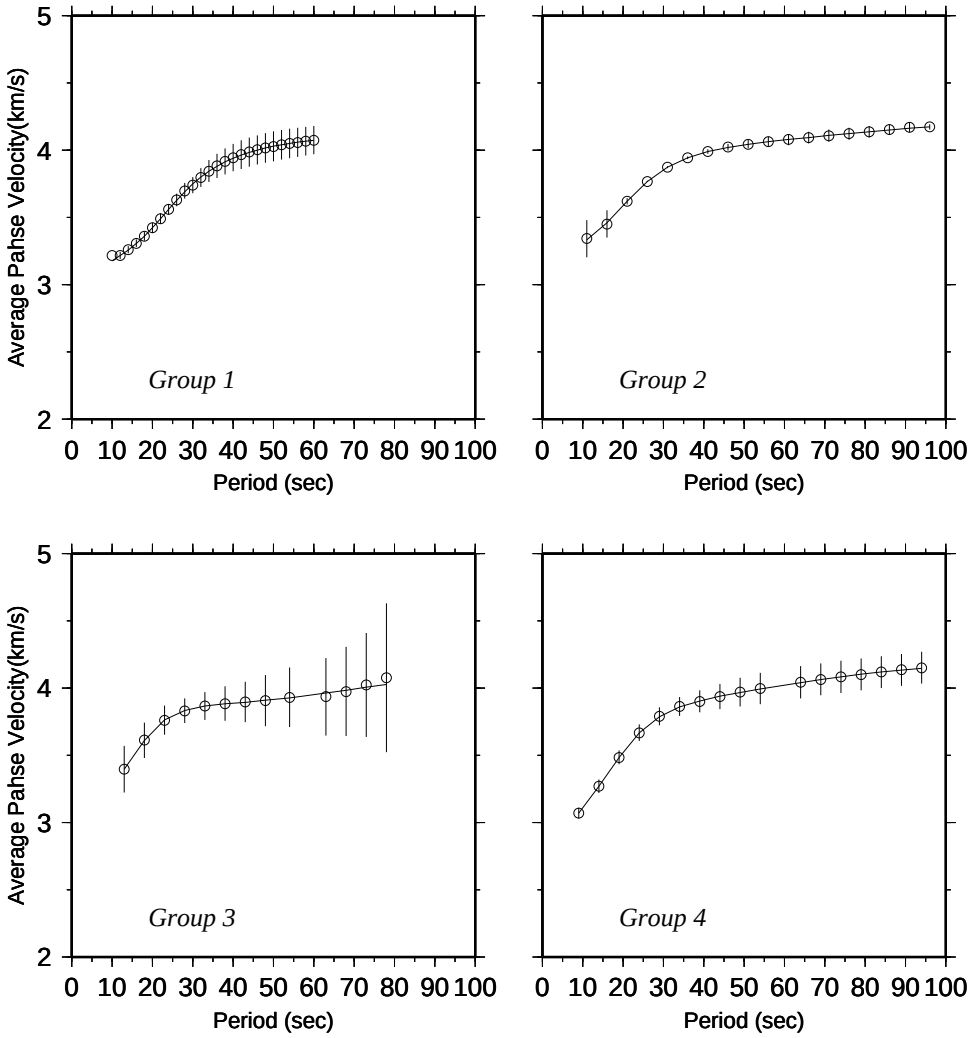

Figure 4.1: Average interstation phase velocities for groups 1-4 used in inversions for shear-wave velocity structure. Circles are observed velocities and the solid curve is predicted by the shear-velocity structure. The vertical bars are standard deviations of the observations.

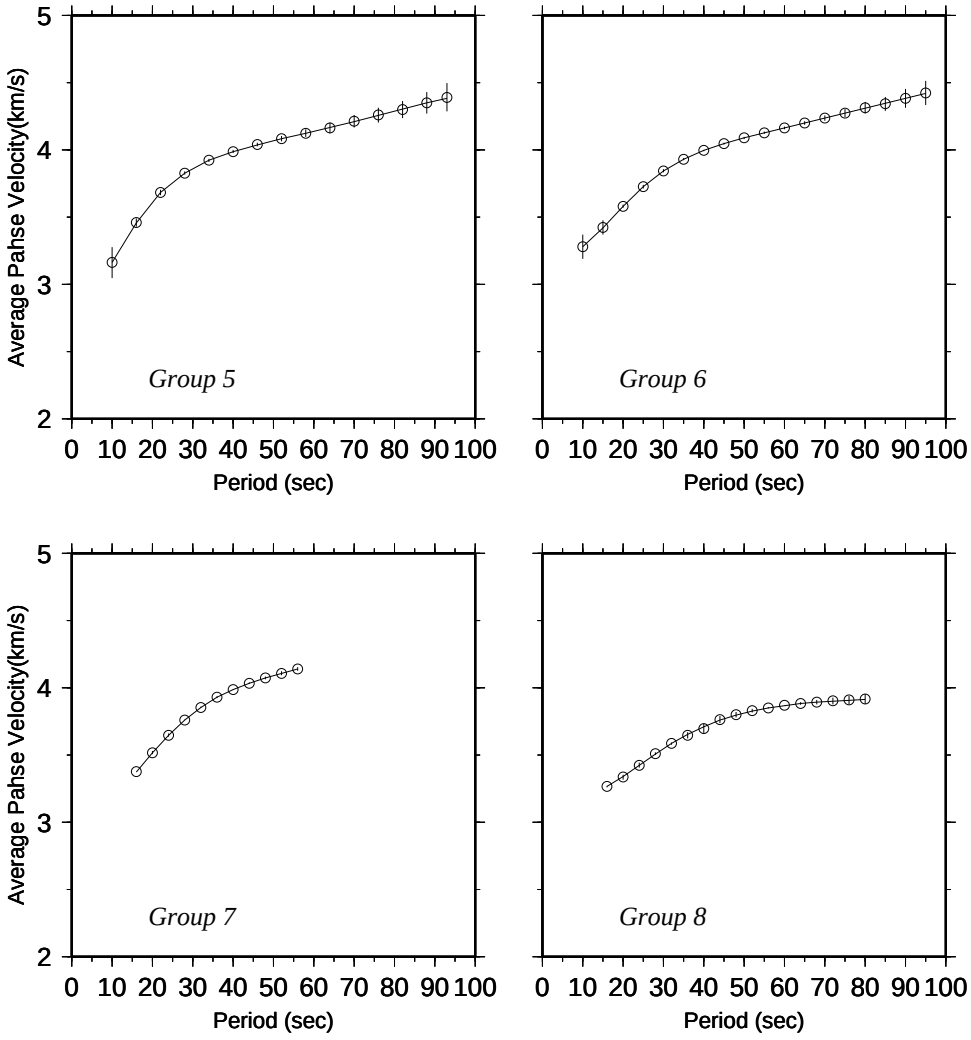

Figure 4.2: Average interstation phase velocities for groups 5-8 used in inversions for shear-wave velocity structure.

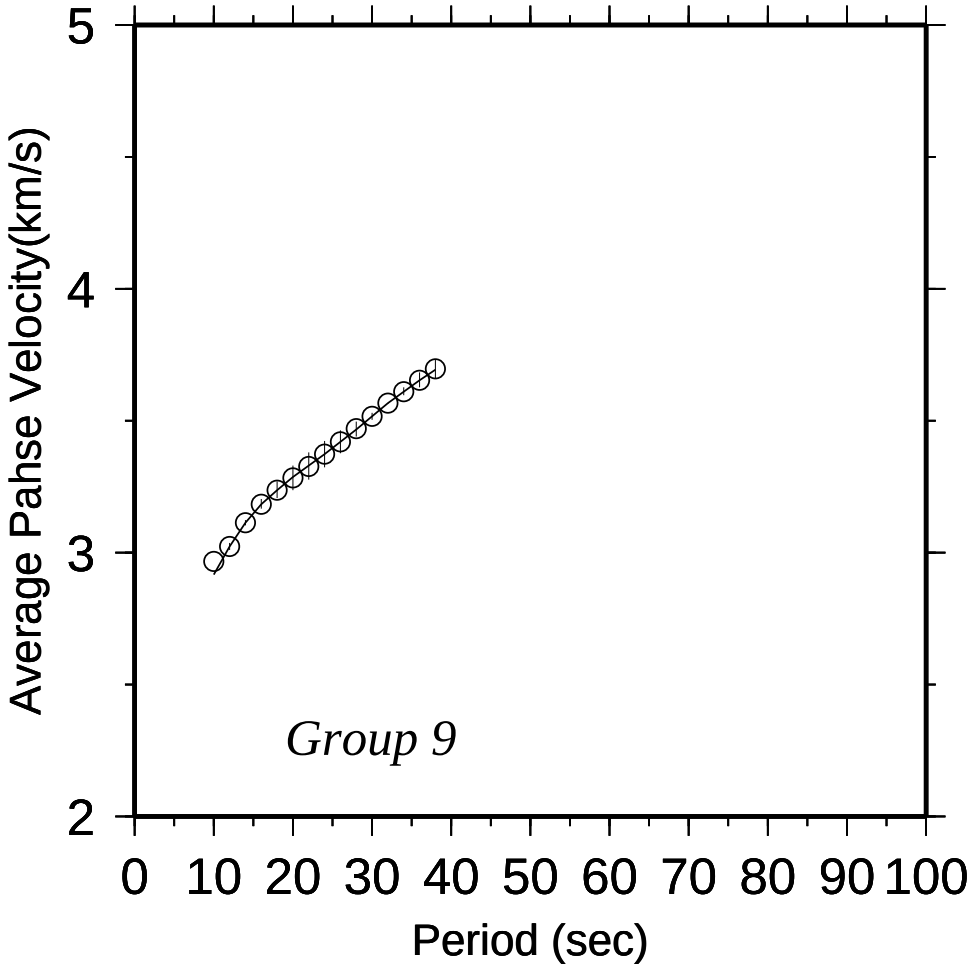

Figure 4.3: Average interstation phase velocities for group 9 used in the inversion for shear-wave velocity structure.

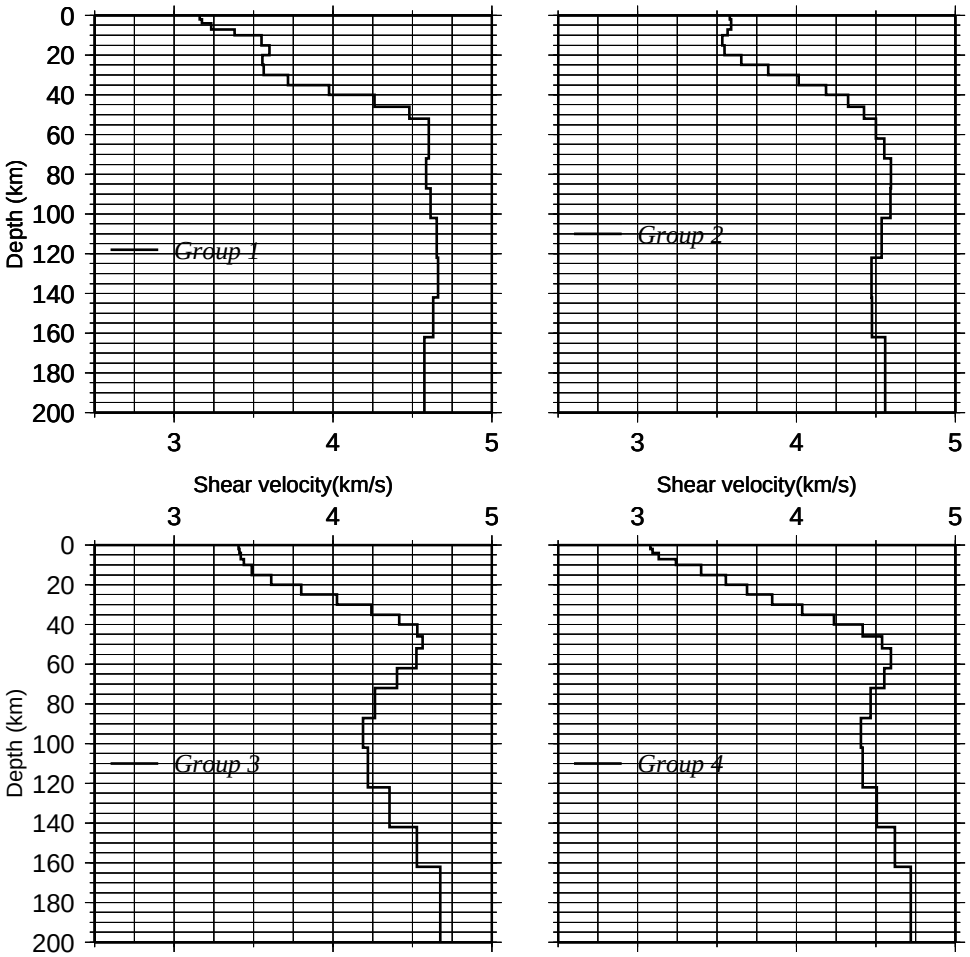

Figure 4.4: Shear-wave velocity structure for groups 1, 2, 3, and 4, presented for clarity of discussion.

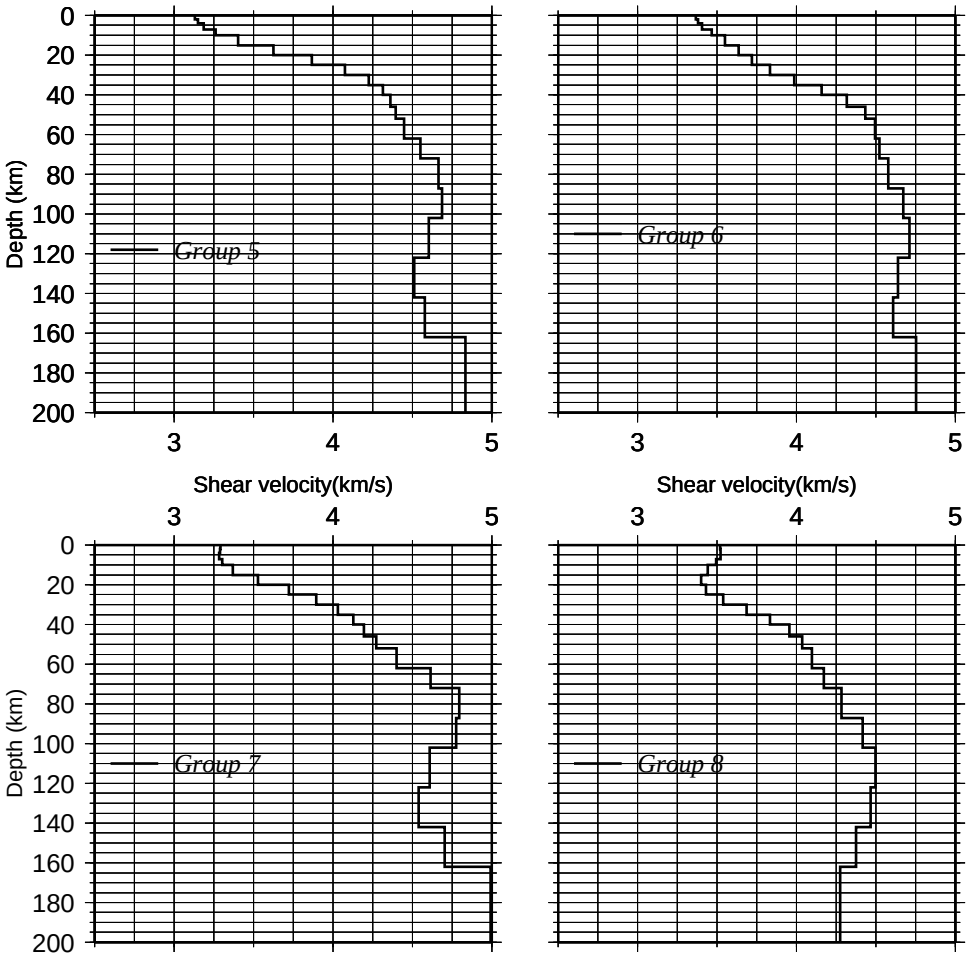

Figure 4.5: Shear-wave velocity structure for groups 5, 6, 7, and 8, presented for clarity of discussion.

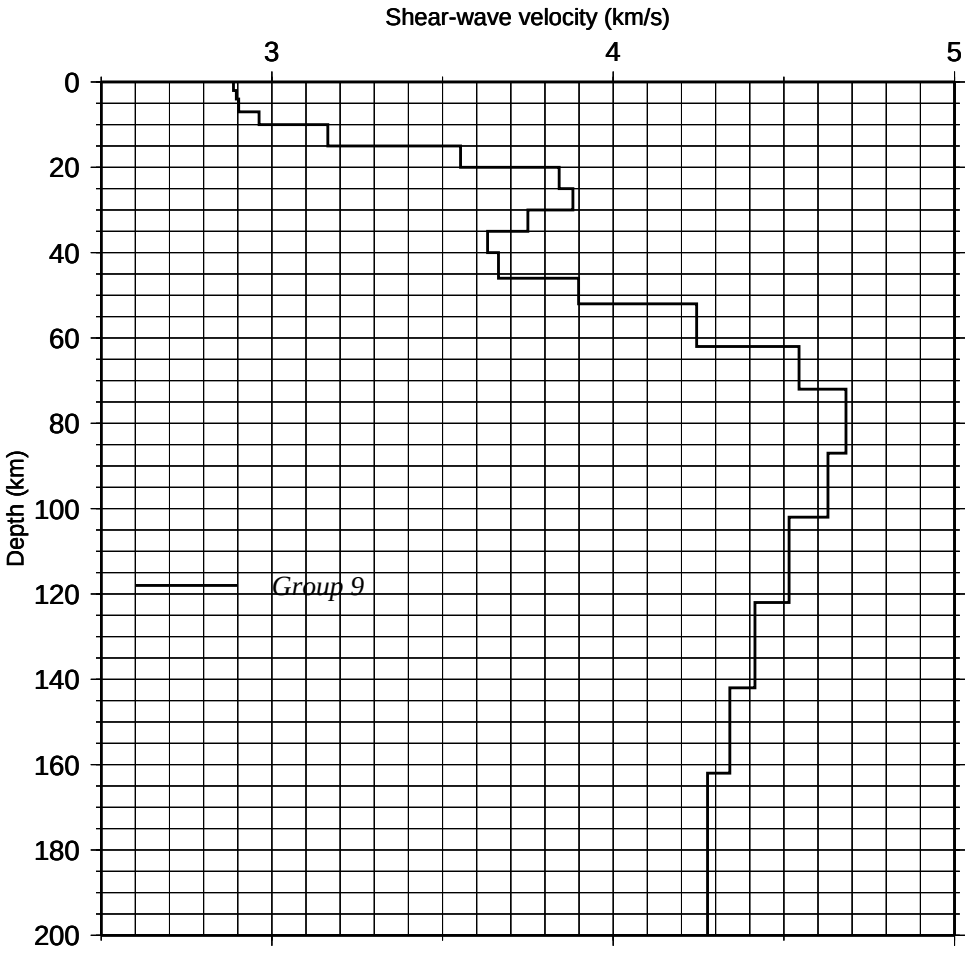

Figure 4.6: Shear-wave velocity structure for group 9, presented for clarity of discussion.

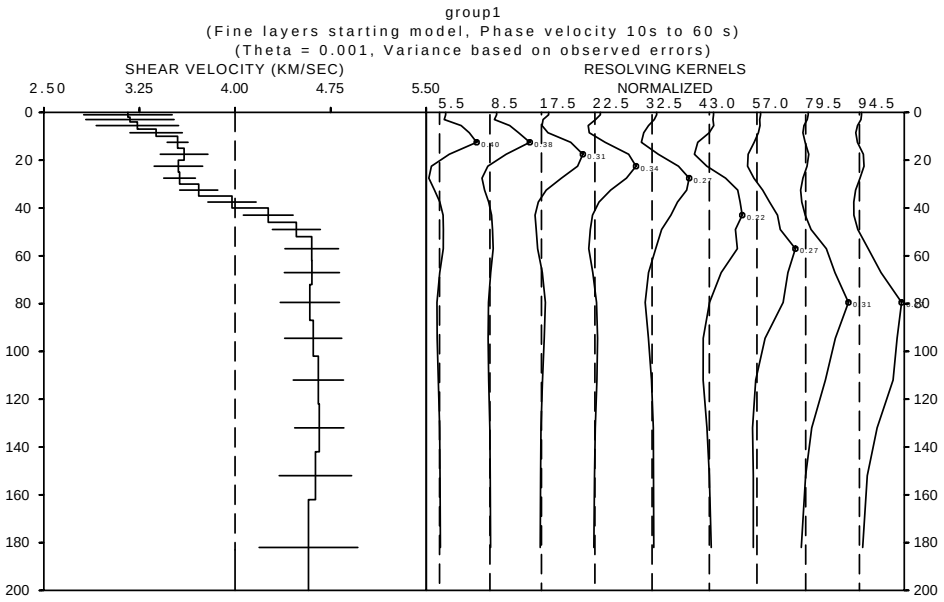

Figure 4.7: Shear-wave velocity structure for group 1. The dashed line at 4 km/s is a uniform starting shear-wave velocity model.

$H(km)$	$\alpha(km/s)$	$\beta(km/s)$	$\rho(gm/cc)$	Q_μ^{-1}	Poisson Ratio	Error $\beta(km/s)$
2.00000	5.47300	3.15980	2.59460	0.	0.250000	0.347000
2.00000	5.50060	3.17580	2.60010	0.	0.250000	0.346000
3.00000	5.60150	3.23400	2.62030	0.	0.250000	0.323000
3.00000	5.85640	3.38120	2.67130	0.	0.250000	0.205000
5.00000	6.14830	3.54970	2.74450	0.	0.250000	0.081600
5.00000	6.23640	3.60060	2.77090	0.	0.250000	0.187000
5.00000	6.15890	3.55590	2.74770	0.	0.250000	0.190000
5.00000	6.17490	3.56510	2.75250	0.	0.250000	0.124000
5.00000	6.43500	3.71530	2.83050	0.	0.250000	0.149000
5.00000	6.88670	3.97610	2.95060	0.	0.250000	0.189000
6.00000	7.37980	4.26070	3.10150	0.	0.250000	0.195000
6.00000	7.76180	4.48130	3.22900	0.	0.250000	0.188000
10.0000	7.97000	4.60150	3.29980	0.	0.250000	0.210000
10.0000	7.97380	4.60370	3.30110	0.	0.250000	0.216000
15.0000	7.94500	4.58710	3.29130	0.	0.250000	0.232000
15.0000	7.99090	4.61360	3.30690	0.	0.250000	0.224000
20.0000	8.06070	4.65390	3.33190	0.	0.250000	0.197000
20.0000	8.07300	4.66100	3.33630	0.	0.250000	0.193000
20.0000	8.02080	4.63080	3.31750	0.	0.250000	0.284000
40.0000	7.92600	4.57610	3.28480	0.	0.250000	0.387000
50.0000	7.99370	4.48700	3.30790	0.	0.270000	0.390000
70.0000	7.76190	4.35680	3.22900	0.	0.270000	0.300000
0.	7.83670	4.18890	3.25450	0.	0.300000	0.158000

Table 4.2: Inversion results from phase velocities of group 1, where H is layer thickness, α is p-wave velocity, β is shear-wave velocity, and ρ is density.

5 km. Between 5 km and 10km it reaches 3.55 km/sec. There is a 5-km thick high-velocity layer (3.6 km/s) between depths of 15 and 20 km. If real, this high-velocity layer could correspond to the ”high-velocity tooth” of amphibolites inferred by Mueller (1977) in his generalized petrological model and a P-wave velocity-depth profile for continental crust. Resolution kernels for this depth (Figure 4.7), however, indicate that this feature cannot really be resolved. The layer between 20 km and 30 km has a constant shear-wave velocity about 3.56 km/s.

At depths greater than 30 km the shear-wave velocity increases to 4.6 km/s at a depth of about 52 km/s. The velocity (4.6 km/s) below the sharp discontinuity at 52 km depth is the same as that in the upper mantle shear-wave velocity model of Muller (1977). The broad zone of positive velocity gradient between 30 km and 52 km could be real and may consist of part of the lower crust and a broad transition from the base of the lower crust to the upper mantle (the Moho) (Prodehl, 1977). The width of the resolving kernel at 43 km (Figure 4.7) however, indicates that we really cannot resolve this feature and it could be much thinner. The region crossed by paths of group 1 show a Moho depth ranging from 48 km to 50 km in agreement with the map of Ma et al. (1987) in Figure 3.2. This comparison suggests that the sharp discontinuity at about 52 km in Figure 4.7 can be the Moho. The almost constant shear velocity (between 4.6 km/sec and 4.7 km/sec) for the depth range between 52 km and about 160 km may represent the lid in the upper mantle. Because the resolution kernels are very broad for depths below about 50 km, it is hard to talk about the deeper structure with confidence. These results, however, suggest that the region

Period (sec)	C(km/s)	STDEV (km/s)
11	3.34197	0.138968
16	3.45122	1.01732E-01
21	3.62040	2.39520E-02
26	3.76799	4.53500E-03
31	3.87332	6.32000E-03
36	3.94353	1.13170E-02
41	3.99006	1.77770E-02
46	4.02174	2.45700E-02
51	4.04487	3.08710E-02
56	4.06301	3.63730E-02
61	4.07862	4.07640E-02
66	4.09305	4.37530E-02
71	4.10735	4.53230E-02
76	4.12204	4.54320E-02
81	4.13739	4.41110E-02
86	4.15369	4.13070E-02
91	4.17090	3.71450E-02
96	4.17293	1.99830E-02

Table 4.3: Average interstation phase velocity used in the inversion of shear-wave velocity structure for group 2.

at the transition between the Tibetan plateau and southeastern China may have a 52 km thick crust and 160 km lithosphere.

The normalized resolution kernels (Figure 4.7) show that, in general, the upper 30 km of the crust is well resolved. The resolution becomes poorer as the depth increases. Below about 50 km the resolution kernels are broad, implying those layers below 50 km are very poorly resolved and hence the shear velocity values for these layers are not reliable. The upper 10 to 20 km is well resolved, but poorly constrained, as indicated by the large standard deviation.

4.1.2 Group 2

Phase velocities (Figure 4.1 and Table 4.3) of group 2 cover the South China Block. The shear-velocity structure for the region (Figures 4.8 and 4.4 and Table 4.4) varies smoothly with depth. The shear-wave velocity for the upper 10 km is about 3.6 km/sec. It decreases slightly to 3.54 km/s for the depth range 10 to 20 km. This low-velocity layer with

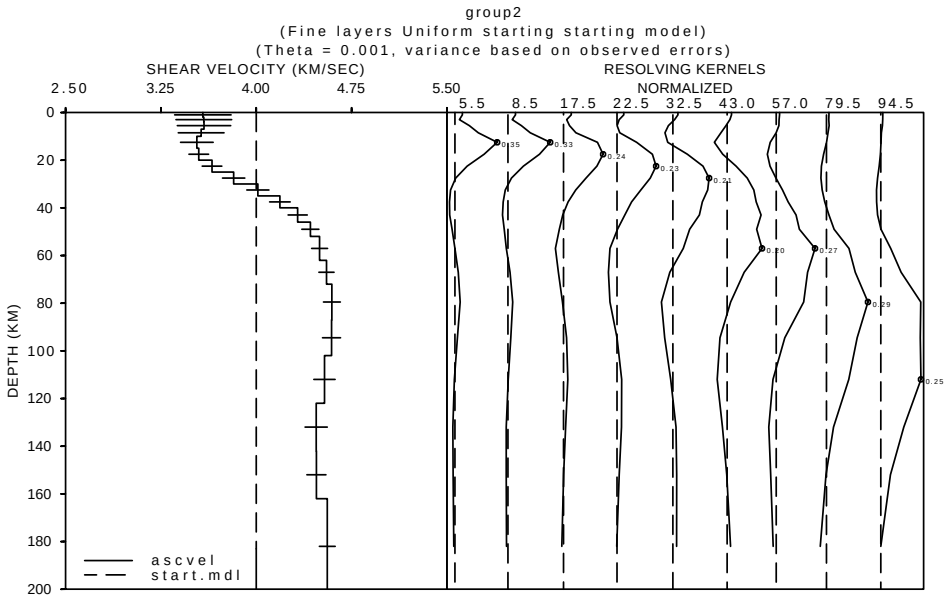

Figure 4.8: Shear-wave velocity structure for group 2. The dashed line at 4 km/s is a uniform starting shear-wave velocity model.

H(km)	$\alpha(km/s)$	$\beta(km/s)$	$\rho(gm/cc)$	Q_μ^{-1}	Poisson Ratio	Error $\beta(km/s)$
2.00000	6.20190	3.58070	2.76060	0.	0.250000	0.222000
2.00000	6.21450	3.58790	2.76430	0.	0.250000	0.219000
3.00000	6.21690	3.58930	2.76510	0.	0.250000	0.210000
3.00000	6.17730	3.56650	2.75320	0.	0.250000	0.180000
5.00000	6.11950	3.53310	2.73580	0.	0.250000	0.128000
5.00000	6.14540	3.54810	2.74360	0.	0.250000	7.76000E-02
5.00000	6.32600	3.65230	2.79780	0.	0.250000	7.71000E-02
5.00000	6.62140	3.82290	2.88160	0.	0.250000	8.77000E-02
5.00000	6.95080	4.01310	2.96720	0.	0.250000	8.71000E-02
5.00000	7.25110	4.18640	3.06030	0.	0.250000	8.13000E-02
6.00000	7.49320	4.32620	3.13780	0.	0.250000	7.55000E-02
6.00000	7.66620	4.42610	3.19650	0.	0.250000	6.72000E-02
10.0000	7.79200	4.49870	3.23930	0.	0.250000	6.29000E-02
10.0000	7.88600	4.55300	3.27120	0.	0.250000	5.97000E-02
15.0000	7.95920	4.59520	3.29610	0.	0.250000	6.63000E-02
15.0000	7.95450	4.59250	3.29450	0.	0.250000	7.10000E-02
20.0000	7.85830	4.53700	3.26180	0.	0.250000	8.37000E-02
20.0000	7.74570	4.47200	3.22350	0.	0.250000	8.74000E-02
20.0000	7.74860	4.47370	3.22450	0.	0.250000	7.48000E-02
40.0000	7.89670	4.55910	3.27490	0.	0.250000	6.21000E-02
50.0000	8.36950	4.69790	3.44300	0.	0.270000	7.94000E-02
70.0000	8.37230	4.69940	3.44400	0.	0.270000	0.109000
0.	8.33910	4.45740	3.43210	0.	0.300000	9.10000E-02

Table 4.4: Inversion results from phase velocities of group 2, where H is layer thickness, α is p-wave velocity, β is shear-wave velocity, and ρ is density.

a thickness of 10 km appears to correspond to the sialic low-velocity zone (a laccolithic zone of granitic intrusions) of Mueller (1977) in his generalized petrological model and P-wave velocity-depth profile of the continental crust. The width of the resolving kernels and standard deviations at that depth, however, preclude any definite statement about the feature from this study. The depth range between 20 km and 40 km is marked by a positive velocity gradient, changing from 3.5 km/sec to about 4.3 km/sec. Below 40 km depth, the velocity increases from 4.3 km/sec to 4.6 km/sec with a steep gradient. The Moho is not clearly identifiable from Figure 4.8. However, the steep velocity transition from about 4.3 km/sec to 4.6 km/sec between the depths 40 km and about 70 km may indicate that the Moho, with large uncertainty, is at about 40 km depth.

This depth is a little greater than the Moho depth, 36 km, shown in Figure 3.2, but is in a very good agreement with the ZH-1 model of Wier (1982) (Figure 4.10). The layer between 40 km and about 100 km has a positive velocity increase from about 4.3 km/sec to about 4.6 km/sec. However, the study of Weir (1982) (model ZH-1) limits the shear velocity of the 'lid' part of the upper mantle to a lower value of 4.45 km/sec except for a 5-km thick portion of the 'lid' with a velocity of 4.65 km/sec. He explained that, the 'unusually' low 'lid' velocity is due to asthenosphere extending to the base of the crust, and that the mantle lithosphere is weak or missing. The shear velocity model obtained in this study (Figure 4.8) lacks the resolution to reach this conclusion.

Although the resolution is poor, as indicated by wide resolution kernels, for deeper layers, a low-velocity mantle layer seems to exist be-

Period (sec)	C(km/s)	STDEV (km/s)
13	3.39608	0.173284
18	3.61223	0.130876
23	3.76151	0.108625
28	3.83153	9.16780E-02
33	3.86669	1.03062E-01
38	3.88498	0.127149
43	3.89788	0.150273
48	3.90626	0.191032
54	3.93089	0.220792
63	3.93503	0.287032
68	3.97456	0.331659
73	4.02390	0.386690
78	4.07610	0.553119

Table 4.5: Average interstation Phase velocity used in the inversion of shear-wave velocity structure for Group3.

tween about 100 km and 165 km depth. The normalized resolving kernels show that there is good resolution for layers above about 20 km. Layers between 20 km and about 50 km are well resolved. Layers below 50 km are however, poorly resolved.

4.1.3 Group 3

The phase velocities (Figure 4.1 and Table 4.5) for this region cover the path between Taiwan and Shanghai. The upper 10 km of the structure for this region (Figures 4.9 and 4.4 and Table 4.6) shows shear-velocity values from 3.4 km/sec to 3.45 km/sec. The shear velocity increases to about 4.41 km/sec at a depth of 35 km. At a depth of 40 km the velocity reaches about 4.54 km/sec which is the upper mantle shear-wave velocity. This indicates that the Moho is situated about 35 km below the surface. This result agrees well with that of Figure 3.2 and with the study of Pines et al. (1980) (Figure 4.11). The structure indicates that the lid portion of the upper mantle is very thin, about 20 km, between depths 40 km and 60km. At depths of about 62 km there is a thick low-velocity layer (as low as 4.2 km/sec) which extends

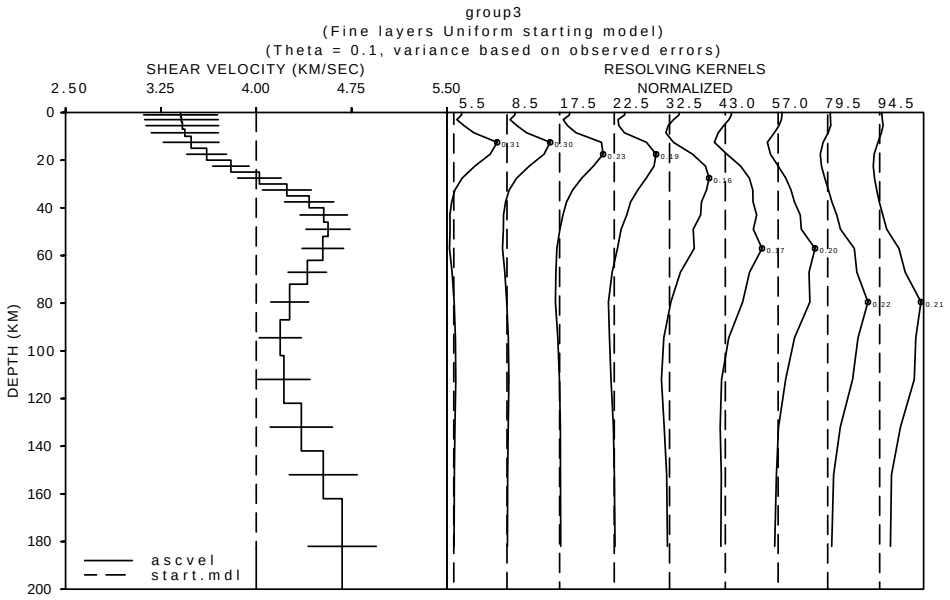

Figure 4.9: Shear-wave velocity structure for group 3. The dashed line at 4 km/s is a uniform starting shear-wave velocity model.

H(km)	$\alpha(km/s)$	$\beta(km/s)$	$\rho(gm/cc)$	Q_μ^{-1}	Poisson Ratio	Error $\beta(km/s)$
2.00000	5.89820	3.40540	2.67960	0.	0.250000	0.291000
2.00000	5.90940	3.41180	2.68190	0.	0.250000	0.289000
3.00000	5.92240	3.41930	2.68450	0.	0.250000	0.285000
3.00000	5.95590	3.43860	2.69120	0.	0.250000	0.264000
5.00000	6.04100	3.48780	2.71230	0.	0.250000	0.219000
5.00000	6.25340	3.61040	2.77600	0.	0.250000	0.157000
5.00000	6.58340	3.80090	2.87170	0.	0.250000	0.143000
5.00000	6.97150	4.02500	2.97260	0.	0.250000	0.171000
5.00000	7.34640	4.24140	3.09080	0.	0.250000	0.192000
5.00000	7.65050	4.41700	3.19120	0.	0.250000	0.194000
6.00000	7.84920	4.53170	3.25870	0.	0.250000	0.186000
6.00000	7.90700	4.56510	3.27840	0.	0.250000	0.173000
10.0000	7.83590	4.52410	3.25420	0.	0.250000	0.163000
10.0000	7.62440	4.40200	3.18230	0.	0.250000	0.151000
15.0000	7.38380	4.26300	3.10280	0.	0.250000	0.149000
15.0000	7.25490	4.18860	3.06160	0.	0.250000	0.166000
20.0000	7.30600	4.21810	3.07790	0.	0.250000	0.206000
20.0000	7.54310	4.35500	3.15470	0.	0.250000	0.245000
20.0000	7.84200	4.52760	3.25630	0.	0.250000	0.267000
40.0000	8.09960	4.67630	3.34590	0.	0.250000	0.268000
50.0000	8.36840	4.69730	3.44260	0.	0.270000	0.230000
70.0000	8.12750	4.56200	3.35590	0.	0.270000	0.165000
0.	8.06200	4.30930	3.33230	0.	0.300000	0.084800

Table 4.6: Inversion results from phase velocities of group 3, where H is layer thickness, α is p-wave velocity, β is shear-wave velocity, and ρ is density.

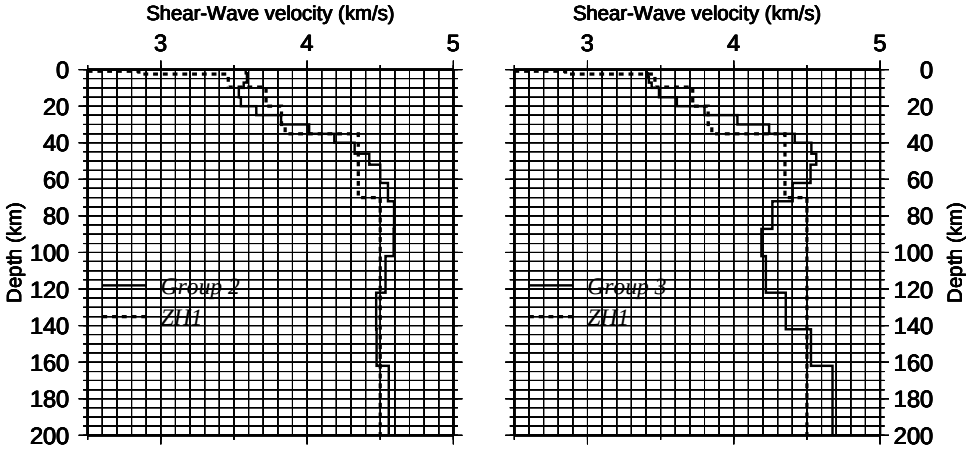

Figure 4.10: Shear-wave velocity structure comparisons for model ZH1 (Wier, 1982) with groups 2 and 3.

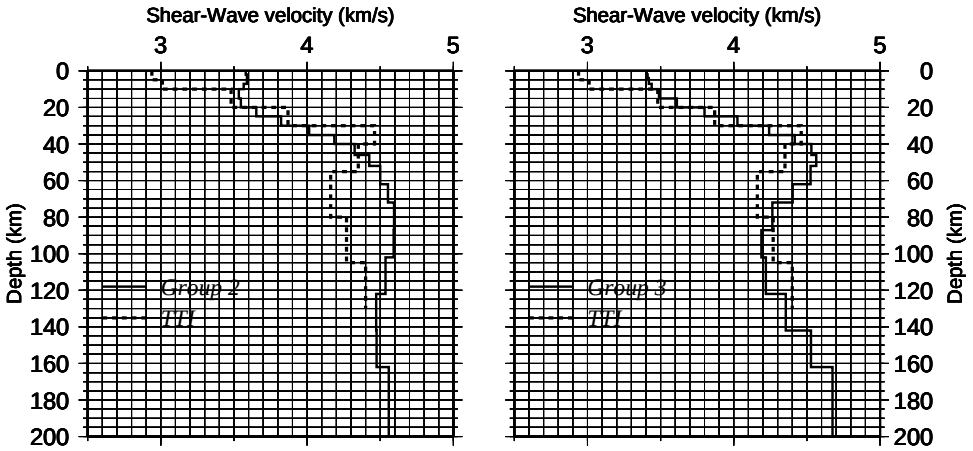

Figure 4.11: Shear-wave velocity structure comparisons for model TTI (Pines et al., 1981) with groups 2 and 3.

Period (sec)	C(km/s)	STDEV (km/s)
9	3.06926	4.04520E-02
14	3.27006	4.91660E-02
19	3.48458	5.14480E-02
24	3.66828	6.01730E-02
29	3.78922	6.63030E-02
34	3.86285	6.96170E-02
39	3.90108	8.10100E-02
44	3.93760	9.30920E-02
49	3.96981	0.106754
54	3.99759	0.116485
64	4.04300	0.118726
69	4.06389	0.118726
74	4.08315	0.118726
79	4.10128	0.118726
84	4.11857	0.118726
89	4.13515	0.118726
94	4.15122	0.118726

Table 4.7: Average interstation phase velocity used in the inversion of shear-wave velocity structure for group 4.

to depths between about 125 and 160 km. These may imply a shallow low-velocity asthinosphere beneath the eastern cost of China at a shallow depth about 62 km. A similar conclusion is given by Weir (1982) based on his ZH-1 model (Figure 4.10). This low-velocity layer is also seen in Pines et al. (1980) model TTI between depths of 40 km and 105 km.

The resolution kernels are wider as we go deeper than about 20 km. For depths below about 60 km the resolution is poor.

4.1.4 Group 4

Phase velocities (Figure 4.1 and Table 4.7) of group 4 cover eastern and northern China. The paths of this group cross different topographic and tectonic regions in this region. Thus the crustal shear-velocity structure (Figures 4.12 and 4.4 and Table 4.8) is an average of the varying structure along the various paths. The shear velocity is about 3.1 km/sec at the surface and increases to 4.41 km/sec at 40

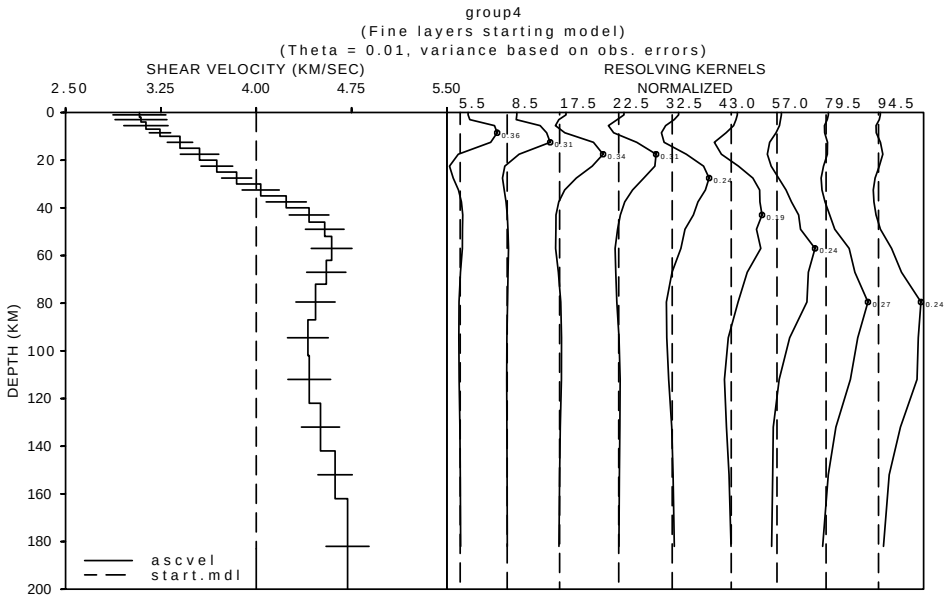

Figure 4.12: Shear-wave velocity structure for group 4. The dashed line at 4 km/s is a uniform starting shear-wave velocity model.

$H(km)$	$\alpha(km/s)$	$\beta(km/s)$	$\rho(gm/cc)$	Q_μ^{-1}	Poisson Ratio	Error $\beta(km/s)$
2.00000	5.33710	3.08140	2.56740	0.	0.250000	0.208000
2.00000	5.35790	3.09340	2.57160	0.	0.250000	0.204000
3.00000	5.42570	3.13260	2.58510	0.	0.250000	0.174000
3.00000	5.61650	3.24270	2.62330	0.	0.250000	0.084000
5.00000	5.88950	3.40030	2.67790	0.	0.250000	0.099500
5.00000	6.15640	3.55440	2.74690	0.	0.250000	0.151000
5.00000	6.39140	3.69010	2.81740	0.	0.250000	0.125000
5.00000	6.66150	3.84600	2.89200	0.	0.250000	0.118000
5.00000	6.98930	4.03530	2.97720	0.	0.250000	0.146000
5.00000	7.33710	4.23600	3.08790	0.	0.250000	0.158000
6.00000	7.64840	4.41580	3.19040	0.	0.250000	0.156000
6.00000	7.86190	4.53900	3.26300	0.	0.250000	0.152000
10.0000	7.95580	4.59330	3.29500	0.	0.250000	0.160000
10.0000	7.88330	4.55140	3.27030	0.	0.250000	0.154000
15.0000	7.73660	4.46670	3.22040	0.	0.250000	0.154000
15.0000	7.63250	4.40660	3.18500	0.	0.250000	0.160000
20.0000	7.65070	4.41710	3.19120	0.	0.250000	0.168000
20.0000	7.80430	4.50580	3.24340	0.	0.250000	0.150000
20.0000	8.00340	4.62070	3.31120	0.	0.250000	0.135000
40.0000	8.17270	4.71850	3.37220	0.	0.250000	0.169000
50.0000	8.41160	4.72150	3.45820	0.	0.270000	0.215000
70.0000	8.18840	4.59620	3.37780	0.	0.270000	0.219000
0.	8.13510	4.34840	3.35860	0.	0.300000	0.148000

Table 4.8: Inversion results from phase velocities of group 4, where H is layer thickness, α is p-wave velocity, β is shear-wave velocity, and ρ is density.

km depth. The shear-velocity discontinuity at about 40 km may be the Moho. But this depth is a little higher than that shown in Figure 3.2. Between 45 km and 72 km the shear velocities increase to about 4.6 km/sec. Below about 72 km depth, the shear velocity decreases to about 4.4 km/sec until it reaches a depth of 120 km. This low-velocity zone continues to a depth of about 160 km. Although the resolution is poor, this low-velocity zone may represent a shallow asthinosphere. The North China Basin, crossed by group 4 is an extensional zone (Nábělek et al., 1987). This path also crosses the northeastern China fold systems where Cenozoic basalts are found (Menzies and Xu, 1998).

Using mantle xenoliths and volcanic rocks in eastern China, Menzies and Xu (1998) developed models for the temporal evolution of the North China Craton (the Sino-Korean Craton). Their models show that the Phanerozoic lithosphere is thick (about 200 km), cold, refractory and stable in contrast to Cenozoic lithosphere which is thin (about 75 km), hot, less refractory and unstable. Possible thickening of the lithosphere since the Mesozoic is suggested, but a thickness of less than 80 km as is confirmed by recent geophysical studies.

Seismic tomography in China (Liu, 1992) indicates that, in the eastern part of the North China Craton, the thickness of the lithosphere is less than 80 km. This tomographic map shows that the thin lithosphere is associated with a shallow low-velocity structure between 80 and 180 km. Heat flow studies in eastern China (Teng et al., 1983) reveal a region of very high heat flow (greater than $100 mW/m^2$) in the North China Craton in the vicinity of the Bo Sea and Beijing. The thin litho-

Period (sec)	C(km/s)	STDEV (km/s)
10	3.16226	0.115338
16	3.45863	3.01000E-02
22	3.68233	1.98990E-02
28	3.82811	1.08530E-02
34	3.92232	1.22440E-02
40	3.98816	1.13140E-02
46	4.03938	1.36690E-02
52	4.08360	1.99170E-02
58	4.12444	2.84640E-02
64	4.16402	3.90990E-02
70	4.21295	4.60500E-02
76	4.25889	5.42400E-02
82	4.30057	6.38990E-02
88	4.34947	8.00930E-02
93	4.39164	1.04594E-01

Table 4.9: Average interstation phase velocity used in the inversion of shear-wave velocity structure for group 5.

sphere (about 72 km) and the low-velocity zone between depths 72 km and about 160 km found in this study, are therefore consistent with the geophysical observations mentioned above, as well as with the models of Menzies and Xu (1998).

4.1.5 Group 5

Phase velocities for group 5 (Figure 4.2 and Table 4.9) cover the region in northeastern China. The shear-velocity structure for this region (Figures 4.13 and 4.5 and Table 4.10) is about 3.12 km/sec at the surface and increases rapidly to about 4.3 km/sec at 35 km depth. The velocity increases more slowly to about 4.7 km/sec at a depth of 95 km. A low-velocity layer is indicated between 120 km and about 160 km where the shear velocities reach values as low as 4.5 km/sec. This layer could be a shallow asthenosphere starting at a depth of about 95 km. The base of the shear-velocity gradient at about 35 km may correspond to the Moho, about the same Moho depth is also shown in Figure 3.2.

The lithospheric thickness (about 120 km) and the crustal thickness

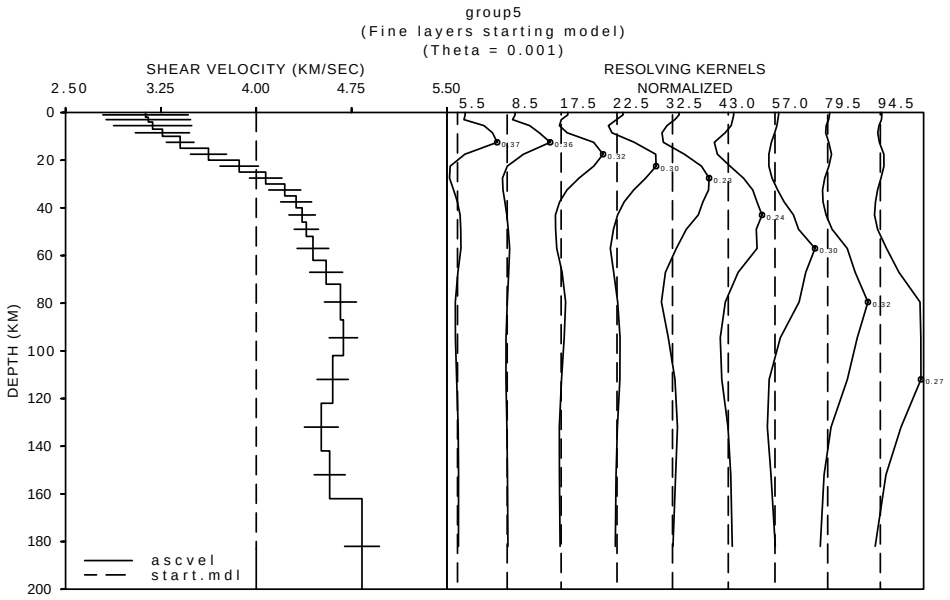

Figure 4.13: Shear-wave velocity structure for group 5. The dashed line at 4 km/s is a uniform starting shear-wave velocity model.

$H(km)$	$\alpha(km/s)$	$\beta(km/s)$	$\rho(gm/cc)$	Q_μ^{-1}	Poisson Ratio	Error $\beta(km/s)$
2.00000	5.42120	3.12990	2.58420	0.	0.250000	0.336000
2.00000	5.45830	3.15130	2.59170	0.	0.250000	0.332000
3.00000	5.51700	3.18530	2.60340	0.	0.250000	0.307000
3.00000	5.65050	3.26230	2.63010	0.	0.250000	0.213000
5.00000	5.89190	3.40170	2.67840	0.	0.250000	0.109000
5.00000	6.27810	3.62470	2.78340	0.	0.250000	0.142000
5.00000	6.69670	3.86640	2.90110	0.	0.250000	0.151000
5.00000	7.05770	4.07480	2.99850	0.	0.250000	0.128000
5.00000	7.31670	4.22430	3.08140	0.	0.250000	0.126000
5.00000	7.47200	4.31400	3.13100	0.	0.250000	0.122000
6.00000	7.55430	4.36150	3.15840	0.	0.250000	0.104000
6.00000	7.61150	4.39450	3.17790	0.	0.250000	0.095700
10.0000	7.70160	4.44650	3.20860	0.	0.250000	0.124000
10.0000	7.88110	4.55020	3.26960	0.	0.250000	0.130000
15.0000	8.07590	4.66260	3.33730	0.	0.250000	0.126000
15.0000	8.11610	4.68590	3.35180	0.	0.250000	0.112000
20.0000	7.97030	4.60170	3.29990	0.	0.250000	0.123000
20.0000	7.81540	4.51220	3.24720	0.	0.250000	0.133000
20.0000	7.92960	4.57810	3.28610	0.	0.250000	0.122000
40.0000	8.36990	4.83230	3.44320	0.	0.250000	0.137000
50.0000	9.30300	5.22180	3.78120	0.	0.270000	0.200000
70.0000	9.51770	5.34240	3.86670	0.	0.270000	0.238000
0.	9.24050	4.93920	3.75620	0.	0.300000	0.175000

Table 4.10: Inversion results from phase velocities of group 5, where H is layer thickness, α is p-wave velocity, β is shear-wave velocity, and ρ is density.

Period (sec)	C(km/s)	STDEV (km/s)
10	3.28135	9.00330E-02
15	3.42174	5.33210E-02
20	3.58031	1.18850E-02
25	3.72759	1.35540E-02
30	3.84446	1.13380E-02
35	3.93152	7.17400E-03
40	3.99639	4.81400E-03
45	4.04727	6.32800E-03
50	4.08987	8.24200E-03
55	4.12807	9.07600E-03
60	4.16433	9.90200E-03
65	4.20019	1.28700E-02
70	4.23659	1.93950E-02
75	4.27422	2.93080E-02
80	4.31349	4.20880E-02
85	4.34236	5.20150E-02
90	4.38253	6.96200E-02
95	4.42466	8.97930E-02

Table 4.11: Average interstation phase velocity used in the inversion of shear-wave velocity structure for group 6.

(about 35 km) in this study are consistent with other geophysical studies in northeastern China around the Great Xing'an Mountains (Zhang et al., 1998; Ma, 1987). The top 40 -50 km of this region is well resolved as compared to the deeper layers. The resolution kernels are relatively narrow for the upper 20 km.

4.1.6 Group 6

Phase velocities for group 6 (Figure 4.2 and Table 4.11) cover the region in southeastern Siberia. The shear-velocity for this region (Figures 4.14 and 4.5 and Table 4.12) is about 3.38 km/sec at the surface and increases to about 4.5 km/sec at a depth of about 53 km. Below 53 km, the shear velocity increases to 4.7 km/sec until 120 km but decreases below this depth to 4.6 km/sec until about 160 km. The shear velocity discontinuity at a depth of 53 km suggests a Moho at that depth. This may be true because group 6 paths cross the Stanovoy Range in southeastern Siberia (Wei and Seno, 1998).

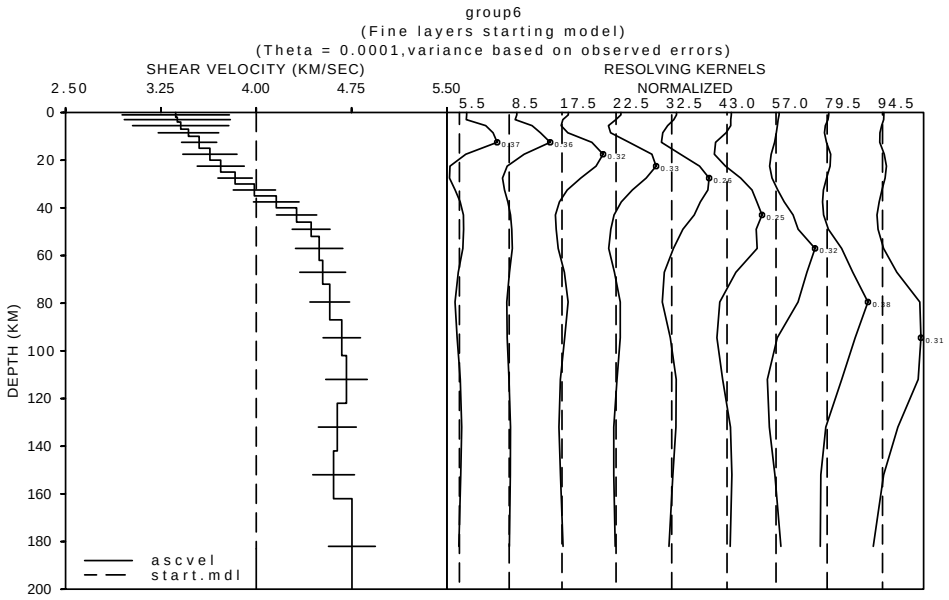

Figure 4.14: Shear-wave velocity structure for group 6. The dashed line at 4 km/s is a uniform starting shear-wave velocity model.

$H(km)$	$\alpha(km/s)$	$\beta(km/s)$	$\rho(gm/cc)$	Q_μ^{-1}	Poisson Ratio	Error $\beta(km/s)$
2.00000	5.83170	3.36690	2.66630	0.	0.250000	0.422000
2.00000	5.85290	3.37920	2.67060	0.	0.250000	0.417000
3.00000	5.89930	3.40600	2.67990	0.	0.250000	0.378000
3.00000	6.00540	3.46720	2.70160	0.	0.250000	0.238000
5.00000	6.15080	3.55120	2.74520	0.	0.250000	0.138000
5.00000	6.29780	3.63610	2.78930	0.	0.250000	0.213000
5.00000	6.44470	3.72080	2.83340	0.	0.250000	0.185000
5.00000	6.63990	3.83360	2.88640	0.	0.250000	0.135000
5.00000	6.90340	3.98570	2.95490	0.	0.250000	0.166000
5.00000	7.20170	4.15790	3.04450	0.	0.250000	0.179000
6.00000	7.47840	4.31760	3.13310	0.	0.250000	0.158000
6.00000	7.67650	4.43200	3.20000	0.	0.250000	0.149000
10.0000	7.78680	4.49570	3.23750	0.	0.250000	0.186000
10.0000	7.83410	4.52300	3.25360	0.	0.250000	0.180000
15.0000	7.93050	4.57870	3.28640	0.	0.250000	0.156000
15.0000	8.09440	4.67330	3.34400	0.	0.250000	0.147000
20.0000	8.15810	4.71010	3.36690	0.	0.250000	0.163000
20.0000	8.03330	4.63800	3.32200	0.	0.250000	0.149000
20.0000	7.98260	4.60880	3.30410	0.	0.250000	0.164000
40.0000	8.23280	4.75320	3.39380	0.	0.250000	0.184000
50.0000	9.19850	5.16320	3.73940	0.	0.270000	0.188000
70.0000	9.61100	5.39480	3.90220	0.	0.270000	0.316000
0.	9.44860	5.05050	3.83940	0.	0.300000	0.301000

Table 4.12: Inversion results from phase velocities of group 6, where H is layer thickness, α is p-wave velocity, β is shear-wave velocity, and ρ is density.

Period (sec)	C(km/s)	STDEV (km/s)
16	3.37583	6.15000E-04
20	3.51828	1.20490E-02
24	3.64806	1.10660E-02
28	3.76093	1.45000E-03
32	3.85491	5.25400E-03
36	3.92931	5.72800E-03
40	3.98769	1.37900E-03
44	4.03472	4.61000E-03
48	4.07385	1.01470E-02
52	4.10831	1.38450E-02
56	4.14000	1.47710E-02

Table 4.13: Average interstation phase velocity used in the inversion of shear-wave velocity structure for group 7.

Although the resolution is poor as we go deeper, my model indicates that the lithosphere is about 120 km thick and the low-velocity asthenosphere begins at that depth.

4.1.7 Group 7

Phase velocities (Figure 4.2 and Table 4.13) for group 7 cover the Mongolian Plateau along a path in which the lithosphere varies in thickness between 50 and 150 km (Zorin et al. 1990) and heat flow varies between 60 and 120 mW/m^2 (Khutorskoy and Yarmoluk, 1989). The shear velocity (Figures 4.15 and 4.5 and Table 4.14) is about 3.3 km/sec in the upper 5-10 km of the model. It increases to 4.4 km/sec at about 52 km where the Moho may be located. This Moho depth is much higher than that inferred (about 30 km) from the similarities in phase velocities of western Mongolia and the Basin and Range Province of the United States (Windley and Allen, 1993). Below 52 km the velocity increases to 4.8 km/sec at 70 km and continues at about that value to a depth of 100 km. Between 100 km and 160 km the shear velocity decreases to 3.54 km/sec.

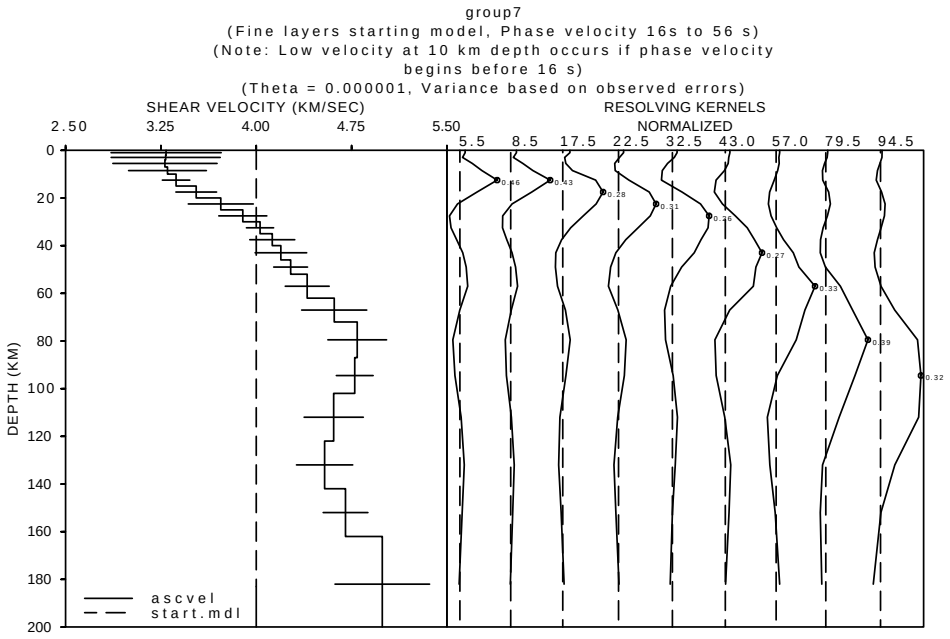

Figure 4.15: Shear-wave velocity structure for group 7. The dashed line at 4 km/s is a uniform starting shear-wave velocity model.

$H(km)$	$\alpha(km/s)$	$\beta(km/s)$	$\rho(gm/cc)$	Q_μ^{-1}	Poisson Ratio	Error $\beta(km/s)$
2.00000	5.70040	3.29110	2.64010	0.	0.250000	0.433000
2.00000	5.69470	3.28780	2.63890	0.	0.250000	0.429000
3.00000	5.68490	3.28220	2.63700	0.	0.250000	0.410000
3.00000	5.71890	3.30180	2.64380	0.	0.250000	0.306000
5.00000	5.83630	3.36960	2.66730	0.	0.250000	0.108000
5.00000	6.11070	3.52800	2.73320	0.	0.250000	0.160000
5.00000	6.44570	3.72140	2.83370	0.	0.250000	0.256000
5.00000	6.74520	3.89430	2.91370	0.	0.250000	0.189000
5.00000	6.98060	4.03020	2.97490	0.	0.250000	0.107000
5.00000	7.14770	4.12670	3.02730	0.	0.250000	0.177000
6.00000	7.26450	4.19420	3.06460	0.	0.250000	0.203000
6.00000	7.39750	4.27090	3.10720	0.	0.250000	0.133000
10.0000	7.62290	4.40110	3.18180	0.	0.250000	0.173000
10.0000	7.99120	4.61370	3.30700	0.	0.250000	0.256000
15.0000	8.30490	4.79480	3.41980	0.	0.250000	0.231000
15.0000	8.27060	4.77500	3.40740	0.	0.250000	0.145000
20.0000	7.98430	4.60970	3.30470	0.	0.250000	0.233000
20.0000	7.86030	4.53810	3.26250	0.	0.250000	0.221000
20.0000	8.14540	4.70270	3.36230	0.	0.250000	0.176000
40.0000	8.64570	4.99160	3.53950	0.	0.250000	0.372000
50.0000	9.14370	5.13250	3.71750	0.	0.270000	0.506000
70.0000	8.78770	4.93260	3.58780	0.	0.270000	0.441000
0.	8.41800	4.49960	3.46050	0.	0.300000	0.238000

Table 4.14: Inversion results from phase velocities of group 7, where H is layer thickness, α is p-wave velocity, β is shear-wave velocity, and ρ is density.

Period (sec)	C(km/s)	STDEV (km/s)
16	3.26532	5.87400E-03
20	3.33616	1.82870E-02
24	3.42494	1.97950E-02
28	3.51026	1.10680E-02
32	3.58529	9.33800E-03
36	3.64755	2.31470E-02
40	3.69736	3.72260E-02
44	3.76325	2.53430E-02
48	3.80016	2.06480E-02
52	3.82894	1.39160E-02
56	3.85141	6.27900E-03
60	3.86854	1.95900E-03
64	3.88229	9.80800E-03
68	3.89324	1.75150E-02
72	3.90204	2.47350E-02
76	3.90932	3.11760E-02
80	3.91560	3.71020E-02

Table 4.15: Average interstation phase velocity used in the inversion of shear-wave velocity structure for group 8.

This indicates that the lithosphere is about 100 km thick, which is in a good agreement with the results of Zorin et al. (1990). The low-velocity asthenospheric layer in this region is about 60 km thick. The resolution is good for the upper 40 km of the crust, but becomes poor as the depth increases.

4.1.8 Group 8

Phase velocities (Figure 4.2 and Table 4.15) of group 8 cover the western part of the Mongolian plateau, the Altai Range and also the Junngar block. The shear velocity (Figures 4.16 and 4.5 and Table 4.16) for the upper 5-10 km in this region is 3.51 km/sec. Velocities decrease to about 3.4 km/sec between 10 km and 25 km depth. This well-developed low-velocity layer may correspond to the sialic thin low velocity zone of Mueller (1977). There is no clear shear-velocity discontinuity that shows the location of the Moho. The Moho map in Figure (3.2) shows that the crust is between 42 km and 50 km thick for the

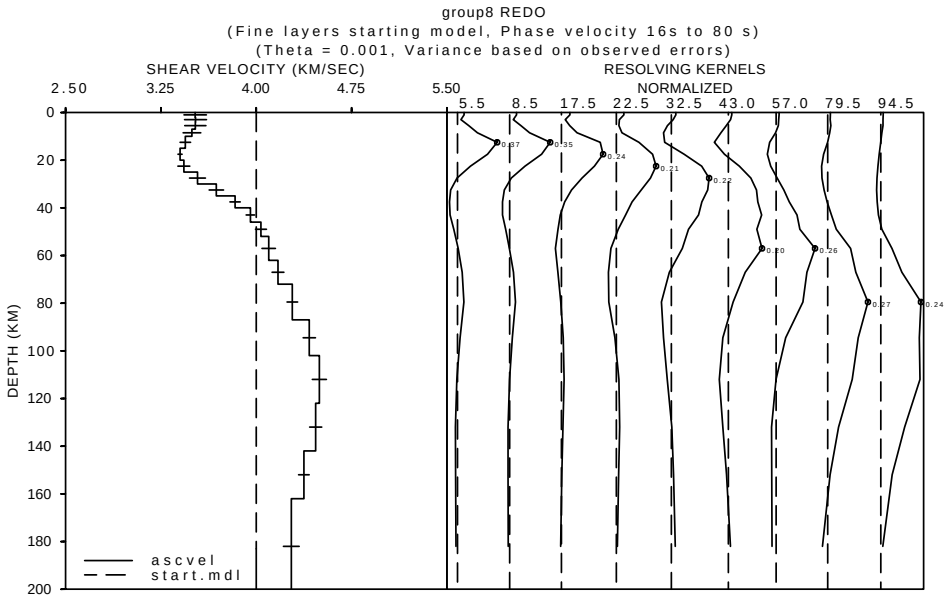

Figure 4.16: Shear-wave velocity structure for group 8. The dashed line at 4 km/s is a uniform starting shear-wave velocity model.

$H(km)$	$\alpha(km/s)$	$\beta(km/s)$	$\rho(gm/cc)$	Q_μ^{-1}	Poisson Ratio	Error $\beta(km/s)$
2.00000	6.09660	3.51990	2.72900	0.	0.250000	8.80000E-02
2.00000	6.10150	3.52270	2.73040	0.	0.250000	8.65000E-02
3.00000	6.09890	3.52120	2.72970	0.	0.250000	8.31000E-02
3.00000	6.05240	3.49430	2.71570	0.	0.250000	6.93000E-02
5.00000	5.96240	3.44240	2.69250	0.	0.250000	4.14000E-02
5.00000	5.89060	3.40090	2.67810	0.	0.250000	1.61000E-02
5.00000	5.94250	3.43090	2.68850	0.	0.250000	4.68000E-02
5.00000	6.12820	3.53810	2.73850	0.	0.250000	6.25000E-02
5.00000	6.38500	3.68640	2.81550	0.	0.250000	5.69000E-02
5.00000	6.64000	3.83360	2.88640	0.	0.250000	4.06000E-02
6.00000	6.84900	3.95430	2.94070	0.	0.250000	3.32000E-02
6.00000	6.99300	4.03740	2.97820	0.	0.250000	4.29000E-02
10.0000	7.09880	4.09850	3.01160	0.	0.250000	5.28000E-02
10.0000	7.22490	4.17130	3.05200	0.	0.250000	4.68000E-02
15.0000	7.42050	4.28420	3.11460	0.	0.250000	4.18000E-02
15.0000	7.65180	4.41770	3.19160	0.	0.250000	4.82000E-02
20.0000	7.78900	4.49700	3.23820	0.	0.250000	5.53000E-02
20.0000	7.73870	4.46790	3.22120	0.	0.250000	4.74000E-02
20.0000	7.57790	4.37510	3.16650	0.	0.250000	4.17000E-02
40.0000	7.40660	4.27620	3.11010	0.	0.250000	6.20000E-02
50.0000	7.53210	4.22780	3.15090	0.	0.270000	8.13000E-02
70.0000	7.47880	4.19790	3.13320	0.	0.270000	7.69000E-02
0.	7.71970	4.12640	3.21470	0.	0.300000	4.63000E-02

Table 4.16: Inversion results from phase velocities of group 8, where H is layer thickness, α is p-wave velocity, β is shear-wave velocity, and ρ is density.

Period (sec)	C(km/s)	STDEV (km/s)
10	2.96566	0.
12	3.02290	1.29190E-02
14	3.11246	9.43300E-03
16	3.18443	1.77700E-02
18	3.23827	3.21310E-02
20	3.28332	4.52550E-02
22	3.32708	5.17810E-02
24	3.37258	5.01900E-02
26	3.41998	4.20090E-02
28	3.46846	2.92880E-02
30	3.51722	1.42270E-02
32	3.56514	1.22300E-03
34	3.61137	1.56340E-02
36	3.65500	2.74360E-02
38	3.69556	3.55530E-02

Table 4.17: Average interstation phase velocity used in the inversion of shear-wave velocity structure for group 9.

Junggar block and the border region. Shear velocities increase to 4.5 km/sec until about 120 km. Again resolution is poor at greater depths. The shear velocity begins to decrease below about 120 km.

4.1.9 Group 9

Phase velocities (Figure 4.3 and Tabel 4.17) for group 9 cover western China. The shear-wave velocity model for this region (Figures 4.17 and 4.6 and Table 4.18) has values near 2.9 km/sec for the upper 5-7 km. Velocities increase to about 3.55 km/sec at 15 km. The model includes a high-velocity (about 3.85 km/sec) layer at depths between 20 and 30 km. This layer may correspond to the amphibolite layer (high-velocity tooth) of Mueller's (1977) model of the continental crust. The Moho is probably associated with the velocity gradient between 50 and 60 km, which is in good agreement with Figure 3.2. Shear velocities increase to about 4.7 km/sec to a depth of about 100 km, where velocities decrease with increasing depth. The resolution for deeper layers is also very poor here.

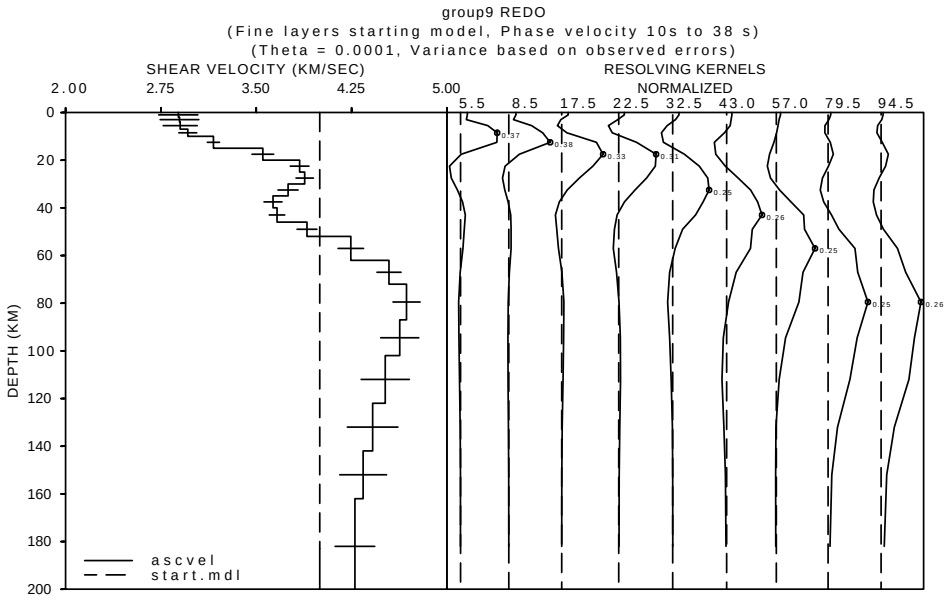

Figure 4.17: Shear-wave velocity structure for group 9. The dashed line at 4 km/s is a uniform starting shear-wave velocity model.

H(km)	$\alpha(km/s)$	$\beta(km/s)$	$\rho(gm/cc)$	Q_μ^{-1}	Poisson Ratio	Error $\beta(km/s)$
2.00000	5.00100	2.88730	2.50020	0.	0.250000	0.154000
2.00000	5.01680	2.89650	2.50340	0.	0.250000	0.152000
3.00000	5.02670	2.90220	2.50530	0.	0.250000	0.134000
3.00000	5.13040	2.96200	2.52610	0.	0.250000	7.04000E-02
5.00000	5.47970	3.16370	2.59590	0.	0.250000	4.79000E-02
5.00000	6.15300	3.55240	2.74590	0.	0.250000	8.55000E-02
5.00000	6.65420	3.84180	2.89010	0.	0.250000	7.36000E-02
5.00000	6.72310	3.88160	2.90800	0.	0.250000	6.84000E-02
5.00000	6.49610	3.75050	2.84880	0.	0.250000	7.91000E-02
5.00000	6.29080	3.63200	2.78720	0.	0.250000	7.10000E-02
6.00000	6.34540	3.66350	2.80360	0.	0.250000	6.14000E-02
6.00000	6.75360	3.89920	2.91590	0.	0.250000	7.82000E-02
10.0000	7.35120	4.24420	3.09240	0.	0.250000	1.00000E-01
10.0000	7.87170	4.54470	3.26640	0.	0.250000	9.52000E-02
15.0000	8.11050	4.68260	3.34980	0.	0.250000	0.107000
15.0000	8.01800	4.62920	3.31650	0.	0.250000	0.150000
20.0000	7.82020	4.51500	3.24890	0.	0.250000	0.190000
20.0000	7.64860	4.41590	3.19050	0.	0.250000	0.199000
20.0000	7.51930	4.34130	3.14660	0.	0.250000	0.184000
40.0000	7.40680	4.27630	3.11020	0.	0.250000	0.156000
50.0000	7.50050	4.21010	3.14020	0.	0.270000	0.118000
70.0000	7.37670	4.14060	3.10050	0.	0.270000	7.87000E-02
0.	7.61490	4.07030	3.17910	0.	0.300000	3.94000E-02

Table 4.18: Inversion results from phase velocities of group 9, where H is layer thickness, α is p-wave velocity, β is shear-wave velocity, and ρ is density.

4.1.10 Comparisons among different Groups

The location of the Moho, in most cases is not difficult to identify except for group 8 where there is no clear shear-velocity discontinuity. Most of the Moho depths identified in this study are in good agreement with that of Ma et al. (1987). In southeastern China, along the eastern coast of China, northeastern China and the Mongolian Plateau (groups 2, 3, 5 and 7) the lithospheric thickness estimated in this study are consistent with those of other studies in those areas.

A comparison of shear velocity between group 1 and group 2 (Figure 4.4) shows that models for the latter group have higher values for the upper 45 km and the models for group 1 have higher velocities at greater depths. This implies that the high topographic and tectonically active region crossed by Group 1 is underlain by low crustal velocities. Southeastern China, crossed by group 2, is relatively stable and has higher crustal velocities. The lower shear velocities below 45 km in southeastern China may be due to a hot asthenospheric mantle that begins at the base of the crust.

A comparison of shear-velocity models for group 2 and group 3 (Figure 4.4) shows that the latter has higher shear velocities for the depth range 15-60 km. The upper 15 km of the crust along the eastern coast of China (group 3) has lower shear velocities than group 2, which may be due to the sediments present along the coast.

Group 4 has slightly higher shear velocities than group 2 for the depth range between 15 km and 70 km. Group 4 has lower shear velocities than group 2 for the top 15 km, which may be due to the pres-

ence of Mesozoic sediments in the North China Plain (Menzies and Xu, 1998) and Yellow Sea crossed by group 4 paths. Between 40 km and 70 km Group 2 has higher shear velocities than group 4, but between 70 km and 130 km the relation is reversed.

Group 2 has higher shear velocities for the top 15 km than group 5. This may due to the presence of sediments in the Songliao Basin in northeastern China which is crossed by path of group 5. But below 15 km Group 2 shows lower shear velocity values than Group 5 at almost all depths.

Comparisons of group 2 with groups 4 and 5 (Figure 4.4 and 4.5) show that the South China Block (crossed by group 2) has a relatively higher shear velocity for the top 15 km than groups 4 and 5 but a reversed relation below 15 km. If this is a real feature, then the more tectonically active regions in north and northeastern China (crossed by groups 4 and 5) have lower shear-velocity values than the less tectonically active South China Block (crossed by group 2) for the top 15 km. Below 15 km, the South China Block shows lower shear velocities than does northern and northeastern China, which may be due to a thinner lithosphere in the south than the north.

For the depth range between 20 km and 70-90 km the shear velocities in northern and northeastern China (groups 4 and 5) have higher values than does group 6 which crosses the Stanovoy Range in southeastern Siberia. For the top 20 km, group 6 has higher shear-velocity values than groups 4 and 5. The differences in the top 20 km may be explained by the presence of sediments in the basins of north and northeastern China.

A comparison of the South China Block (group 2) with the Mongolian Plateau (group 7) shows that the South China Block has higher shear velocities for the upper 60 km, but the Mongolian Plateau is faster at greater depths. Exactly the same relation is observed between group 3 and group 7.

The Mongolian Plateau (crossed by group 7) has lower shear velocities for the upper 60 km when compared with groups 2, 3, and 6, but is faster at depths greater than 60 km. Between 10 km and 60 km group 7 has lower shear velocities than do groups 4 and 5 (Figures 4.4 and 4.5), but for the upper 10 km and for depths greater than 60 km group 7 has higher shear velocities.

Group 8, which crosses western Mongolia Plateau, the Altai range, and the Junngar Block, has lower shear velocities for layers depths greater than 15 km than do groups 1, 4, 5, 6 and 7 (Figures 4.4 and 4.5), but the latter groups are faster for the upper 15 km. The eastern coast of China (group 3) has higher shear velocities between 15 km and 70 km when compared with group 8, but the model for group 8 is faster for the upper 15 km and at depths greater than 70 km. The South China Block (group 2) has higher shear velocities at all depths compared with group 8.

The model for group 9, which crosses the Tianshan fold system, the Tarim Basin, and the Western Kunlun fold system, has lower shear velocities for the top 70 km, except between 20 and 35 km, when compared with groups 1, 2, 3, 4, 6, and 7, but group 9 is faster at depths between 70 and 100-140 km (Figures 4.4, 4.5 and 4.6). Group 5 has higher shear velocities at all depths compared with the model for group

9.

The model for group 8 has lower shear velocities between 20 and 35 km and at depths greater than 50 km than does the model for group 9. For the upper 20 km and between 35 and 50 km group 8 has higher shear velocities than the model for group 9.

4.2 Shear-Wave Q (Q_μ) structure results and discussion

The average interstation attenuation coefficients for each group used for inversion of Q_μ^{-1} are shown in Figures 4.18, 4.19, and 4.20. The vertical bars are the standard deviations calculated at each period.

Although, the average interstation attenuation coefficients are inverted for Q_μ^{-1}, I have used the Q_μ plots (Figures 4.21, 4.22 and 4.23) to explain the variation of the quality factor as a function of depth.

4.2.1 Group 1

The attenuation coefficient data of group 1 (Figure 4.18 and Table 4.19) were inverted to obtain the values of Q_μ shown in Table 4.20 and Figure 4.24. Q_μ values are about 215-220 for the upper 5-12 km of the crust and increase to about 550 at a depth of about 40 km. Q_μ decreases from about 220 at 70 km depth to about 150 at 100 km depth and about 100 at 150 km depth. Although, the resolution becomes poorer as the depth increases, there is a well-developed zone of low Q_μ beginning at 70 km. The high Q_μ layer between 20 km and about 50 km is much thicker than the corresponding high-velocity tooth in the shear-wave velocity structure for this group.

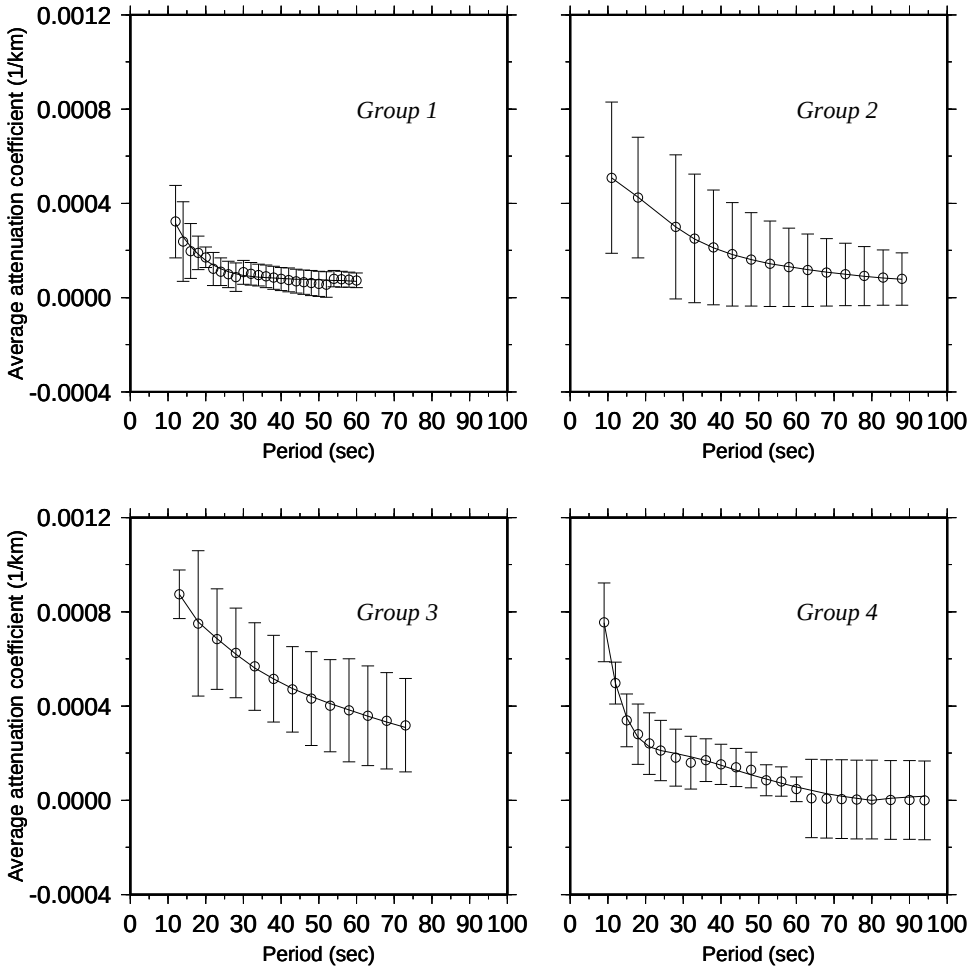

Figure 4.18: Average interstation attenuation coefficients used in the inversion for Q_μ structure for groups1, 2, 3, and 4. The circles with error bars are observed values and the solid curve is predicted by the Q_μ structure.

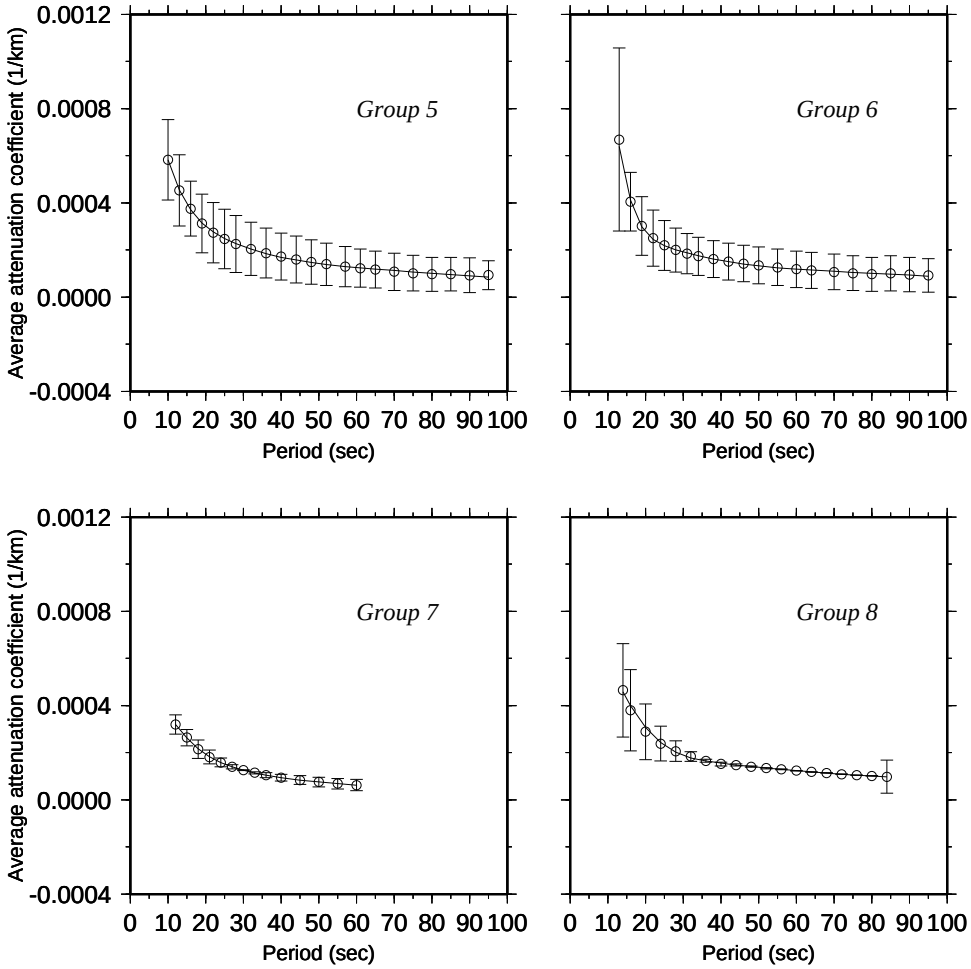

Figure 4.19: Average interstation attenuation coefficients used in the inversion for Q_μ structure for groups 5, 6, 7, and 8. The circles with error bars are observed values and the solid curve is predicted by the Q_μ structure.

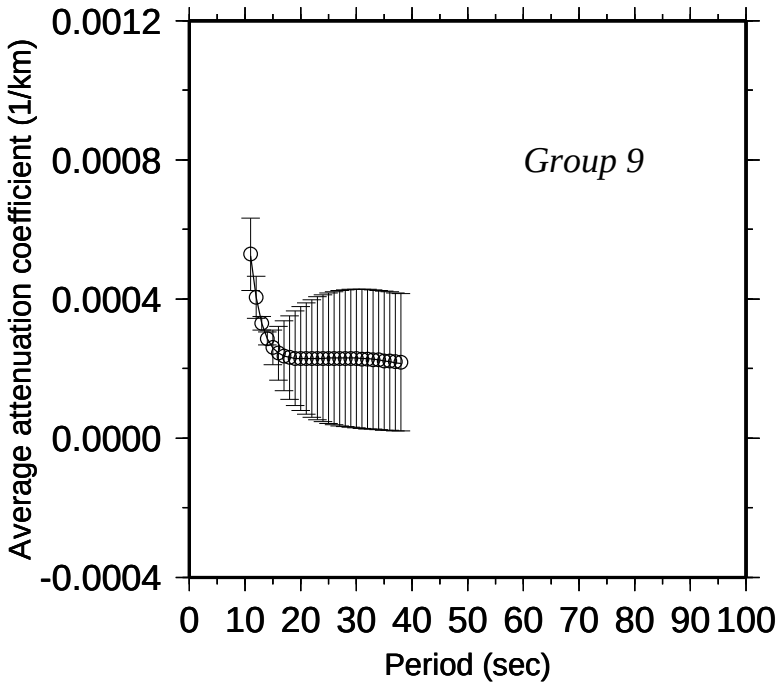

Figure 4.20: Average interstation attenuation coefficients used in the inversion for Q_μ structure for group 9. The circles with error bars are observed values and the solid curve is predicted by the Q_μ structure.

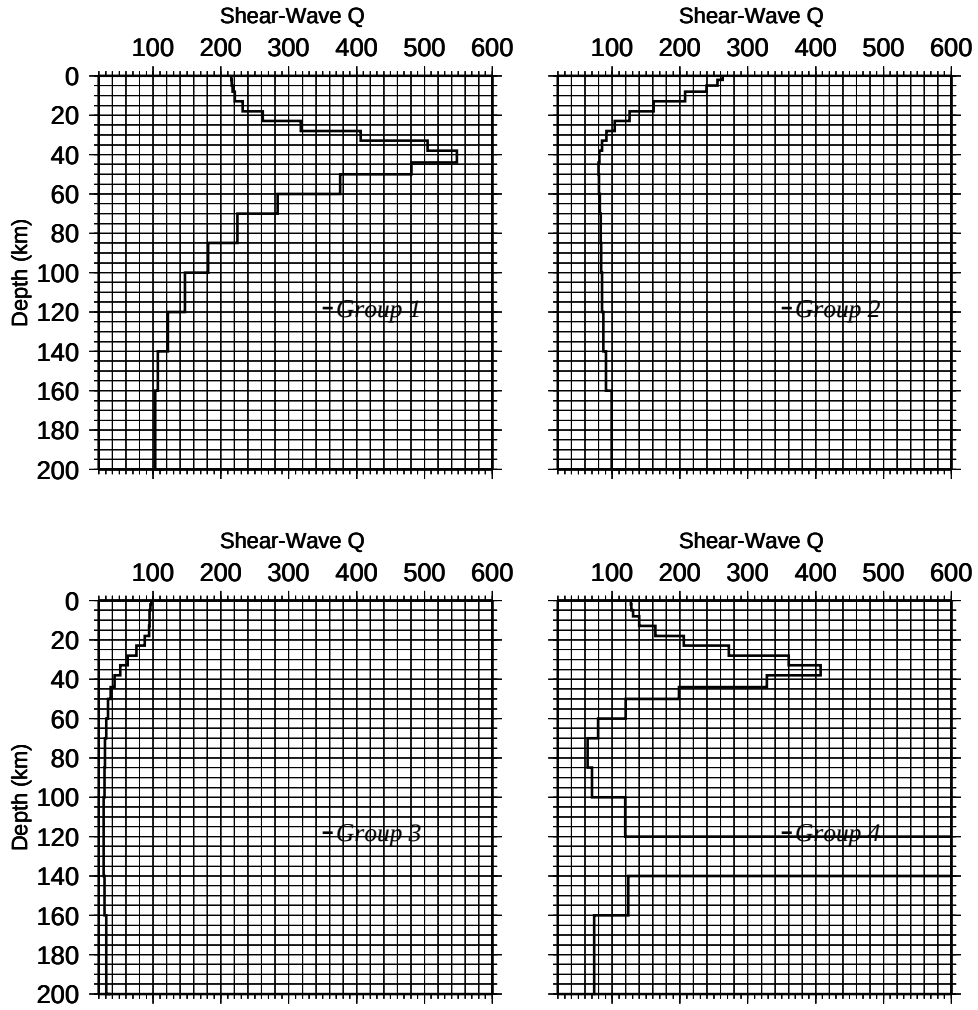

Figure 4.21: Shear-wave Q (Q_μ) structures for groups 1, 2, 3, and 4, displayed for comparison and convenience of discussion.

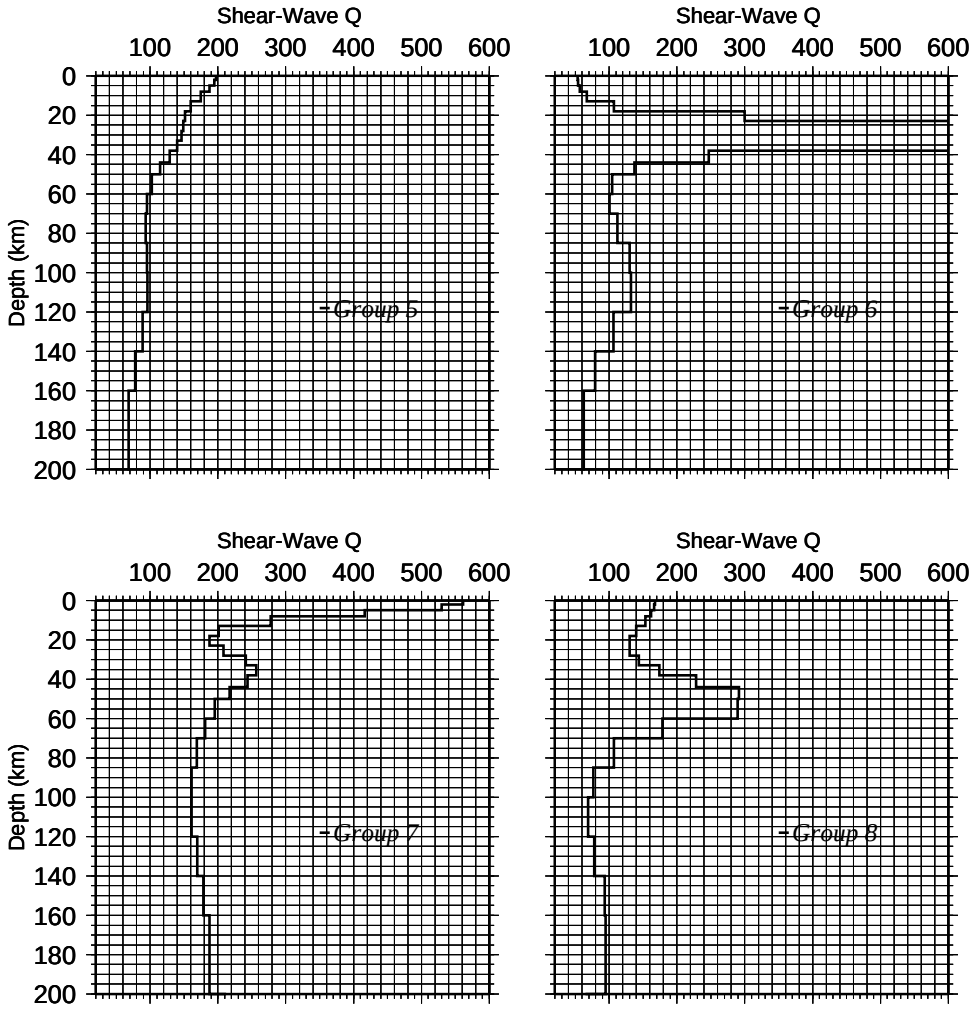

Figure 4.22: Shear-wave Q (Q_μ) structures for groups 5, 6, 7, and 8, displayed for comparison and convenience of discussion.

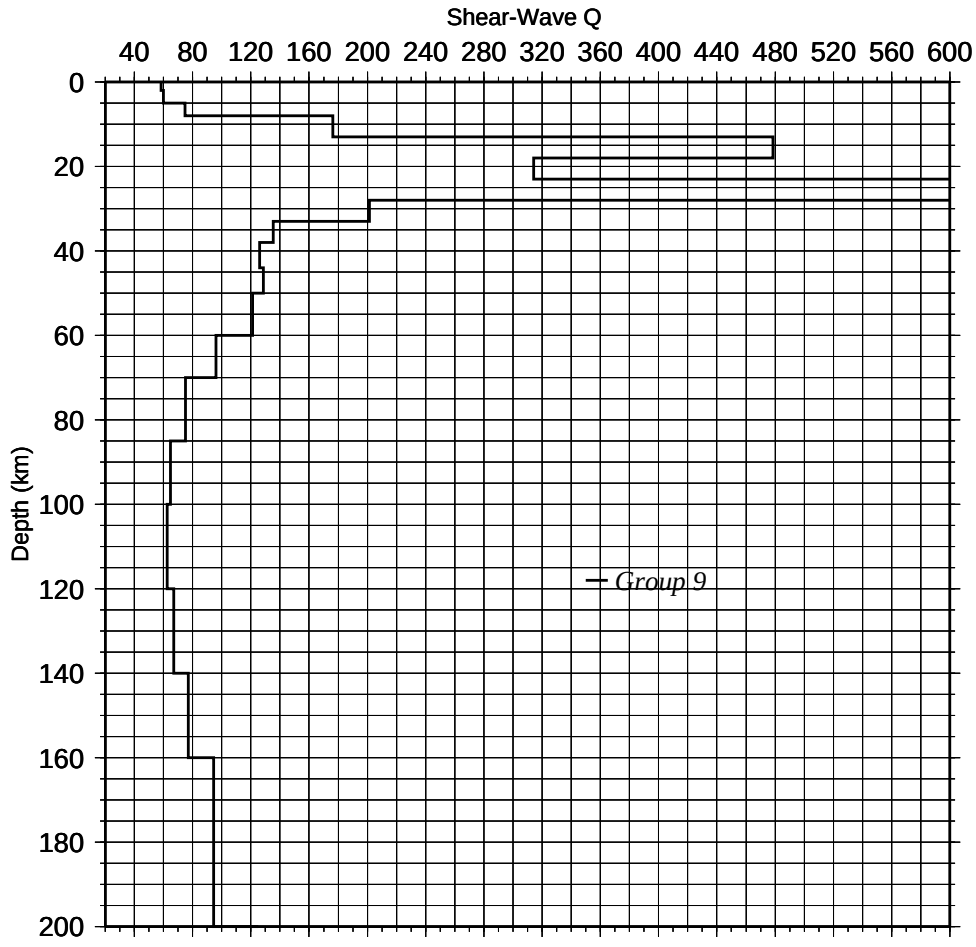

Figure 4.23: Shear-wave Q (Q_μ) structures for group 9, displayed for comparison and convenience of discussion.

T(sec)	$\gamma(1/km)$	STDEV (1/km)
12	3.23000E-04	1.54000E-04
14	2.38000E-04	1.69000E-04
16	1.98000E-04	1.17000E-04
18	1.90000E-04	7.12000E-05
20	1.71000E-04	4.33000E-05
22	1.22000E-04	7.05000E-05
24	1.10000E-04	5.81000E-05
26	9.87000E-05	5.65000E-05
28	8.76000E-05	6.05000E-05
30	1.08000E-04	5.03000E-05
32	1.02000E-04	4.80000E-05
34	9.59000E-05	4.70000E-05
36	9.01000E-05	4.77000E-05
38	8.47000E-05	4.87000E-05
40	7.92000E-05	4.92000E-05
42	7.48000E-05	5.08000E-05
44	7.02000E-05	5.15000E-05
46	6.60000E-05	5.19000E-05
48	6.23000E-05	5.27000E-05
50	5.88000E-05	5.31000E-05
52	5.59000E-05	5.38000E-05
54	8.04000E-05	3.48000E-05
56	7.82000E-05	3.36000E-05
58	7.58000E-05	3.21000E-05
60	7.36000E-05	3.10000E-05

Table 4.19: Average interstation attenuation coefficients used for the inversion of shear-wave Q_μ structure of group 1. T is period, γ is attenuation coefficient, and STDEV is standard deviation.

H(km)	Q_α	Q_μ
2	484.288	215.239
3	486.171	216.076
3	489.343	217.486
5	496.470	220.653
5	522.648	232.288
5	588.235	261.438
5	715.194	317.864
5	914.262	406.339
5	1135.22	504.541
6	1232.20	547.645
6	1082.25	481.000
10	845.547	375.799
10	638.660	283.849
15	504.597	224.266
15	408.126	181.389
20	330.639	146.951
20	273.324	121.477
20	241.390	107.285
40	231.720	102.9866
50	263.435	117.082
70	365.438	162.417
0	710.003	315.557

Table 4.20: Q structure inverted from interstation attenuation coefficients of group 1 . H is layer thickness, Q_α is P-wave quality factor, and Q_μ is S-wave quality factor.

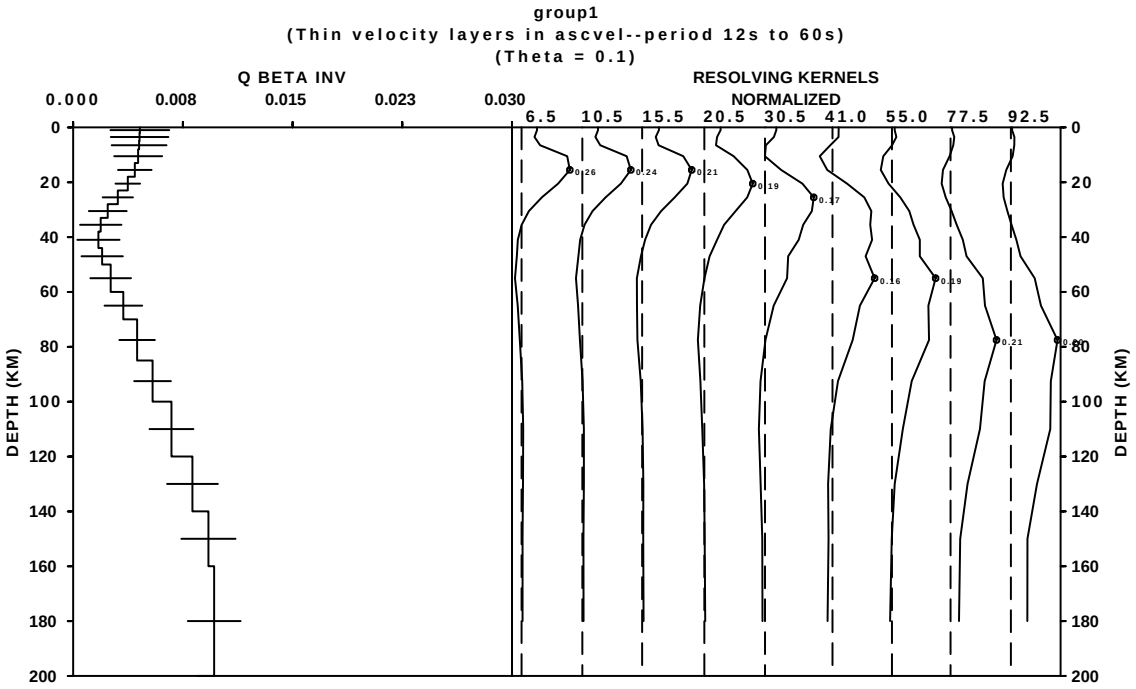

Figure 4.24: Q_μ^{-1} structure for group 1.

T(sec)	$\gamma(1/km)$	STDEV (1/km)
11	5.09000E-04	3.21000E-04
18	4.25000E-04	2.56000E-04
28	3.01000E-04	3.06000E-04
33	2.51000E-04	2.73000E-04
38	2.13000E-04	2.43000E-04
43	1.84000E-04	2.19000E-04
48	1.62000E-04	1.98000E-04
53	1.44000E-04	1.81000E-04
58	1.29000E-04	1.66000E-04
63	1.17000E-04	1.54000E-04
68	1.07000E-04	1.43000E-04
73	9.88000E-05	1.33000E-04
78	9.16000E-05	1.25000E-04
83	8.50000E-05	1.17000E-04
88	7.95000E-05	1.11000E-04

Table 4.21: Average interstation attenuation coefficients used for the inversion of shear-wave Q_μ structure of group 2. T is period, γ is attenuation coefficient, and STDEV is standard deviation.

$H(km)$	Q_α	Q_μ
2	592.105	263.158
3	573.687	254.972
3	537.891	239.063
5	466.902	207.512
5	362.669	161.186
5	282.948	125.755
5	234.277	104.1233
5	206.422	91.7431
5	190.840	84.8176
6	182.927	81.3008
6	180.288	80.1282
10	180.868	80.3859
10	183.673	81.6327
15	186.722	82.9875
15	189.076	84.0336
20	191.002	84.8896
20	195.143	86.7303
20	204.732	90.9918
40	223.214	99.2063
50	268.017	119.119
70	373.568	166.030
0	714.513	317.561

Table 4.22: Q structure inverted from interstation attenuation coefficients of group 2. H is layer thickness, Q_α is P-wave quality factor, and Q_μ is S-wave quality factor.

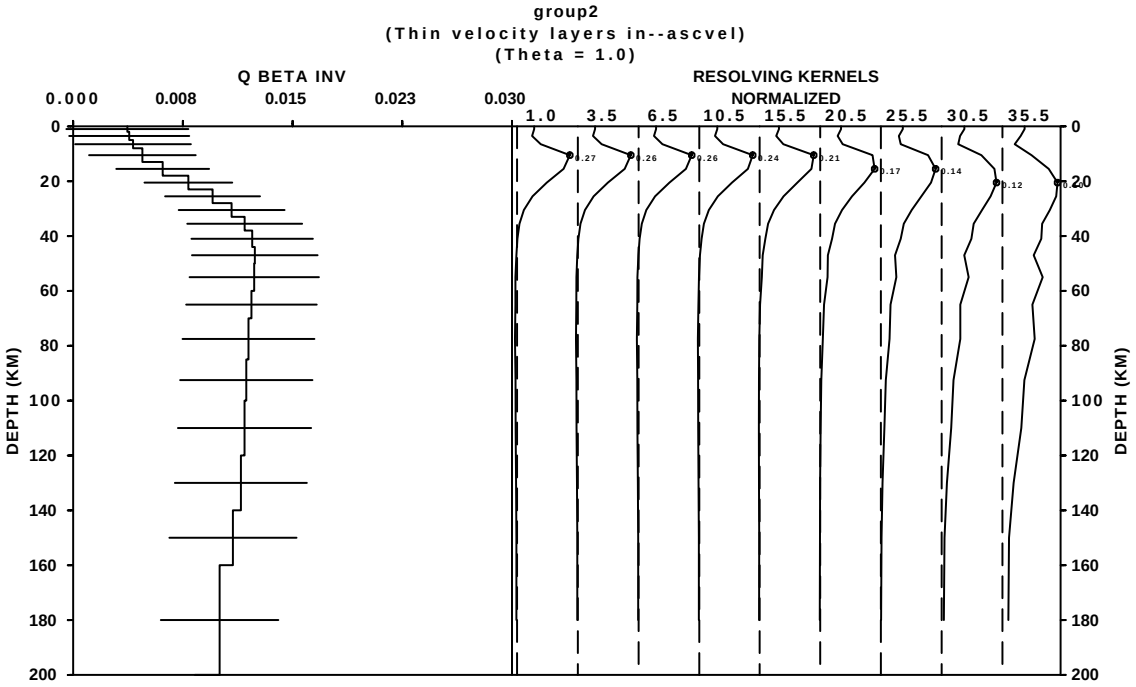

Figure 4.25: Q_μ^{-1} structure for group 2.

4.2.2 Group 2

The attenuation coefficient data of group 2 (Figure 4.18 and Table 4.21) were inverted to obtain the values of Q_μ shown in Table 4.22 and Figure 4.25.

Q_μ is about 260 near the surface and decreases to about 80 at 35 km. Q_μ has almost constant values (80-100) for layers deeper than 35 km. Comparing the shear-velocity structure with the Q_μ structure of this group, we can see that, except for the low velocity layer between 10 and 20 km, the two models are inversely related. That is, as the shear velocity increases to higher values below 20 km, the Q_μ value decreases to 80 for depths below about 35 km. The negative correlation between the shear velocity and Q_μ cannot be explained by multipathing effects on spectral amplitudes since that region is relatively uniform. There are lots of high temperature ($\geq 80^0C$) thermal springs in southeast China (Dingheng et al., 1996). The high temperature springs, and weak or absent upper mantle lithosphere (Weir, 1982), may explain the low Q_μ values below 35 km.

4.2.3 Group 3

The attenuation coefficient data of group 3 (Figure 4.18 and Table 4.23) were inverted to obtain the values of Q_μ shown in Table 4.24 and Figure 4.26. Q_μ for this group is about 100 and remains between 90 and 100 for the upper 15-17 km of the crust. Below about 17 km, Q_μ decreases to about 30 at about 50-60 km, and for depths below 60 km Q_μ remains constant at about 30.

T(sec)	$\gamma(1/km)$	STDEV (1/km)
13	8.74000E-04	1.03000E-04
18	7.51000E-04	3.08000E-04
23	6.84000E-04	2.13000E-04
28	6.26000E-04	1.90000E-04
33	5.68000E-04	1.85000E-04
38	5.16000E-04	1.84000E-04
43	4.71000E-04	1.82000E-04
48	4.32000E-04	2.00000E-04
53	4.02000E-04	1.96000E-04
58	3.82000E-04	2.19000E-04
63	3.59000E-04	2.12000E-04
68	3.38000E-04	2.05000E-04
73	3.19000E-04	1.98000E-04

Table 4.23: Average interstation attenuation coefficients used in the inversion for shear-wave Q_μ structure of group 3. T is period, γ is attenuation coefficient, and STDEV is standard deviation.

H(km)	Q_α	Q_μ
2	218.872	97.2763
3	215.724	95.8773
3	213.270	94.7867
5	213.270	94.7867
5	211.665	94.0734
5	197.368	87.7193
5	170.197	75.6430
5	140.449	62.4220
5	115.503	51.3347
6	97.0246	43.1220
6	84.0493	37.3552
10	75.1252	33.3890
10	69.5948	30.9310
15	65.9051	29.2912
15	63.2556	28.1136
20	61.3915	27.2851
20	61.1413	27.1739
20	63.4160	28.1849
40	69.2095	30.7598
50	84.4595	37.5375
70	120.903	53.7346
0	237.417	105.519

Table 4.24: Q structure inverted from interstation attenuation coefficients of group 3. H is layer thickness, Q_α is P-wave quality factor, and Q_μ is S-wave quality factor.

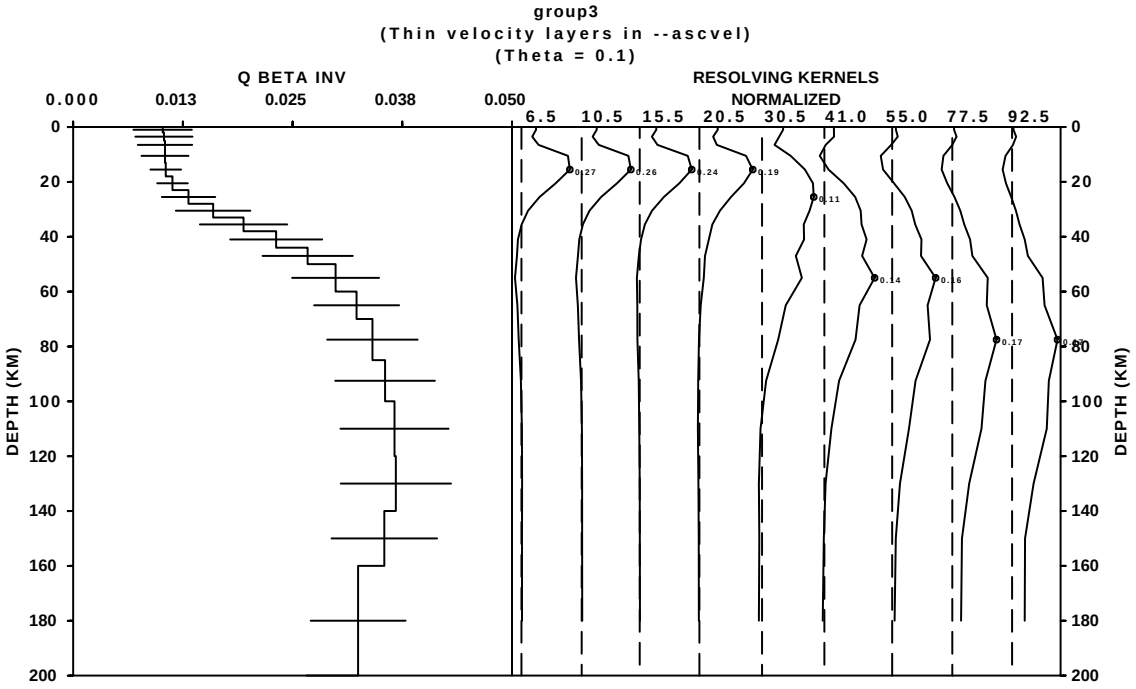

Figure 4.26: Q_μ^{-1} structure for group 3.

The path that forms this group runs parallel to the coast of southeast China from Taiwan to Shanghai. The model for shear-velocity structure indicates a very thin lithosphere (about 62 km thick) and a shallow asthenosphere beneath it. High-temperature ($\geq 80^0C$) thermal springs occur in Taiwan and middle to lower-temperature thermal springs occur near Shanghai (Dingheng et al., 1996). The low Q_μ values for layers below about 17 km may be explained by the thinness of the lithosphere and by a shallow high-temperature asthenosphere.

4.2.4 Group 4

The attenuation coefficient data of group 4 (Figure 4.18 and Table 4.25) were inverted to obtain the values of Q_μ shown in Table 4.26 and Figure 4.27. Q_μ for this group is 130 is the upper 5-7 km of the crust

T(sec)	$\gamma(1/km)$	STDEV (1/km)
9	7.55000E-04	1.67000E-04
12	4.98000E-04	8.88000E-05
15	3.39000E-04	1.12000E-04
18	2.81000E-04	1.28000E-04
21	2.41000E-04	1.31000E-04
24	2.11000E-04	1.28000E-04
28	1.82000E-04	1.21000E-04
32	1.60000E-04	1.12000E-04
36	1.70000E-04	9.06000E-05
40	1.53000E-04	8.56000E-05
44	1.40000E-04	8.06000E-05
48	1.29000E-04	7.60000E-05
52	8.60000E-05	6.58000E-05
56	7.97000E-05	6.26000E-05
60	4.72000E-05	5.24000E-05
64	8.00000E-06	1.67000E-04
68	6.30000E-06	1.67000E-04
72	4.90000E-06	1.67000E-04
76	3.80000E-06	1.67000E-04
80	2.90000E-06	1.67000E-04
85	1.90000E-06	1.67000E-04
90	1.10000E-06	1.67000E-04
94	6.00000E-07	1.67000E-04

Table 4.25: Average interstation attenuation coefficients used in the inversion for shear-wave Q_μ of group 4. T is period, γ is attenuation coefficient, and STDEV is standard deviation.

H(km)	Q_α	Q_μ
2	287.540	127.796
3	288.721	128.320
3	294.618	130.941
5	314.553	139.801
5	368.068	163.586
5	462.773	205.677
5	611.746	271.887
5	810.227	360.101
5	916.124	407.166
6	737.947	327.976
6	447.138	198.728
10	269.914	119.962
10	178.713	79.4281
15	144.046	64.0205
15	158.339	70.3730
20	268.049	119.133
20	13066.2	5807.20
20	278.224	123.655
40	165.320	73.4754
50	162.104	72.0461
70	217.181	96.5251
0	427.026	189.789

Table 4.26: Q structure inverted from interstation attenuation coefficients of group 4. H is layer thickness, Q_α is P-wave quality factor, and Q_μ is S-wave quality factor.

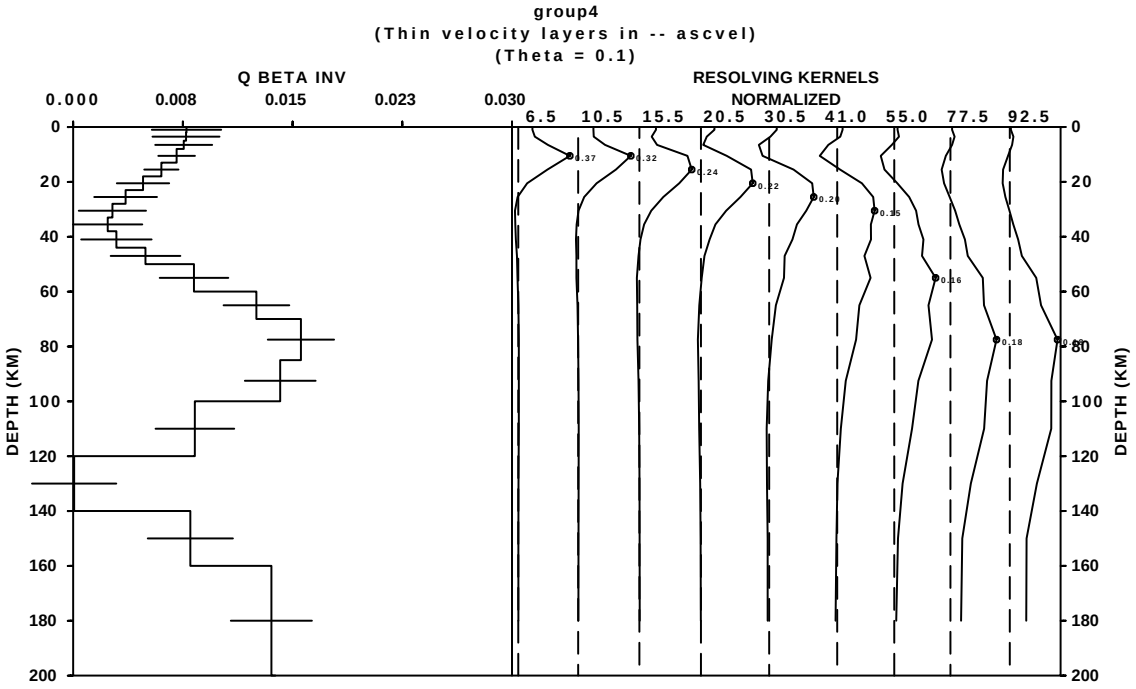

Figure 4.27: Q_μ^{-1} structure for group 4.

and increases to about 420 at about 35 km depth. The high Q_μ value persists until about 50 km. Below 50 km there is about 70-km thick (from 50-120 km) low Q_μ layer, which roughly coincides with the low shear-velocity layer of this group. The extremely high Q_μ value between 120 km and 140 km may be due to numerical errors that make the solution of the inverse problem diverge.

The extensional tectonics (Nabelek et al., 1987), high heat flow (Teng et al., 1983), and the thin lithosphere (Menzies and Xu, 1998) in the North China Craton may be responsible for the low Q_μ values for depths below about 50 km.

T(sec)	$\gamma(1/km)$	STDEV (1/km)
10	5.83000E-04	1.71000E-04
13	4.54000E-04	1.51000E-04
16	3.76000E-04	1.17000E-04
19	3.13000E-04	1.24000E-04
22	2.74000E-04	1.28000E-04
25	2.47000E-04	1.26000E-04
28	2.26000E-04	1.21000E-04
32	2.05000E-04	1.13000E-04
36	1.87000E-04	1.06000E-04
40	1.73000E-04	9.96000E-05
44	1.60000E-04	9.93000E-05
48	1.49000E-04	9.44000E-05
52	1.40000E-04	8.98000E-05
57	1.30000E-04	8.50000E-05
61	1.23000E-04	8.12000E-05
65	1.17000E-04	7.82000E-05
70	1.08000E-04	7.87000E-05
75	1.02000E-04	7.51000E-05
80	9.71000E-05	7.20000E-05
85	9.84000E-05	7.10000E-05
90	9.31000E-05	7.37000E-05
95	9.34000E-05	6.16000E-05

Table 4.27: Average interstation attenuation coefficients used in the inversion for shear-wave Q_μ structure for group 5. T is period, γ is attenuation coefficient, and STDEV is standard deviation.

H(km)	Q_α	Q_μ
2	444.050	197.355
3	437.999	194.666
3	422.535	187.793
5	393.563	174.917
5	359.425	159.744
5	340.599	151.378
5	334.871	148.832
5	329.960	146.649
5	315.170	140.076
6	289.240	128.551
6	257.850	114.600
10	230.438	102.4170
10	214.286	95.2381
15	210.084	93.3707
15	214.900	95.5110
20	215.517	95.7854
20	199.468	88.6525
20	174.961	77.7605
40	154.110	68.4931
50	149.402	66.4011
70	174.284	77.4593
0	291.526	129.567

Table 4.28: Q structure inverted from interstation attenuation coefficients of group 5. H is layer thickness, Q_α is P-wave quality factor, and Q_μ is S-wave quality factor.

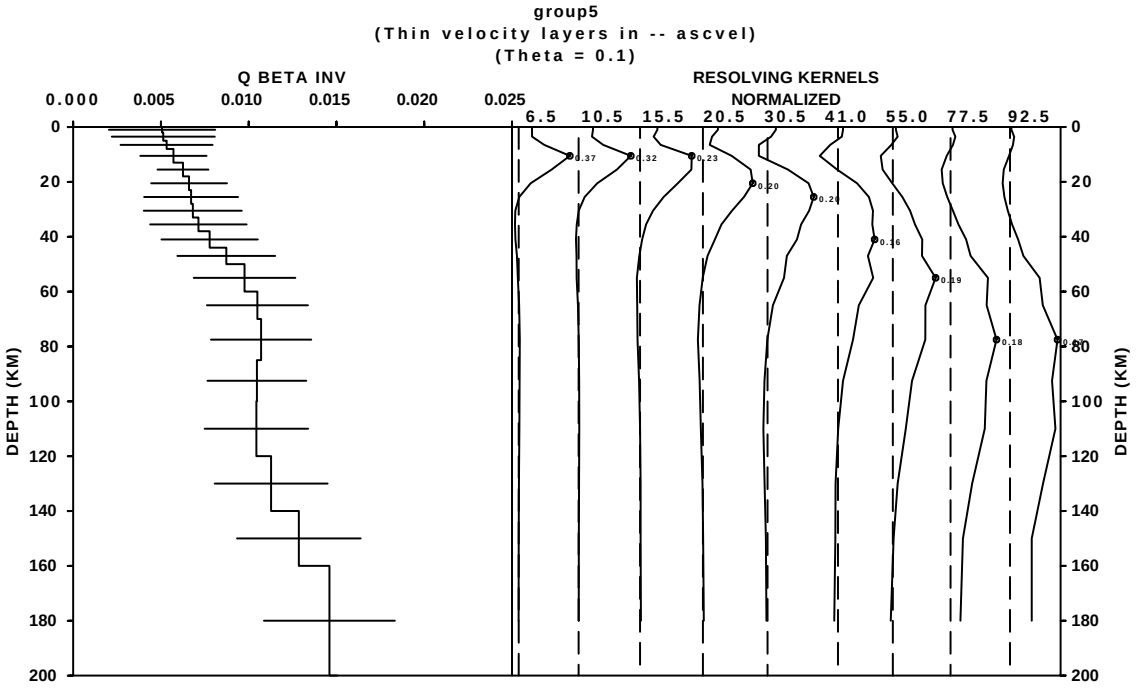

Figure 4.28: Q_μ^{-1} structure for group 5.

4.2.5 Group 5

The attenuation coefficient data of group 5 (Figure 4.19 and Table 4.27) were inverted to obtain the values of Q_μ shown in Table 4.28 and Figure 4.28. Q_μ for group 5 in northeastern China is about 200 at the surface and decreases linearly to about 100 at about 50 km. Below 50 km, Q_μ decreases to low values between 60 and 100.

These paths cross the Cenozoic basalts of northeastern China, fold systems, and the northern end of the Songliao basin, where high heat flow is recorded. Barry and Kent (1998) suggested that a hot asthenosphere (temperature $\geq 1400^0C$) underlies this region and Mongolia at depths just below 100 km in order to account for the quantity and composition of Cenozoic basalt found in these two regions. The high ther-

T(sec)	$\gamma(1/km)$	STDEV (1/km)
13	6.69000E-04	3.88000E-04
16	4.05000E-04	1.25000E-04
19	3.02000E-04	1.25000E-04
22	2.50000E-04	1.19000E-04
25	2.20000E-04	1.06000E-04
28	2.00000E-04	9.41000E-05
31	1.85000E-04	8.60000E-05
34	1.74000E-04	8.11000E-05
38	1.62000E-04	7.84000E-05
42	1.51000E-04	7.75000E-05
46	1.43000E-04	7.78000E-05
50	1.35000E-04	7.79000E-05
55	1.27000E-04	7.77000E-05
60	1.19000E-04	7.74000E-05
64	1.14000E-04	7.66000E-05
70	1.07000E-04	7.54000E-05
75	1.02000E-04	7.42000E-05
80	9.69000E-05	7.27000E-05
85	1.01000E-04	7.43000E-05
90	9.63000E-05	7.27000E-05
95	9.23000E-05	7.12000E-05

Table 4.29: Average interstation attenuation coefficients used in the inversion for shear-wave Q_μ structure of group 6. T is period, γ is attenuation coefficient, and STDEV is standard deviation.

mal activity at depth may be responsible for the low Q_μ values below about 50 km in northeastern China.

4.2.6 Group 6

The attenuation coefficient data of group 6 (Figure 4.19 and Table 4.29) were inverted to obtain the values of Q_μ shown in Table 4.30 and Figure 4.29. The paths of this group cross the Stanovoy Range in southeastern Siberia. Q_μ for the upper crust (upper 10 -15 km) is between 40 and 60. A very high Q_μ layer (about 20 km thick) exists between depths of about 20 km and 40 km. The rapid increase in Q_μ values at mid-crustal depths is consistent with what is observed in Central and Western United States (Mitchell, 1995). The relatively low Q_μ values in the upper crustal layers can be explained by the possible presence of fluid-filled fractures (Mitchell, 1995).

$H(km)$	Q_α	Q_μ
2	119.936	53.3049
3	121.951	54.2005
3	128.059	56.9152
5	150.301	66.8003
5	240.951	107.089
5	674.258	299.670
5	5795.98	2575.99
5	2294.51	1019.78
5	2480.71	1102.54
6	555.281	246.792
6	309.576	137.589
10	234.399	104.1775
10	226.655	100.7354
15	252.724	112.322
15	293.160	130.293
20	297.304	132.135
20	239.336	106.372
20	179.140	79.6178
40	140.977	62.6566
50	129.014	57.3394
70	147.251	65.4450
0	244.991	108.885

Table 4.30: Q structure inverted from interstation attenuation coefficients of group 6. H is layer thickness, Q_α is P-wave quality factor, and Q_μ is S-wave quality factor.

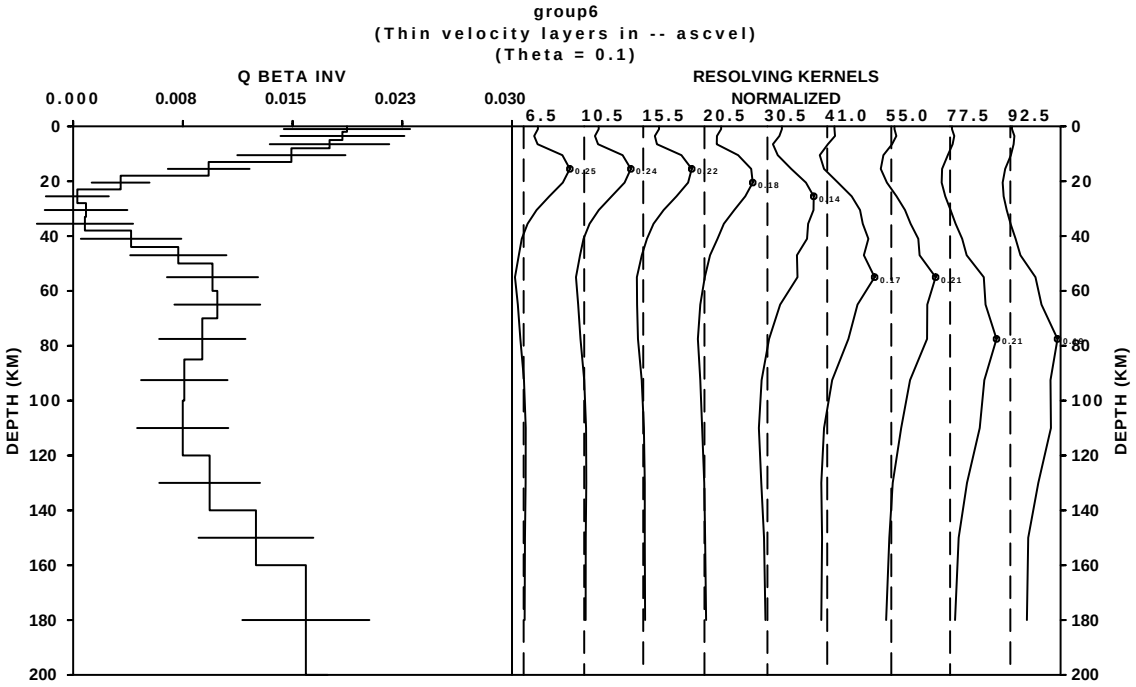

Figure 4.29: Q_μ^{-1} structure for group 6.

T(sec)	$\gamma(1/km)$	STDEV (1/km)
12	3.20000E-04	4.06000E-05
15	2.64000E-04	3.42000E-05
18	2.15000E-04	3.93000E-05
21	1.82000E-04	2.96000E-05
24	1.59000E-04	1.89000E-05
27	1.41000E-04	9.20000E-06
30	1.26000E-04	1.20000E-06
33	1.15000E-04	5.00000E-06
36	1.05000E-04	1.00000E-05
40	9.44000E-05	1.47000E-05
45	8.39000E-05	1.86000E-05
50	7.56000E-05	2.11000E-05
55	6.88000E-05	2.26000E-05
60	6.31000E-05	2.33000E-05

Table 4.31: Average interstation attenuation coefficients used in the inversion for shear-wave Q_μ structure of group 7. T is period, γ is attenuation coefficient, and STDEV is standard deviation.

Between 50 km and 90 km the Q_μ value is about 100; below 90 km, it increases slightly to about 130. However the resolution kernels are very wide for depths deeper than about 20 km. Any narrow features at deeper depths may therefore not be realistic.

4.2.7 Group 7

The attenuation coefficient data of group 7 (Figure 4.19 and Table 4.31) were inverted to obtain the values of Q_μ shown in Table 4.32 and Figure 4.30. The Mongolian Plateau, crossed by the group 7 path, is affected by a combined collision-mantle uplift tectonics. The late Cenozoic uplift of the entire Mongolian Plateau and associated rifting, magmatism, high heat flow (up to $120mW/m^2$), and lithospheric thinning (as thin as about 50 km) are due to the interaction of a mantle plume with overlying lithosphere (Windley and Allen, 1993). Major strike-slip faults may be expressions of the collision between India and Asia in the south (Windley and Allen, 1993).

The Q_μ structure of this path has very high values (up to 560) for the

$H(km)$	Q_α	Q_μ
2	1263.34	561.482
3	1192.37	529.942
3	937.110	416.493
5	625.000	277.778
5	452.625	201.167
5	422.615	187.829
5	468.945	208.420
5	542.169	240.964
5	577.367	256.608
6	548.513	243.784
6	488.812	217.250
10	438.853	195.046
10	406.872	180.832
15	380.325	169.033
15	361.969	160.875
20	362.728	161.212
20	381.809	169.693
20	401.929	178.635
40	421.427	187.301
50	477.707	212.314
70	654.070	290.698
0	1271.19	564.972

Table 4.32: Q structure inverted from interstation attenuation coefficients of group 7. H is layer thickness, Q_α is P-wave quality factor, and Q_μ is S-wave quality factor.

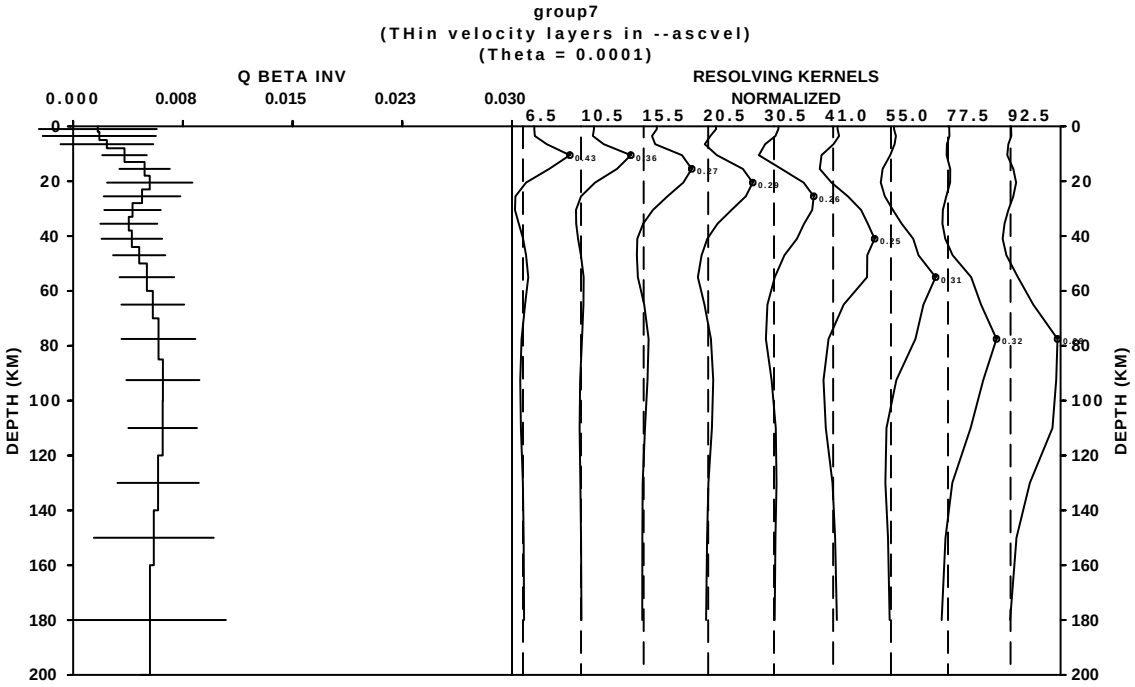

Figure 4.30: Q_μ^{-1} structure for group 7.

top 10 km of the crust. However, this high value of Q_μ is very unlikely for such a tectonically active region. Therefore, this may be due to numerical errors that let the solution of the inverse problem diverge to higher values. The other possibility is that, since in the two-station method the earthquakes recorded by stations HIA and TLY are coming from the Kuril Trench in the Pacific Ocean, they may be focused as they cross the continent-oceanic margin. Focusing of the seismic waves at the more distant station will amplify their amplitudes and hence giving rise to higher Q_μ values.

Between about 15 km and 25 km there Q_μ has relatively low values (about 190), but it increases to about 250 at a depth of about 35 km. Below 45 km it decreases to lower values (about 160) at a depth of about 120 km. The resolution kernels are narrow for the upper 20 km of the crust but become wider as depth increases. The standard deviations are large at almost all depths.

4.2.8 Group 8

The attenuation coefficient data of group 8 (Figure 4.19 and Table 4.33) were inverted to obtain the values of Q_μ shown in Table 4.34 and Figure 4.31. Most part of this path is within the western part of the Mongolian Plateau and the Altai Range. Outside the border of Mongolia it is within the Junggar basin and fold system.

Q_μ is about 170 in the upper 5-7 km of the crust. A low Q_μ value (as low as 130) exists between about 10 km and 35 km. The shape and depth range of this low-Q_μ layer is almost identical to that of the low shear-velocity layer for this group. The low Q_μ and shear-velocity val-

T(sec)	$\gamma(1/km)$	STDEV (1/km)
14	4.65000E-04	1.97600E-04
16	3.81000E-04	1.72200E-04
20	2.89000E-04	1.18400E-04
24	2.39000E-04	7.43000E-05
28	2.07000E-04	4.28000E-05
32	1.84000E-04	2.06000E-05
36	1.66000E-04	6.10000E-06
40	1.52000E-04	7.30000E-06
44	1.48000E-04	4.10000E-06
48	1.41000E-04	3.20000E-06
52	1.35000E-04	2.60000E-06
56	1.29000E-04	1.70000E-06
60	1.24000E-04	1.20000E-06
64	1.19000E-04	1.00000E-06
68	1.14000E-04	1.00000E-06
72	1.09000E-04	6.00000E-07
76	1.05000E-04	4.00000E-07
80	1.02000E-04	3.00000E-07
84	9.85000E-05	7.00000E-05

Table 4.33: Average interstation attenuation coefficients used in the inversion for shear-wave Q_μ structure of group 8. T is period, γ is attenuation coefficient, and STDEV is standard deviation.

H(km)	Q_α	Q_μ
2	377.580	167.813
3	373.630	166.058
3	364.668	162.075
5	345.569	153.586
5	314.817	139.919
5	293.312	130.361
5	293.695	130.531
5	322.951	143.534
5	391.372	173.943
6	513.699	228.311
6	655.977	291.545
10	650.853	289.268
10	401.070	178.253
15	241.106	107.158
15	173.210	76.9823
20	156.033	69.3481
20	175.644	78.0640
20	210.477	93.5454
40	213.270	94.7867
50	146.389	65.0618
70	113.579	50.4796
0	140.100	62.2665

Table 4.34: Q structure inverted from interstation attenuation coefficients of group 8. H is layer thickness, Q_α is P-wave quality factor, and Q_μ is S-wave quality factor.

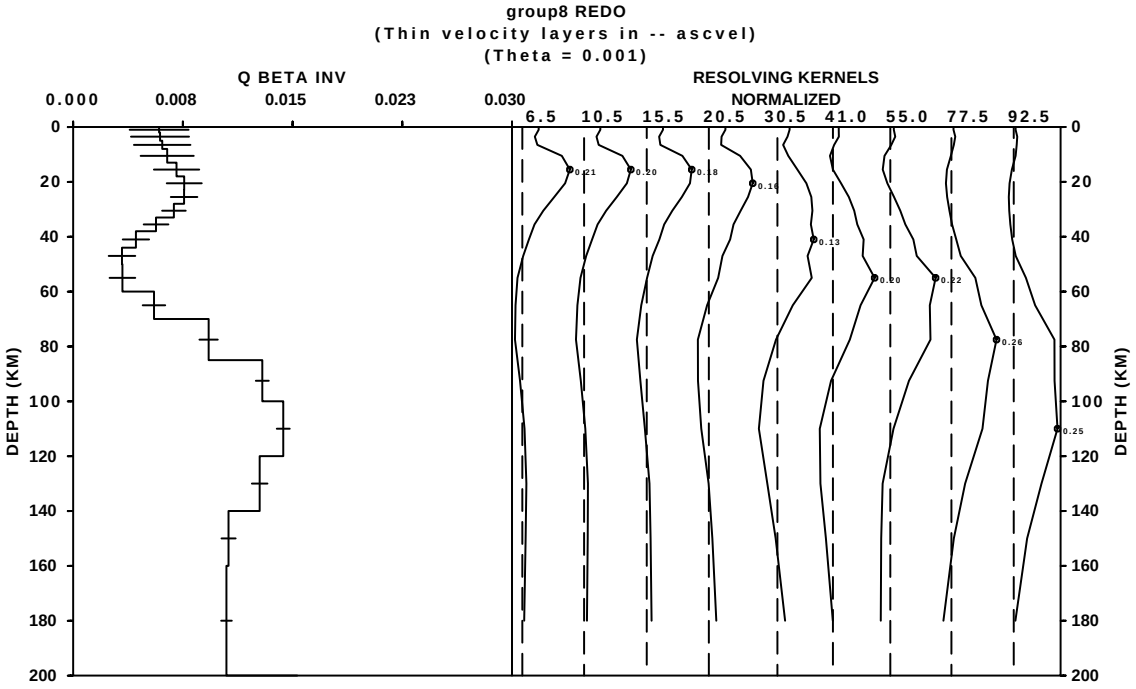

Figure 4.31: Q_μ^{-1} structure for group 8.

ues in the depth range 10-35 km can be caused by fluid-filled fractures and thicker crust there. The existence of fluid-filled fractures make Q_μ low, as seismic energy goes into moving fluids in the interconnected fractures (Mitchell, 1995).

The Q_μ value increases to 290 for the depth range between 40 km and 70 km, but this thin relatively high Q_μ layer is not really resolvable as indicated by the broad resolution kernels at depths below about 15 km. Below 70 km the Q_μ value decreases to about 70 to a depth of 140 km.

4.2.9 Group 9

The attenuation coefficient data of group 9 (Figure 4.20 and Table 4.35) were inverted to obtain the values of Q_μ shown in Table 4.36 and

T(sec)	$\gamma(1/km)$	STDEV (1/km)
11	5.29000E-04	1.04500E-04
12	4.05000E-04	6.06000E-05
13	3.31000E-04	1.96000E-05
14	2.87000E-04	1.80000E-05
15	2.61000E-04	4.97000E-05
16	2.45000E-04	7.71000E-05
17	2.37000E-04	1.00500E-04
18	2.32000E-04	1.19800E-04
19	2.30000E-04	1.35800E-04
20	2.29000E-04	1.49500E-04
21	2.29000E-04	1.60100E-04
22	2.29000E-04	1.69400E-04
23	2.30000E-04	1.77100E-04
24	2.30000E-04	1.82700E-04
25	2.30000E-04	1.87700E-04
26	2.30000E-04	1.91700E-04
27	2.30000E-04	1.94700E-04
28	2.30000E-04	1.96700E-04
29	2.30000E-04	1.98600E-04
30	2.29000E-04	1.99600E-04
31	2.28000E-04	1.99800E-04
32	2.27000E-04	2.00700E-04
33	2.26000E-04	2.00000E-04
34	2.25000E-04	2.00100E-04
35	2.23000E-04	1.99300E-04
36	2.22000E-04	1.98600E-04
37	2.20000E-04	1.97800E-04
38	2.19000E-04	1.97000E-04

Table 4.35: Average interstation attenuation coefficients used in the inversion for shear-wave Q_μ structure of group 9. T is period, γ is attenuation coefficient, and STDEV is standard deviation.

$H(km)$	Q_α	Q_μ
2	131.195	58.3090
3	135.135	60.0601
3	168.413	74.8503
5	396.895	176.398
5	1076.55	478.469
5	706.880	314.169
5	3659.13	1626.28
5	453.081	201.369
5	304.424	135.300
6	283.804	126.135
6	289.650	128.733
10	272.364	121.051
10	215.931	95.9693
15	169.300	75.2445
15	145.820	64.8088
20	140.449	62.4220
20	150.502	66.8896
20	173.344	77.0416
40	212.264	94.3396
50	281.778	125.235
70	422.456	187.758
0	844.912	375.516

Table 4.36: Q structure inverted from interstation attenuation coefficients of group 9. H is layer thickness, Q_α is P-wave quality factor, and Q_μ is S-wave quality factor.

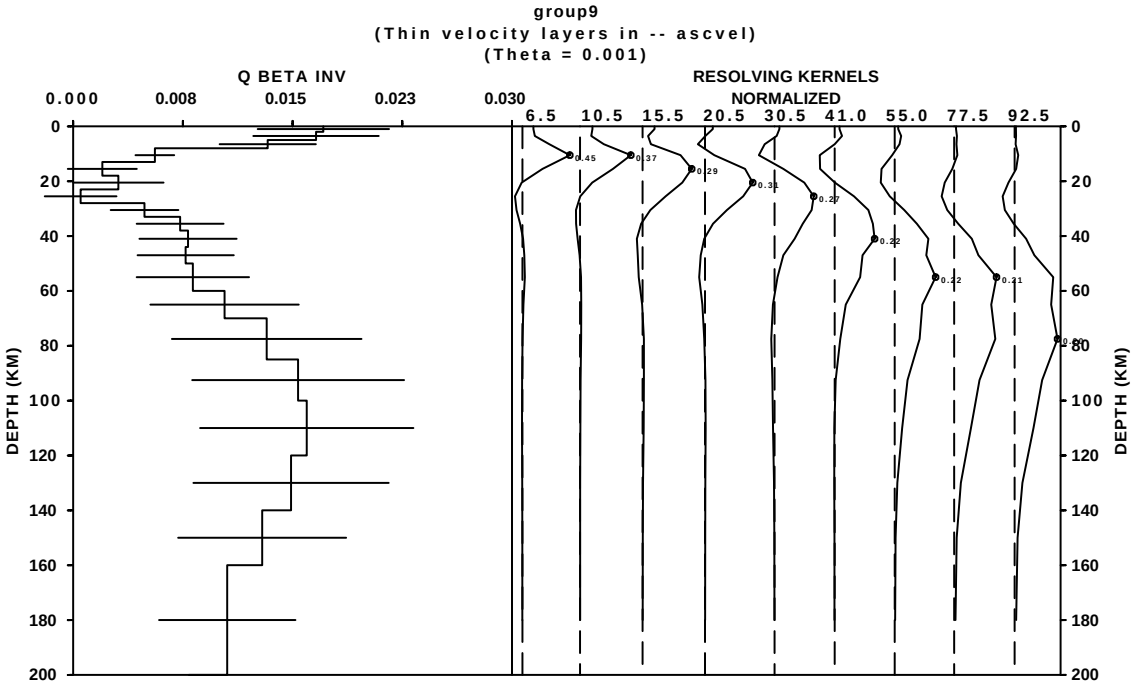

Figure 4.32: Q_μ^{-1} structure for group 9.

Figure 4.32. This path crosses the Tianshan fold system, the Tarim basin and the Western Kunlun fold system.

Q_μ is about 60-70 for the upper 5-7 km of the crust and increases to about 480 or larger at about 20 km. The low Q_μ values for the upper 5-7 km may be related to fluid-filled fractures that may exist in the Tianshan and Western Kunlun fold systems. The effect of the thick sediments in the Tarim Basin are seen in the shear-velocity structure, and it may also reduce Q_μ.

The high-Q_μ layer in the mid-crust between about 15 km and 30 km is consistent with what is observed in the United States for that depth range (Mitchell, 1995). A high shear velocity is also seen at these depths for this group. Between 30 and 60 km Q_μ is almost constant (between 120 and 110) but becomes as low as 60, below 60 km.

4.2.10 Comparisons in Q_μ among different groups

The shape of the Q_μ variation with depth in groups 2, 3, and 5 is identical. Group 2 has higher Q_μ values at all depths when compared with group 3. Group 2 has higher Q_μ for depths above 15 km when compared with group 5, but a reversed relation below 15 km.

Groups 1, 4, and 6 all have a high Q_μ layer at mid to lower-crustal depths (between 15 km and about 60 km), and the shape of Q_μ variation is identical for these groups. Group 1 has the highest Q_μ values at all depths when compared with groups 2, 3, 4, 5, 6, 8, and 9. Group 7 has higher Q_μ values above 15 km and below 100 km when compared with group 1.

Group 4 has higher Q_μ values above 15 km when compared with

group 6, but about the same value between 15 km and 60 km. Below 60 km, group 6 has higher Q_μ value when compared with group 4.

Groups 2 and 5 have higher Q_μ values above 15 km and between 60 km and 100 km when compared with group 4. But between 15 km and 60 km, group 4 has higher Q_μ values than groups 2 and 5. Group 5 has higher Q_μ values above 15 km when compared with group 6, but a reversed relation below 15 km.

Let us assume that seismic waves that form group 4 are amplified by focusing as they travel different tectonic units of East China. Therefore if we ignore group 4, then there is a systematic decrease in Q_μ values for the upper 15 km from South China Block in the south to Siberia in the north. But there is a systematic increase in Q_μ values below 15 km from south to north.

Group 8 has higher Q_μ values when compared with group 9 for the uppermost 7 km of the crust and below 35 km. Between 7 km and 35 km, group 9 has very high Q_μ values. This implies there is a systematic increase in Q_μ values above 7 km and below 35 km from south to north in the western half of the study area.

The South China Block in the east (group 2) has higher Q_μ values above 15 km and below 70 km when compared with western China (group 9). Let us assume that the very high Q_μ value in group 9 between 15 km and 70 km is due to focussing of those waves at periods corresponding to the depth range 15 km - 70 km. Therefore, there is a systematic decrease in Q_μ values from east to west in China.

4.3 Summary of the results from the two-station studies

The text below gives a summary of the results from the two-station determinations of velocity and Q_μ structure, neglecting possible effects of focusing/defocusing that might be produced by laterally complex elastic structure.

1. There is a systematic increase in shear velocity from the South China Block to North and NE China for the top 15 km but a reversed relation below this depth.

2. A major change in shear-velocity structure occurs between Tibet (group 1) and the South China Block. Relatively low shear-velocity values characterize the uppermost 45 km of Tibet and relatively high velocities occur in that depth range for the South China Block (group 2).

3. Between 15 km and 60 km, the eastern coast of China from Taiwan to Shanghai (group 3) shows higher shear velocities than does the South China Block (group 2), but the relation is reversed for the uppermost 15 km and for depths greater than 60 km.

4. The Mongolian Plateau (crossed by group 7) shows lower shear velocities between 10 km and 60 km than do north and northeastern China (groups 4 and 5) but the relation is reversed for the uppermost 10 km and for depths greater than 60 km.

5. Western Mongolia and the Junggar Block (group 8) have lower

shear velocities below 15 km when compared with the groups in eastern China and southeastern Siberia.

6. Western China (group 9) has lower shear velocities for the uppermost 70 km, except between 20 km and 35 km, when compared with the groups in eastern China and southeastern Siberia.

7. The tectonically active region of western China and the western part of the Mongolia plateau have lower shear velocities at least for the depth ranges between 15 km and 70km, when compared with eastern China and southeastern Siberia. However there is an exceptional high-velocity tooth present in western China between 20 km and 35 km.

8. Q_μ increases systematically above 7 km and below 35 km from south to north in the western half of the study area.

9. For both shear velocity and Q_μ structure, the resolution kernels become broader as the depth increases because the long wavelengths which penetrate to those depths sample large depth intervals. As a result, it is more difficult to resolve features of the models at greater depths than at shallower depths.

4.4 Comparison of the shear-wave velocity structures of southeastern Asia with those of the Canadian Shield and the Middle East

The shear-velocity structure of the Canadian shield (Brune and Dorman, 1963) shows higher values at all depths when compared with

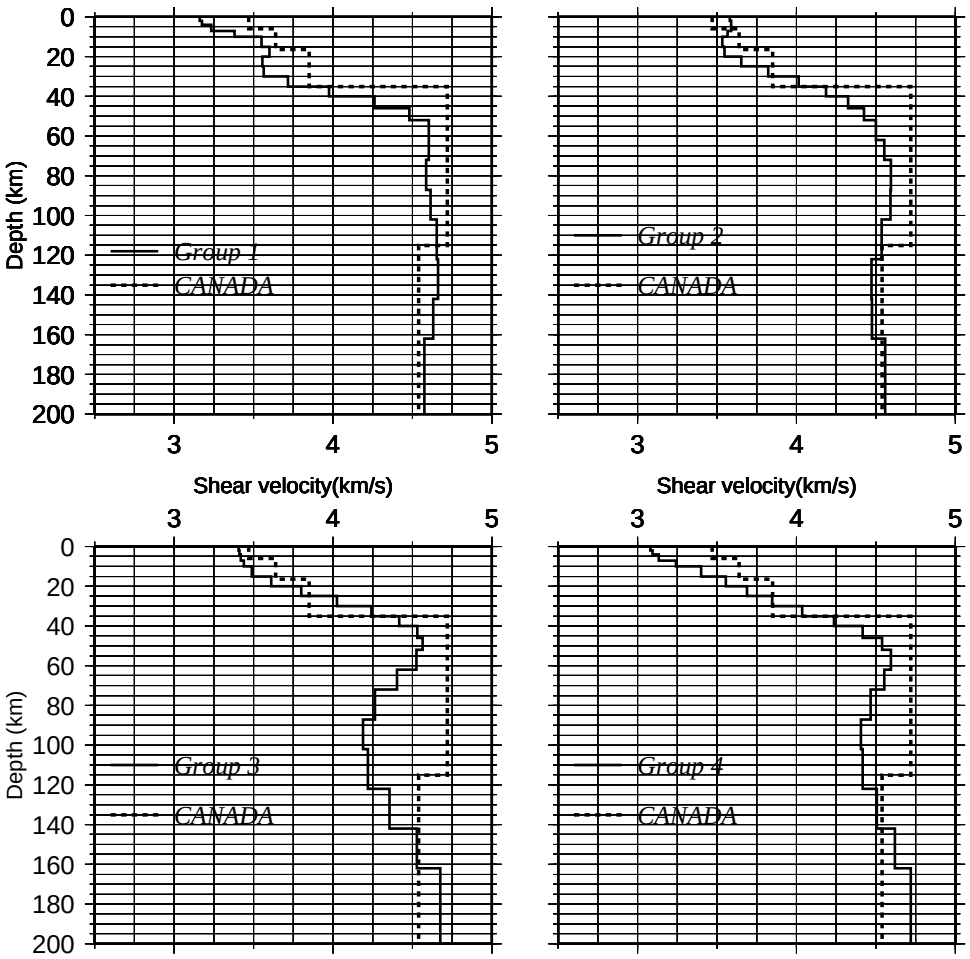

Figure 4.33: Comparisons of the shear-wave velocity structures of the Candian Shield and groups 1, 2, 3, and 4 in southeastern Asia.

those of groups 1, 3, 4, 5, 6, 7, 8, and 9 (Figures 4.33, 4.34, and 4.35) in this study. Group 2 also shows lower values at all depths, except for the upper 5 km, which may be due to absence of phase velocity data for group 2 for periods less than 10 sec. The Rayleigh wave phase velocity data used to invert for the Canadian shield shear-velocity structure starts from 3.5 sec period.

Groups 1, 2, 3, 4, 5, 6, and 7 have higher shear velocities for the upper 80-100 km layers when compared with those of the Turkish and

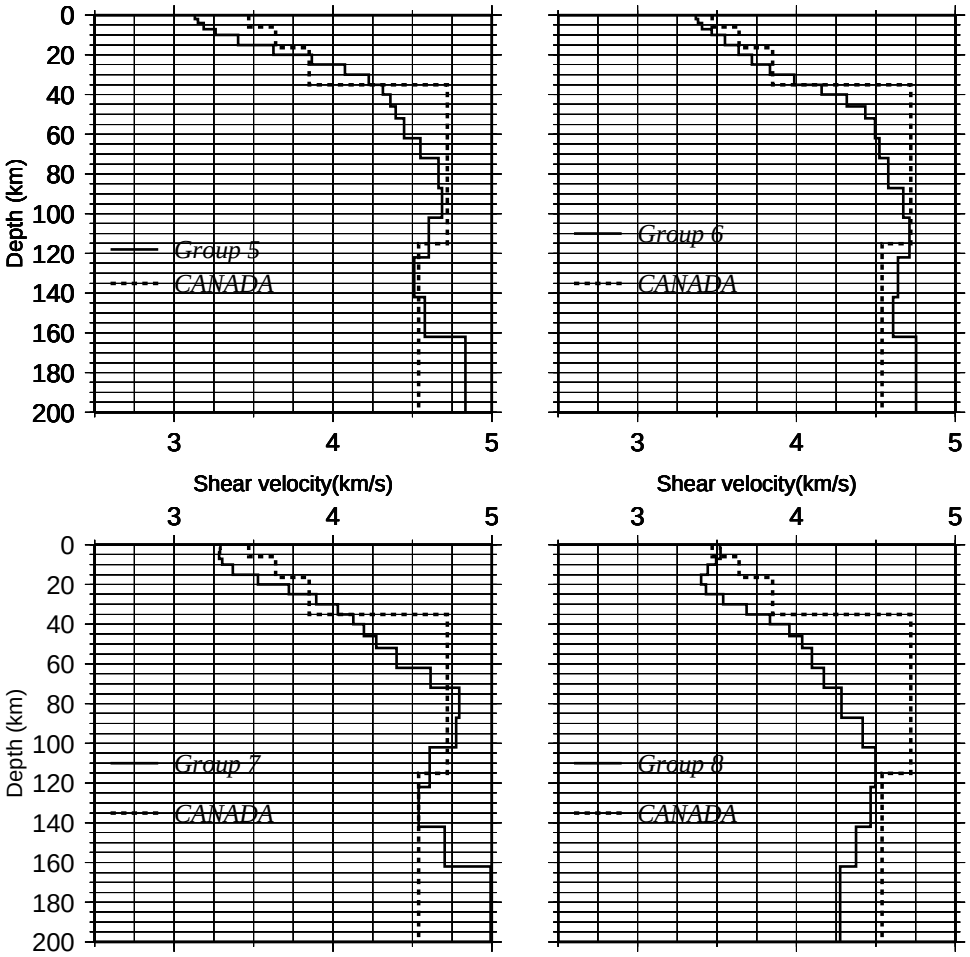

Figure 4.34: Comparisons of the shear-wave velocity structures of the Candian Shield and groups 5, 6, 7, and 8 in southeastern Asia.

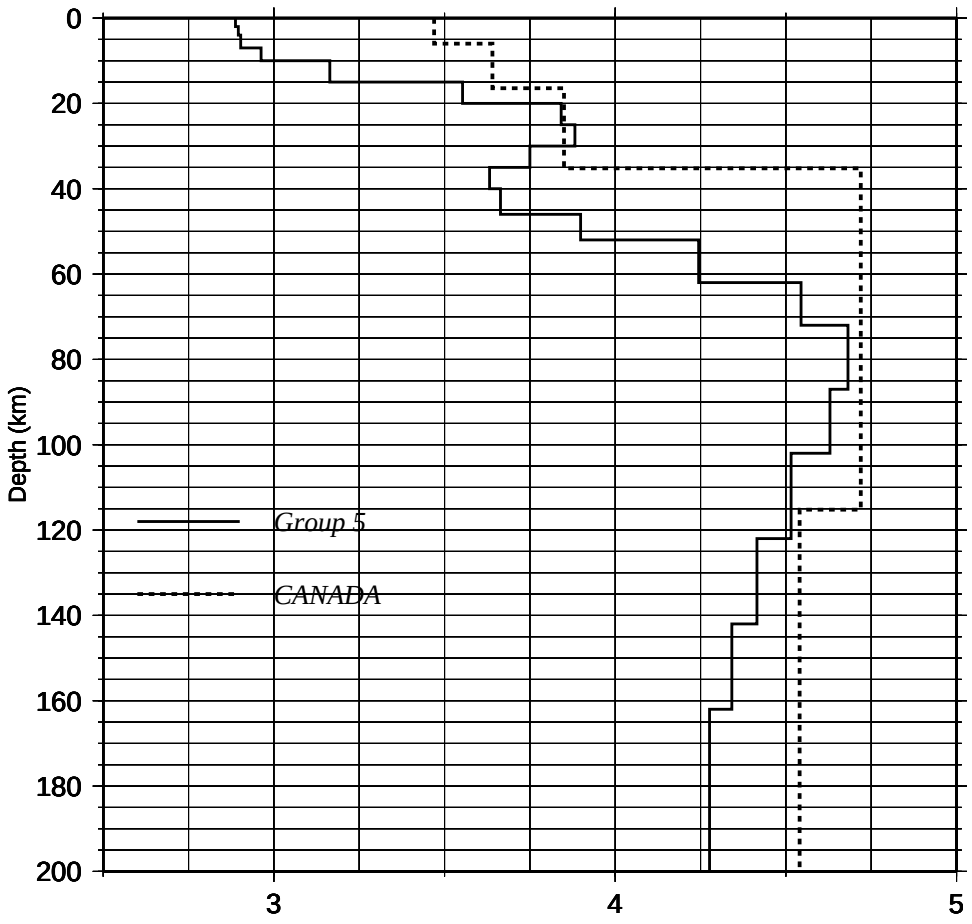

Figure 4.35: Comparisons of the shear-wave velocity structures of the Candian Shield and group 9 in southeastern Asia.

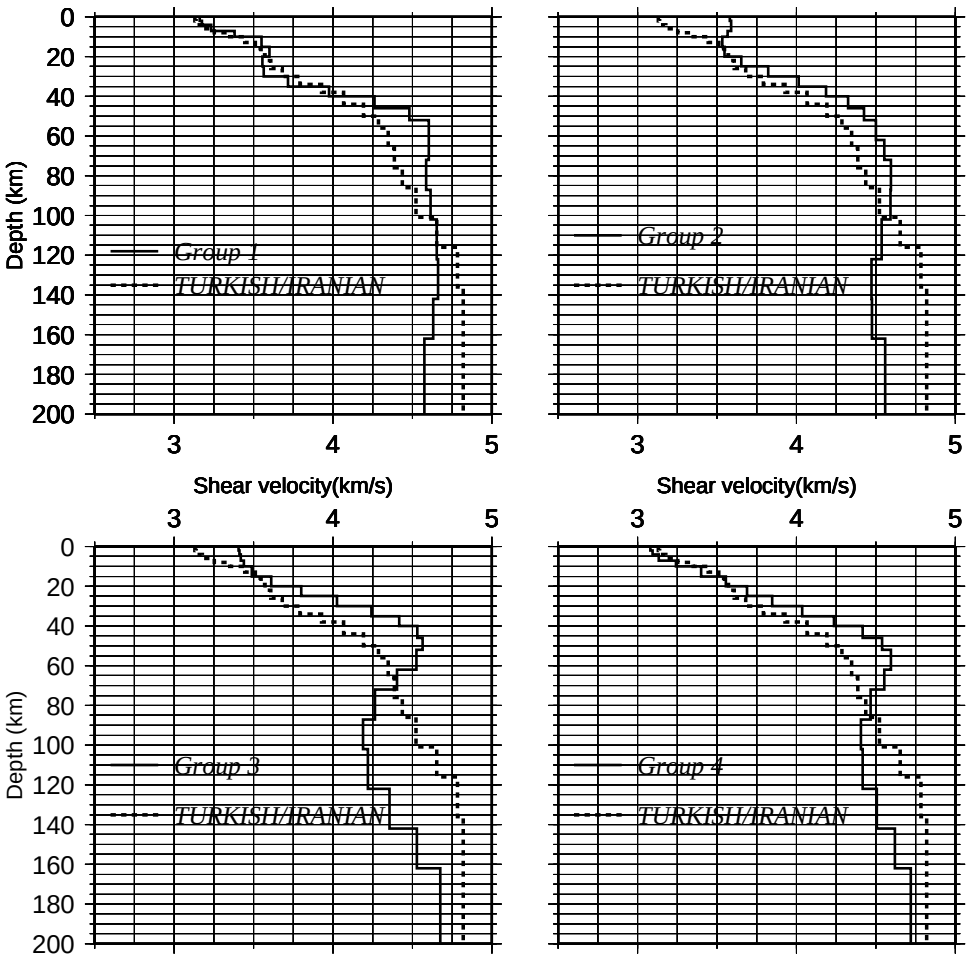

Figure 4.36: Comparisons of the shear-wave velocity structures of the Turkish and Iranian Plateaus and groups 1, 2, 3, and 4 in southeastern Asia.

Iranian Plateaus (Cong, 1997) (Figures 4.36 and 4.37). Group 8 has lower shear velocities than do the Turkish and Iranian Plateaus for depths greater than 10 km. Group 9 (Figure 4.38) shows lower shear velocities than the Turkish and Iranian Plateaus for all depths except for a layer between depths 20 and 35 km and a layer between 60 and 90 km.

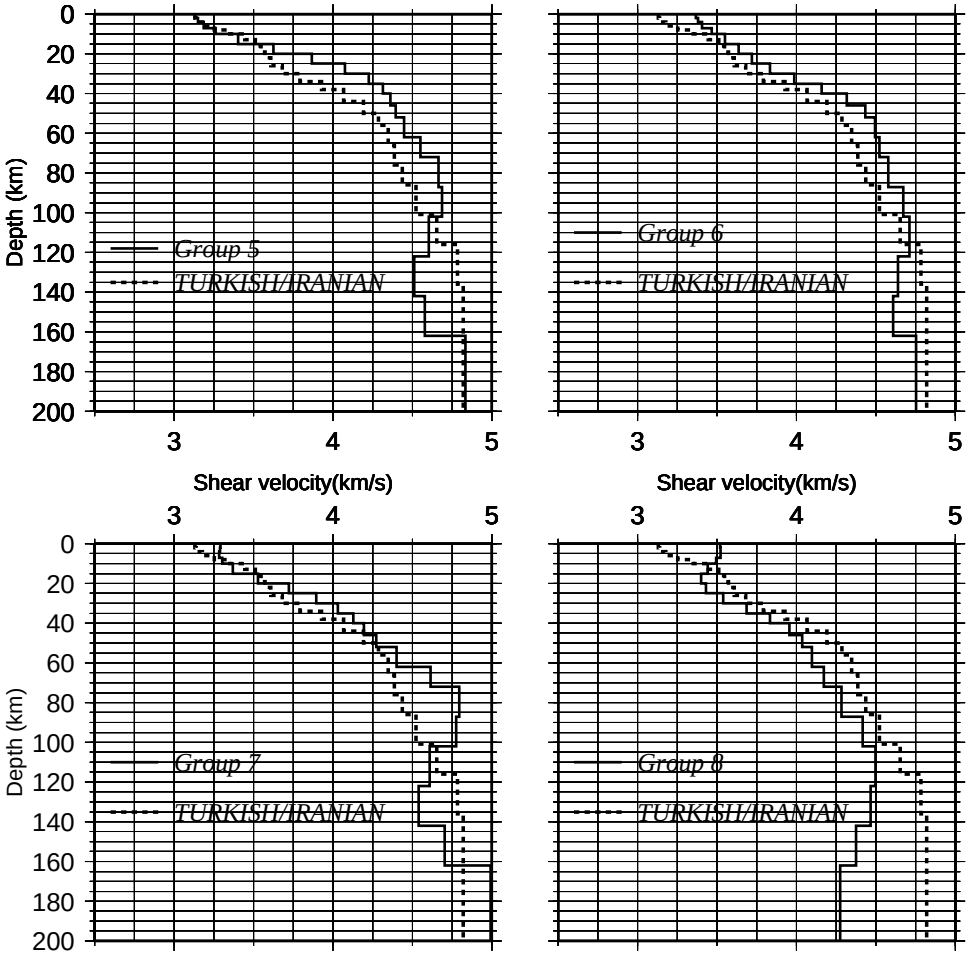

Figure 4.37: Comparisons of the shear-wave velocity structures of the Turkish and Iranian Plateaus and groups 5, 6, 7, and 8 in southeastern Asia.

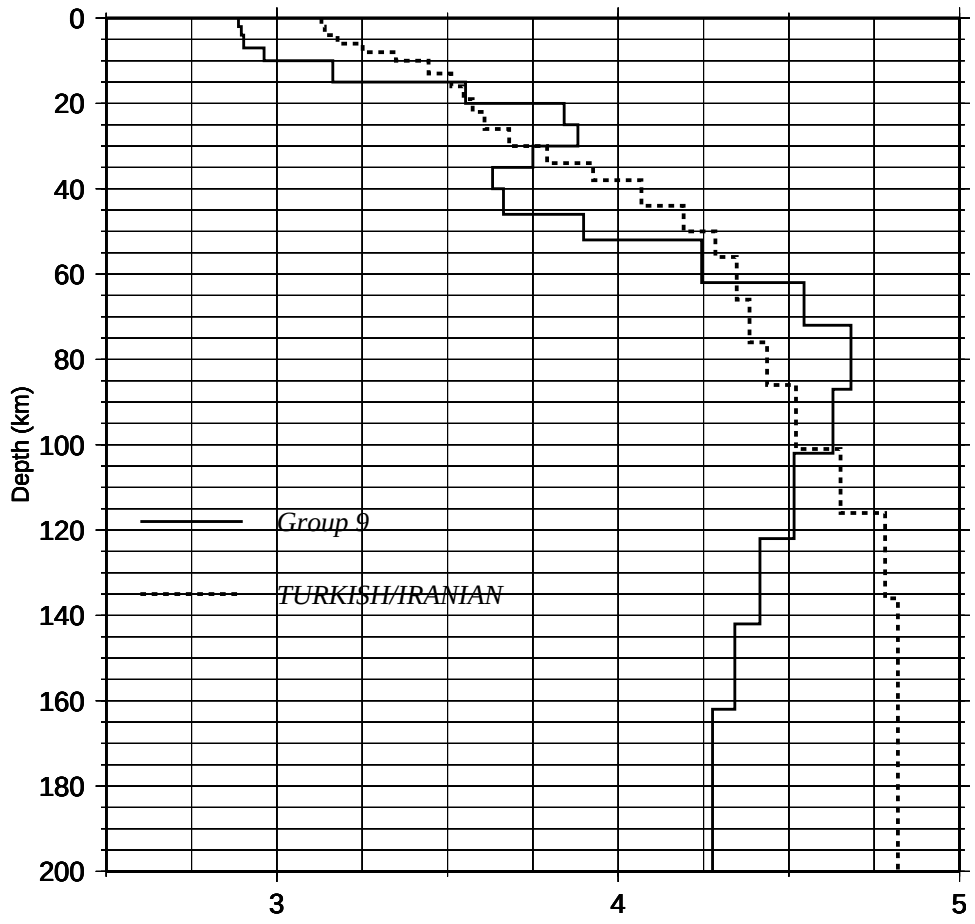

Figure 4.38: Comparisons of the shear-wave velocity structures of the Turkish and Iranian Plateaus and group 9 in southeastern Asia.

5. Shear-wave Q structure of southeastern Asia using the single-station method

5.1 DATA

A single-station method (described in Chapter 2) was used to obtain shear-wave Q structure (Q_μ) of southeastern Asia over a region that includes China, Mongolia, Siberia, Kazakhstan, Afghanistan and a small portion of Pakistan (Figure 5.1). Some of these regions were not covered using the two-station method.

A large number of earthquakes from the NOAA PDE catalogue was searched using a program that searches for specified magnitude and depth ranges, and event station distances. These earthquakes occurred between the years 1990 and 1999 within and around southeastern Asia. They were recorded by all of the digital stations in China and surrounding regions.

When performing the search I required that the earthquakes meet the following criteria:

1. The m_b magnitude must be between 4.8 and 6.5,
2. The source depth must be less than or equal to 50 km depth,
3. The event-station distance must be between 300 km and 3000 km,

These criteria were used for the same reasons discussed in the description of the two-station method.

Broadband vertical-component (BHZ) seismograms were requested from the IRIS DMC for events meeting the above criteria and which

Event										
Code	Origin date	Origin Time	d(km)	m_b	M_0	ϕ	δ	λ	EVLA	EVLO
117/90	04/27/90	05:29:28.3	33	5.2	22700	358	57	8	28.66	66.27
316/90	11/12/90	12:28:49.0	05	5.9	329000	211	65	23	42.94	78.08
108/93	04/18/93	04:55:40.0	23	5.1	6920	194	48	-143	11.96	94.97
198/93	07/17/93	09:46:34.3	27	5.4	13600	140	33	-55	28.00	99.64
275/93	10/02/93	08:42:32.8	16	6.2	164000	326	42	146	38.14	88.64
096/94	04/06/94	07:03:27.7	33	5.6	71500	96	57	26	26.19	96.84
250/94	09/07/94	13:56:25.1	33	5.1	7720	238	58	-6	38.42	90.19
258/94	09/15/94	07:07:08.6	53	5.0	7380	142	26	45	23.64	121.75
283/94	10/10/94	14:07:57.1	33	5.0	4920	327	45	109	36.04	100.15
347/94	12/13/94	00:50:52.4	33	5.0	10280	240	07	113	24.05	122.61
151/95	05/31/95	13:51:20.5	33	5.3	25300	74	05	-85	30.20	67.93
173/95	06/22/95	01:01:21.7	33	5.5	16700	97	34	97	50.33	89.92
180/95	06/29/95	23:02:31.2	33	5.6	52000	63	39	-44	51.92	103.07
305/95	11/01/95	12:29:28.7	33	5.5	8690	270	13	100	42.99	80.31
317/95	11/13/95	08:43:14.7	24	5.9	55000	56	43	-59	56.07	114.48
009/96	01/09/96	06:27:54.4	33	5.2	13500	108	23	118	43.70	85.65
005/97	01/05/97	08:47:25.4	33	5.6	24500	279	19	68	29.84	80.53
080/97	03/21/97	21:04:48.6	33	4.9	11810	35	26	-43	32.93	84.61
096/97	04/06/97	04:36:35.2	33	5.6	105100	253	43	-36	39.54	77.00
101/97	04/11/97	05:34:42.7	15	5.8	206000	240	37	-45	39.53	76.94
102/97	04/12/97	21:09:08.9	20	5.2	10620	243	48	-65	39.47	76.90
105/97	04/15/97	18:19:10.1	23	5.4	65600	170	66	-162	39.63	76.99
212/97	07/31/97	15:59:37.0	33	5.5	9060	330	16	40	23.89	93.16
221/97	08/09/97	04:48:00.7	33	5.2	7780	73	27	-90	30.29	96.98
236/97	08/24/97	13:15:21.9	33	5.3	33200	258	28	74	30.08	68.00
129/98	05/09/98	02:16:14.4	33	5.0	5990	160	32	63	20.09	121.00
149/98	05/29/98	22:49:34.1	19	5.6	10020	238	42	62	41.17	75.65
176/98	06/25/98	06:39:20.3	33	5.2	5500	262	27	129	41.55	80.14
267/98	09/24/98	18:53:40.2	33	5.5	24300	91	67	08	46.31	106.29
325/98	11/21/98	16:59:48.0	10	5.2	7410	136	18	80	49.23	89.19
070/99	03/11/99	13:18:09.3	33	5.1	5900	295	65	-9	41.13	114.66
147/99	05/27/99	16:01:22.9	10	4.9	5150	269	78	-7	55.81	110.04
251/99	09/08/99	02:38:48.5	10	4.9	5190	240	54	-162	57.43	120.16
266/99	09/23/99	12:44:34.7	33	5.3	8830	350	13	83	23.81	121.26

Table 5.1: Events used in the single-station method with hypocentral information. d is depth, M_0 is seismic moment in units of 10^{20} dyn-cm, ϕ is strike, δ is dip and λ is rake of the fault plane. EVLA and EVLO are event latitude and longitude, respectively.

were also reported in the Harvard CMT (Centroid moment catalogue). The source information provided with the Harvard CMT solutions are focal depth, fault strike, rake, dip and seismic moment.

5.2 Methodology

As explained in Chapter 2, the single-station method tries to match theoretical fundamental-mode and higher-mode spectra with that of

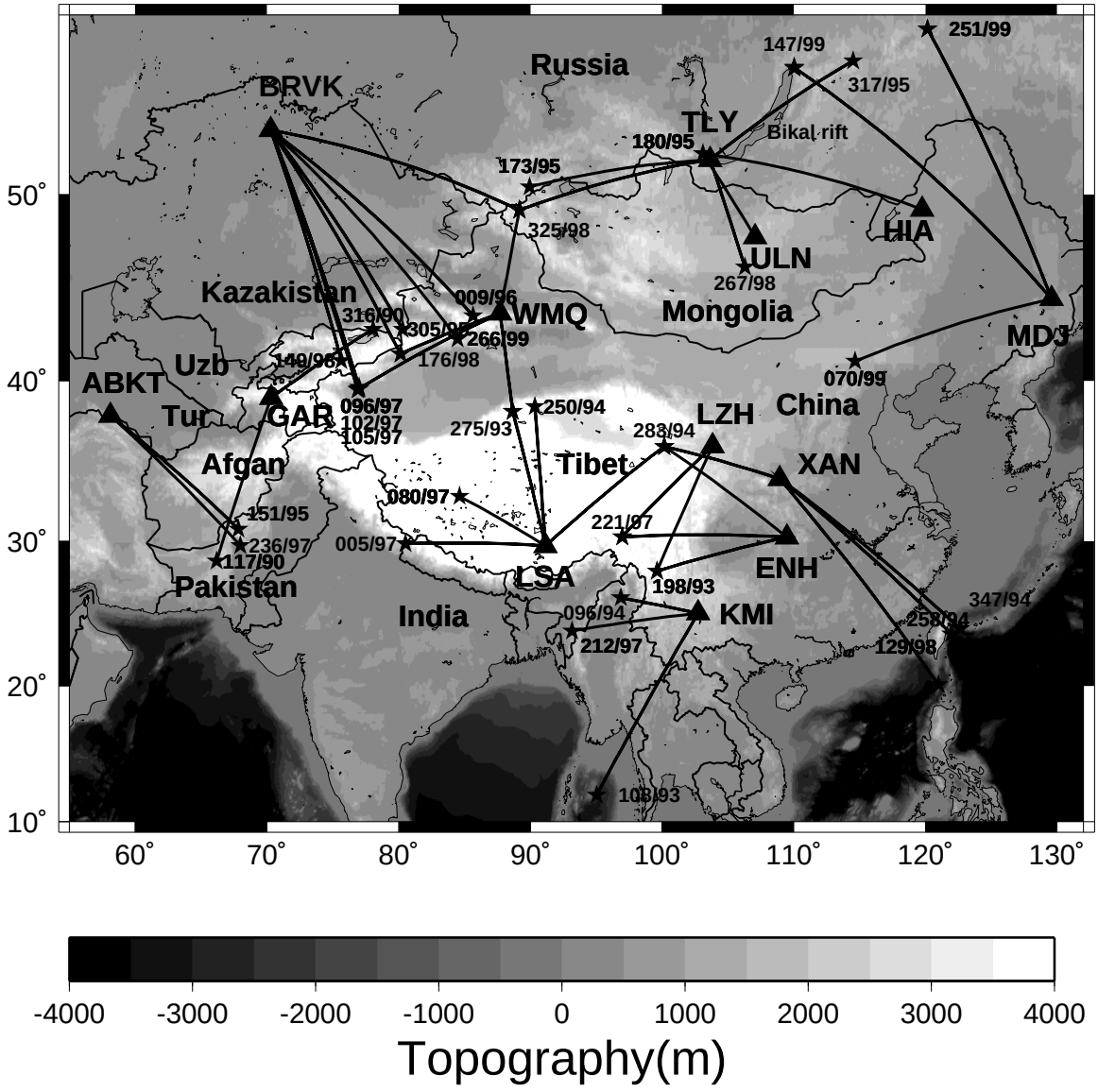

Figure 5.1: Single-station paths.

observed spectra. Theoretical fundamental-mode amplitudes and a superposition of 40 higher modes were computed from the knowledge of the earthquake source parameters, shear-velocity structure of the region, and an assumed Q_μ structure. The programs used in the computation of the theoretical spectral amplitudes are discussed in Chapter 2.

The source depth is mostly used from the USGS PDE catalogue unless it is reported as 33 km (computed using the Jeffreys - Bullen travel time curves). Whenever the reported depth from the USGS PDE catalogue is 33 km, I used the depth reported by HARVARD CMT catalogue or other agencies such as ISCCD, NOAA PDE and MHDF. The reason I use mostly from USGS PDE is that they have better hypocenter depth determination than others. HARVARD gives the depth of the Centroid.

The observed spectrum of the Rayleigh-wave fundamental mode and the superposition of higher modes are obtained by applying the multiple filter analysis (Herrmann, 1987, Vol II) to the observed vertical-component seismogram (Figures 2.1 and 2.2). A large number of events that occurred between the years 1990 and 1999 were processed to obtain very smooth spectral amplitudes, i.e., those not much affected by lateral variations of earth structure. It is, however, often difficult to obtain many smooth observed spectral amplitudes. Even if I found smooth amplitude spectra, some of them are either much lower or higher than the theoretical spectral amplitudes.

The theoretical spectral shapes of surface wave amplitudes, for the period range 10 to 50 seconds, are more sensitive to the focal depth than to the other temporal and spatial source parameters and crustal

structure (Tsai and Aki, 1970). For some events, whatever the published depth is used, it is not possible to match the theoretical spectral amplitudes to those observed. This might be due to an incorrect seismic moment reported by the Harvard CMT online catalogue or because the reported source depth is incorrect.

In some cases, to get a better fit between the observed and theoretical fundamental mode spectra, I changed the value of the seismic moment by a factor of about 2.50 (Table 5.2). I have observed that a change in the seismic moment by a factor of about 2.50 does not greatly change the value of the theoretical superposition of higher-mode spectra.

Of the many earthquakes processed, only 34 of them were used to obtain the observed fundamental- and higher-mode spectral amplitudes. Information for each event used is shown in Tables 5.1 and 5.2. The depths reported by the USGS and HARVARD, the seismic moments reported by the HARVARD CMT, and those used in the computation of theoretical spectral amplitudes for each event are shown in Table 5.2.

In the following sections, the Q_μ structure of each sub-region of southeastern Asia will be discussed. I tried to obtain as many sets of useable earthquake data as possible that cross the same geological and topographic regions. Because of the scarcity of usable data and a problem (which I do not understand) with station BJT, the north-central part of China and much of Mongolia lacks path coverage. The eastern part of China and the Tarim basin also lack good coverage. Another factor contributing to this problem might be the geological complexity of

	Depth(km)			M_0	
Event Code	USGS	HRV	This study	HRV	This study
117/90	33	15	15	22700	same
316/90	05	15	19	329000	same
108/93	23	17	23	6920	same
198/93	27	15	15	13600	same
275/93	16	15	16	164000	364000
096/94	33	15	15	71500	same
250/94	33	33	33	7720	same
258/94	53	37	37	7380	10380
283/94	33	33	06	4920	6900
347/94	33	25	36	10280	same
151/95	33	15	24∗	25300	same
173/95	33	15	15	16700	same
180/95	33	15	19	52000	89000
305/95	33	15	20†	8690	4000
317/95	24	21	24	55000	same
009/96	33	33	33	13500	same
005/97	33	15	15	24500	same
080/97	33	15	15	11810	same
096/97	33	15	15	105100	same
101/97	15	15	15	206000	same
102/97	20	16	20	10620	same
105/97	23	23	23	65600	same
212/97	33	42	08	9060	same
221/97	33	33	17	7780	13670
236/97	33	23	23	33200	83200
129/98	33	15	33	5990	same
149/98	19	32	19	10020	same
176/98	33	15	15	5500	8500
267/98	33	33	33	24300	same
325/98	10	15	10	7410	4410
070/99	33	15	23	5900	same
147/99	10	15	33	5150	same
251/99	10	20	10	5190	same
266/99	33	33	27	8830	same

Table 5.2: Depth and seismic moments in units of 10^{20} dyn-cm reported by USGS and HARVARD and those used in this study. Symbols $*$ and † mean that depths are taken from ISCCD and NOAA PDE catalogues, respectively.

southeastern Asia, which makes it difficult to find seismic recordings that are free from scattering and multi-pathing that adversely affect spectral amplitudes.

I decided upon a Q_μ Earth structure consisting of four layers for which to compute theoretical spectra. The model consists of layer 1 which is 10 km thick, layer 2 which is 20 km thick and layer 3 which is 30 km thick, overlying a uniform half space. The total thickness of 60 km for the three layers extends nearly to the largest crustal thickness in southeastern Asia. The layering is based on the fact that the thickness of surface sediments and the upper crust is not more than 10 km and the middle crust and the lower crust might be as thick as 20 km and 30km, respectively. Wherever the crust is thin as in southeastern China, where it is as small as 30 km along the coast, layer 3 should be within the upper mantle.

The shear-wave velocity models from Chapter 4 (Tables: 4.2, 4.4, 4.6, 4.8, 4.10, 4.12, 4.14, 4.16, and 4.18) were used to compute theoretical amplitude spectra. For each single station-event path in a region, the corresponding shear-wave velocity model from the two-station method, for that region, is used. For Tibet I used crustal structure model "TP-4" of Chun et al. (1977). In the following paragraphs I used a consistent code to identify each event. For example, LSA005/97 means an event recorded by station LSA on day 5 of the year 1997.

5.3 Tibet

Although, there is only one permanent station (LSA) in Tibet, it has better path coverage than most of the rest of southeastern Asia (Figure 5.1). Most of the events recorded by this station do not show higher-mode dispersion on the group velocity versus period plot (Figure 2.1). Station LZH, which is near the northeastern margin of Tibet, also shows little indication of higher-mode spectra.

The best way to get fits between observed and theoretical spectral amplitudes is to systematically vary the Q_μ values of each layer. I started with a reasonable guess of the Q_μ values for the three layers and the half space and computed synthetic spectral amplitudes for that guessed model. Then, I decreased or increased the Q_μ value of layer 1, depending on whether the fundamental-mode theoretical spectral amplitude is higher or lower, respectively, than the observed. Once I get a fit between the fundamental-mode theoretical and observed spectral amplitudes at short periods, I vary the value of Q_μ for layer 2 until I get the best fit between the theoretical and observed spectral amplitudes, for both the fundamental and higher modes. The same process is repeated for layer 3 and the half space (Figures 5.2 to 5.5).

Useful events recorded by station LSA give good azimuthal coverage for Tibet. Layer 1 in southwestern Tibet has a Q_μ value of 35 which is the lowest value in the plateau. This can be seen for the path from event LSA005/97 to station LSA (Figure 5.4). The highest Q_μ value for Layer 1 in the plateau is about 100 which occurs for the paths between events 221/97, and 198/93 and station LZH. As can be seen from Table

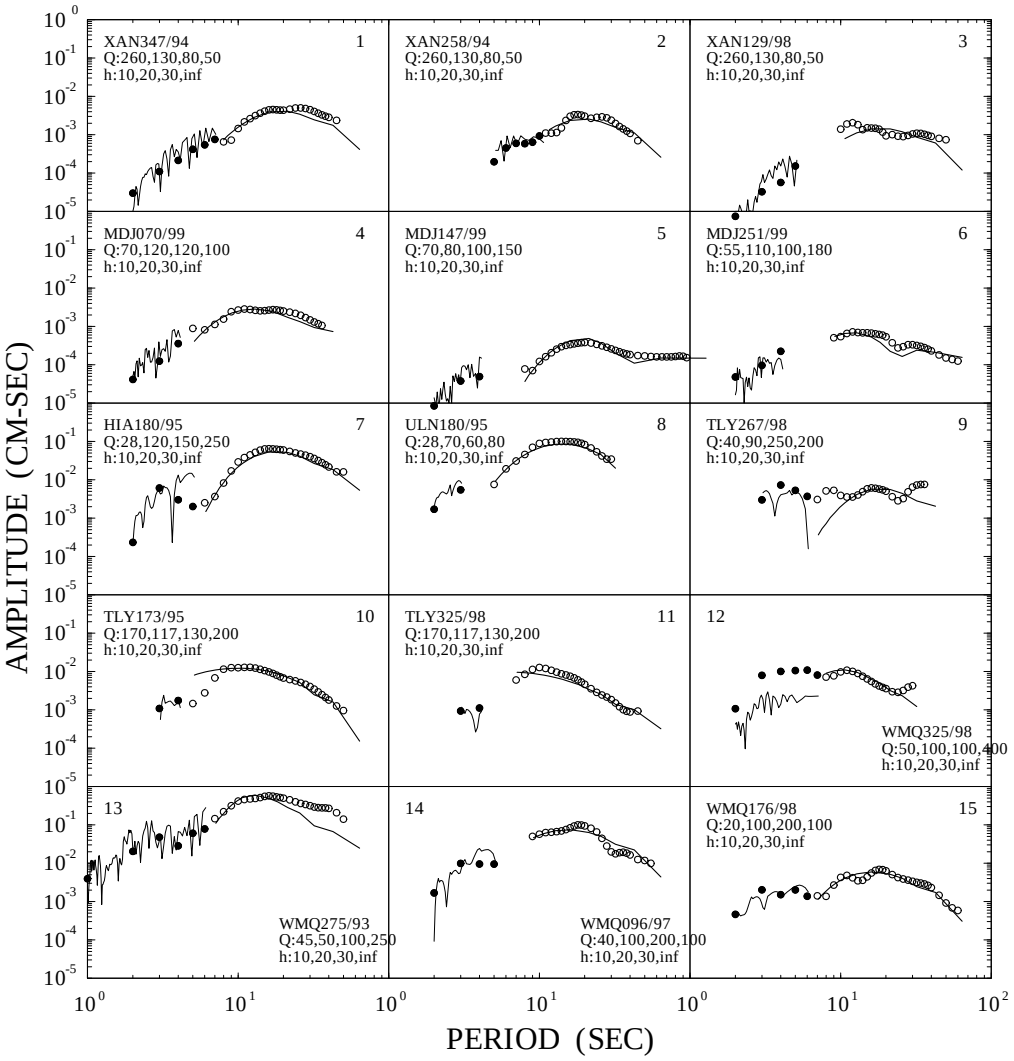

Figure 5.2: Theoretical and observed fundamental-mode and higher-mode amplitude spectra for 15 paths.

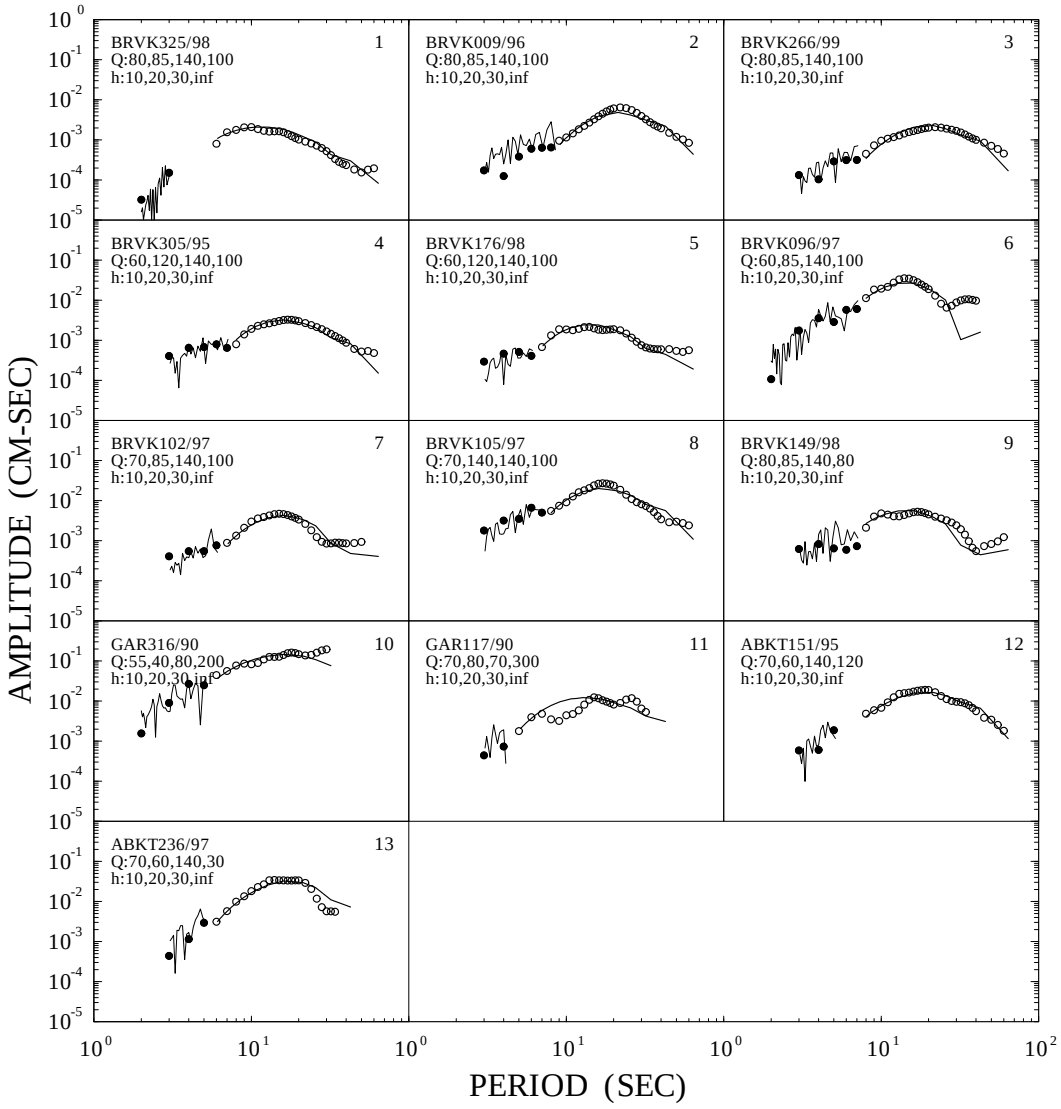

Figure 5.3: Theoretical and observed fundamental-mode and higher-mode amplitude spectra for 13 paths.

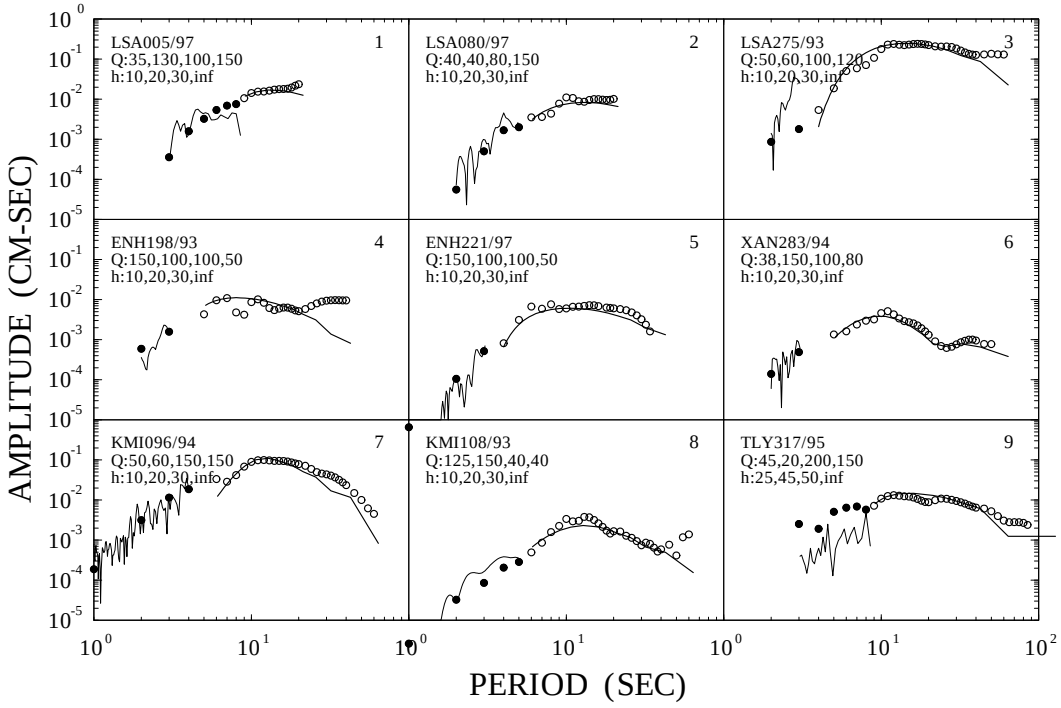

Figure 5.4: Theoretical and observed fundamental-mode and higher-mode amplitude spectra for 9 paths.

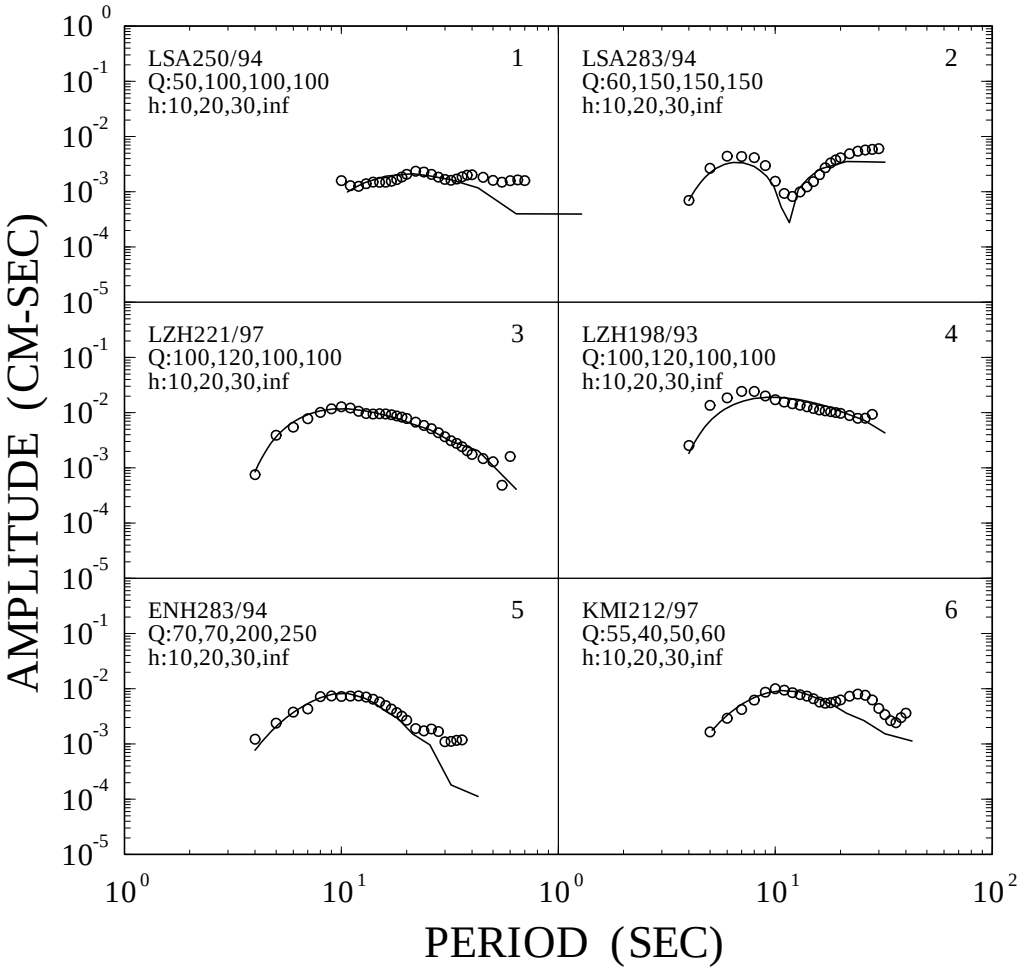

Figure 5.5: Theoretical and observed fundamental-mode amplitude spectra for 6 paths.

5.2, the seismic moments used for events 221/97 and 275/93 are greater, by factors of 1.76 and 2.22, respectively, than the ones reported by the HARVARD CMT catalogue.

The Q_μ values obtained for layer 1 for paths between events 080/97, 275/93, 250/94, and 283/94 and station LSA are 40, 50, 50 and 60, respectively. The paths between events 221/97 and 198/93 and station LZH all have the same Q_μ value of about 100 for layer 1.

The seismic moment used for event 283/94 is greater, by a factor of 1.41, than that reported by the HARVARD CMT catalogue. The observed fundamental-mode spectral amplitude shape of the signal recorded by station LSA shows that there is a hole at about 12 seconds (Figure 5.5). None of the reported depths produce a theoretical spectral amplitude that matches the observed spectra. I changed the depth several times until I obtained a theoretical spectral amplitude with a hole that matches the observed spectral amplitude. The depth for this event is found to be 6 km, a shallow event, which is much smaller than the values reported by the USGS and HARVARD (Table 5.2).

As we can see from the Q_μ values for all paths on the Tibetan plateau (Figures 5.4 and 5.5), there is a systematic increase in Q_μ for Layer 1 from the southwestern part of the plateau, where it reaches 35, to the eastern part of the plateau , where it reaches 100.

The Q_μ values of layer 2 between events 005/97, 080/97, 275/93, 250/94, and 283/94 and station LSA are 130, 40, 60, 100, and 150, respectively (Figure 5.4 and 5.5). With the exception of event 005/95, all of these show a systematic increase in Q_μ value from west to east across the Tibetan plateau. The paths between events 221/97, and 198/93 and

station LZH have the same Q_μ value of 120 (Figure 5.5) for layer 2.

The theoretical fundamental-mode spectral amplitudes, for the period range used, are much less sensitive to the values of Q_μ in layer 3 than to the values in layers 1 and 2. The higher-mode spectral amplitudes sense the Q_μ values of layer 3, but not as much as they sense layers 1 and 2. Because higher-modes sample deeper than the fundamental mode, the former is more sensitive to Q_μ values for layers 3.

The Q_μ values for layer 3 between events 005/97, 080/97, 275/93, 250/94, and 283/94 and station LSA are 100, 80, 100, 100, and 150, respectively. The paths between events 221/97 and 198/93 and station LZH all have the same Q_μ value of 100 for layer 3. These values suggest either that there is an almost constant Q_μ value for layer 3 all over the plateau or that the spectra have little sensitivity to layer 3.

Both the theoretical fundamental-mode spectra and the spectrum for higher modes are, in almost all cases, not sensitive to small variations of the Q_μ value of the half space. Because of this lack of sensitivity, a change in Q_μ values in the order of a 1000 may result in only a slight change in the spectral amplitudes of the superposition of the higher modes. For this reason the Q_μ values obtained for layer 4 will not be reported in this study. The Q_μ values of the half space for each path are shown in each panel (Figures 5.2 to 5.5).

5.4 Southeastern China

The event-station paths in this region cross part of the tectonically stable, Yangtze platform, the south China fold system, and part of east-

ern Tibet (Figures 5.1 and 1.1).

The paths between events 221/97 and 198/93 and station ENH have the same Q_μ values for all layers. Q_μ in layer 1 is 150, in layer 2 is 100, and in layer 3 is 100. These two paths cross the Yangtze platform and part of the southeastern portion of Tibet.

Paths between event 283/94 and stations ENH and XAN are within the South China Block and a small portion of the Tibetan Plateau. These paths do not sample a geologically uniform region as seen from Figures 5.1 and 1.1. The Q_μ values for these paths are different since they may pertain to geologic regions. For the path between event 283/94 and station ENH the Q_μ values for layers 1, 2 , and 3 are 70, 70, and 200, respectively (Figure 5.5). For the path between event 283/94 and station XAN, layers 1, 2, and 3, have Q_μ values of 38, 150, and 100, respectively (Figure 5.4).

The Yangtze platform and the south China fold system are crossed by paths between events 347/94, 258/94, and 129/98 and station XAN. All of these paths have the same Q_μ structure with values 260, 130 and 80, for layers 1, 2 and 3, respectively. These paths show the highest Q_μ value for layer 1 for the region of study.

5.5 Southern China and the Burma-Thailand region

The path between events 096/94, 212/97, and 108/93 and station KMI cross the southern portion of China, Thailand and Burma (Figure 5.1). The Q_μ values for paths 096/94-KMI, 212/97-KMI, and 108/93-KMI in layer 1 are 50, 55 and 125, respectively, in Layer 2 are 60, 40

and 150, respectively, and in layer 3 are 150, 50, and 40, respectively (Figures 5.4 and 5.5).

Path 096/94-KMI is almost entirely within a region of high topography while more than half of the path 212/97-KMI crosses the lowland area (Figure 5.1). The southern section of path 108/93-KMI may lie within an oceanic crust. The high Q_μ value along the path 212/97-KMI for layers 1 and 2 may be due to thin crust along most parts of the path.

5.6 Northeastern China and southeastern Siberia

The only station that records usable events in this region is MDJ. The path between event 070/99 and this station (Figure 1.1), crosses most of the northeastern China fold systems where there are Cenozoic basalts (Figure 3.21). This path (070-MDJ) has Q_μ values of 70, 120,and 120 for layers 1, 2, and 3, respectively (Figure 5.2).

The Q_μ value for Layer 1 in this region is lower than that of southeastern China. This may be due to the presence of high thermal activity where temperatures reach as high as $90mW/m^2$ in northeastern China (Zhang et al., 1998).

Paths between events 147/99 and 251/99 and station MDJ cross more than one tectonic region (Figures 5.1 and 3.21) . Because I could not find event-station pure paths that can sample a single geologic region, I processed these data so that they may give us average Q_μ values. Layer 1 has Q_μ values of 70 and 55, layer 2 has values of 80 and 110, and layer 3 has values of 100 and 100 for paths 147/99-MDJ and 251/99-MDJ, respectively (Figure 5.2).

5.7 The Baikal region and northern Mongolia

This region is crossed by paths between events 317/95 and 267/98 and station TLY, between event 180/95 and station ULN, and between event 180/95 and station HIA (Figure 5.1).

The path between event 317/95 and station TLY crosses the Baikal rift where heat flow is high (Khutorskoy and Yarmoluk, 1989). I had difficulty in fitting the theoretical and observed spectral amplitudes of the superposition of higher modes for this path. The layers' thicknesses must be different from the usual values in order to fit the fundamental mode spectral amplitudes. Layers 1, 2, and 3 needed to be 25 km, 45 km, and 50 km thick, respectively. The corresponding Q_μ values are respectively 45, 20, and 200 (Figure 5.4). The lower Q_μ values for layers 1 and 2 correlate with the high heat flow in the Baikal rift.

The path between event 180/95 and station HIA shows a Q_μ value of 28 for layer 1. The low value is consistent with the high heat flow in that region. Layers 2 and 3 have Q_μ values of 120 and 150, respectively (Figure 5.2).

The Path between event 180/95 and station ULN also exhibits a Q_μ value of 28 for layer 1. This path also crosses the high heat flow region of Baikal. Layers 2 and 3 for this path have Q_μ values of 70 and 60, respectively (Figure 5.2).

I had expected similar Q_μ values for the path between event 267/98 and station TLY and for the path between event 180/95 and station ULN. The Q_μ values for path 267/98-TLY are, however, 40, 90, and 250 for layers 1, 2, and 3, respectively. These values differ slightly from

those for the path 180/95-ULN for layers 1 and 2.

5.8 Northwestern Mongolia and southern Siberia

In this region there are only two paths between events 173/95 and 325/98 and station TLY (Figure 5.1). The largest portion of this path crosses the coldest part of the region (Khutorskoy and Yarmoluk, 1989). The Q_μ values here are consistently relatively higher than those in the Baikal region. The Q_μ values for layers 1, 2 and 3 are 170, 117, and 150, respectively, for both paths (Figure 5.2).

5.9 Western China

Event 325/98 is also recorded by station WMQ in northwestern China. The path between the event and station is entirely in the Junggar block (Figures 5.1 and 1.1). The Q_μ values for layers 1, 2, and 3 are 50, 100, and 100 respectively (Figure 5.2). The fit of the higher-mode spectral amplitudes for this path is not satisfactory. If I would increase the Q_μ values of layers 2 and 3, then the theoretical fundamental mode would be higher than the observed.

Paths between events 176/98 and 096/97 and station WMQ have similar Q_μ values for all of the layers except layer 1. Path 176/98-WMQ has Q_μ values 20, 100, and 200 for layers 1, 2 and 3, respectively. The value in layer 1 is the lowest Q_μ value in all of southeastern Asia. Path 096/97-WMQ has Q_μ values 40, 100, and 200 for layers 1, 2, and 3, respectively (Figure 5.2).

The eastern part of the Tarim basin and part of the eastern Kunulun

fold system are crossed by the path between event 275/93 and station WMQ (Figures 1.1 and 5.1). The Q_μ values for layers 1, 2 and 3 for this path are 45, 50, and 100, respectively (Figure 5.2). The low Q_μ values for layers 1 and 2 may be due to the presence of thick sediments in the Tarim basin and fluid-filled cracks in the fold systems. The seismic moment used for this event is greater than the reported value by a factor of 2.22 (Table 5.2).

5.10 Western Kazakhstan

Most events recorded by station BRVK in Kazakhstan have very smooth spectral amplitudes. Paths between events 325/98, 009/96, and 266/99 and this station all have the same Q_μ values 80, 85, and 140, for layers 1, 2, and 3, respectively (Figure 5.3). The seismic moment used for event 325/98 is lower than that reported by HARVARD by a factor of 1.68 (Table 5.2).

The Q_μ values for layers 1, 2, and 3 are 60, 120, and 140, respectively, for paths between events 305/95 and 176/98 and station BRVK (Figure 5.3). The seismic moments used for events 305/95 and 176/98 are lower than those reported by HARVARD by factors of 2.17 and 1.57, respectively (Table 5.2).

I would expect to have the same Q_μ values for paths between events 096/97, 102/97, 105/97, and 149/98 and station BRVK that are all very similar since there is little difference in the trend of paths. The Q_μ values for layers 1 and 2, however, differ slightly. The Q_μ values for path 096/97-BRVK are 60, 85, and 140; for the path 102/97-BRVK,

the values are 70, 80, and 140, for layers 1, 2, and 3, respectively. Path 105/97-BRVK has Q_μ values 70, 140, and 140, while path 149/98-BRVK has 80, 85, and 140, for layers 1, 2, and 3, respectively (Figure 5.3).

5.11 Afghanistan

I tried hard to find as many paths as possible that cross both Pakistan and Afghanistan. Unfortunately there are very few usable data that cross only Afghanistan from stations ABKT and GAR (Figure 5.1).

One event, 316/90 recorded by GAR crosses the Pamir thrust region. The Q_μ values for this path are 55, 40, and 80 for layers 1, 2, and 3, respectively (Figure 5.3).

Most of the path between event 117/90 and station GAR lies in Afghanistan where topography varies, and a very short part of this path is in Pakistan. The Q_μ values of this path are 70, 80 and 70, for layers 1, 2, and 3 respectively (Figure 5.3).

Events 151/95 and 236/97 recorded by station ABKT cross the southern central part of Afghanistan in a southeasterly direction (Figure 5.1). Both of these paths show the same Q_μ values 70, 60, and 140 for layers 1, 2, and 3, respectively (Figure 5.3). The seismic moment used for event 236/97 is higher than that reported by HARVARD by a factor of 2.51 (Table 5.2).

6. Q_μ maps

The previous chapter describes how Q_μ values for the three crustal layers were determined for each path in southeastern Asia. In order to have a clear picture of the lateral variations of the Q_μ values, I constructed a contour map of Q_μ throughout the region of study.

Although this study provides the densest coverage of fundamental-mode surface-wave attenuation that, to my knowledge, is currently available, there are still some gaps in path coverage. I looked at two ways to present the maps of Q_μ variations. The program "surface" of the GMT package (Wessel and Smith, 2001) gives very smooth contour maps, but a disadvantage of this program is that it extrapolates to regions where there are no data. The other program "triangulate" contours only the region where there is data, but the curves are very sharp at turning points, causing the contour maps to appear unrealistic. Therefore, I used "surface" and removed those portions of the contours that lay outside the study area.

The station-event map was divided into a grid of $1^0 \times 1^0$ cells so that point coordinates could be picked for each path. Corresponding Q_μ values were assigned to points and contours were drawn by "surface" connecting equal values of Q_μ. Figures 6.1, 6.2, and 6.3 show the Q_μ contour maps for layers 1, 2, and 3, respectively.

The path coverage in much of southeastern China, north-central China, parts of Mongolia, and the Tarim basin is poor (Figure 5.1). However, the Q_μ contours are interpolated to cover those parts of southeastern Asia. In the following sections, I will describe the lateral vari-

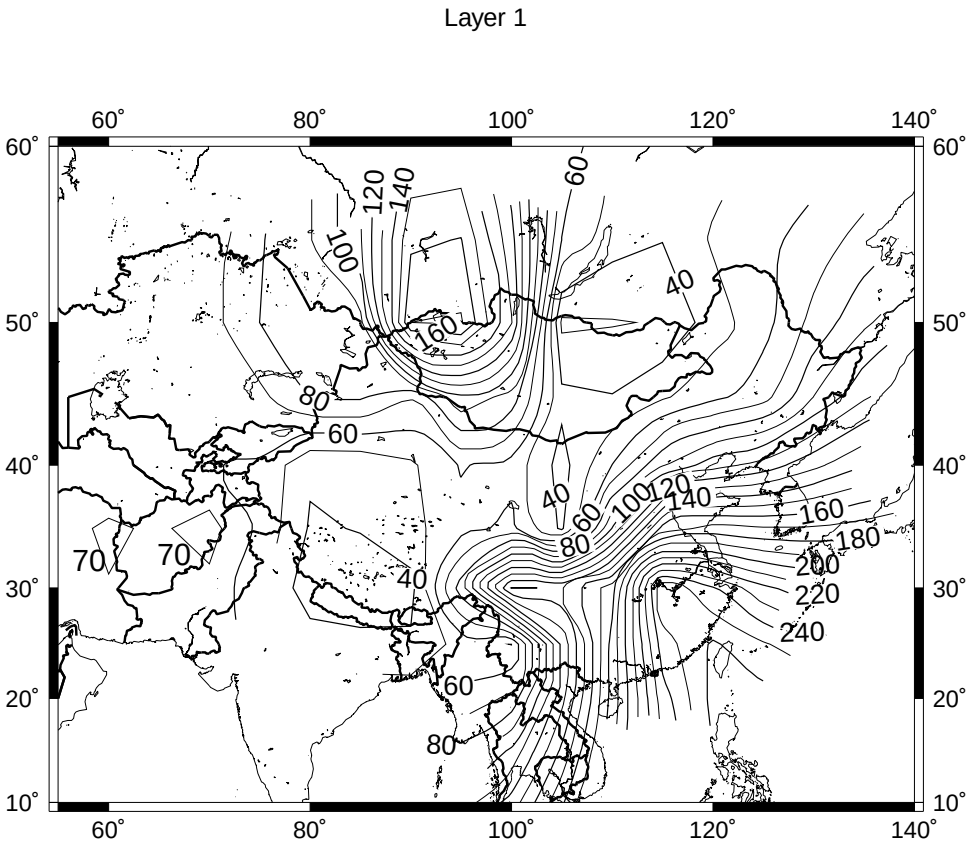

Figure 6.1: Q_μ map for layer 1.

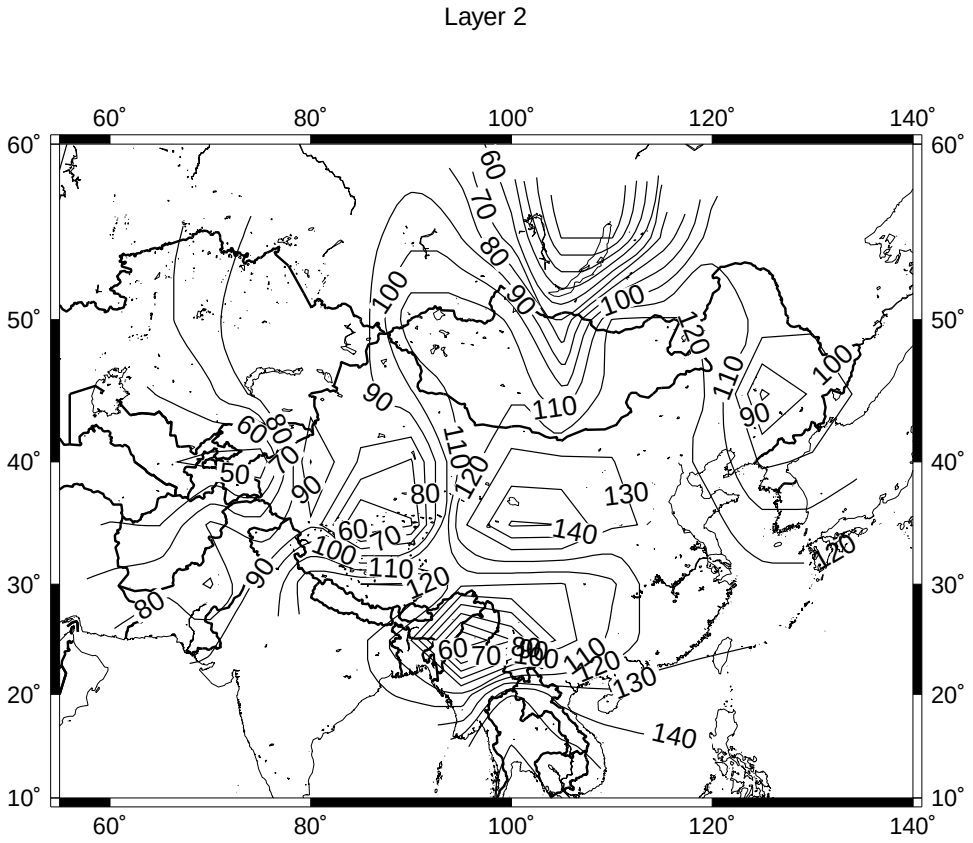

Figure 6.2: Q_μ map for layer 2.

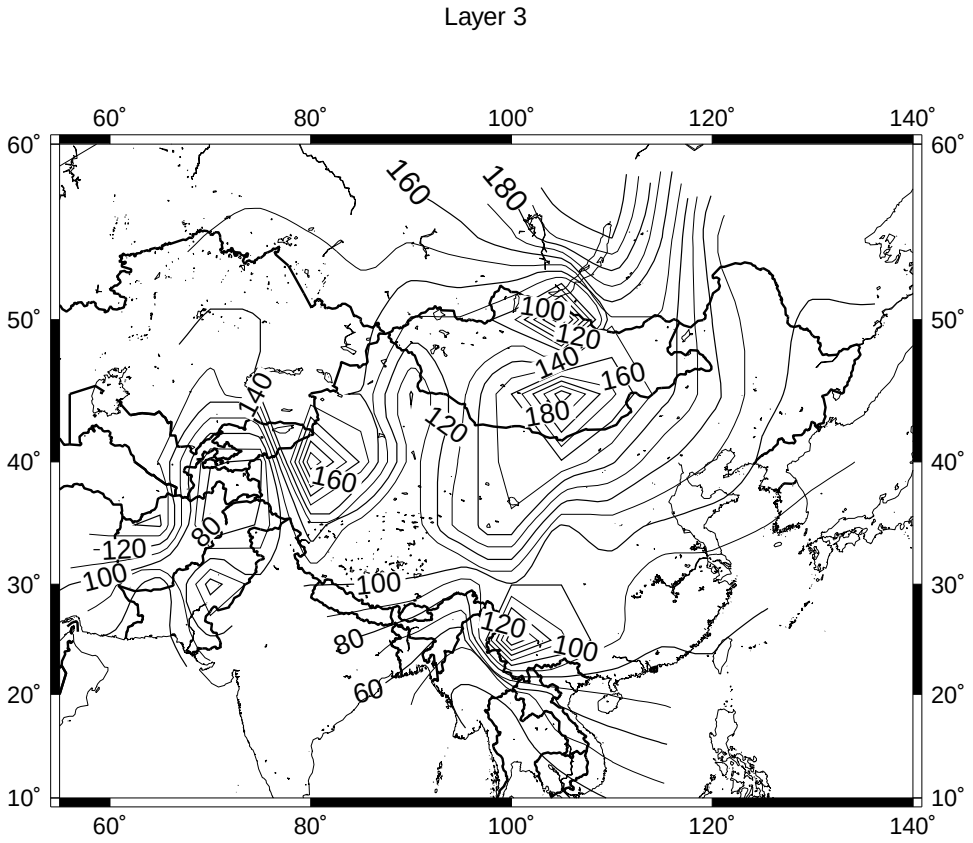

Figure 6.3: Q_μ map for layer 3.

ations of Q_μ for each layer.

6.1 Layer 1

Figure 6.1 indicates that Q_μ for layer 1 is lowest across the Tibetan plateau, the Baikal rift region and in the Sino-Korean platform (Figure 1.1). It is as small as 30 in the southern portion of the Baikal rift and 40 in southern Tibet and in the Sino-Korean platform. The low values in Tibet extend as far north as the Tarim Basin.

The South China Block shows the highest Q_μ values, about 260 near Taiwan. Western Mongolia has a relatively high Q_μ value of about 170.

There is a steep positive gradient of Q_μ as we go from the eastern part of the Tibetan plateau to the South China Block. This may correspond to a sharp decrease in crustal thickness as we go from the plateau to the lowland area in southeastern China where the crust is thinner. The Q_μ value over Burma is about 60.

The uppermost crust of northeastern China, where there are Cenozoic basalts (Figure 3.21), is defined by low (about 50) to intermediate (about 100) Q_μ values. The Jungar Basin and the Tianshan fold system, are marked by low Q_μ values in the range 60 to 90. Eastern Kazakhstan is also marked by low Q_μ values between 70 and 90.

The contour line crossing the Pamir thrust belt and Pakistan has a Q_μ value about 60. Afghanistan is marked by Q_μ values of about 70.

6.2 Layer 2

Figure 6.2 indicates the lowest Q_μ values (about 50) for layer 2 lie beneath the Tibetan Plateau, in and around the Baikal Rift, in Burma, and in the Pamir thrust belt. The highest Q_μ value, about 140, shifts from southeastern China to Central China, at or near the northeastern tip of Tibet and the Sino-Korean Platform. The Q_μ values in southeastern China (100-130) are lower than those in layer 1 (200-250). The decrease in the Q_μ values as we go deeper may be related to a shallow asthenosphere which may extend to the base of the crust due to the absence or weak presence of the lithospheric mantle (Wier, 1982). The Q_μ values in northeastern China range between 80 and 120. The low Q_μ point in this region coincides with the region of Cenozoic basalts that occur there (Figure 3.21).

The Baikal Rift region still shows low Q_μ values; however as we go to southern Mongolia, the value increases to about 120. Western Mongolia is also marked by high Q_μ values, between 100 and 120. There is a good correlation between the low heat flow in this region and values of high Q_μ. The low Q_μ values in and around the Baikal Rift coincide with the region of high heat flow while the higher Q_μ values in southern and western Mongolia coincide with the low heat flow (Figure 6.4).

The Q_μ values in eastern Kazakhstan are generally low, ranging between 70 and 90. The Tarim basin has intermediate Q_μ values between about 90 and 100. One of the lowest Q_μ points in this layer (about 50) is in the Pamir thrust belt. Those low Q_μ values extend into Afghanistan and Pakistan. In Afghanistan the values range between about 60 and

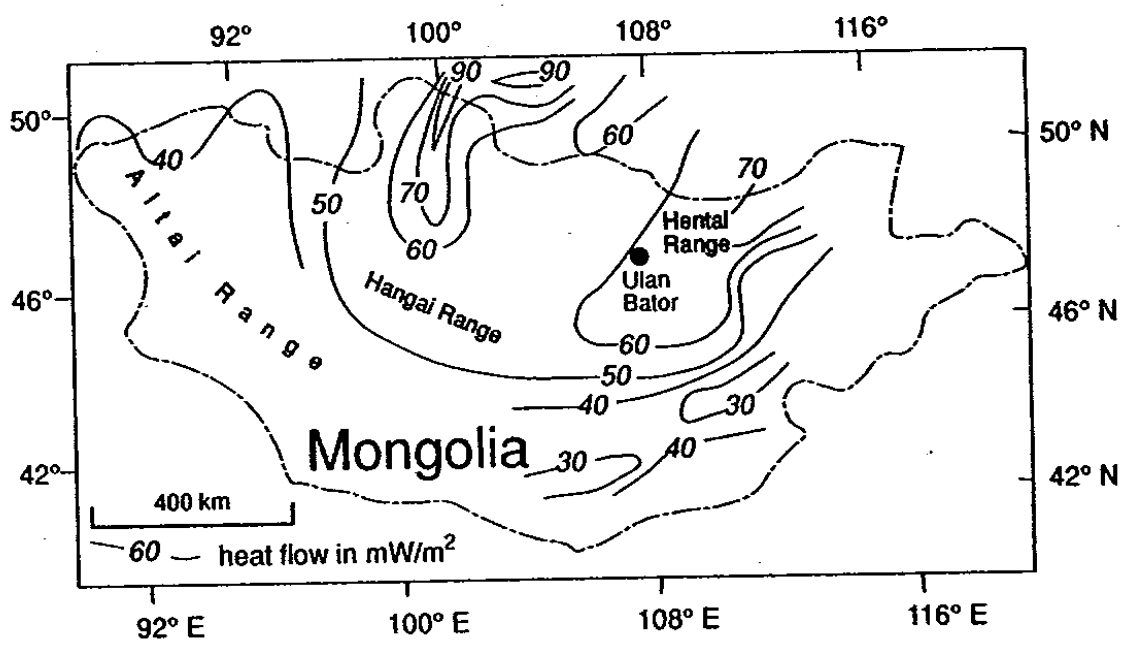

Figure 6.4: Heat Flow map of Mongolia (Khutorskoy and Yarmoluk, 1989).

80, while in Pakistan they are between about 80 and 90.

6.3 Layer 3

Figure 6.3 presents the Q_μ variations found for layer 3. Although the spectral amplitudes in that layer are less sensitive to Q_μ variations than they are for layers 1 and 2, there are some major lateral changes that appear to be related to the properties and/or processes occurring in the lower crust and uppermost mantle.

Q_μ values in southern Mongolia are as high as 180 (Figure 6.3). The next highest value (160) occurs in the Tarim basin. Q_μ values in the transition from Tibet to southern China change from about 100 to about 160 over a distance of about 1000 km. Q_μ values in southernmost

China lie between about 50 and 100, values which are lower than those in layer 2. Q_μ in northeastern China is relatively low, ranging from about 90 to 120. The low values here correlate with surface exposure of Cenozoic basalts.

The region around the southern tip of the Baikal Rift shows a low Q_μ value of about 100. This is consistent with the high heat flow values reported there. However Q_μ increases to 200 as we go northward. The Q_μ values in western Mongolia, the Jungar basin, and the Tianshan fold system range between about 100 and 140. Eastern Kazakistan shows high Q_μ values between 140 and 150. Q_μ values are lowest in the Pamir thrust region where they reach about 80. These low values extend into to northern Afghanistan and Pakistan.

6.4 Effect of attenuation on amplitudes

Knowledge of Q^{-1} is of practical importance for nuclear test monitoring for at least three reasons. First, values of Q^{-1} have a significant effect on magnitude and yield determinations of earthquakes and nuclear events. Second, in regions of high Q^{-1} (low Q); detection of small events may be difficult unless event-station distances are small. Third, different depth distributions of Q^{-1} can affect amplitude ratios of regional phases, such as P_g/L_g, in different ways, preventing them from being transportable from region to region unless they can be corrected for the effect of the variability. For these reasons, the effect of attenuation on amplitudes must be known.

I used the Q_μ models from the results of the single-station method to

predict (compute) the attenuation coefficient (γ) as a function of period for two paths between event 347/94 and station XAN (Figure 6.5), and between event 005/97 and station LSA (Figure 6.6). The amplitude decay as a function of distance is computed for periods at 10, 20, 30, and 50 sec using the function $e^{-\gamma \times x}$, where γ is the attenuation coefficient in km^{-1} units and x is the distance in km.

Figures 6.5 and 6.6 present the attenuation function ($e^{-\gamma \times x}$) as a function of distance and period for the Q_μ models determined using paths 347/94-XAN and 005/97-LSA. The purpose is to indicate the period and distance ranges over which there would be significant differences in observed amplitudes. If one considers paths with distances less than 2000 km, then spectral amplitudes with periods less than 20 sec would be significantly different. This is important to keep in mind since the inversion of small magnitude seismic events will require the use of these shorter periods.

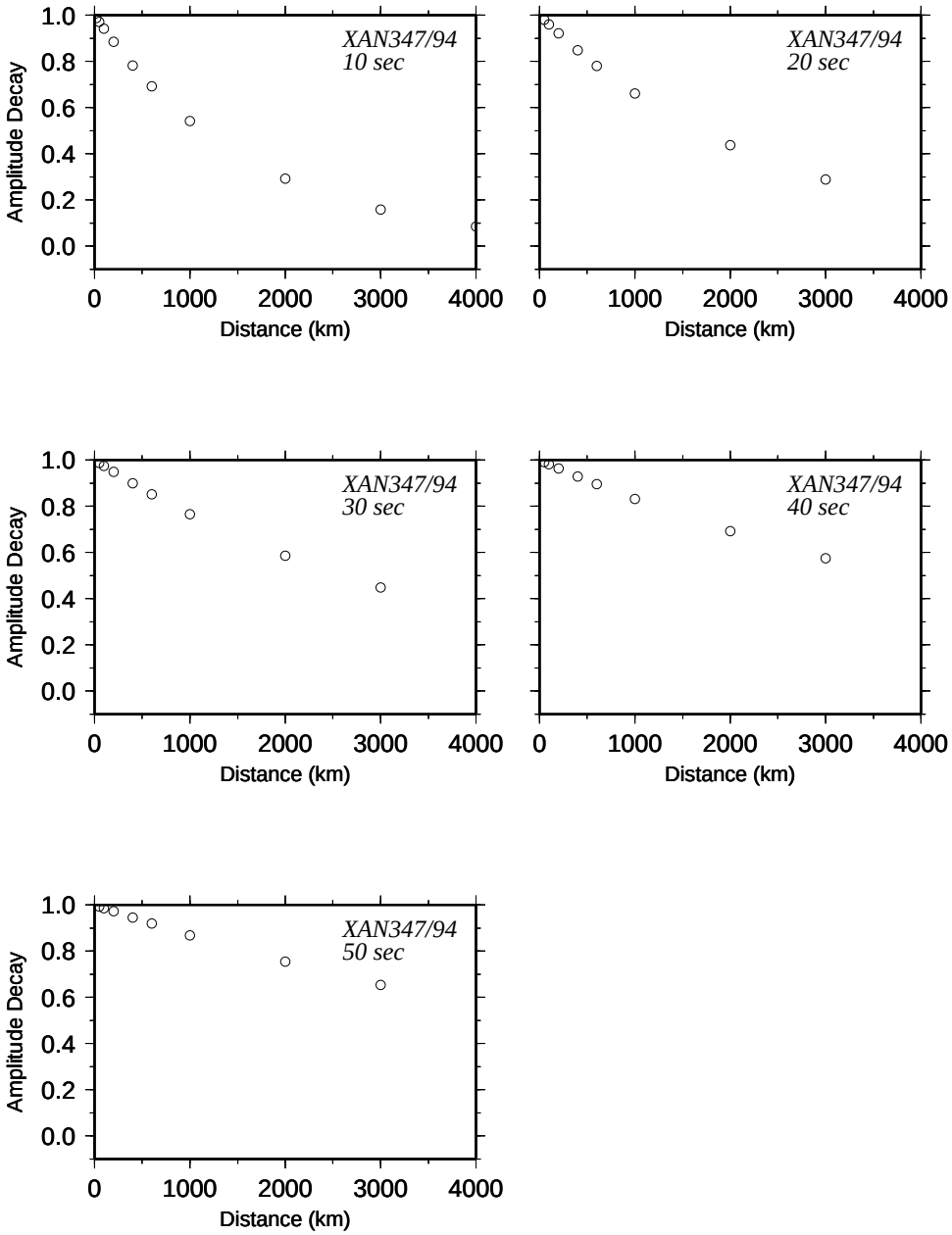

Figure 6.5: Amplitude decay for the path between event 347/94 and station XAN. The panels displayed are for periods at 10, 20, 30 ,40 and 50 sec.

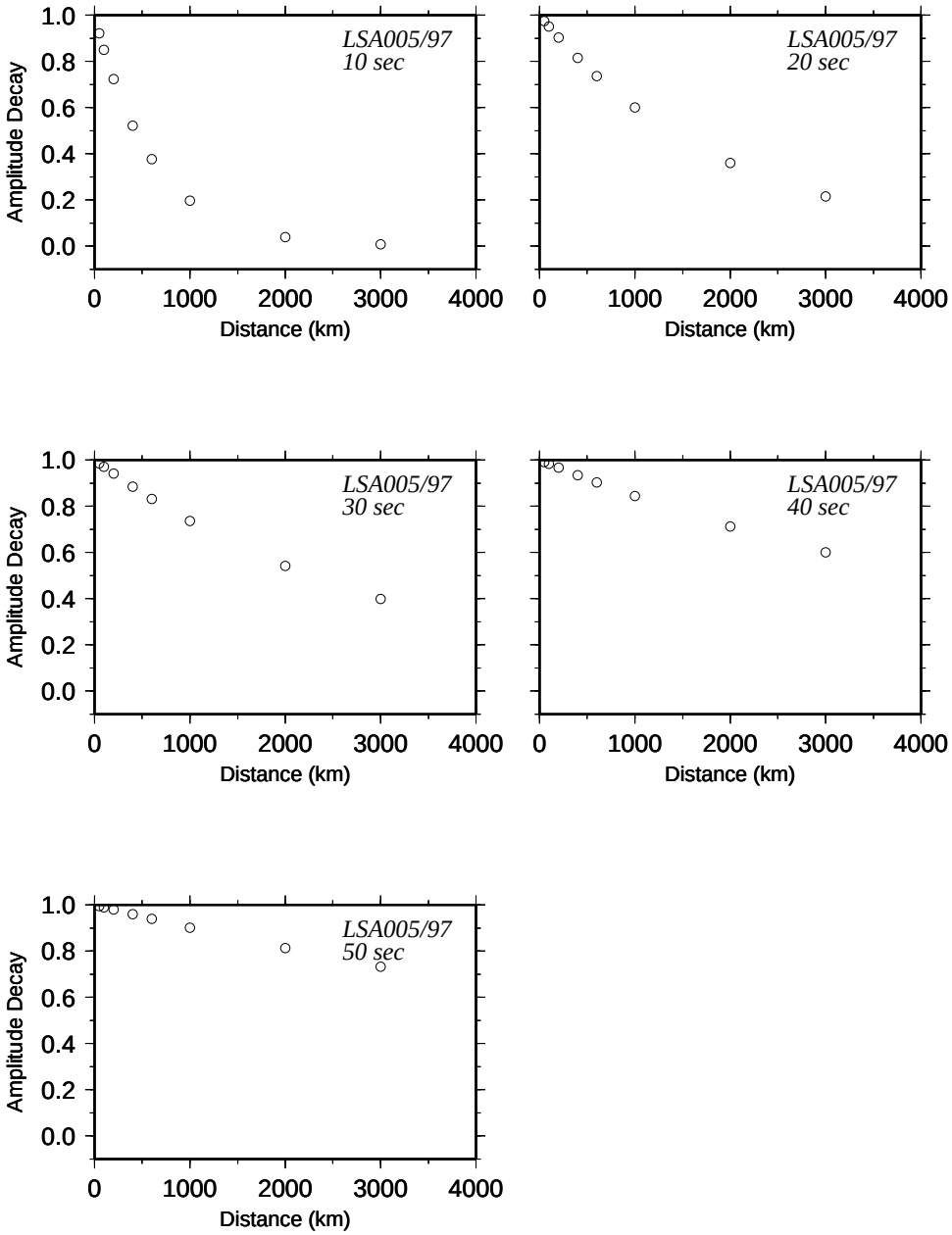

Figure 6.6: Amplitude decay for the path between event 005/97 and station LSA. The panels displayed are for periods at 10, 20, 30 ,40 and 50 sec.

7. Discussion and conclusions

In this chapter I will summarize the results obtained in the two-station and single-station methods and discuss them in relation with the tectonics of southeastern Asia. I will also compare the results of the two methods and discuss the similarities between some of the results obtained using the two methods for the same geological region. The possible causes of differences between the results obtained for the same geologic region using the two methods are also discussed.

7.1 Discussion on the results of the two-station method

Toksöz and Anderson (1966) noted that shield areas have relatively high average group velocities, whereas active tectonic regions have relatively low group velocities. As a result, surface wave paths crossing different tectonic regions should show different trends in their average group velocity dispersion curves. Based on this fact, I divided southeastern Asia into different tectonic regions (groups) in the two-station method. The average interstation group velocities for the nine groups so formed were discussed in Chapter 3.

Lower than average group velocities may be due to relatively low shear velocities in the crust and/or thicker than average crust. Rayleigh waves that are trapped in the crust will have lower group velocities than those that penetrate into the mantle (Wu and Levshin, 1994). Thick sediments have also the effect of lowering group and phase velocities (Levshin and Ritzwoller, 1995).

Southeastern Asia is diverse in its geological and tectonic struc-

tures. Surface relief is as great as 6 km in some places. Sedimentary thicknesses range from about zero near the Baikal Rift (near station TLY) to more than 15 km in the eastern part of the Tarim Basin (Levshin and Ritzwoller, 1995). Crustal thickness ranges form about 36 km in southeastern China to 70 km in Tibet. Seismicity is more intense in the western portion of the study area than in the east. Active fold belts are more common in the west than the east. Heat flow varies from place to place but shows no systematic east-west or north-south pattern. These differences in geology and tectonics give rise to differences in group and phase velocities between the different groups in southeastern Asia.

Western China is more tectonically active than eastern China as indicated by seismicity and the presence of active folds. This difference is also shown in the group velocities, that is, western China has lower group velocities than eastern China.

Comparisons between average group velocities of group 2 (South China Block) and Wier's (1982) "6-ANP" group velocities for southeastern China shows that the two agree very well at periods where both results are available. For periods between 15 and 35 sec group velocities of group 2 agree well with those of Pines (1980) for the path from Tangshan to Taipei.

For periods shorter than 50 sec, all phase velocities determined for southeastern Asia are lower than those of the Canadian Shield. Those low phase velocities may be related to the higher tectonic activity there as indicated by the presence of active folds, seismicity, and volcanics, present in southeastern Asia than the Canadian Shield.

There is not much difference between the attenuation coefficients of all groups, except group 3, at all periods. The attenuation coefficients of some groups are not consistent with the expected relationship with the group or phase velocities. This inconsistency may be due to effects of lateral heterogeneity which focus or defocus seismic waves.

To invert the interstation attenuation data for Q_μ structure, we need to know the shear-velocity structure of the region that we deal with. Shear-velocity structures are obtained by inverting the interstation phase velocities of each group. Interstation group velocities are not used to invert for shear-velocity structure because of much greater scatter in my group velocity determinations than in my phase velocity determinations and because of the additional non-uniqueness of the solutions discussed in Pilant and Knopoff (1970).

The location of the Moho, in most cases, is not difficult to identify. Most of the Moho depths identified in this study are in good agreement with those of Ren et al. (1987). To identify some features present in the shear-velocity structures and to give them geological interpretation, I compare each shear-velocity structure with the generalized petreological model and P-wave velocity-depth profile for continental crust of Mueller (1977).

There are differences in shear-velocity structures between the different groups, especially between groups for western and eastern China. The tectonically active region of western China and the western part of the Mongolia plateau have lower shear velocities at least for the depth ranges between 15 km and 70km, when compared with eastern China and southeastern Siberia. However there is a depth range in group

9 between 20 km and 35 km where velocities are exceptionally high. My results give no indication of a systematic variation (increase or decrease) in shear-velocity structure in south-north direction in either eastern or western China.

The shear-velocity structure of group 2 agree with model ZH1 of Wier (1982) (the shear-velocity structure of Southeastern China) for depths greater than 10 km but differs from that model for greater depths. There is a good agreement between model ZH1 and group 3 for depths between 5 and 70 km.

The tectonically stable Candian shield shows higher shear velocities at almost all depths than those obtained for any of the groups in southeastern Asia. The shear velocities for models obtained for eastern China (groups 1-6) and southern Siberia (group 7), however are higher than those found in the Turkish and Iranian Plateaus (Cong, 1997) for the upper 80-100 km. Shear velocities for the models for western Mongolia and western China (groups 8 and 9) are lower than those for the Turkish and Iranian Plateaus at most depths.

The Q_μ^{-1} structures for groups 2 and 3 in southeastern China correlate positively with the shear-wave velocity structures for depths greater than about 35 km. That is, as shear velocity increases for depths greater than 35 km and Q_μ^{-1} also increase. This correlation is probably not due to multipathing effects on spectral amplitudes since that region is relatively uniform. The weak or absent upper mantle lithosphere in that region may explain the high Q_μ^{-1} (or low Q_μ) values below 35 km and is consistent with high temperature spring that occur in that region.

Low Q_μ (high Q_μ^{-1}) values at greater depths (greater than 50 km) exist in the North China craton (group 4) and in northeastern China (groups 5). The low Q_μ values for depths greater than 50 km may be associated with extensional tectonics, high heat flow, and thin lithosphere found in that region. High thermal activity at depth may be responsible for the low Q_μ values for depths greater than 50 km in northeastern China.

Low Q_μ in the upper crustal layers (as in group 9) may be explained by the possible presence of fluid-filled fractures. The existence of fluid-filled fractures make Q_μ low, as seismic energy goes into moving fluids through interconnected fractures (Mitchell, 1995). A rapid increase in Q_μ values observed at mid-crustal depths for this region is similar to what is observed in the central and western United states (Mitchell, 1995).

Seismic waves can be focused as they cross continent-oceanic margin. This may be the reason for the very high Q_μ values for the upper 10 km of group 7. The Q_μ values of that group for the upper 10 km is not likely to be as high as that shown in the Q_μ structure of group 7, because that region is characterized by very high heat flow and active tectonics. The low Q_μ values in western China (group 9) at shallower depths is consistent with the active tectonics in western China and presence of sediments in the Tarim basin.

For both shear velocity and Q_μ structure, the resolution kernels become broader as the depth increases because the long wavelengths which penetrate to those depths sample large depth intervals. As a result, it is more difficult to resolve features of the models at greater

depths than at shallower depths.

Using the two-station method, it is very hard to avoid effects of lateral heterogeneities on spectral amplitudes for a geologically complex region like southeastern Asia. This problem gives rise to some unrealistic results, for example, group 1 has higher Q_μ values at all depths than those found for all other groups, except group 7. This is not likely to be correct since the region crossed by group 1 is tectonically more active than many of the other regions. The seimic waves recorded by stations used in group 1 are probably focused as they travel through different geological structures to the second recording station. For shallow depths western China has lower Q_μ values compared to eastern China. It is difficult to see north-south systematic variations in Q_μ values which may be masked by multipathing effects on seismic waves.

7.2 Discussion on the results of the single-station method

I have used a single-station method to determine the variation of Q_μ in the crust throughout much of southern Asia. Because of restricted path coverage, it is difficult to obtain detailed sampling for some regions, such as the Sino-Korean platform or the Qilian fold system in western China. This single-station method was developed earlier and used for limited studies in the United States (Cheng and Mitchell, 1981) and the Middle East (Cong and Mitchell, 1998).

The fit of the spectra, in most cases, is good between about 5 and 50 seconds for the fundamental mode and between about 3 and 8 seconds for the higher modes. There are some cases, however, when higher-

mode energy is not well recorded. In some cases this is probably because paths include a short oceanic segment of oceanic crust (where higher modes do propagate well at short periods). In others, it may be because severe lateral changes crustal structure disrupt the propagation of higher modes. In those cases, I use only the fundamental mode in our inversion process.

The map of Q_μ variation in layer 1 shows that southeastern China has the highest Q value (about 250). Southeastern China is tectonically stable as indicated by the small number of earthquakes that occur there.

Northeastern Mongolia and the tectonically stable Siberian craton are also characterized by relatively high Q values (about 160). The Baikal Rift and surrounding regions have the lowest Q values (about 40). This region also is marked by high heat flow.

Low Q values also characterize the Tibetan Plateau, the north-central China fold systems, and the Tarim Basin. The first two of these are tectonically active regions where Q may be influenced by interstitial fluids that occur in faults, and fractures and permeable deformed rock. The Tarim Basin includes a thick accumulation of sediments that may be responsible for the low Q values there. Layer 1, beneath Kazakhstan, Afghanistan and Pakistan is everywhere marked by moderately low Q_μ values (about 70).

The Q_μ map for layer 2 indicates that the highest Q values (about 150) lie in the central part of the China, in the Sino-Korean platform and in the Baikal Rift region. The lowest Q values (about 50) occur in Tibet and the Pamir fold belt. The map shows an overall increase in Q_μ

going from south to north.

The resolution achieveable for layer 3 is poorer than for either layer 1 or layer 2. My results, however, show that Q is highest (about 180) beneath the Tarim Basin and in south-central Mongolia and lowest (about 80) in the Pamir fold belt.

7.2.1 Effect of Shear-velocity model on Q_μ model

Two very different shear-velocity models (Figure 7.1) from two different tectonic regions are used to compute a Q_μ model for one of the regions using the single-stations method.

I use the shear-velocity structure of group 8, which crosses western Mongolia and the Jungar block, to obtain a Q_μ model for southeastern China (Figure 7.2). Comparison of the Q_μ models for southeastern China obtained using shear-velocity models of groups 2 and 8 shows very little dependence of Q_μ on shear-velocity structure.

7.2.2 Effect of depth on Q_μ model

Figure 7.3 is used to demonstrate the effect of earthquake source depth on spectral amplitude and hence on Q_μ determinations. The theoretical spectral amplitudes for the five panels shown are computed using the same Q_μ values for all layers but different source depths: 10 km, 15 km, 20km, 21km, 25km, and 30km for panels 1, 2, 3, 4, 5, and 6, respectively.

The source depth reported by NOAA PDE is 20km (panel 3), a departure from this value by 1km does not affect the shape of the theoretical spectral amplitudes, as shown in panel 4. But a deviation of

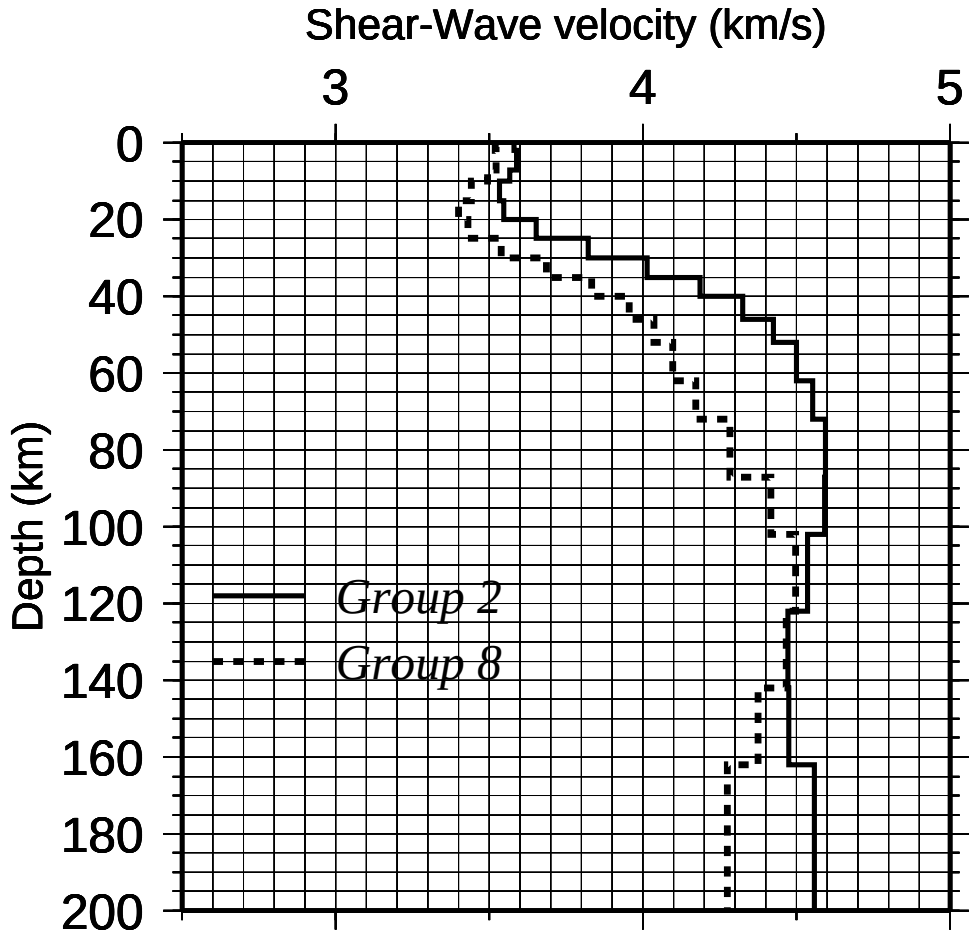

Figure 7.1: Shear-wave velocity structures for groups 2 and 8.

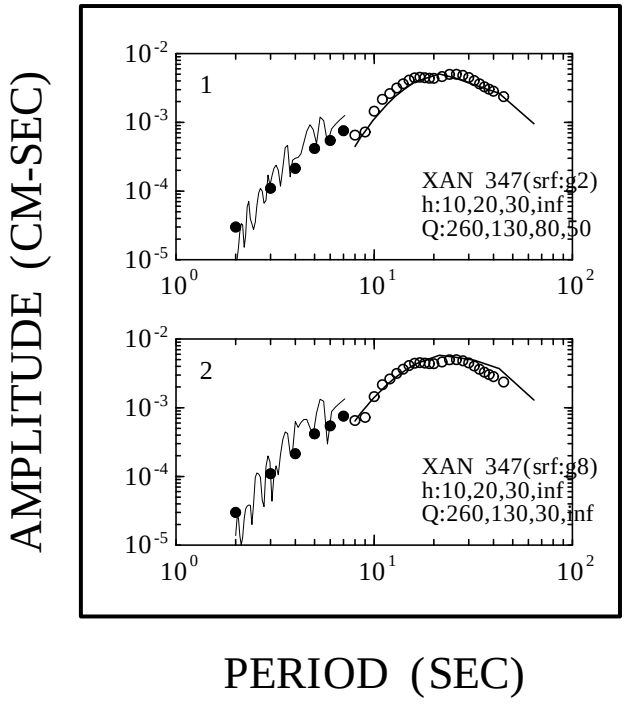

Figure 7.2: Q_μ models obtained by using different shear-wave velocity structures. srfg2 and srfg8 denote shear-wave velocity structures of groups 2 and 8, respectively, and are used to compute the theoretical spectral amplitudes for panals 1 and 2.

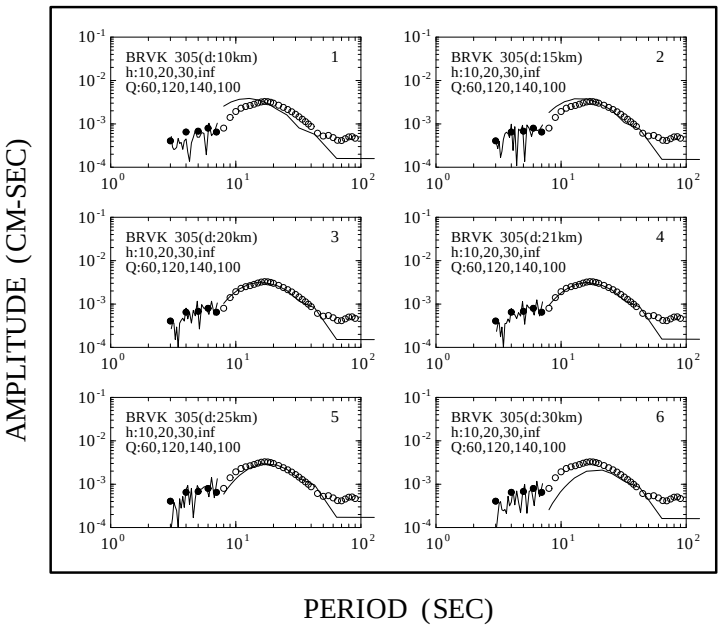

Figure 7.3: Q_μ models obtained using different source depths: 10 km, 15 km, 20 km, 21 km, 25 km, and 30 km, for panales, 1, 2, 3, 4, 5, and 6, respectively. The reported depth from NOAA PDE is 20 km.

$\pm 5km$ slightly affects the shape of the theoretical spectral amplitudes as shown in panels 2 and 5. A change in depth of $\pm 10km$ (panels 1 and 6) significantly affects the shape of the theoretical amplitude spectra.

7.2.3 How well is Q_μ at depths greater than 20 km determined?

To see how sensitive are the theoretical amplitude spectra to Q_μ values of the three layers, I varied the Q_μ values in steps of 10%.

Layer 1

For layer 1 (Figure 7.4), an increase or decrease in Q_μ value by 10% changes shape of the fundamental-mode amplitude spectra only slightly when Q_μ is about 60. Increasing Q_μ value by more than 10% slightly raises up the fundamental-mode amplitude spectra at short periods. But increasing Q_μ by more than 40% does not raise the fundamental-mode spectral amplitude more unless I increase it to larger values (panel 6). The superposition of higher-modes spectral amplitude is sensitive to only very large increases in Q_μ value (panal 6).

Decrease in Q_μ affects both the fundamental- and higher-mode spectral amplitudes much more than increase in Q_μ values. As can be seen from figure 7.5, a decrease in Q_μ by 30-40 $\%$ lowers both the short period fundamental-mode and higher-mode spectral amplitudes. A decrease in Q_μ from 60 to 10 lowers very much both the fundamental- and higher-mode spectral amplitudes.

Layer 2

An increase in Q_μ values for layer 2 (Figure 7.6) by 10-30 $\%$ does not raise much both the fundamental- and higher-more spectral ampli-

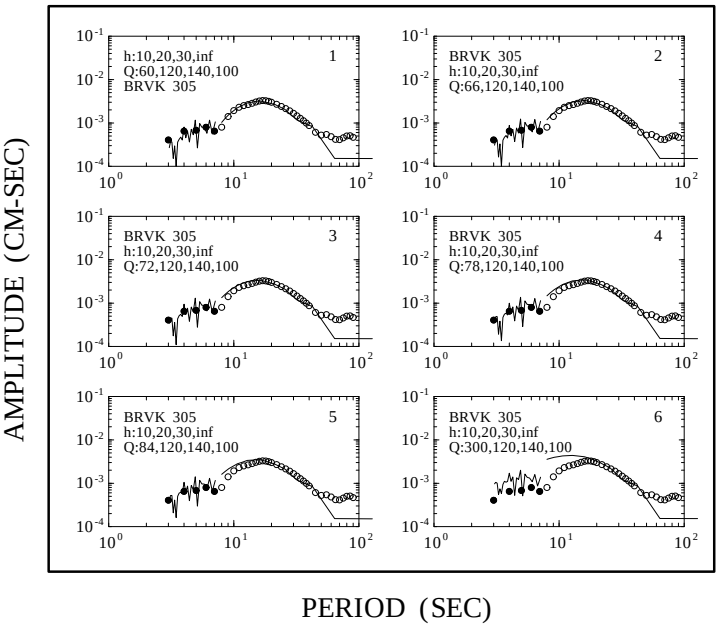

Figure 7.4: Effect of increasing Q_μ values of layer 1 on the amplitude spetra.

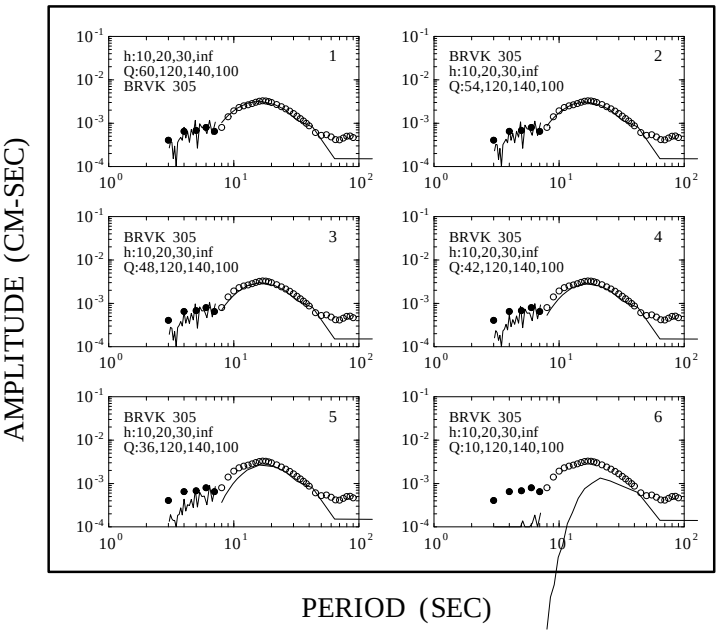

Figure 7.5: Effect of decreasing Q_μ values of layer 1 on the amplitude spetra.

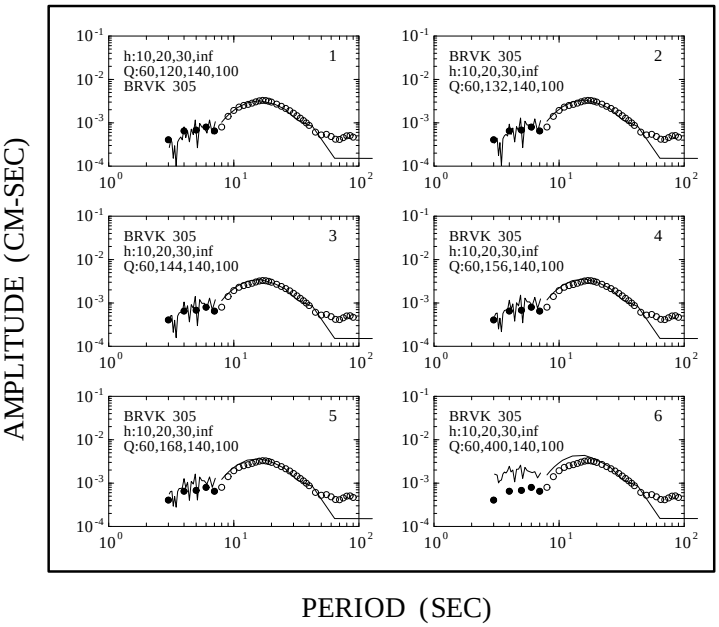

Figure 7.6: Effect of increasing Q_μ values of layer 2 on the amplitude spetra.

tudes. The higher-mode spectral amplitude becomes more sensitive to increase in Q_μ values by more than 30 $\%$. An increase in Q_μ value form 120 to 400 (about 300 $\%$) raises very high both the fundamental- and higher-mode spectral amplitudes, especially the later.

A decrease in Q_μ values (Figure 7.7) affects the higher-mode spectral amplitudes more than an increase in Q_μ values. A decrease in Q_μ value by 20 $\%$ and more lowers the higher-mode spectral amplitude very much. The fundamental-mode spectral amplitude becomes lower when Q_μ decreases by 40$\%$ and more. When Q_μ decreases from 120 to 10, both the fundamental- mode and the higher-mode spectral amplitudes become extremely low.

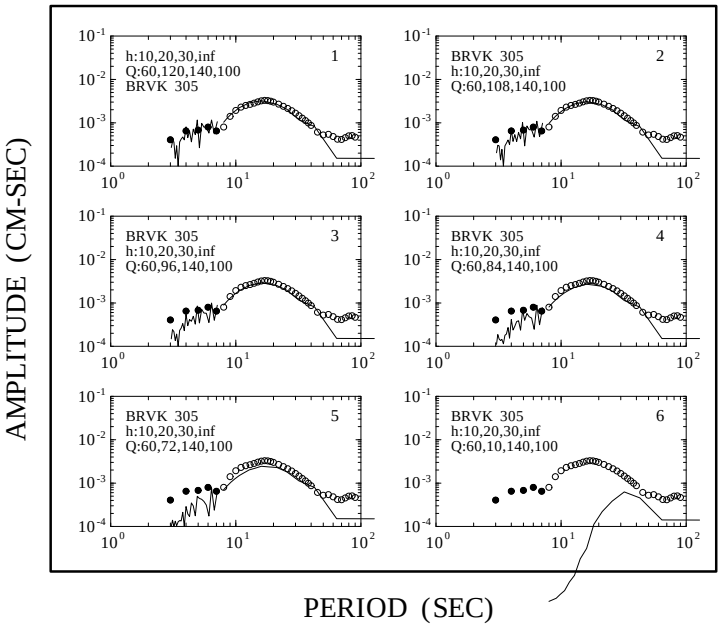

Figure 7.7: Effect of decreasing Q_μ values of layer 2 on the amplitude spetra.

Layer 3

Neither the fundamental- nor higher-mode spectral amplitudes seem are very sensitive to increases in Q_μ values for layer 3 (Figure 7.8). I increased Q_μ from 140 to 8000, but we cannot see significant changes in either the fundamental- nor higher-mode spectral amplitudes.

I do not see any significant effect on either the fundamental- nor higher-mode spectral amplitudes when the Q_μ values is decreased by a factor of 10-40 $\%$. However, decreasing Q_μ from 140 to 10 significantly lowers the long period fundamental-mode and the higher-mode spectral amplitudes (Figure 7.9).

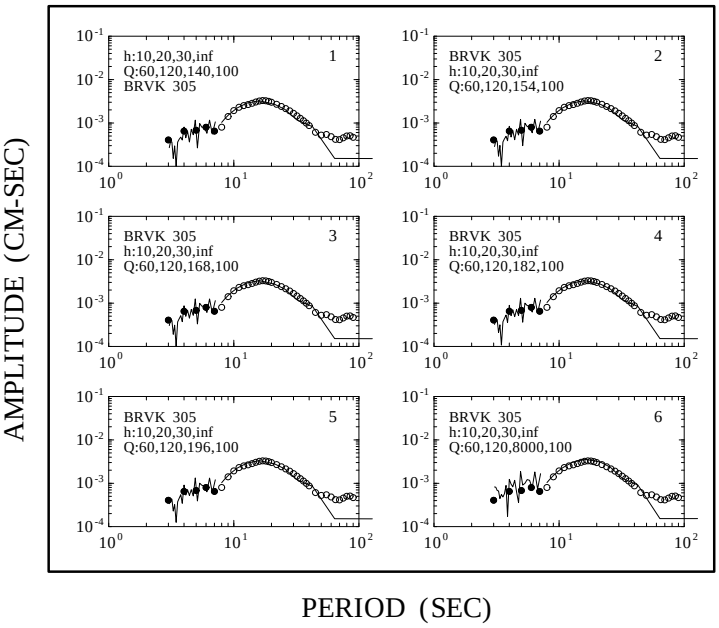

Figure 7.8: Effect of increasing Q_μ values of layer 3 on the amplitude spetra.

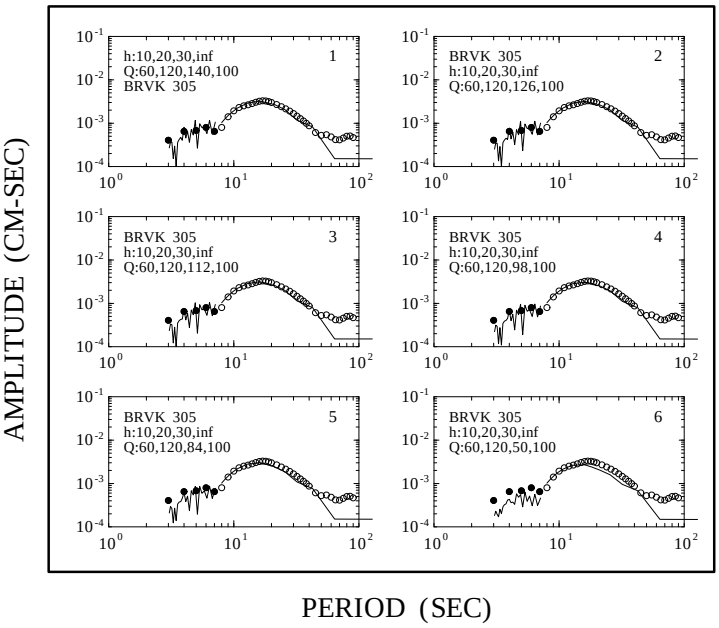

Figure 7.9: Effect of decreasing Q_μ values of layer 3 on the amplitude spetra.

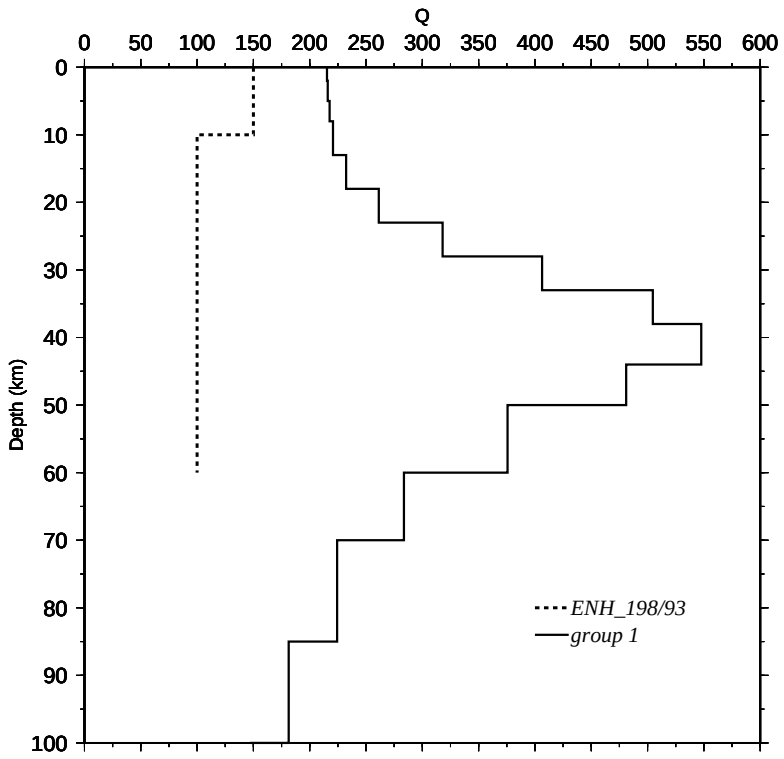

Figure 7.10: Comparison of the Q_μ models obtained from the two-station (group 1) and single-station (ENH198/93) methods.

7.2.4 Comparison of Q_μ structures obtained from the two-station and the single-station method where both models are available

I make comparisons between Q_μ models obtained from the two-station and single-station method where both models are available. The single-station models are coded with station name followed by day and year of occurrence of the event, for example, ENH198/93. The two-station models are coded with their group name, for example, group 1.

Comparison between ENH198/93 (Q_μ model from single-station method) and group 1 (Q_μ model from two-station method) shows that the two models are quit different at all depths (Figure 7.10). This differ-

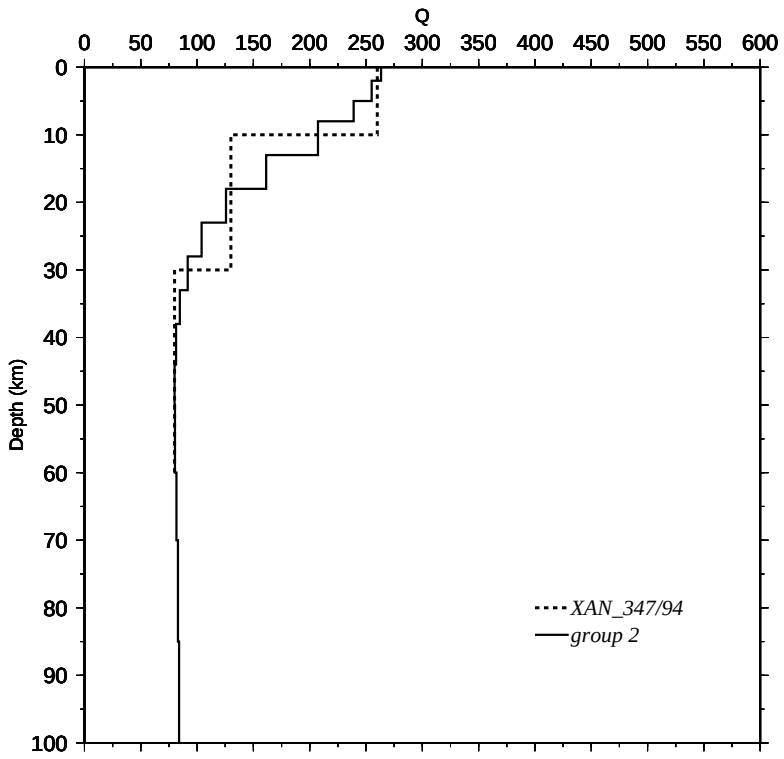

Figure 7.11: Comparison of the Q_μ models obtained from the two-station (group 2) and single-station (XAN347/94) methods.

ence may be attributed to focusing of seismic waves in the two station method which gives rise to higher Q_μ values.

The Q_μ models between XAN347/94 and group 2 agree very well at all depths (Figure 7.11). This agreement may be explained by absences of multipathing effects on the seismic waves used for the two-station method.

Comparison between Q_μ models of group 4 and MDJ070/99 show differences at shallow depths (Figure 7.12). Group 5 and MDJ147/99 are very different at all depths, except below 50 km (Figure 7.13). The similarity at greater depths may be simply due to the poor resolution at large depths.

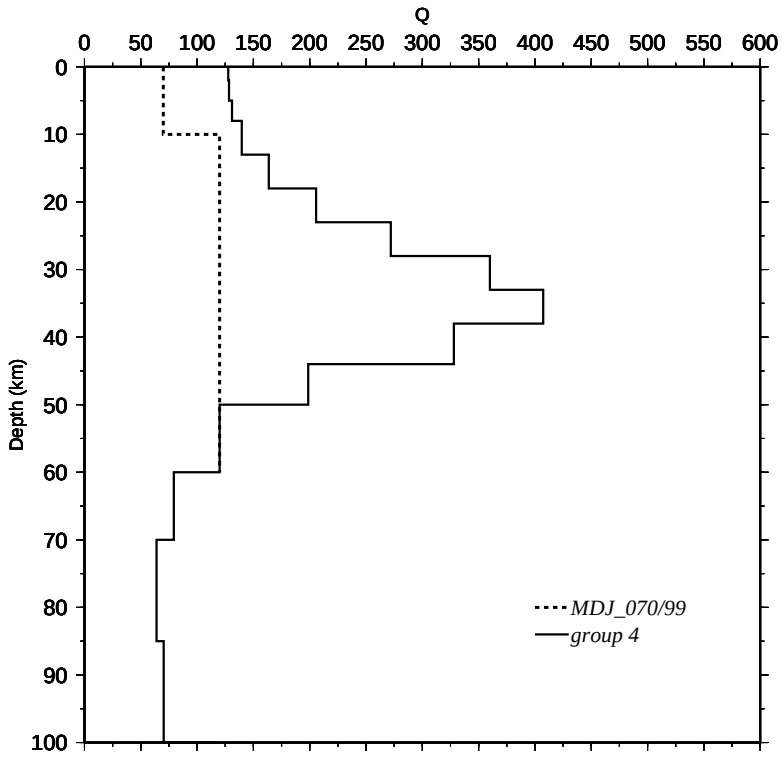

Figure 7.12: Comparison of the Q_μ models obtained from the two-station (group 4) and single-station (MDJ070/99) methods.

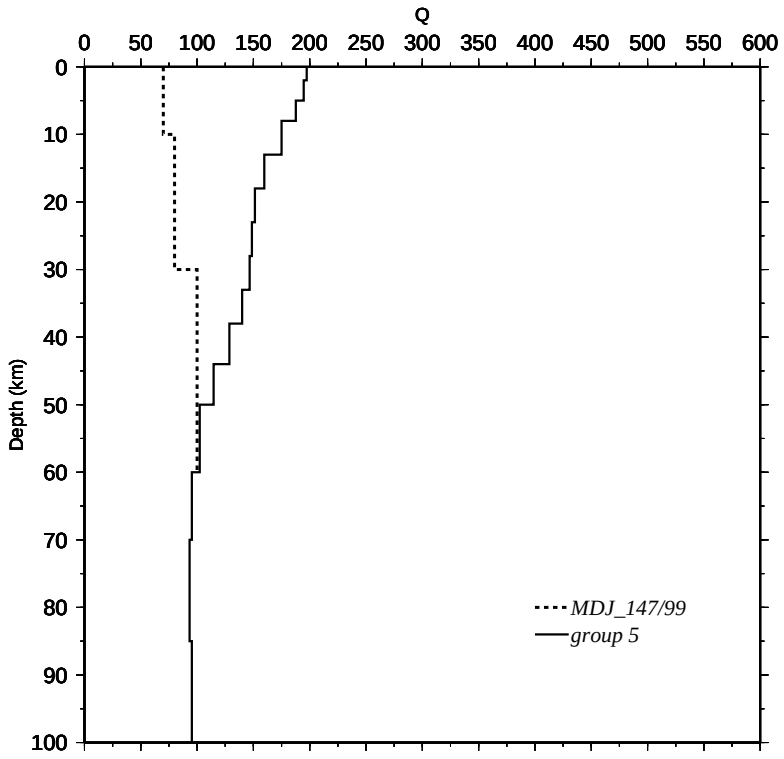

Figure 7.13: Comparison of the Q_μ models obtained from the two-station (group 5) and single-station (MDJ147/99) methods.

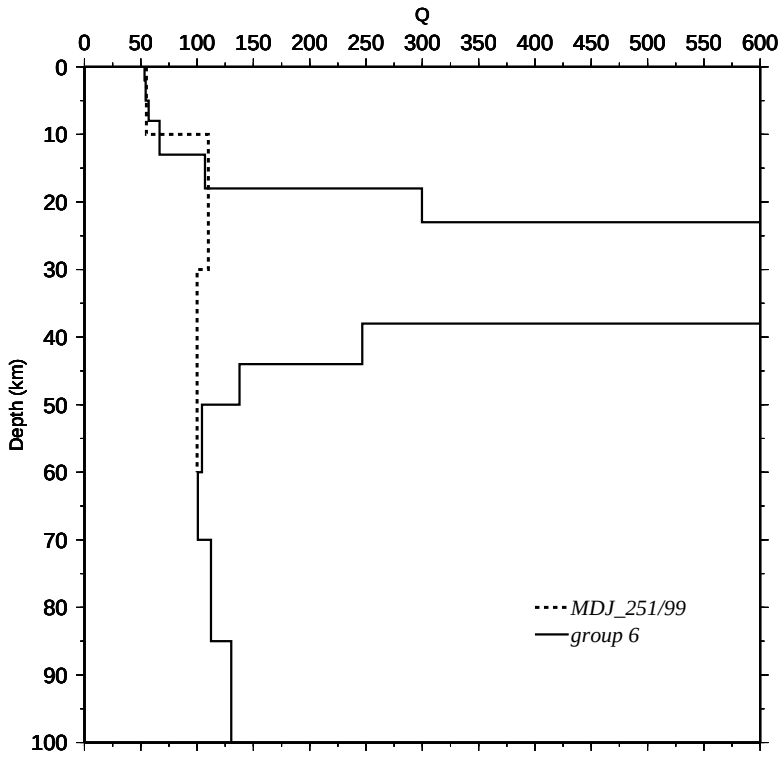

Figure 7.14: Comparison of the Q_μ models obtained from the two-station (group 6) and single-station (MDJ251/99) methods.

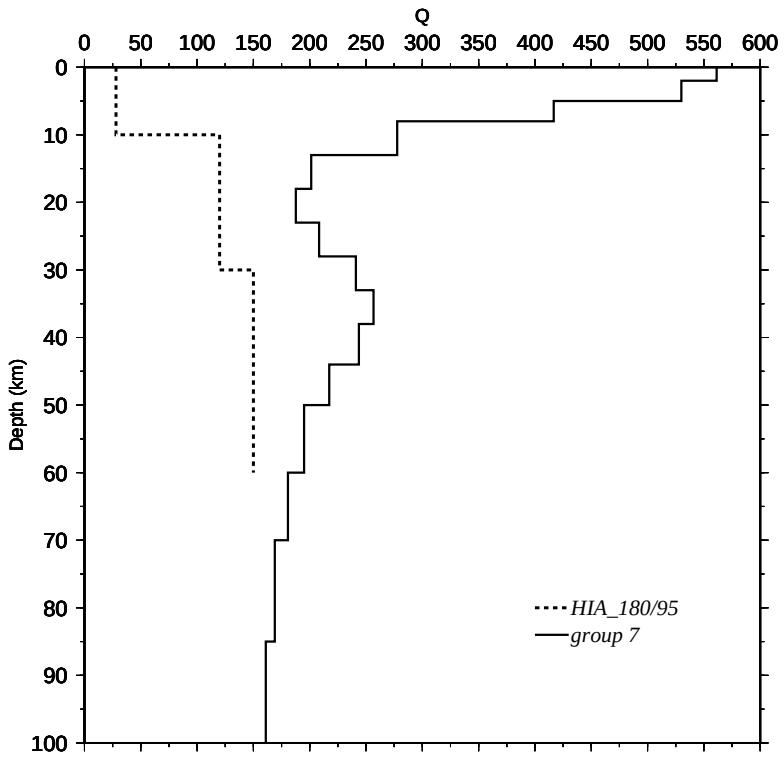

Figure 7.15: Comparison of the Q_μ models obtained from the two-station (group 7) and single-station (HIA180/95) methods.

Comparison between group 6 and MDJ251/99 Q_μ models agree very well for upper about 20 km and below 50 km (Figure 7.14). There is a high Q_μ value layer between about 20 and 50 km in the two-station result (group 6). This very high Q_μ layer is probably not realistic, being due to effects of focusing at the more distant station at intermediate periods.

There is a large difference between the Q_μ models of HIA180/95 and group 7 for all depths (Figure 7.15). I attribute these differences again to focusing at the distant station in the two-station method.

A comparison of the Q_μ model of group 8 and that of TLY173/95 shows that the two agree well for the upper 30 km (Figure 7.16). The

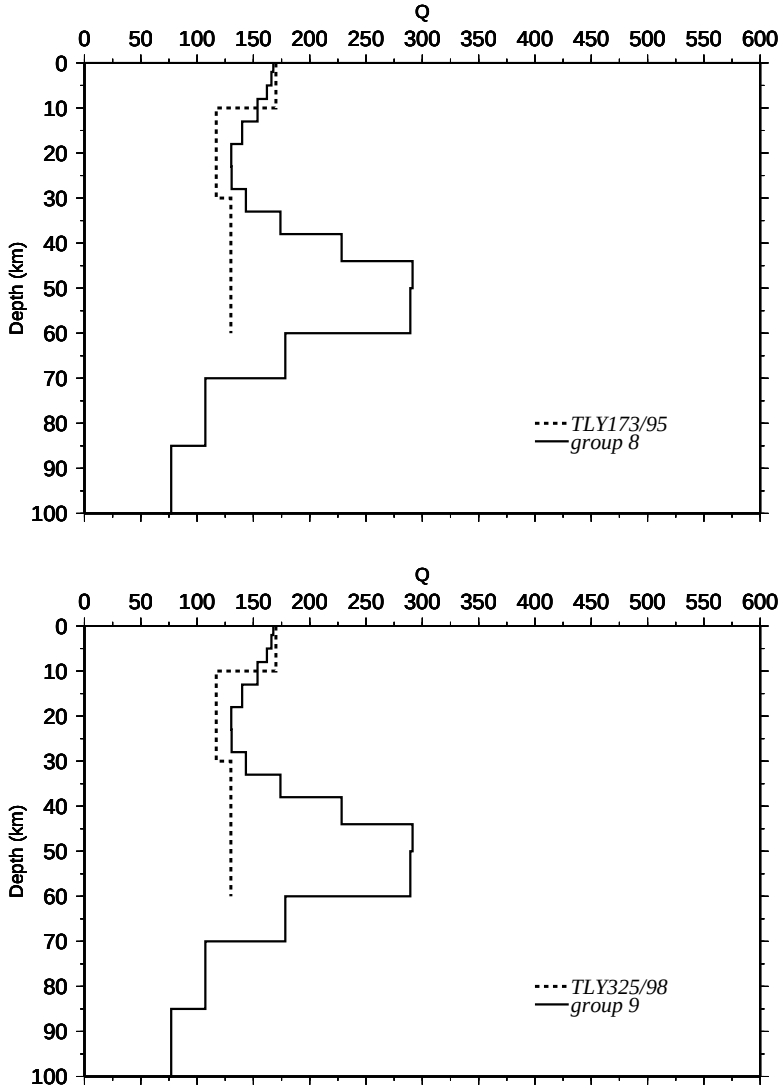

Figure 7.16: Comparison of the Q_μ models obtained from the two-station (group 8) and single-station (TLY173/95 and TLY325/98) methods.

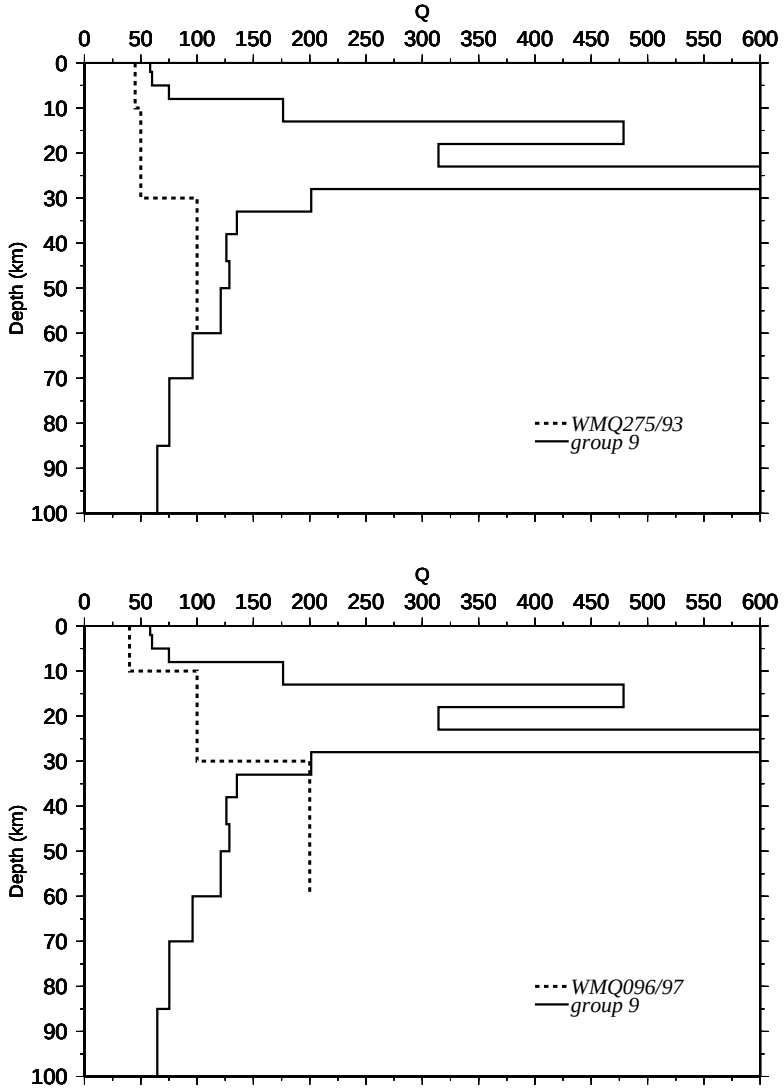

Figure 7.17: Comparison of the Q_μ models obtained from the two-station (group 9) and single-station (WMQ275/93 and WMQ096/97) methods.

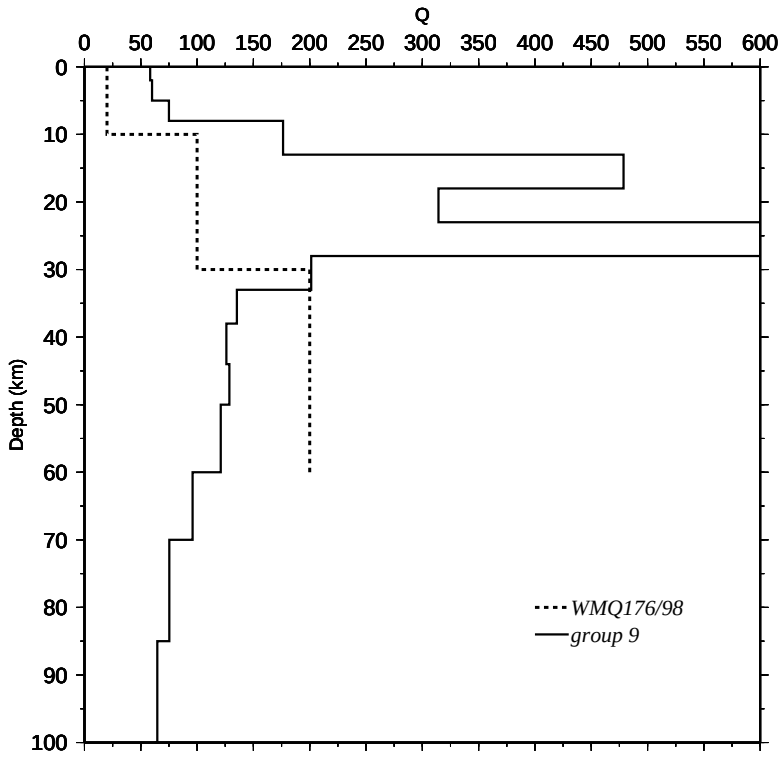

Figure 7.18: Comparison of the Q_μ models obtained from the two-station (group 9) and single-station (WMQ176/98) methods.

same agreement is shown between TLY325/98 and group 8. This probably occurs because shorter periods in the two-station method are not greatly affected by focusing/defocusing while longer periods are.

The Q_μ model of group 9 agrees well with those of WMQ275/93, WMQ096/97, and WMQ176/98 (Figures 7.17 and 7.18), only at very shallow depths. The large differences at greater depths can, again, be attributed to focusing of larger-period waves.

7.2.5 Comparison of the Q_μ models of southeastern Asia with those of eastern North America and the Middle East

The continental crust of eastern North America (ENA) has much higher Q_μ values when compared with those Q_μ values from single-station results for most of southeastern Asia. The upper 10 km of ENA has Q_μ values ranging form 200 to about 450 (Mitchell, 1980) while southeastern Asia has a maximum of about 250 for the stable South China Block, and about 160 for western Mongolia for the upper 10 km.

The depth range between 10 and 30 km has Q_μ values between about 300 and 1000 for ENA. The Q_μ values in southeastern Asia for that depth range (Layer 2) is between about 50 and 150.

For the upper 10 km, comparisons between Q_μ values from the single-station method of southeastern Asia and the Turkish and Iranian Plateaus (Cong, 1997) show that the Tibetan plateau and the Lake Baikal region have lower Q_μ values than those of the Turkish and the Iranian Plateaus. The South China Block and western Mongolia have higher Q_μ values than does the Turkish and Iranian Plateaus.

For Layer 2 (in southeastern Asia), the Q_μ values for the Turkish

and Iranian Plateaus are lower than most parts of southeastern Asia except for the Tibetan plateau, the Pamir thrust belt and the Burma-Thailand regions. The latter regions have Q_μ values that are similar to those of the Turkish and Iranian Plateaus.

7.3 Conclusions from two-station results

Differences in phase/group velocities between different regions in southeastern Asia reflect differences in tectonic activity, crustal thickness, and presence of thick sediments. Western China has lower phase or group velocities compared to those of eastern China.

Group velocity comparisons between this study and other studies in southeastern Asia show very good agreement at periods where both data sets are available. Southeastern Asia which is tectonically active, shows lower phase velocities than does the tectonically stable Canadian Shield.

The average interstation attenuation coefficients of some groups are inconsistent with the expected relationship with the corresponding group/phase velocities. This inconsistency may be due to effects of lateral heterogeneity which focus or defocus the seismic rays.

The tectonically active regions of western China and the western Mongolia have lower shear velocities at least for depth ranges between 15 km and 70 km than do the more stable regions of eastern China and southeastern Siberia. There is a systematic decrease in Q_μ values for shallow depths from eastern China to western China. Q_μ^{-1} structure correlates positively with the shear-wave velocity structure in south-

eastern China; this may be attributed to the weak or absent upper mantle lithosphere.

There is a good agreement between the shear-wave velocity structures obtained in this study with models obtained form earlier studies in Southeastern Asia. Southeastern Asia shows lower shear-wave velocities at almost all depths when compared with that of the Canadian Shield. The Turkish and Iranian Plateau in the Middle East has lower shear-wave velocities for the upper 80-100 km than does eastern China. Western China and western Mongolia have lower shear-wave velocities than the Turkish and Iranian Plateaus.

7.4 Conclusions from single-station results

My results from the single-station method, show that there are large lateral variations in Q_μ throughout the crust of southern Asia. These differences can easily affect regional determinations of magnitude if they are not taken into account.

In addition, the distributions of Q_μ with depth is also laterally variable. For instance, Q decreases with depth in the first 30 km of the crust in southeastern China but increases with depth through that depth range in southwestern China. These differences may cause difficulties in discriminating between earthquakes and explosions. Discriminants based on ratios of regional phases that travel through different depth ranges in the crust may not be applicable everywhere unless corrections can be made for the differing attenuation along the paths of those phases.

My results show that tectonically active regions in southeastern Asia, as indicated by higher seismicity and active folds, have low Q values while stable regions have relatively high Q values. This is consistent with Q determinations in other stable and tectonically active regions (e.g. Mitchell, 1995; Cong and Mitchell, 1998).

The low Q values in tectonically active regions may be due to fluid-filled fractures or permeable materials in the crust, for example in Tibet and the active fold systems, or the presence of high heat flow as in the Baikal region.

Comparison of Q_μ models from the two-station and single-station methods, wherever both models are available, show that the two results agree only for groups 2, 6, 8, and 9. Q_μ models for other groups, obtained by the two-station method are higher than those from the single-station models at all depths. The high Q_μ values in most of the groups in the two-station method may be due to focusing of seismic waves as they traverse different geological structures as they travel a long distance.

The Q_μ values for southeastern Asia are affected by lateral complexities along surface-wave paths, in most cases. This degrades the resolution for Q_μ models that are obtained for this region. Nevertheless, my results show that Q_μ values for this region are among the lowest in the world. They are comparable to those found earlier for the Middle East and lower than those found in most stable regions such as the United States.

Bibliography

Aki, K., Crustal structure in Japan from the phase velocity of Rayleigh waves, *Bull. Earthquake res. Inst. Tokyo Univ.*, 39, 255-283, 1961.

Aki, K., and K. Kaminuma, Phase velocity of Love waves in Japan, 1, Love waves from the Aleutia shock of March 9, 1957, *Bull. Earthquake Res. Inst. Tokyo Univ.*, 41, 243-259, 1963.

Anderson, D. L., and C. B. Archambeau, The anelasticity of the Earth, *J. Geophys. Res.*, 69, 2071-2084, 1964.

Anderson, D. L., A. Ben-Menahem, and C. B. Archambeau, Attenuation of seismic energy in the upper mantle, *J. Geophys. Res.*, 70, 1441-1448, 1965.

Barry, T. L., and R. W. Kent, Cenozoic Magmatism in Mongolia and the Origin of Central and East Asian Basalts, in Martin et al. (editors), *Mantle Dynamics and Plate Interactions in East Asia, Geodynamics Ser.*,27, AGU, Washington, D. C., 347-364, 1998.

Ben-Menahem, A., Observed attenuation and Q values of seismic surface waves in the upper mantle, *J. Geophys. Res.*, 70, 4641-4651, 1965.

Ben-Menahem, A., and S. J. Singh, Seismic waves and sources, Dover Publications, Inc., 2000.

Bird, G. P., Thermal and mechanical evolution of continetal convergence zones: Zagros and Himalayas, *Ph.D. thesis*, 422 pp., Mass. Inst. Of Technol., Cambridge, Mass., 1976.

Bloch, S., A. L. Hales, New techniques for the determination of surface wave phase velocities, *Bull. Seismol. Soc. Am.*, 58, 1021-1034, 1968.

Bloch, S., A. L. Hales, and M. Landisman, Velocities in the crust and upper mantle of southern Africa from multi-mode surface wave dispersion, *Bull. Seismol. Soc. Am.*, 59, 1599-1629, 1969.

Brune, J. N., and J. Dorman, Seismic waves and Earth structure in the Canadian shield, *Bull. Seismol. Soc. Am.*, 53, 167-210, 1963.

Brune, J. N., J. E. Nafe, and J. E. Oliver, A simplified method for the analysis and synthesis of dispersed wave trains, *J. Geophys. Res.*, 65, 287-304, 1960.

Burton, P., Estimates of Q^{-1} from seismic Rayleigh waves, *Geophys. J. Roy. Astron. Soc.*, 36, 167-189, 1974.

Cheng, C. C., and B. J. Mitchell, Crustal Q structure in the United States from Multi-mode Surface Waves, *Bull. Seismol. Soc. Am.*, 71, 161-181, 1981.

Chun, K. Y., and T. Yoshi, Crustal structure of the Tibetan plateau: A surface-wave study by a moving window analysis, *Bull. Seismol. Soc. Am.*, 67, 735-750, 1977.

Chung, S. -L., B. -M. Jahn, G. Wu, C. -H. Lo., and B. Cong, The Emeishan flood basalt in SW China: A mantle plume initiation model and its connection with continenatl breakup and mass extinction at the Permian-Triassic boundary, in Martin et. al., (editors) *Mantle Dynamics and Plate Interactions in East Asia, Geodynamics Ser.*,27, AGU, Washington, D. C., 47-58, 1998.

Cong, L., Lateral variation of velocity & Q in Middle East, *Ph.D. Dissertation*, 243 pp., Saint Louis University, St. Louis, Mo., 1997.

Cong, L., and B. J., Mitchell, Seismic velocity and Q structure of the Middle Eastern crust and upper mantle from surface wave dispersion and attenuation, *Pure Appl. Geophys.*, 153, 503-538, 1998.

Crosson, R. S., Crustal Structure Modeling of Earthquake Data 1. Simultaneous Least Squares Estimation of Hypocenter and Velocity Parameters, *J. Geophys., Res.*, 81, 3036-3046, 1976.

Der, Z., R. Masse, and M. Landisman, Effects of observational errors on the resolution of surface waves at intermediate distances, *J. Geophys. Res.*, 75, 3399-3409, 1970.

Dewey, J., and J. M. Bird, Mountain belts and the new global tectonics, *J. Geophys. Res.*, 2625-2647, 1970.

Dewey, J., and K. C. A. Burke, Tibet, Varsican, and Precambrian basement reactivation: products of continental collision, *Geology*, 81, 683-692, 1973.

Dingheng, Y., W., Z. Yuming, Z. Xiaoqing, W. Xinzheng, and L. Zengyue, Neotectonic Map of China and adjacent seas, 1:5000000, Geological Publishing House, Beijing, China, 1996.

Dziewonski, A., S. Bloch, and M. Landisman, Improvements in the transient analysis of seismic signals (abstract), *Trans. Am. Geophys. Un.*, 49, 508, 1968.

Dziewonski, A., S. Bloch, and M. Landisman, A technique for the analysis of transient seismic signals, *Bull. Seism. Soc. Am.*, 59, 427-444, 1969.

Dziewonski , A.M., and A.L. Hales, Numerical Analysis of Dispersed Seismic Waves, *In B.A. Bolt (editor), Seismology: Surface Waves and Earth Oscillations (Methods in Computational Physics, Vol. 11)*. New York: Academic Press, 1972.

Ewing, W. M., W. S. Jardetsky, and F. Press, Elastic waves in layered Media , McGraw-Hill, New York, 380 pp., 1957.

Feng, C.C, and T.L. Teng, Three Dimensional Crust and Upper Mantle structure of the Eurasian continent, *J. Geophys. Res.*, 88, 2261-2272, 1983.

Futterman, W. I., Dispersive body waves, *J. Geophys. Res.*, 67, 5279-5291, 1962.

Harkrider, D. G., Surface waves in multi-layered media, 1. Rayleigh and Love waves from buried sources in a multi-layered elastic half-space, *Bull. Seismol. Soc. Am.*, 54, 627-671, 1964.

Haskell, N.A., The dispersion of surface waves on multi-layered media, *Bull. Seismol. Soc. Am.*, 43, 17-34, 1953.

Herrin, E., and T. Goforth, Phase-matched filters: Application to the study of Rayleigh waves, *Bull., Seism., Soc., Am.*, 67, 1259-1272, 1977.

Herrmann, R. B., Some aspects of band-pass filtering of surface waves, *Bull. Seism. Soc. Am.*, 63, 663-671, 1973.

Herrmann, R. B. (editor), Computer Programs in seismology, Volume III, *Saint Louis University*, St. Louis, Mo., 1985.

Herrmann, R. B. (editor), Computer Programs in seismology, Volume II, *Saint Louis University*, St. Louis, Mo., 1987.

Herrmann, R. B. (editor), Computer Programs in seismology, Volume IV, *Saint Louis University*, St. Louis, Mo., 1987.

Jackson, D. D., Interpretation of inaccurate, insufficient and inconsistent data, *Geophys. J. Roy. Astron. Soc.*, 28, 97-110, 1972.

Jackson, D. D., and D. L. Anderson, Physical mechanisms for seismic wave attenuation, *Rev. Geophys.*, 8, 1-63, 1970.

Jackson, D. D., and N. R. Burkhard, Density and surface wave inversions, *Geophys. Res. Lett.*, 3(11), 637-638, 1976.

Kaminuma, K., The crust and upper mantle structure in Japan, *Bull. Earthquake Res. Inst. Tokyo Univ.*, 44, 495-510, 1966.

Kaminuma, K., and K. Aki, Crustal structure in Japan from the phase velocity of Rayleigh waves, 2, Rayleigh waves from the Aletutian shock of March 9, 1957, *Bull. Earthquake Res. Inst. Tokyo Univ.*, 41, 217-241, 1963.

Khutorskoy, M. D., and V. V. Yarmoluk, Heat flow, structure and evolution of the lithosphere of Mongolia, *Tectonophysics*, 164, 315-322, 1989.

Knopoff, L., S. Mueller, and W. L. Pilant, Structure of the crust and upper mantle in the Alps from the phase velocity of Rayleigh waves, *Bull. Seismol. Soc. Am.*, 56, 1009-1044, 1966.

Kovach, R., Seismic Surface Waves and Crustal and Upper mantle Structure, *Rev. Geophys. and Space Phys.*, 16, 1-13, 1978.

Lanczos, C., Linear differential perators, Dover publications, inc., 1997.

Landisman, M., A. Dziewonski, and Y. Sato, Recent improvements in the analysis of surface wave observations, *Geophys. J.*, 17, 369-403, 1969.

Lay, T., and T. W. Wallace, Modern Global Seismology, Academic Press, 1995.

Lee, W., and S. Solomon, Inversion schemes for surface wave attenuation and Q in the crust and upper mantle, *Geophys. J. Roy. Astron. Soc.*, 43, 47-71, 1975.

Levenberg, K., A method for the solution of certain non-linear problems in least squares, *Quant. Appl. Math.*, 2, 164-168, 1944.

Levshin, A. L., M. H. Ritzwoller, Characteristics of surface waves generated by events on and near the Chinese nuclear test site, *Geophys. J. Int.*, 123, 131-148, 1995.

Liu, D. Y., Seismic tomography in China, *International Geological Congress, Tokyo*, 3, 668, 1992.

Ludwig, W. J., J. E. Nafe, and C. L. Drake, Seismic refraction, *In The Sea*, 4, Maxwell, A. E. ed., Wiley-Interscience, New York, 53-84, 1970.

Lysmer, J., and L. A. Drake, The propagation of Love waves across nonhorizontally layerd strusctures, *Bull. Seism. Soc. Am.*, 61, 1233-1251, 1971.

Ma, X. Y., Lithospheric dynamics map of China and adjacent seas (1:4,000,000) and explanatory notes, 53 pp., Publishing House of Geology, Bejing, 1987.

Mahdi, H., and G. L. Pavlis, Velocity variations in the crust and upper mantle beneath the Tien Shan inferred from Rayleigh wave dispersion: Implications for tectonic and dynamic processes, *J. Geophys. Res.*, 103, 2693-2703, 1998.

Marquardt, D. W., An algorithm for least-squares estimation of nonlinear parameters, *J. Soc. Ind. Appl. Math.*, 11, 431-441, 1963.

McGarr, A., Amplitude variations of Rayleigh waves-Horizontal Refraction, *Bull. Seismol. Soc. Am.*, 59, 1307-1334, 1969.

Mendenhall, W., and R. L., Scheaffer, Mathematical Statistics with Applications, Wadsworth Publishing Company, Inc., 1973.

Menke, W., Geophysical Data analysis: Discrete inverse theory, Academic Press, Inc., 1984.

Menzies, M. A., Y. Xu, Geodynamics of the North China Craton, in Martin et. al., (editors) *Mantle Dynamics and Plate Interactions in East Asia, Geodynamic Series*, AGU, Washington, D. C., 27, 155-165, 1998.

Metcalfe, I., Allochthonous terrane processes in Southeast Asia, *Phil. Trans. Roy. Soc. London*, A331, 625-640, 1990.

Mitchell, B. J., Frequency dependence of shear wave internal friction in the continental crust of eastern North America, *J. Geophys. Res.*, 85, B10, 5212-5218, 1980.

Mitchell, B. J., Anelastic structure and evolution of the continental crust and the upper mantle from seismic surface wave attenuation, *Rev. Geophys.*, 33, 441-462, 1995.

Mitchell, B. J., Y. Pan, J. Xie, and L. Cong, L_g coda Q variation across Eurasia and its relation to crustal evolution, *J. Geophys. Res.*, 102, 22767-22779, 1997.

Molnar, P., The geological evolution of the Tibetan plateau, *Ame. Sci*, 77, 350-360, 1989.

Molnar, P., and P. Tapponnier, Cenozoic Tectonics of Asia: Effects of a Continental Collision, *Science*, 189, 419-426, 1975.

Molnar, P., T. J. Fitch, and F. T. Wu, Fault plane solutions of shallow earthquakes and contemporary tectonics in Asia, *Earth Plan. Sci. Lett.*, 19, 101-112, 1973.

Mueller, S., A new model of the continental crust, In *Geophysical Monograph 20: The Earth's Crust*, Heacock, J. G., ed., Amer. Geophys. Union, Washington, D.C., pp. 289-317, 1977.

Nábělek, J., W. P. Chen, and H. Ye, The Tangshan Earthquake Sequence and Its Implications for the Evolution of the North China Basin, *J. Geophys. Res.*, 92, 12651-12628, 1987.

Nafe,J. E., Assembled velocity density data, *Sea*, 4(1), 53-84, 1970.

Oliver, J., A summary of observed seismic surface wave dispersion, *Bull. Seismol. Soc. Am.*, 52, 81-86, 1962.

Patton, H., Crust and upper Mantle structure of the Eurasian continent from the phase velocity and Q of surface waves. *Rev. Geophys.*, 18, 605-625, 1980.

Pavlis, G. L., and H. Mahdi, Surface wave propagation in central Asia: Observations of scattering and multipathing with the Kyrgyzstan broadband array, *J. Geophys. Res.*, 101, 8437-8455, 1996.

Pilant, W. L., and L. Knopoff, Observations of multiple seismic event, *Bull. Seismol. Soc. Am.*, 54, 19-39, 1964.

Pilant, W. L., and L. Knopoff, Inversion of phase and group slowness, *J. Gephys. Res.*, 15, 2135-2136, 1970.

Pines, I., T. Teng, and R. Rosenthal, A surface wave dispersion study of the crustal and upper mantle structure of China, *J. Geophys., Res.*, 85, 3829-3844, 1980.

Powell, C. M., P. J. Conagham, Tectonic models of the Tibetan plateau, *Geology*, 3, 727-731, 1975.

Press, F., M. Ewing, and J. Oliver, Crustal structure and surface wave dispersion in Africa, *Bull. Seismol. Soc. Am.*, 46, 97-103, 1956.

Prodehl, C.), The structure of the crust-mantle boundary beneath North America and Europe as derived from explosion seismology, In *Geophysical Monograph 20: The Earth's Crust*, Heacock, J. G., ed., Amer. Geophys. Union, Washington, D.C.,349-369,1977.

Ren, J., C. Jiang, Z. Zhang, and D. Qin, Geotectonic Evolution of China, *Science Press, Springer-Verlag*, 1987.

Rosenthal, R., and T. Teng, A surface wave study of the South-China subplate, Tech. Rep. 77-9, Univ. of S. Calif., Los Angeles, Calif., 1977.

Sato, Y., Analysis of dispersed surface waves by means of the Fourier transform, 1, *Bull. Earthquake Res. Inst. Tokyo Univ.*, 33, 33-47, 1955.

Sato, Y., Analysis of dispersed surface waves by means of the Fourier transform, 2, Synthesis of movement near the origin, *Bull. Earthquake Res. Inst. Tokyo Univ.*, 34, 9-18, 1956.

Sato, Y., Attenuation, dispersion and the wave guide of the G wave, *Bull. Seismol. Soc. Am.*, 48, 231-251, 1958.

Smith, A. D., The Geodynamic Significance of the Dupal Anomaly in Asia, in Martin et. al., (editors) *Mantle Dynamics and Plate Interactions in East Asia. Geodynamic Series*, AGU, Washington, D. C., 27, 89-105, 1998.

Takeuchi, H., J. Dorman, and M. Saito, Partial derivatives of surface wave phase velocity with respect to physical parameter changes within the earth, *J. Geophys. Res.*, 69, 3429-3442, 1964.

Tapponnier, P., and P. Molnar, Active faulting and Tectonics in China, *J. Geophys., Res.*, 82, 2905-2930, 1977.

Tapponier, P., and P. Molnar, Active faulting and Cenozoic tectonics of the Tien Shan, *J. Geophys. Res.*, 84, 3425-3457, 1979.

Taylor, S.R., and M.N. Toksöz, Measurement of Inter-station phase and group velocities and Q using Wiener filtering, *Bull. Seismol. Soc. Am.*, 72, 73-91, 1982.

Teng, J. W., Q. S. Wang, Y. C. Liu, and S. Y. Wei, Geophysical field characteristics, distribution and formation of hydrocarbon bearing basins of eastern China, *Journal of Geophysics*, 26, 4, 319-330, 1983.

Toksöz, M. N., and D.L. Anderson, Phase velocities of long-period surface waves and structure of the upper mantle, 1, Great-circle Love and Rayleigh wave data, *J. Geophys. Res.*, 71, 1649-1658, 1966.

Tryggvason, E., Dissipation of Rayleigh wave energy, *J. Geophys. Res.*, 70, 1449-1455, 1965.

Tsai, Y. B., and K. Aki, Precise focal depth determination from amplitude spectra of surface waves, *J. Geophys. Res.*, 75, 5729-5743, 1970.

Tseng, J.-S., and Z. Sung, Phase velocities of Rayleigh waves in China, *Acta Geophys., Sinica*, 12 148-165, 1963.

Turin, G. L., An introduction to Matched Filters, *I. R. E. Trans., IT-6*, 311-329, 1960.

Wei, D., T. Seno, Determination of the Amurian Plate Motion, in Martin et. al., (editors) *Mantle Dynamics and Plate Interactions in East Asia. Geodynamic Series*, AGU, Washington, D. C., 27, 337-346, 1998.

Wessel, P., and W. H. F. Smith, The Generic Mapping Tools, version 3.4, 2001.

Weir, S., Surface Wave dispersion and Earth structure in south-eastern China, *Geophys. J. R. Astron. Soc.*, 69, 33-47, 1982.

Wiggins, R. A., The general linear inverse problem: implications of surface waves and free oscillations for Earth structure, *Rev. geophys. Space Phys.*, 10, 251-285, 1972.

Windley, B. F., and M. B. Allen, Mongolian plateau: Evidence for a late Cenozoic mantle plume under central Asia, *Geolgy*, 21, 295-298, 1993.

Wu, F. T., and A.L. Levshin, Surface-Wave group velocity tomography of East Asia, *Phys. Earth Planet. Inter.*, 84, 59-77, 1994.

Wu, F., A. L. Levshin, and V. M. Kozhevnikov, Rayleigh wave Group Velocity Tomography of Siberia, China and the Vicinity, *Pure Appl. Geophys.*, 149, 447-473, 1997.

Yacoub, N. K., and B. J. Mitchell, Attenuation of Rayleigh-Wave amplitudes across Eurasia, *Bull. Seismol. Soc. Am.*, 67, 751-769, 1977.

Yang, Z. Y., Y. Q. Cheng, and H. Z. Wang, The geology of China, *Oxford, England, Clarendon Press*, 303p, 1986.

Yu, G. K. and B. J. Mitchell, Regionalized shear velocity models of the Pacific upper mantle from observed Love and Rayleigh wave dispersion, *Geophys. J. R. Astr. Soc.*, 57, 311-341, 1979.

Zhang, Y.-S, Three-Dimensional Upper Mantle Structure beneath East Asia and its Tectonic Implications, in Martin et al., (editors) *Mantle Dynamics and Plate Interactions in East Asia. Geodynamic Series*, AGU, Washington, D. C., 27, 11-23, 1998.

Zorin, Yu. A., M. R. Novoselova, E. Kh. Turutanov, V. M. Kozhevnikov, Structure of the lithosphere of the Mongolian-Siberian mountainous province, *Journal of Geodynamics*, 11, 327-342, 1990.

Biography of the Author

Alemayehu Lakew Jemberie was born in Debremarkos, Gojjam, Ethiopia on February 18, 1967. He was born to and raised by a very disciplined and loving family. He was taught to respect others and protect his rights.

Alemayehu has studied hard since elementary school as a result of the courage he acquired from the example of his family and teachers. He always remembers what his father used to tell him, "If you stood first in your class, I will buy you a bulla gabardine (white suit)".

He joined Addis Ababa University in 1984 and earned his first degree in Physics in 1988. He taught college physics from 1989 to 1991 at Arbaminch Water Technology Institute, Ethiopia. Those two years provided golden opportunities for strengthening his background in theoretical and experimental physics. He learned a lot from an Indian expatriate Professor Dr. V. R. Prakash.

He joined the Graduate School of Addis Ababa University in 1991 to study for a Masters degree in Physics. After taking many Physics courses he had the opportunity, in 1992, to register for a Geophysics course. That course caused him to be interested in Geophysics. Dr. Tilahun Mamo inspired him, the way he taught him Geophysics, in particular seismology.

After graduating in 1993 from the Graduate School, he taught college physics for almost two years. During those two years the teachers' assembly elected him as a teachers' representative in the academic

Commission of Arabaminch Water Technology Institute. He fought hard for the rights of teachers against the corrupt government appointees of the Institute.

In 1995 he was awarded a scholarship from the Training and Research in Italian Labs (TRIL) of the International Center for Theoretical Physics (ICTP), Trieste, Italy. He received the basic training for research from June 1995 to April 1996 at the ICTP. From August 1997 to the present he has been at the Graduate School of Saint Louis University, USA.

Alemayehu's wife, Menbere Ejigu Getu, and his two daughters, Biruh Alemayehu and Wossenyelesh Alemayehu have been very supportive of him. On August 22, 2001, his wife bore him a son named Befekadu Alemayehu.